Mechanochemical induction of phase transition in mineralogical compounds

Dissertation

zur Erlangung des Grades

„Doktor der Naturwissenschaften“

im Promotionsfach Chemie

im Fachbereich Chemie, Pharmazie und Geowissenschaften der

Johannes Gutenberg – Universität Mainz

Marcel Maslyk

geboren in Wiesbaden

Mainz, 2022

Dekanin: [redacted]

Erster Berichtserstatter: [redacted]

Zweite Berichtserstattering: [redacted]

Tag der mündlichen Prüfung: 15.05.2022

Declaration

The thesis has been prepared as part of the Ph.D. programme in Chemistry at Mainz University in the period between September 2018 and December 2021 under the supervision of Univ. Prof. Dr. Wolfgang Tremel at the Department of Chemistry, Johannes Gutenberg – University Mainz. I certify that I have written this dissertation independently and without external assistance. All sources and tools used are fully acknowledged.

Erklärung

Hiermit erkläre ich, dass die vorliegende Arbeit in der Zeit von September 2018 bis Dezember 2021 unter der Leitung von Univ.-Prof. Dr. Wolfgang Tremel am Institut für Anorganische Chemie und Analytische Chemie der Johannes Gutenberg–Universität Mainz angefertigt wurde. Ich versichere, die vorliegende Arbeit selbstständig und ohne fremde Hilfe verfasst zu haben. Alle verwendeten Quellen und Hilfsmittel sind vollständig angegeben.

Mainz, January 2022

Für meine Familie

"I am among those who think that science hast great beauty. A scientist in his laboratory is not only a technician: he is also a child placed before natural phenomena which impress him like a fairy tale."

Maria Skłodowska-Curie

Abstract

In this PhD thesis, the mechanochemically induced amorphization and phase transformation of mineral phases with prospects for industrial applications were investigated using inorganic “impurities” and organic dispersants. In particular, hopeite ($Zn_3(PO_4)_2 \times 4H_2O$), a material which finds application as a dental cement, limestone ($CaCO_3$), one of the main constituents in cement manufacturing and gypsum ($CaSO_4 \times 2H_2O$), mainly used in plasterboard production, were investigated. The fundamental interest in these phases stems from the synthetic challenges regarding their metastable intermediates and the control of the underlying recrystallization pathways. By using a high-energy ball mill with different reaction parameters, new synthetic approaches to metastable intermediates in mineral phases could be achieved.

This thesis can be subdivided into three main projects: (i) the synthesis of amorphous zinc phosphate by adding iron impurities (BM-AZP-Fe), (ii) the development of a new alkali activated binder *via* an amorphous sodium silicate calcium carbonate (aNaSiCC) and a new mechanochemical approach to stable bassanite dispersions (BMCS-MeOH). Although these minerals have little in common at first glance, there are several common features that led to the selection of these systems. These minerals contain anionic building blocks, which have a similar chemical connectivity pattern (i.e., phosphates/silicates, carbonates/sulfates). They are all readily available, which makes them excellent basic materials for industrial scale production, and they have a pronounced polymorphism. Since amorphous intermediates appeared in almost all systems, structural characterization by powder X-ray diffraction was not possible due to the lack of long-range order. Therefore, local probes such as Fourier – transformed infrared spectroscopy (FTIR), solid-state nuclear magnetic resonance spectroscopy (ssNMR) and total scattering analysis were used to gain insight into the local structures. This work not only provides new insights into the mechanochemical synthesis pathways and the underlying reaction parameters, but also allows the control of recrystallization pathways through the selective use of dispersants.

The first project addresses on the formation of amorphous zinc phosphate (AZP) starting from hopeite ($Zn_3(PO_4)_2 \times 4H_2O$). In the search for a top-down process to amorphous intermediates, iron impurities in zinc phosphate were found to trigger amorphization during grinding in a high-energy ball mill. The amorphization process was followed by Fourier transform infrared spectroscopy (FTIR), powder X-ray diffraction (PXRD), nuclear magnetic resonance spectroscopy (NMR), differential thermal analysis (DTA) and

thermogravimetric analysis (TG). ^{57}Fe Mössbauer spectroscopy was used to study the iron environment at the intermediate stages. Since amorphous intermediates eventually recrystallize to stable polymorphs, thermal recrystallization of BM-AZP-Fe and recrystallization in water were studied.

In the search for new routes to cementitious materials via mechanochemistry, a new synthesis protocol for a calcium silicate hydrate (C-S-H) phase was developed in the second project. The first part of this study focused on the reaction of calcite (limestone) and sodium metasilicate to produce an activated amorphous precursor with calcium and silicate components. By analyzing the crystallization pathway it could be shown that the amorphous precursor (aNaSiCC) crystallizes *via* several metastable intermediates, *pirssonite* ($Na_2Ca(CO_3)_2 \times 2H_2O$), *gaylussite* ($Na_2Ca(CO_3)_2 \times 5H_2O$) and *monohydrocalcite* ($CaCO_3 \times 1H_2O$). Moreover, it could be demonstrated that aNaSiCC forms through a simple metathesis reaction between calcium carbonate ($CaCO_3$) and sodium metasilicate (Na_2SiO_3). The leads to a (sodium) calcium silicate matrix, which reacts to a C-S-H like phase after activation with NaOH. In essence, this is a novel mechanochemical route for producing a cementitious phase that bypasses the conventional thermal decomposition of limestone and the associated release of the greenhouse gas carbon dioxide during cement production.

Mechanochemical reactions use dispersants, which until now have mainly been used to act as heat dissipation agents. In fact, these dispersants can also be involved in the reaction as reactive components. The next chapter not only shows that the phase change from gypsum ($CaSO_4 \times 2\ H_2O$) to bassanite ($CaSO_4 \times 0.5\ H_2O$) is controlled by the dispersant, but also analyzes at the molecular level the interactions leading to this phase transformation. Cyclohexane as dispersant only led to the formation of a mixture of bassanite and gypsum, and the reaction product did not exhibit a distinct morphology. With methanol, bassanite nanoparticles (BMCS-MeOH) were formed by milling, based on the reversible binding of the dispersant. Prolonged grinding allowed the formation of a stable alcoholic dispersion of bassanite nanocrystals formed from needle-shaped crystallites containing methanol as a reversibly bound surface ligand.

Finally, the amorphization of monohydrocalcite ($CaCO_3 \times H_2O$) using ethanol as reactive dispersant and the synthesis of magadiite with partial ion exchange ($Na_2Si_{14}O_{28}(OH)_2\ yH_2O$) were studied in two side projects. Ion-exchanged magadiite was used in a collaboration using ADT (Automated Diffraction Tomography) to build a structural model for the natural mineral magadiite.

Kurzzusammenfassung

In dieser Dissertation wurde die mechanochemische Amorphisierung und Phasenumwandlung von Mineralphasen mit der Perspektive für industrielle Anwendungen unter Verwendung anorganischer „Verunreinigungen“ und organischer Dispersionsmittel untersucht. Im Einzelnen wurden Hopeit ($Zn_3(PO_4)_2$ x $4H_2O$), ein Material, das als Zahnzement Vernwedung findet, Kalkstein ($CaCO_3$), einer der Hauptbestandteile bei der Zementherstellung und Gips ($CaSO_4$ x $2H_2O$), der für die Herstellung von Gipsplatten verwendet wird, untersucht. Das grundlegende Interesse an diesen Systemen ergibt sich aus den synthetischen Herausforderungen hinsichtlich ihrer metastabilen Zwischenstufen und der Kontrolle der zugrundeliegenden Rekristallisationswege. Durch Verwendung einer Hochenergie-Kugelmühle konnten neue synthetische Ansätze zur Herstellung metastabiler Zwischenprodukte in diesen Mineralphasen erreicht werden. Dieser Arbeit kann in drei Hauptprojekte unterteilt werden: (i) die Synthese von amorphen Zinkphosphat durch Zugabe von Eisenverunreinigungen (BM-AZP-Fe), (ii) die Entwicklung eines neuen alkaliaktivierten Bindemittels über ein amorphes Natriumsilikat-Calciumcarbonat (aNaSiCC) und (iii) ein einen neuen mechanochemischen Ansatz für stabile Bassanit-Dispersionen (BMCS-MeOH). Obwohl diese Minerale auf den ersten Blick wenig gemeinsam haben, gibt es mehrere gemeinsame Merkmale, die zur Auswahl dieser Systeme führten. Sie enthalten anionische Bausteine, die ein ähnliches chemisches Konnektivitätsmuster aufweisen (d.h. Phosphate/Silikate, Carbonate/Sulfate). Sie sind alle leicht verfügbar, was sie zu ausgezeichneten Grundstoffen für die industrielle Produktion macht und sie besitzen eine ausgeprägte Polymorphie. Da in fast allen Systemen amorphe Zwischenstufen auftraten, war eine strukturelle Charakterisierung durch Pulverröntgendiffraktometrie wegen fehlender Fernordnung nicht möglich. Daher wurden lokale Sonden wie Fourier-transformierte Infrarotspektroskopie (FTIR), Festkörper-Kernresonanz-Spektroskopie (ssNMR) und Totalstreuungsanalyse eingesetzt. Diese Arbeit liefert nicht nur neue Einblicke in die mechanochemischen Synthesewege und die zugrundeliegenden Reaktionsparameter, sondern ermöglicht auch die Steuerung der Rekristallisationswege durch den selektiven Einsatz von Dispersionsmitteln.

Das erste Projekt befasst sich mit der Bildung von amorphem Zinkphosphat (AZP) ausgehend von Hopeit ($Zn_3(PO_4)_2 \times 4H_2O$). Bei der Suche nach einem Top-down-Prozess zur Herstellung amorpher Zwischenprodukte zeigte sich, dass Eisenverunreinigungen im

Zinkphosphat die Amorphisierung während des Mahlens in einer Hochenergie-Kugelmühle triggern. Der Amorphisierungsprozess wurde mittels Fourier-Transformations-Infrarot-spektroskopie (FTIR), Pulverröntgendiffraktometrie (PXRD), kernmagnetischer Resonanz-spektroskopie (NMR), Differentialthermoanalyse (DTA) und thermogravimetrischer Analyse (TG) verfolgt. ^{57}Fe-Mössbauer-Spektroskopie wurde zur Untersuchung der Eisenumgebung in den Zwischenstufen eingesetzt. Die thermische Rekristallisation der amorphen Zwischenstufe BM-AZP-Fe und die Rekristallisation in Wasser wurden analysiert.

Auf der Suche nach einem alternativen Weg zu zementartigen Materialien durch den Einsatz der Mechanochemie wurde im zweiten Projekt ein neues Syntheseprotokoll für eine Calcium-Silikat-Hydrat (C-S-H)-Phase entwickelt. Der erste Teil dieser Untersuchung befasst sich mit der Reaktion von Calcit (Kalkstein) und Natriummetasilikat zur Herstellung einer aktivierten amorphen Vorstufe mit Calcium- und Silikatkomponenten. Durch die Analyse des Kristallisationsweges konnte gezeigt werden, dass der amorphe Vorläufer (aNaSiCC) über mehrere metastabile polymorphe Zwischenstufen kristallisiert: *Pirssonit* ($Na_2Ca(CO_3)_2 \times 2H_2O$), *Gaylussit* ($Na_2Ca(CO_3)_2 \times 5H_2O$) und *Monohydrocalcit* ($CaCO_3 \times H_2O$). aNaSiCC wird durch eine einfache Metathesereaktion zwischen Calciumcarbonat ($CaCO_3$) und Natriummetasilikat (Na_2SiO_3) gebildet. Dabei entsteht eine reaktive (Natrium-)Calciumsilikatmatrix, die sich nach Aktivierung durch NaOH in eine C- S-H-ähnliche Phase umwandelt. Unter dem Strich bleibt ein neuartiger mechano-chemischer Weg zur Herstellung einer zementartigen Phase, der die herkömmliche thermische Zersetzung von Kalkstein und die damit verbundene Freisetzung des Treibhausgases Kohlendioxid bei der Zementherstellung umgeht.

Bei mechanochemischen Reaktionen werden Dispergiermittel eingesetzt, deren hauptsächlicher Einsatz die Wärmeableitung darstellt. Tatsächlich können diese Dispergiermittel aber auch als reaktive Komponenten an der mechanochemischen Reaktion beteiligt sein. Das folgende Kapitel zeigt einerseits, dass der Phasenübergang von Gips ($CaSO_4 \times 2H_2O$) zu Bassanit ($CaSO_4 \times ½H_2O$) durch das Dispergiermittel gesteuert wird. Es analysiert zudem auf molekularer Ebene die Wechselwirkungen, die zu dieser Phasenumwandlung führen. Während Cyclohexan als Dispergiermittel lediglich zur Bildung eines Gemischs aus Bassanit und Gips führte und das Reaktionsprodukt keine ausgeprägte Morphologie aufwies, bilden sich mit Methanol beim Mahlen aufgrund der reversiblen Bindung des Dispergiermittels Bassanit-Nanopartikel (BMCS-MeOH). Längeres Mahlen ermöglichte die Bildung einer stabilen alkoholischen Dispersion von

Bassanit-Nanokristallen, die aus nadelförmigen Kristalliten mit Methanol als reversibel gebundenem Oberflächenliganden bestehen.

Schließlich wurden in zwei Nebenprojekten die Amorphisierung von Monohydrocalcit ($CaCO_3 \times H_2O$) unter Verwendung von Ethanol als reaktivem Dispersionsmittel und die Synthese von Magadiit mit partiellem Ionenaustausch ($Na_2Si_{14}O_{28}(OH)_2 \times yH_2O$) untersucht. Die Struktur des ionenausgetauschten Magadiit wurde in einer Zusammenarbeit mit einer Mainzer Gruppe und mehreren externen Partnern verwendet, um mittels ADT (Automated Diffraction Tomography) ein Strukturmodell für das natürliche Mineral Magadiit zu erstellen.

List of publications

M. Maslyk, S. Bach. W. Li, S. I. Shylin, M. Panthöfer, B. Barton, V. Ksenofontov, K. Xu, B. Meermann, U. Kolb, J. Schmedt auf der Günne, W. Tremel. Understanding the Stability and Recrystallization Behavior of Amorphous Zinc Phosphate. *J. Phys. Chem. C.* **2021**, 125, 2636-2647

M. Maslyk, T. Gäb, G. Matveeva, P. Opitz, M. Mondeshki, Y. Krysiak, U. Kolb, W. Tremel. Multistep Crystallization Pathways in the Ambient-Temperature Synthesis of a New Alkali-Activated Binder, *Adv. Funct. Mater.* **2021,** *31*, 2108126

M. Maslyk, Z. Dallos, M. Koziol, S. Seiffert, T. Hieke, K. Petrovic, U. Kolb, M. Mondeshki, W. Tremel. A fast and sustainable route to bassanite nanocrystals from gypsum. *Adv. Funct. Mater.*, **2022**, *31*, accepted

M. Maslyk, M. Mondeshki, W. Tremel. "Amorphous monohydrocalcite" with a defect hydrate network by mechanochemical processing of monohydrocalcite using ethanol as auxiliary solvent. *Chem. Mater.* **2021**. submitted

M. Maslyk, H. C. Sanchez, T. Hieke, J. Schmedt auf der Günne, W. Tremel, The Effect of Crystalline Bound Water in Mechanochemical Synthesis of Alkali Zincphosphate, in preparation

M. Maslyk, D. Kin, F. Ekinci, S. Burgr, T. Yüksel, S. Berger, J. Nolde, M. Mondeshki, W. Tremel, NMR and Titration coupled Hydrolysis study of $LaCl_3$, La_2O_3 and $La_2(CO_3)_2$ as a function of pH, in preparation

Y. Krysiak, **M. Maslyk**, B. N. Silva, S. Plana-Ruiz, H. M. Moura, E. O. Munsignatti, V. S.Vaiss, U. Kolb, W. Tremel, L. Palatinus, A. A. Leitao, B. Marler, H. Pastore. The Elusive Structure of Magadiite, Solved by 3D Electron Diffraction and Model Building, Chem. Mater. **2021**, 33, 3207-3219

P. Opitz, Y. Kryrisak, S. Plana-Ruiz, G. Matveeva, P. Nocon, **M. Maslyk**, M. Mondeshki, U. Kolb W. Tremel. Arrested precipitation from amorphous precursors as a tool to explore pathways of mineral precipitation, *Angew. Chem.* **2022**, submitted

Acknowledgements

[redacted]

[redacted]

Table of content

List of tables

List of figures

1

Theoretical Background

1.1 Nucleation and crystal growth

A generalized view on crystallization describes the phase transition in which the formation of a new solid phase from a supersaturated solution, a melt or a gaseous phase. This process can be separated into two parts: (1) Nucleation due to the formation of a phase boundary in a preceding one-phase system (2) ensuing crystal growth of the newly formed phase.[1] A systematic approach for the formation of nuclei and consequent crystal growth was described by Viktor LaMer and Robert Dinegar.[2] Following the reaction of sodium thiosulfate ($Na_2S_2O_3$) and dilute hydrochloric acid (HCl), a disproportionation reaction from which bisulfite (HSO_3^-), molecularly dissolved sulfur (S_8) and polythionate are formed, concentration and time dependency was found to affect the size distribution of the generated colloidal sulfur (Figure 1.1).

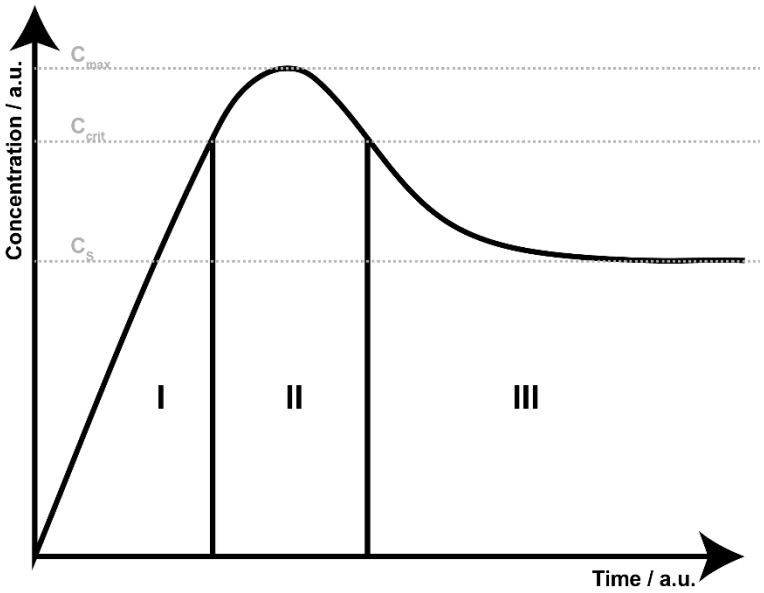

Figure 1.1 LaMer model developed on the precipitation of colloidal sulfur from acidic titration of sodium thiosulfate. (I) Steady increase of concentration. (II) Nucleation due to attaining critical concentration and subsequent partial concentration decrease due to a consumption of the building blocks. (III) Concentration decrease based on diffusion-controlled crystal growth.

At first an increase of sulfur concentration is developed until a critical concentration is reached (stage I, C_{crit}). Minor changes in concentration and timing lead to rapid nucleation so that the nucleation rate is considered infinite (stage II, C_{max}). The formation of nuclei partially decreases the concentration and reduces the degree of supersaturation, subsequently reducing the nucleation rate, which drops to nearly zero. This short span ("burst nucleation") leads to the formation of a monodisperse distribution of nuclei. As the solution is still supersaturated diffusion of molecularly dispersed sulfur for particle growth can occur (stage III). The remarkable finding of this investigation lies in the difference of size distribution of the particles due to changes in the parameters. Changing the concentration of hydrochloric acid leads to a prolonged time span, during which nucleation and growth by mix, thus leading to non-uniform growth.

1.1.1 Nucleation Theory

Nucleation is described as the irreversible formation of a new phase boundary in parental phase, due to changes in the free energy landscape.[1,3] Considering a single chemical component, the driving force for nucleation can be expressed by the change in chemical potentials $\Delta\mu$, i.e., the larger $\Delta\mu$ the greater the driving force. For nucleation to occur the chemical potential in the two-phase system ($\Delta\mu_2$) needs to be lower than the one-phase system ($\Delta\mu_{1)}$.

$$\Delta\mu_2 < \Delta\mu_1 \tag{1}$$

Different models exist to explain the occurring phenomenon during nucleation and crystallization i.e. classical nucleation theory (CNT), prenucleation clusters, two-step nucleation and others[4], which will be discussed in the following sections.

1.1.2 Classical Nucleation Theory

For the sake of simplicity, we consider a solution in which a solid is formed. Based on the works of Weber, Becker and Döring, and Frenkel [5–7], where the condensation of vapor to a liquid is considered, a prediction for the nucleation rates in a system in liquid-solid equilibrium is derived. The two energy terms mainly responsible for the phase formation are the bulk ($\Delta\mu_b$) and surface ($\Delta\mu_{s)}$ term.

$$\Delta G_G(r) = \Delta G_{bulk} + \Delta G_{surface} \tag{2}$$

In a first approximation the nucleation of a spherical nucleus with radius r is taken into account, which has the smallest ratio of surface to volume and the lowest free enthalpy.

$$\Delta G_G(r) = \frac{4\pi}{3} r^3 \Delta G_V + \pi r^2 \gamma \qquad (3)$$

In equation 1.3, the surface tension between liquid and nucleus is given by γ and the enthalpy per unit volume by ΔG_V. From these considerations it follows that the two forces oppose each other. The stability depends on the ratio between surface and volume. Factors like like the chemical composition and crystallographic orientation affect the surface energy. This energy barrier has to be overcome by collision and agglomeration of several blocks to build of nucleus of critical size, whose free enthalpy term exceeds the surface barrier.

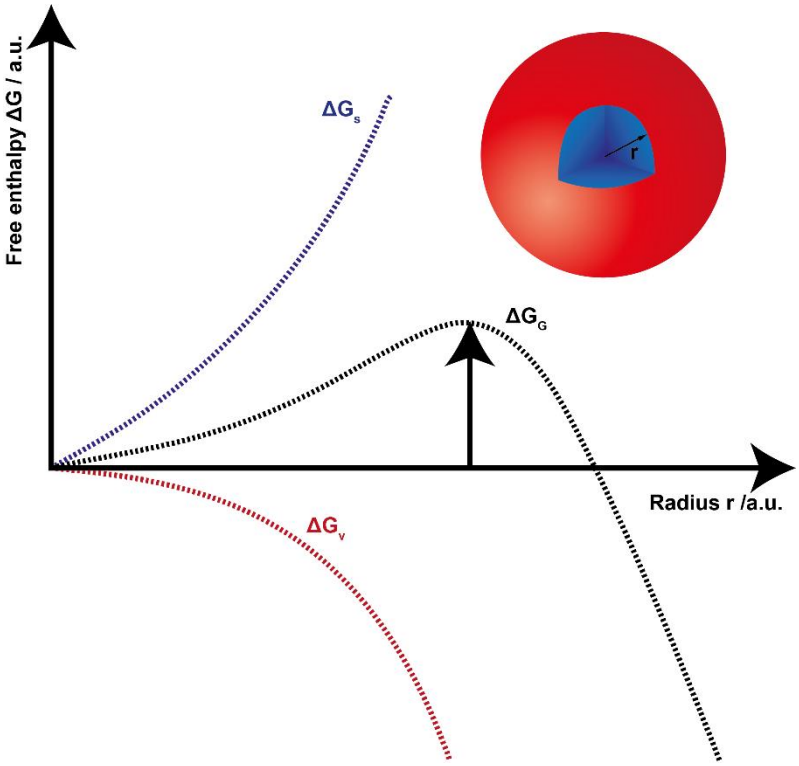

Figure 1.2 Schematic illustration showing the energetic terms responsible for the formation of a new phase in the approximation of classical nucleation theory.

A schematic illustration shows that the surface and volume energy are opposed to each other (Figure 1.2). As the surface term grows with r^2 and the volume term declines with r^3 the sum of these functions leads to an inflection point (ΔG_G^*) at a critical radius r^* which must be overcome to form of a stable nucleus.

$$\frac{\partial \Delta G_G}{\partial r} = 8\pi r + 4\pi r^2 \Delta G_V = 0 \tag{4}$$

$$r^* = -\frac{2\gamma}{\Delta G_V} \tag{5}$$

Substitution of eq 1.5 into eq. 1.3 gives the amount of free energy to overcome the barrier for nucleation.

$$\Delta G_G^*(r) = -\frac{16}{3}\frac{\pi\gamma^3}{\Delta G_v^2} \tag{6}$$

This barrier determines the kinetics of nucleation and the nucleation probability is given by an exponential function in which the height is divided by $k_b T$.

$$J_N = A\exp\left(-\frac{\Delta G_G}{k_B T}\right) \tag{7}$$

As the supersaturation S of a system is related to the chemical potential, equation 6 can be rewritten. Different factors must be taken into account when the saturation of phases is considered, i.e., activity and polymorphism.

$$\Delta G_G^*(r) = -\frac{16}{3}\frac{\pi\gamma^3}{(k_b T \ln(S))^2} \tag{8}$$

Substitution of equation 8 in equation 7 shows that the nucleation probability is governed by the degree of supersaturation, the surface energy and temperature.

$$J_N = A\exp\left(\frac{16}{3}\frac{\pi\gamma^3}{k_B T(\ln(S))^2}\right) \tag{9}$$

It has to be taken into account that this quantitative approach can deviate from experimental results to a high degree[8]. Especially the use of assumptions and simplifications lead to

deviations between idealized and real systems. These can be summarized up as (a) comparable macroscopic properties of the one-phase system and newly formed phase, (b) a spherical and sharp interface between nucleus and solution, and (c) lack of solvent influence.[3,4]

1.1.3 Heterogenous Nucleation

Another – more common– case is a phase transformation between two phases. Due to preferential sites, which lower the surface energy the free energy barrier decreases and nucleation is facilitated, i.e., dust particles, surface impurities in bottles and others.[1]

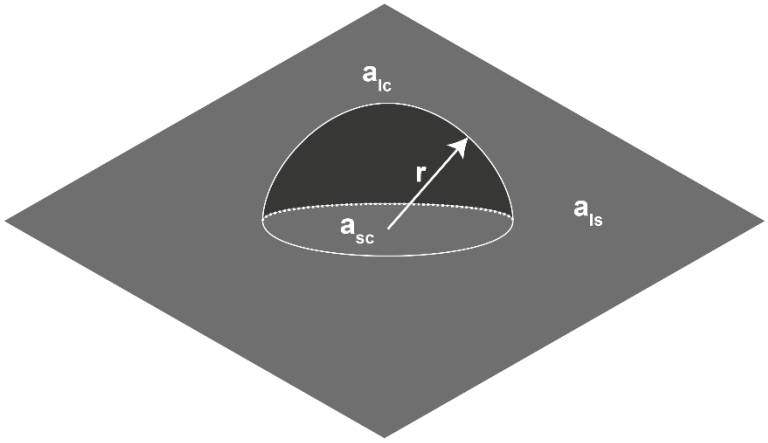

Figure 1.3 Schematic illustration representing the existing phase boundaries in two phase system of a liquid and solid. The boundaries are marked as a_{lc} (liquid-crystalline), a_{ls} (liquid-surface) and a_{sc} (solid-crystalline).

For a droplet of a liquid on a flat surface with fixed volume, the total surface energy of the system depend on the shape and the different interactions a_{sc}, a_{ls} and a_{sc}. For a hemisphere (Figure 1.3) with radius r the energy is given by:

$$\Delta G_G = \left(-\frac{2}{3}\pi r^3 \Delta G_v + \pi r^2 (2\gamma + a_{sc} - a_{ls}\right) \tag{10}$$

Different from the homogenous case the new interface between surface and nucleus must be considered. This leads to the loss of liquid surface interaction, and reduces the surface term. The critical radius is then given by:

$$r_H^* = -\frac{2\gamma}{\Delta G_V}\left(1 - \frac{a_{sl} - a_{sc}}{2\gamma}\right) \tag{11}$$

If the interaction between surface and formed crystal is favored over the liquid and surface ($a_{sl}>a_{sn}$) the nucleation barrier is reduced. Therefore, different approaches can be chosen in which either interactions between surface and a newly formed crystal are promoted or suppressed.

1.1.4 Ostwald-Volmer Rule

Many systems exhibit polymorphism, i.e., when a given compound can adopt different crystal structures. Textbook examples are calcium carbonate (Figure 1.4), carbon, zinc sulfide, and silicon or titanium dioxide. For a given condition one of these forms is thermodynamically stable and others metastable. Typically, a bulk material with the highest density is thermodynamically stable, as the number of attractive forces is maximized, which leads to a minium of free enthalpy.[9] Due to the small energetic differences[10,11], the particle size is cruical. A decrease in surface enthalpy may be accompanied by a decrease in stability, which subsequently is associated with a decrease in density. This observation is described by the Ostwald-Volmer step rule, which states that crystallization proceeds to the thermodynamically most stable phase, by traversing through a sequence of metastable phases.[12]

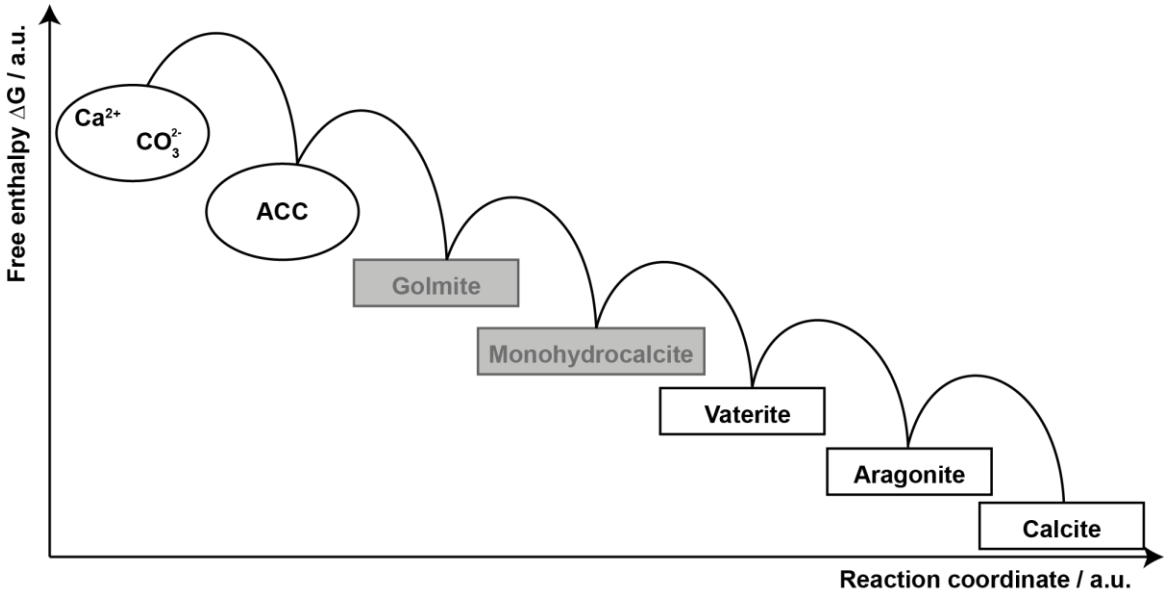

Figure 1.4 Schematic illustration of the Ostwald-Volmer rule for the polymorph transition in the system of calcium carbonate. Amorphous calcium carbonate is the least stable modification and calcite the most stable under ambient conditions. Golmite and Monohydrocalcite are highlighted in grey colours as their constitution differs from calcium carbonate due to the incorporation of water. Sometimes these compounds are termed pseudopolymorphs.

Similar to Hammond's postulate, in which the transition state is closely related to the final structure and only shows a small reorganization, the metastable phases are assumed to be structurally more similar to the precursors in solution. From the correlation between metastability and surface enthalpy, lower activation barriers and lower free energy for the growth may be expected, which may lead to crossovers in thermodynamics between nanoscale and bulk phases. Formation of a metastable phase would then require separate nucleation events (i.e., dissolution/reprecipitation) to form the next stable phase. The systematic progression *via* different metastable phases represents the thermodynamic viewpoint. With respect to the kinetics of the Ostwald-Volmer step rule lower activation barriers and faster changes might provide a qualitative explanation.[13]

1.2 Non-Classical Crystallization Theory

One of the drawbacks in classical nucleation theory (CNT) is the assumption of a one-step event for all order parameters. Whereas in the study from gas-to-liquid phase transitions a single parameter (i.e., density) is sufficient to describe the free energy in both phases, more parameters are needed in the fluid-to-solid transition.[14] In addition, symmetry breaking which is assumed to occur at a certain transition point in CNT, can be achieved by multiple pathways, thus leading to new nonclassical views of the crystallization process.[15]

1.2.1 Spinodal Decomposition

Originally, the appearance of metastable phases was proposed for protein crystallization in which the interaction range is short and particles are assumed to behave like spherical colloids.[16, 17] In such a system two thermodynamically stable phases, a fluid and a solid phase exist (Figure 1.5 A). If the critical point for fluid-fluid phase transition is met the metastable binodal regime is observed and two components are miscible for any given ratio.

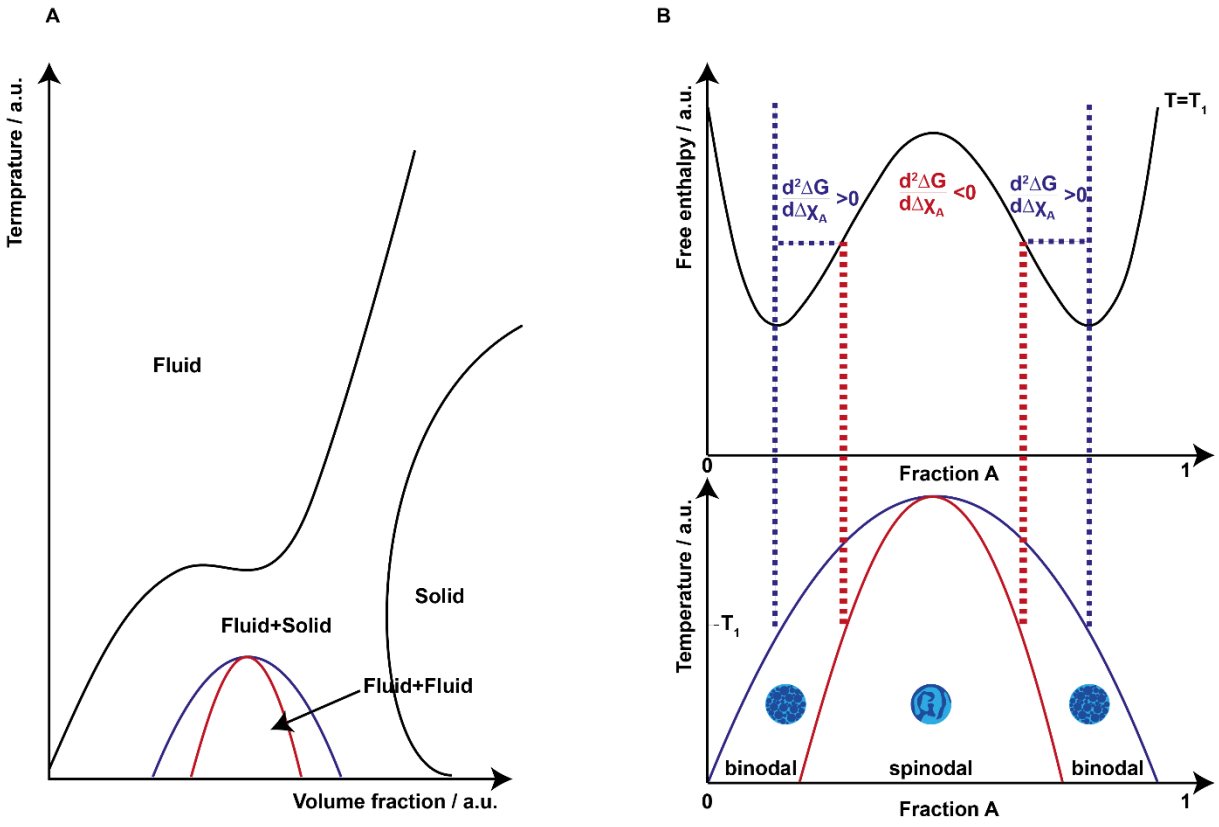

Figure 1.5 (A) Schematic phase diagram in the temperature-volume plane showing the existence of a liquid-liquid coexistence curve. (B) Schematic illustration of two partly miscible components A and B. In the bimodal regime he system is metastable to small fluctuations and upon reaching the spinodal, the system becomes unstable and spontaneously demixes. The free enthalpy curve at a constant temperature T shows the course of ΔG as a function of the fraction.

The driving force for this case is the temperature dependent entropy term of the free enthalpy.

$$\Delta G^{mix} = \Delta H^{mix} - T\Delta S^{mix} \tag{12}$$

The underlying continuous change, stability is attained if the second derivative of the free energy of mixing is positive.

$$\frac{\partial^2 \Delta G_{mix}}{\partial \chi_A^2} > 0 \tag{13}$$

As illustrated in Figure 1.5 B the changes of the free energy pathway show that in the binodal regime the system is metastable, i.e., the second derivative is positive. Local fluctuations can occur which are followed by diffusion and subsequent nucleation. By setting the second derivative to 0 the turning point can be calculated at which the criteria for the spinodal regime are met.

$$\frac{\partial^2 \Delta G_{mix}}{\partial \chi_A^2} > 0 \tag{144}$$

Above this point the free enthalpy changes become negative and the system is unstable. A slight modification of Fick's law shows that the diffusion is proportional to the derivative of the chemical potential with respect to the molar fraction of a component, where K is the mechanical mobility, proportional to the diffusion coefficient *D*.

$$\frac{\partial C_B}{\partial t} = D\nabla^2 C_B - 2M\kappa\nabla^4 C_B \tag{15}$$

Here C_B corresponds to the composition of the material and M and κ are positive parameters, and $D = \frac{\partial^2 f}{\partial C_B^2}$. There are two possibilities for diffusion if the forth order term is neglected. Diffusion occurs downhill (from higher to lower concentration) when the solution is stable, i.e., $\frac{\partial^2 f}{\partial C_B^2} > 0$, as D will be positive.

If on the other hand $\frac{\partial^2 f}{\partial C_B^2} < 0$ the solution becomes unstable and diffusion occurs from lower to higher concentrations, resulting in a phase separation. The fingerprint of this mechanism is the uphill diffusion.[18]

1.2.2 Two Step Nucleation

Another non-classical approach is described by the two-step nucleation pathway where nucleation is divided into two separate processes. Before a solid crystal forms, a dense liquid phase is generated in which the concentration of the buildings blocks is very high. In the second step a second nucleation occurs in which the final nucleus forms and crystallization occurs. In such a process the dense liquid is metastable with respect to the final crystal system but itcan be metastable or unstable with respect to the solution (Figure 1.6).

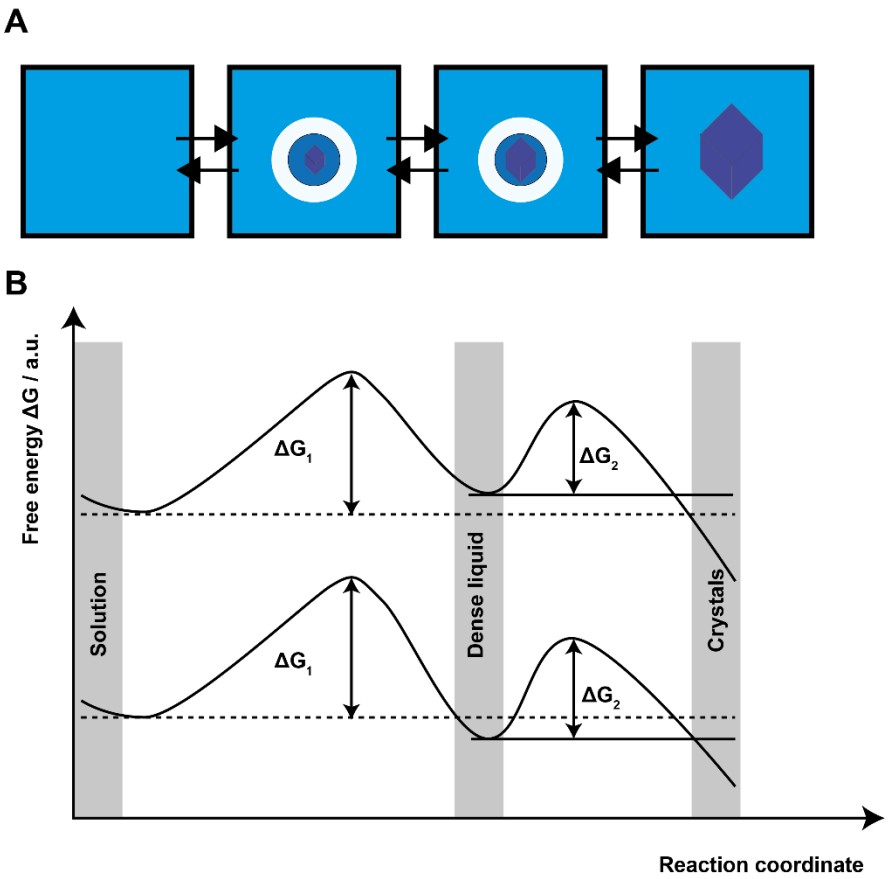

Figure 1.6 (A) Schematic illustration for the two-step nucleation process showing the formation of a dense liquid precursor as a first nucleation event and subsequent nucleation in the dense liquid leading to the formation of the crystalline material. (B) Energetic pathway for the nucleation process. The dense liquid phase can be metastable (top) or unstable (bottom) in respect to the first nucleation event.

In contrast to CNT where a direct reorganization from building blocks to final phase is assumed and two parameters (i.e., concentration and structural order) change abruptly, in the two-step nucleation pathway the formation of a dense liquid from building blocks precedes the reorganization. This process is assumed to proceed by small fluctuations and has been shown to occur for proteins[19], colloidal mixtures[20], mineral related phases[21] and others. Especially the nucleation pathway in biominerals like calcium carbonates, which very often interact with proteins has shown the formation of such dense liquids[22]. In view of these experimental observations polymers were used to control the crystal formation and it could be shown that analogously to nature the formation of a dense liquid phase in form of PILPS (Polymer Induced Liquid Precursors) was be observed.[23]

1.3 Mechanochemistry

The complex chemistry of inorganic compounds leads to a broad spectrum of different approaches for the formation of new materials i.e. combustion reactions, precursor synthesis, topochemical reactions, intercalation, sol-gel methods, high-pressure methods and others.[24] Mechanochemistry, a common method, is defined as a chemical reaction induced by mechanical energy.[25] As early as 315 B.C.E. Theophrastus of Eresus mentioned the mechanochemical reduction of cinnbar to mercury through grinding of cinnabar in a copper mortar.[26] Although, the prevalent use of mechanochemical synthesis was found for inorganic materials[27,28], current research in this area has shown that this approach is also feasible for organic[29] and macromolecular compounds[30]. Even structurally complex compounds as peptides[31] and large porous frameworks[32] have been prepared by ball milling. With regard to the areas of applications, a basic understanding of the processes in relation to the mills, grinding media and materials used is necessary to master the reactions that take place.[33,34] Numerous models have been developed within the framework of mechanochemical research. In hot-spot theory the reason for chemical reactions are explained by frictional events in which temperatures >1000 K on surfaces of about 1 μm^2 can be achieved for very short periods of time (10^{-4} – 10^{-3} s).[35] In contrast, the magma-plasma model describes the formation of excited fragments, electrons and photons due to the formation of a plasmatic state after collision between milling media and material.[36] Depending on the application, different types of ball mills are used, where the technological force transmission is different and also the effect of different materials must be considered. The use of specific milling instruments e.g., tumbler ball mills, vibratory and planetary mills can result in different grinding parameters, which for example, lead to a direct energy transfer to the material. Alternatively, the kinetic energy is first transferred to the milling body and then to the grinding medium

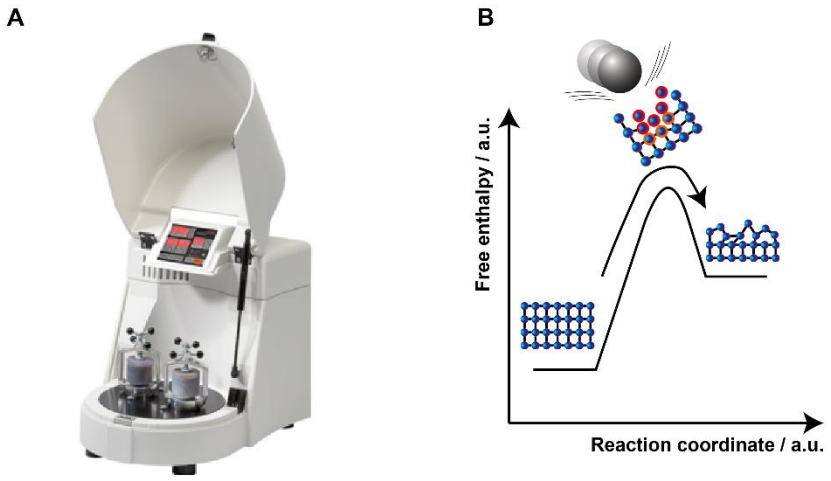

Figure 1.7 High-energy planetary ball mill and a schematic illustration of the magma-plasma model. (A) The ball mill employed in this work (Fritsch Pulverisette 7 Classic Line). (B) Collision of milling media with employed crystalline materials lead to deformation and subsequent activation due to changes in the crystalline structure.

During milling reactions, diffusion occurs with the formation of nanostructures. As these processes are temperature dependent two processes must be considered, local temperature changes due to collisions and general temperature changes in the vial.[37] The small particle size, the associated increase in surface area and the reactivity play a crucial role in mechanochemistry. A high degree of contamination and additional energy supply can thus lead to amorphization.[38,39]

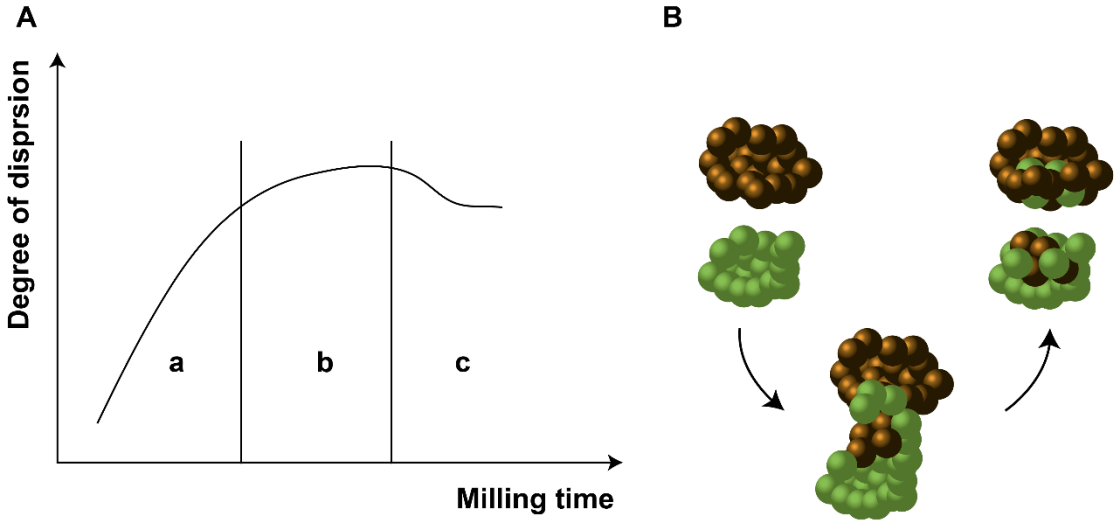

Figure 1.8 Schematic illustration of the kinetic (A) and atomistic (B) pathways in a mechanochemical reaction. (A)The reaction is divided into three steps: (a) in the Rittinger stage a linear reduction of particle size and surface growth is observed (b) during the aggregation range the transfer of kinetic into surface energy is non linear due to the increasing interaction between surfaces (c) in the agglomeration stage the energy of the system is reduced by agglomeration. (B) High energy states allow for the material transfer on surfaces due to collision of particles. Based on [25].

The grinding process is accompanied by reduced efficiency in particle size reduction and an associated form of aggregation and agglomeration. Studies on several systems have shown that the underlying mechanism follows three stages as illustrated in Figure 1.8. During the Rittinger stage (a) no significant interaction between particles is assumed, thus the dispersion degree rises linearly, due to the transformation of kinetic energy into surface energy of the material. The aggregation stage (b) is marked by a non proportional energy input. The surface formation and starting aggregation lead to a lowering of the dispersion rate. During the agglomeration stage (c) a small drop in the dispersion occurs. The surface energy is minimized and the systems remains steady afterwards. Although a clear distinction between thermal and mechanical effects is difficult, it is important to note that mechanochemical processes occur under non-equilibrium conditions. While temperature is an intensive state variable, the energy from mechanochemical treatment is stored in the form of defects, i.e., dislocations, therefore promoting a stabilization of metastable phases. Mechanistically, the chemical and physical changes occur locally and make experimental investigations more complicated. Molecular dynamic simulations provide insight into these systems and show that under certain conditions the interfaces are characterized by kinetic lability and intense deformation. This promotes chemical mixing. These dynamics can be specifically influenced by the geometric arrangement of the system, allowing for specific mass transfer. Also, the parameters controlling the systems in the mechanochemical reaction, i.e., reactants, temperature evolution, chemical hardness and others, show the complexity of these reactions and indicate multistage mechanisms.

1.4 Cementious Materials

The definition of binder comprises substances that harden independently, thereby holding other materials together to form cohesives mechanically or chemically. This binding process can occur by agglomeration or by binding to surfaces. Hydraulic binders are substances that by reaction with water convert the water-binder system into a solid matrix. There are active and latent binders. Active binders react spontaneously with cement, while latent binders require the presence of a suitable alkali activator.[40] A special case in this context are dental cements, which are used for fixing indirect replacements to prepared teeth. They must meet special requirements, such as being not harmful to teeth, having sufficient setting time and hardening quickly.[41] Typical in this context are zinc phosphate cements. They will be addressed in addition to conventional cements. The modern history of cement and concrete began with Joesph Aspdin's patent for "Portland cement" in 1824, although historical discoveries show that cementitious materials have been used for thousands of years.[42] To obtain a basic understanding of the hydration reactions occurring during the setting of cement, the underlying compounds and their processing must be understood. In general, the raw materials used for cement consist of approximately 75% limestone ($CaCO_3$) and 25 % clay ($w(Na_2O/K_2O) \times SiO2 - yAl_2O_3\text{-}zFe_2O_3$). Their chemical composition might be adjusted by addition of other components (e.g. quartz or iron ore) to ensure that the material fulfills the appropriate requirements. The manufacturing process starts with the blending of the materials to ensure that the limestone particles are smaller than 125 µm and those of other raw materials are smaller than 90 µm.[43] The appropriate chemical ratio between the oxides can be controlled by mainly three factors. (i) To quantify the theoretical value of reaction between lime and silica or alumina the *lime saturation factor* (LSF) is introduced. If the LSF value is greater than 1, free lime is accessible to the system, which can have major impact on the phase composition. (ii) The *silica ratio* (SR) is an empirical parameter. It is inversely proportional to the formed liquid in the burning process, since only alumina and ferric (Fe^{3+}) phases melt. (iii) The use of a ratio between alumina and ferric phases, the *alumina ratio* (AR), allows the control over properties and liquid formation in the system.

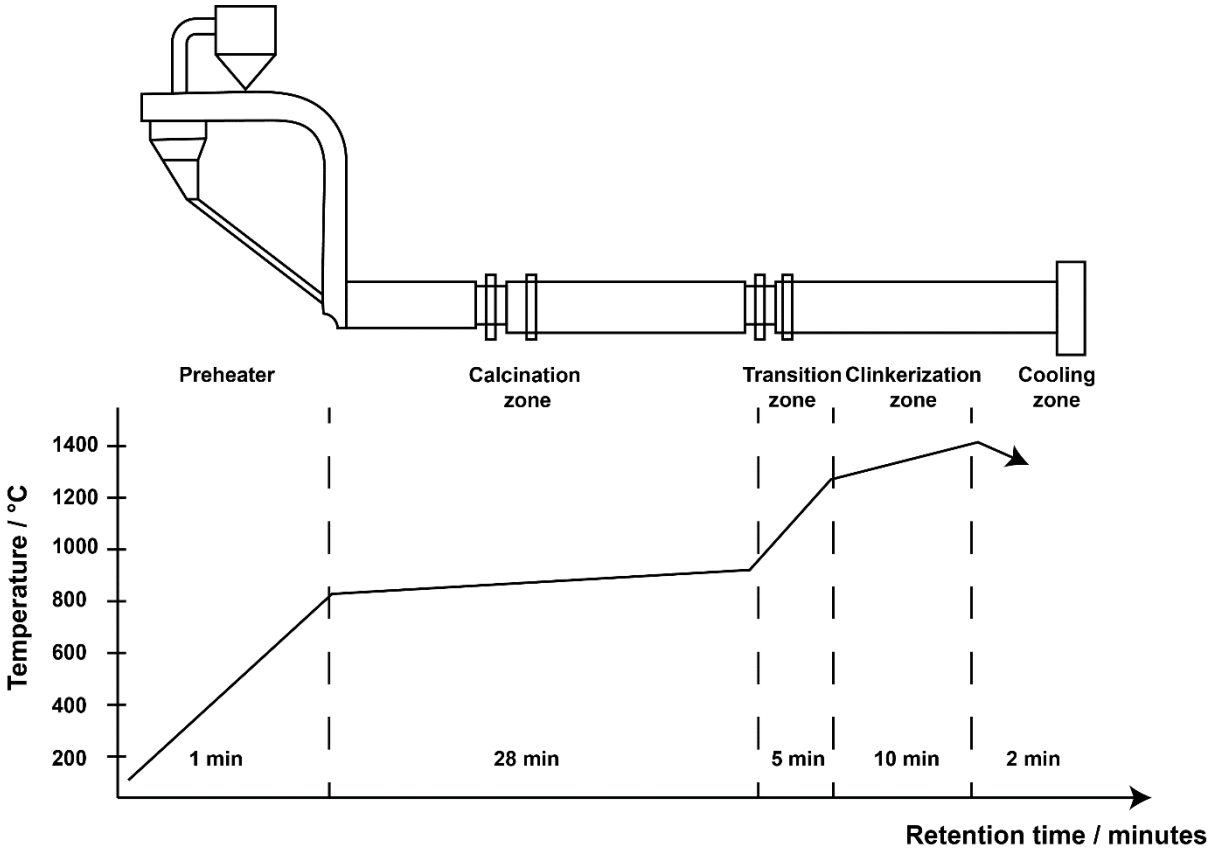

Figure 1.9 Schematic illustration of the temperature kiln and the temperature development during cement processing.

The manufacturing process starts by inserting the material in a preheat tower (Figure 1.9) where dehydration and partial decarbonation of the limestone takes place.

$$CaCO_3 \rightarrow CaO + CO_2 \tag{16}$$

Afterwards the material is conveyed into a cylindrical kiln, with a low inclination and a rotational speed of approximately 2.5 to 5 r.p.m to initiate a small movement in the kiln towards the exit.[44] The steady increase in temperature leads to a decomposition of clay minerals, resulting in silicate and aluminate entering the mixture.

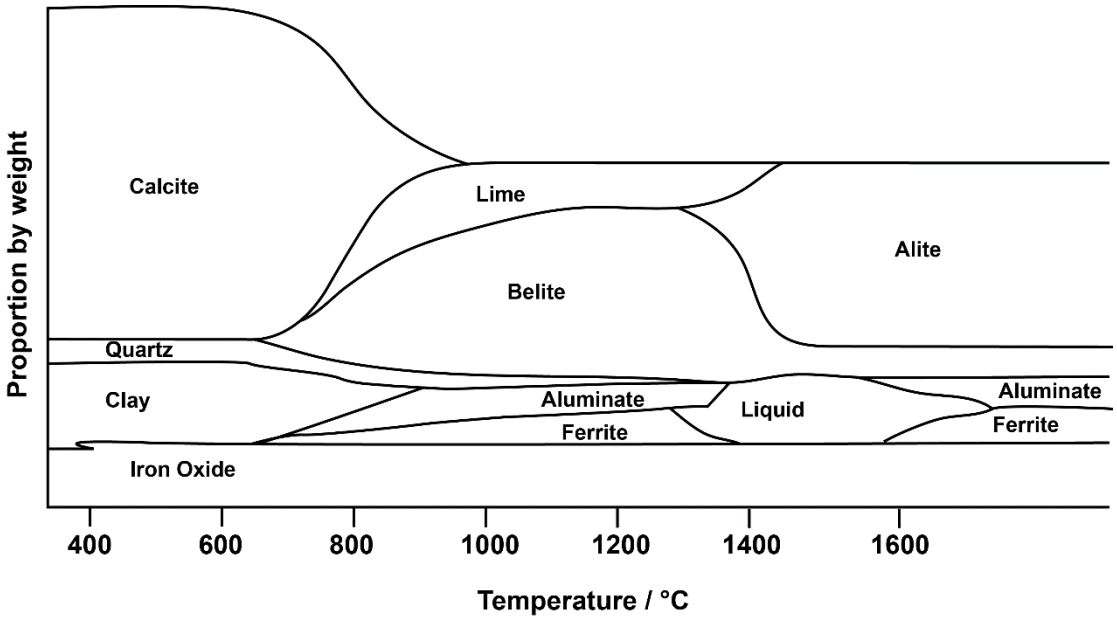

Figure 1.10 Schematic illustration of the change in material composition associated with different temperature ranges.

A large part of the kiln consists of the *calcination zone*, where the temperature is between 700 to 800 °C and decarbonation of limestone ($CaCO_3$) to lime (CaO) occurs (Figure 1.10). In addition belite (eq. 17), calcium aluminate (eq. 18) and calcium aluminoferrite (eq. 19) are formed.

$$2CaCO_3 + SiO_2 \rightarrow Ca_2SiO_4 + CO_2 \tag{17}$$

$$12CaCO_3 + 7Al_2O_3 \rightarrow Ca_{12}Al_{14}O_{33} + 12CO_2 \tag{18}$$

$$4CaCO_3 + Al_2O_3 + Fe_2O_3 \rightarrow Ca_4Al_2Fe_2O_{10} + 4CO_2 \tag{19}$$

When the material enters the *transition zone*, there is a fast rise in temperature from 900 to 1250 °C and the formation of aluminate and aluminoferrite phases is promoted. Afterwards the material is transported to the *clinkerization zone* where temperatures up to 1420 °C can be reached, although average temperature is approximately 1330 °C. These high temperatures lead to melting and facilitate atomic diffusion. The main phases that emerge from this process are alite, belite, aluminate and ferrite. They are the constituents of *clinker*. In a final step the clinker is cooled down rapidly, to ensure that metastable phases are obtained, as they are the more reactive. Commercially available cement is then obtained by grinding the clinker and mixing it with about 5% gypsum ($CaSO_4 \times 2H_2O$). Gypsum is

mainly needed as a regulator to slow down the hydration of tricalcium aluminate, $Ca_3Al_2O_6$, often formulated as $3Cao\text{-}Al_2O_3$ (C_3A) to prevent the occurrence of a rapid setting property of the cement (flash set).

1.4.1 Hydration Reaction in Cement

Upon contact of cement with water a cascade of chemical hydration reactions take place. The interaction of these reactions results in changes in physical and chemical properties. One of the main products in these reactions is calcium silicate hydrate (C-S-H), which is known as the "glue" of cement.[45] The hydration reactions are exothermic, so a heat flow profile for the reaction can be recorded to monitor the behavior as the cement sets (Figure 1.11).

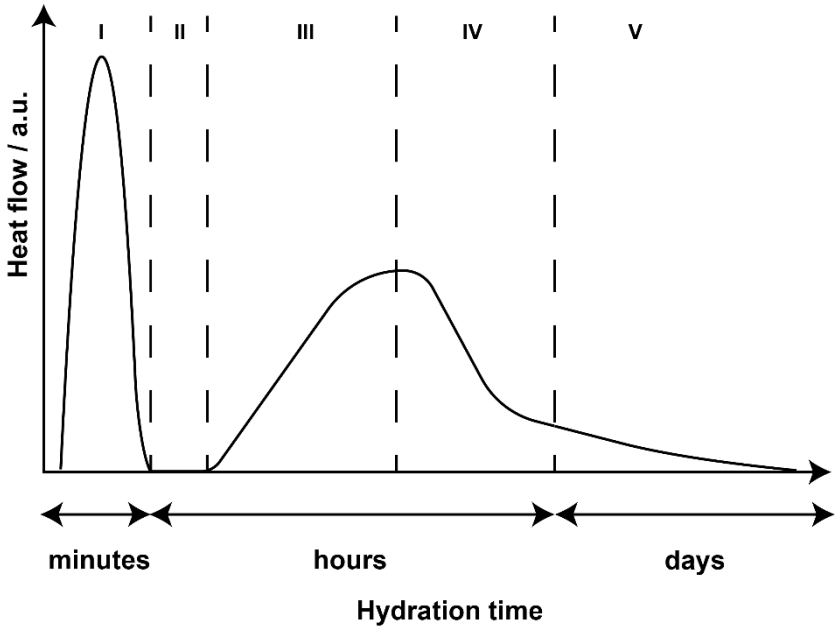

Figure 1.11 Schematic illustration of a typical heat flow measurement during the setting reaction of cement. The hydration can be split into 5 stages: (I) Pre-induction period (II) induction period (III) acceleration period (IV) post-acceleration period (V) diffusion limited reaction.

During the first minutes after contact with water the *pre-induction period* occurs during which tricalcium aluminate ($3CaO{\cdot}Al_2O_3$, C_3A), tetracalcium aluminoferrite ($4CaO{\cdot}Al_2O_3{\cdot}Fe_2O_3$, C4AF) and calcium sulfate ($CaSO_4$, $C\bar{S}$) (Figure 1.12 A) react with water and form an amorphous gel (Figure 1.12 B), which reacts in a follow-up step partially to ettringite ($Ca_6Al_2(SO_4)_3(OH)_{12} \times 26{\cdot}H_2O$).[46] In the following *induction period* there are no changes in the heat flow. The reasons regarding the start and end of this time window remain controversial.[47] Afterwards, the *acceleration period* takes place which usually reaches a maximum of heat release in less than 12 hours, due to reaction of calcium silicates with water. Layers of C-S-H gel form around the cement particles (outer C-S-H) and the

material starts to lose plasticity due to the setting of the cement (Figure 1.12 C). Subsequently, *post-acceleration* occurs where the hydration reaction of calcium silicate slows down and the heat release decreases gradually. As additional C-S-H forms during these phases the C-S-H gel deposits inside the hydration shell (inner C-S-H) and a repeating reaction of aluminates (C_3A and C_4AF) is observed, which leads to the formation of ettringte (AFt) and is sometimes associated with a release of heat (Figure 1.12 D).

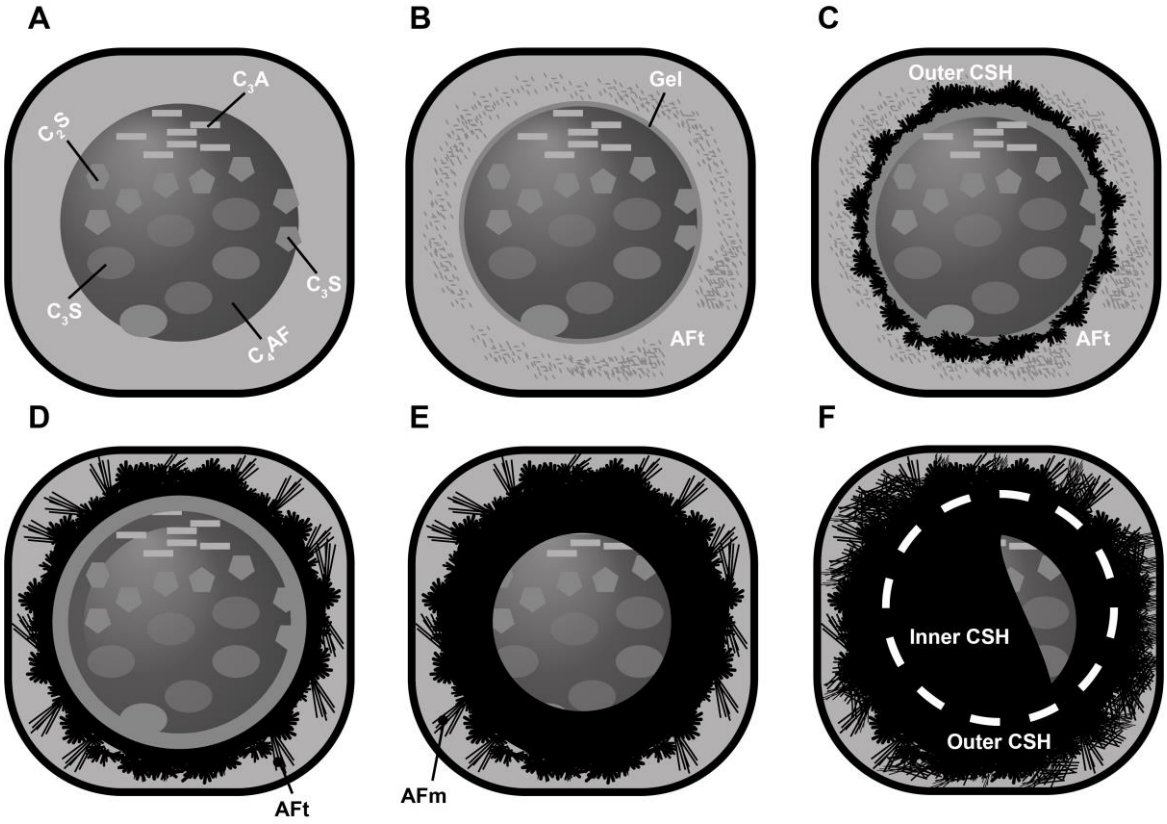

Figure 1.12 Schematic illustration of the hydration progress of a cement grain in contact with water. The steps represent snapshots of the classification taken from the typical heat flow calorimetry curves.

The hydration reaction slows down rapidly after 1 to 3 days in the *post-acceleration period,* since the diffusion is limited by the hardening of the material. In addition, a new aluminate phase $[Ca_2(Al,Fe)(OH)_6] \times \cdot xH_2O$ (AFm) forms and the inner C-S-H grows due to mass transport. (Figure 1.12 E/F).

1.5 Mineralogical phases

In view of the plethora of chemical reactions occurring during clinker production and cement hydration, a basic understanding of the underlying crystalline structures is required if development and adjustment of the aforementioned processes is considered. Only selected crystalline structures important to the researched topics during this work will be examined as the amount of possible phases related to cement chemistry would be beyond the scope of this work.

1.1.1 Calcium Carbonate

In general carbonates belong to a group of minerals in which the essential unit is the carbonate anion(CO_3^{2-}), in which a central carbon atom is surrounded by three oxygen atoms at the apices of an equilateral triangle. The most abundant and also most important carbonate is calcium carbonate which can be found in the form of chalk, marble and limestone.[48–50] In industrial processes it is mainly used as a filler material, i.e., in construction materials[51], paper industry[52] and pharmaceutical industry[53]. A major interest in calcium carbonate arises from its role in many crystalline biogenic minerals, i.e., bones, teeth and shells.[54,55] These compounds can be characterized as composite materials consisting of organic matrices and nano- or micro-scale amorphous or crystalline materials and therefore allow for intriguing mechanical[56], optical[57] and magnetic[58] behavior. In view of the increasing use of calcium carbonate for engineering[59] and sequestration[60] applications, the rich polymorphism (Figure 3) and the associated properties, i.e., density and solubility, need to be understood.

Amorphous calcium carbonate

Amorphous calcium carbonate (ACC) refers to the least stable and hence most soluble form in the calcium carbonate system. It can exist in a precursor state which later transforms to a more crystalline form (“transient ACC”) or as a stabilized phase (“stable ACC”).[61] Despite the emergence of extensive studies in this field a comprehensive explanation for the underlying formation mechanism and stabilization is still missing. In solution stabilization can be achieved by addition of organic additives such a polyphosphonates[62], surface functionalization[63], or inclusion of different ionic constituents as magnesium[64], phosphates[65] and silicates[66]. In addition to these methods mechanochemical reactions in combination with sodium[39], phosphates[67] or magnesium[68] have shown that a top-down approach to ACC from calcite is also accessible.

Calcite

Calcite is the thermodynamically stable phase in the calcium carbonate system. It can be found in huge deposits of chalk and limestone.[69] The structure can be viewed as a rhombohedrally distorted NaCl structure, where Cl^-anions are substituted by CO_3^{2-} anions and $Na^+$by Ca^{2+}cations. The Ca^{2+} cations and CO_3^{2-} anions occupy alternating layers along the z axis and the successive CO_3^{2-} layers have opposite orientations. Therefore the cations are arranged in three-layer periodicity with an ABC stacking and the anions in a six-layer periodicity.[70]

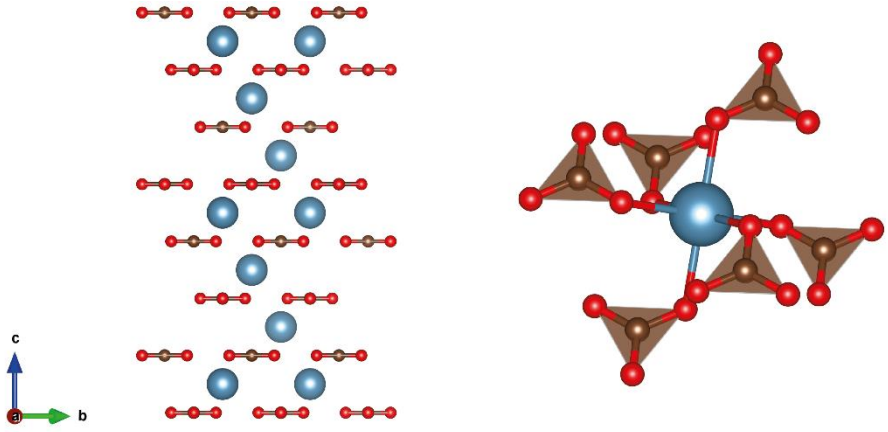

Figure 1.13 Crystal structure of calcite projected along the [100] direction and coordination sphere of a Ca^{2+} cation.[71,72]

composition	$CaCO_3$
space group	$R\bar{3}c$ (167), Z=6
lattice parameters	a=b= 4.991 Å, c= 16.972 Å

Table 1.1 Crystallographic data of calcite. Data taken from ref. [71],[72].

Aragonite

Aragonite is the high-pressure polymorph in the calcium carbonate system and can be found in many archaeological sites and also mollusk shells. [55] Despite its metastability at ambient conditions, it can be found in geological environments, i.e., speleothems. [73] In biogenic systems the case of nacre (mother of pearl) is of special interest due to its 3,000 fold enhanced fracture resistance compared to pure aragonite.[74] It consists of aragonite platelets stacked towards [001] orientation covered by ß-chitin layers[55].

In precipitation experiments aragonite can be formed at elevated temperatures ranging between 60 and 70 °C[75], or in the presence of Mg^{2+} as an additional ion source. It is believed that the adsorption of Mg^{2+} on calcite nuclei prevents integration of Ca^{2+} into the crystal structure and the subsequent inclusion of Mg^{2+} leads to the formation of magnesian calcite. Whereas smaller Mg^{2+} ions can be incorporated into calcite this does not occur for aragonite. The incorporation of Mg^{2+} leads to higher lattice strain and an increase in solubility, thus making aragonite the more thermodynamic stable phase.[76] Aragonite crystallizes in an orthorhombic unit cell and shows the highest coordination number of all calcium carbonate polymorphs (Z=9), as one Ca^{2+} ion is enclosed by six CO_3^{2-} units of which three are bound in a bidentate fashion. Under specific conditions, a nanocrystalline precursor to metastable aragonite crystallizing in a monoclinic unit cell can be isolated.[77]

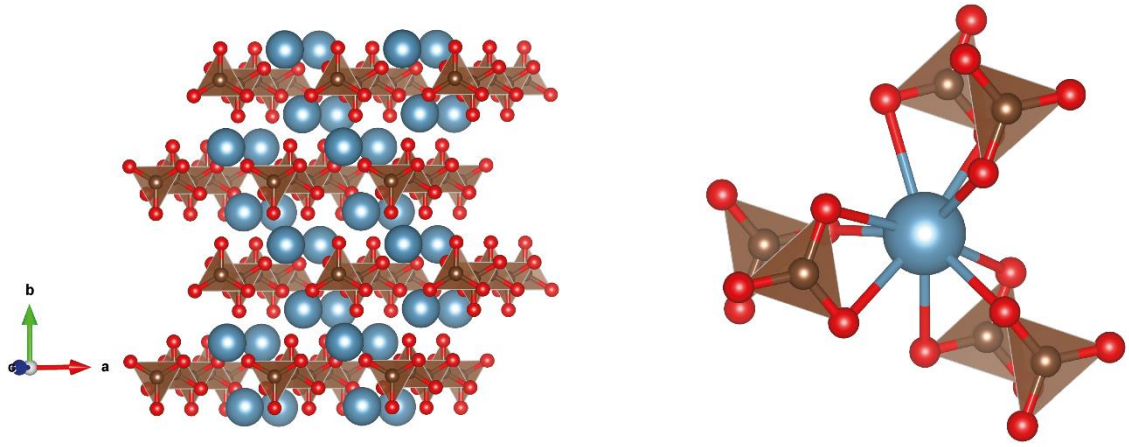

Figure 1.14 Crystal structure of aragonite projected along the [001] direction and coordination sphere of a Ca^{2+} cation.[78]

composition	$CaCO_3$
space group	*Pmcn* (62), Z=4
lattice parameters	a= 4.961 Å, b= 7.969 Å c= 5.743 Å

Table 1.2 Crystallographic data of calcite. Data taken from ref. [72],[78].

Monohydrocalcite

Monohydrocalcite is a hydrous calcium carbonate and metastable in regards to the anhydrous phases.[79] It can be found in saline spring waters[80], marine polar systems[81], as well as in biogenic minerals by certain molluscs[55], guinea pigs[82] and even as a decay product in Saguaro cacti[83]. If in contact with magnesium free water it will transform to calcite, whereas minor amounts of magnesium in the water will change the transformation pathway to aragonite which is believed to results from the inhibiting effect of Mg^{2+} on calcite crystallization. Unlike the anhydrous calcium carbonate phases in monohydrocalcite the structure contains irregular 8-folded Ca-O polyhedra with a central Ca atom coordinated by CO_3^{2-} groups and water molecules (Figure 1,15). As a result, the structure is less dense compared to the anhydrous polymorphs. Although often described as a pure calcium carbonate phase, studies have revealed that Mg^{2+} is usually present in naturally occurring monohydrocalcite.[84] The preparation of synthetic monohydrocalcite is usually associated with a high Mg^{2+} concentration[85], although syntheses in silicate environments were shown to induce the formation of monohydrocalcite as well[86].

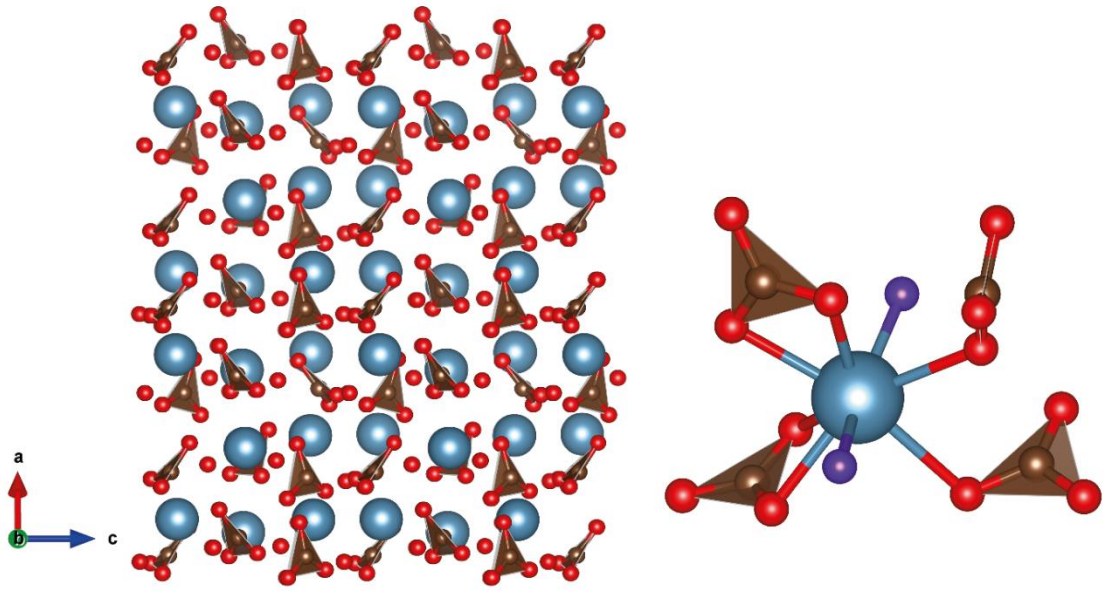

Figure 1.15 Crystal structure of monohydrocalcite projected along the [010] direction and coordination sphere of a Ca^{2+} cation.[87,88]

composition	$CaCO_3 \times 1H_2O$
space group	$P3_121$ (152), Z=9
lattice parameters	a=b=6.093 Å c= 7.554 Å

Table 1.3 Crystallographic data of calcite. Data taken from ref. [87],[88].

1.5.1 Sodium-Calcium-Carbonate (Hydrates)

Different from calcium carbonates, there is a group of carbonates with high sodium content in addition to calcium. These are usually found in the form of carbonatites, i.e., in the form of nyerereite ($(Na,K,)_2Ca(CO_3)_2$)[89]. Under atmospheric conditions nyerereite is unstable and formation of rocks containing pirssonite, calcite, gaylussite and shortite have been observed.[90] Therefore it is considered that a substantial amount of alkaline carbonates should be found in carbonatites initially, thus providing evidence for the resemblance of currently active volcanos as the Oldoinyo-Lengai[91]. The structure of nyerereite can be viewed as a stacking of close-packed Na- and Ca- layers in 6-layered close-packed structures formed by an…ABCBAC…stacking. Unlike the natural mineral the synthetic analogue has a modulated structure (Figure 1.16)

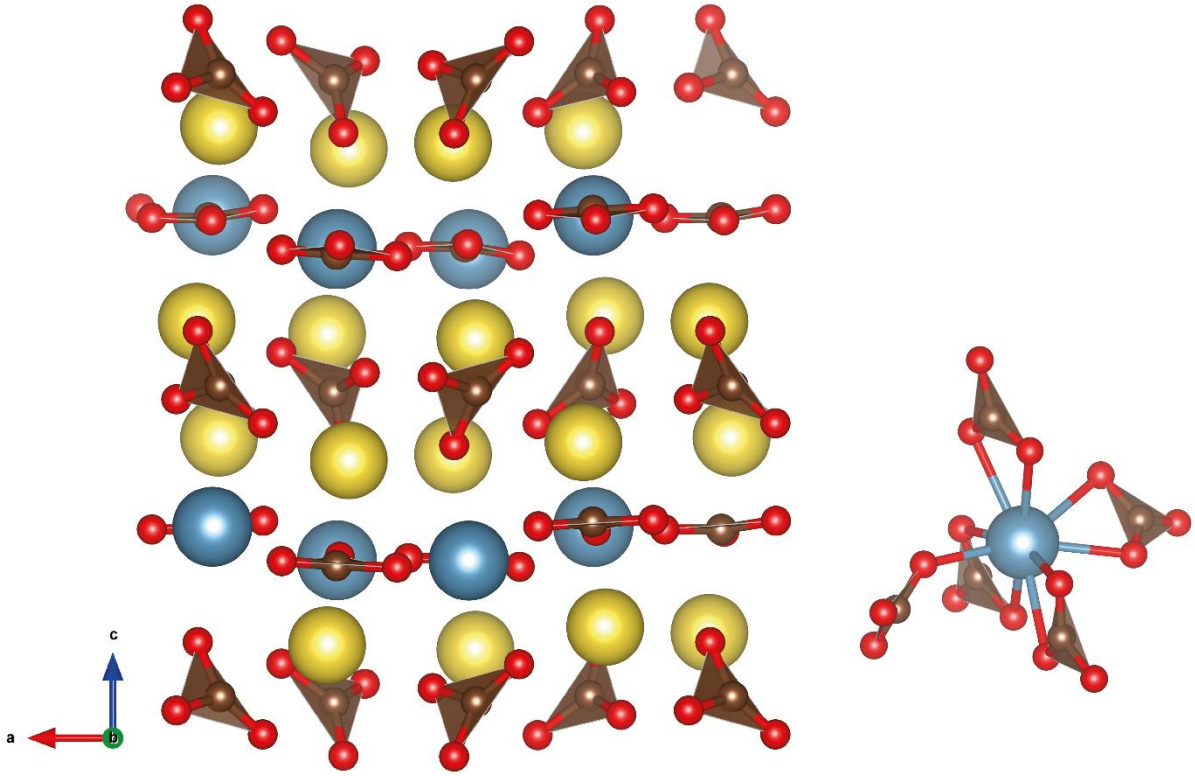

Figure 1.16 Crystal structure of nyerereite projected along the [010] direction and coordination sphere of a Ca^{2+}cation.[91]

composition	$Na_2Ca(CO_3)_2$
space group	$P2_1ca$ (29), Z=8
lattice parameters	a=10.07 Å b=8.72 c=12.24 Å

Table 1.4 Crystallographic data of calcite. Data taken from ref. [91].

In addition to this anhydrous sodium calcium double carbonate, two hydrated forms, pirssonite ($Na_2C(CO_3)_2$ x $2H_2O$) and gaylussite ($Na_2C(CO_3)_2$ x $5H_2O$) are known to occur in nature under conditions of high salinity[92]. Synthetic approaches for the formation of these phases confirm the unusually high concentration of the corresponding ionic constituents[93,94].

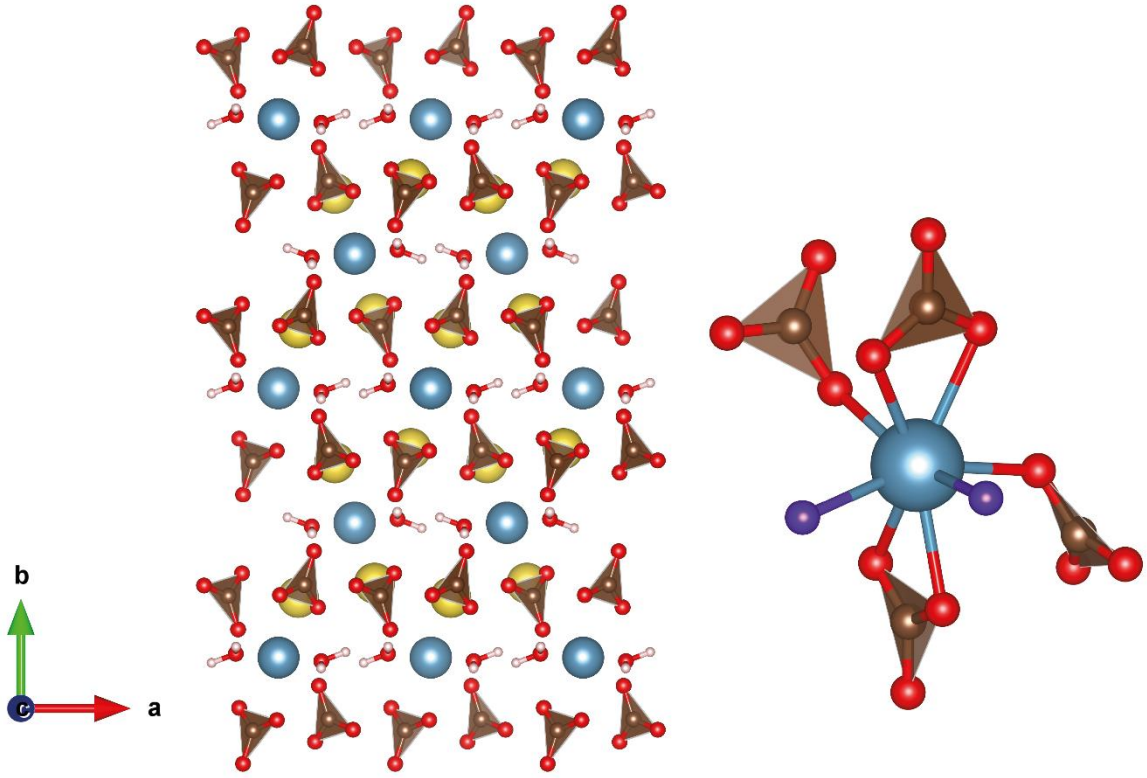

Figure 1.17 Crystal structure of pirssonite projected along the [001] direction and coordination sphere of a Ca^{2+}cation.[94]

composition	$Na_2Ca(CO_3)_2 \times 2H_2O$
space group	$Fdd2$ (43), Z=8
lattice parameters	a=11.34 Å b=20.09 Å c=6.03 Å

Table 1.5 Crystallographic data of calcite. Data taken from ref [94].

Pirssonite crystalizes in an orthorhombic space group and can be described by $Ca(CO_3)_2$ triplets where Ca^{2+} cations are located on diads with coordination to the edges of oxygen from carbonate groups (Figure 1.17), whereas gaylussite has the same $Ca(CO_3)_2$ triplet motif but belongs to a monoclinic spacegroup due to different sodium and water orientations (Figure 1.17).

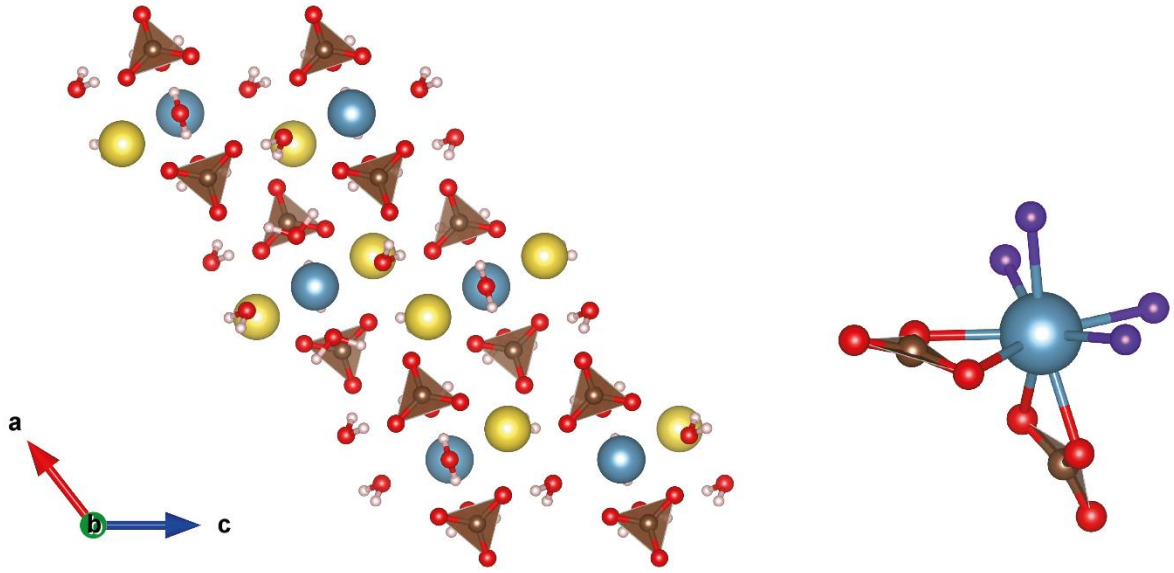

Figure 1.18 Crystal structure of gaylussite projected along the [010] direction and coordination sphere of a Ca^{2+} cation.[94]

composition	$Na_2Ca(CO_3)_2 \times 5H_2O$
space group	$C12_{/c}1$ (15), Z=4
lattice parameters	a=14.36 Å b=7.78 Å c=11.21 Å

Table 1.6 Crystallographic data of calcite. Data taken from ref. [94].

1.5.2 Silicate Minerals

When comparing the Earth's constituents, silicon is the second most abundant element with an occurrence of ca. 26%, next to oxygen with an abundance of ca. 50%.[95] The great importance of silicon arises from the role of clay minerals in the absorption and release of water and cations, thus providing fertility in soils. In addition, silica can be found in a number of plants, as well as in exoskeletons of diatoms, where it contributes to the mechanical stability.[55] Despite the proximity to carbon in the periodic table of elements, the diverse chemistry of silicates is not the result of the same rules governing carbon chemistry. Unlike in carbon chemistry where C-X, C-O, and C-H bonds are almost equally strong and the probability of bond formation is therefore similar, the Si-O bond energy is much larger than that of Si-X and Si-H bonds, so that –Si-O-Si-O- chains are formed preferentially.[96] Due to the high diversity of silicate compounds, there are specific classification schemes in which coordination numbers, degree of bonding, connectivity and other parameters are taken into account. Since these schemes are usually complicated, a more general approach is used that considers silicates on t he basis of common structural

units such as the degree of polymerization, thus dividing them into six classes as shown in Figure 1.19.

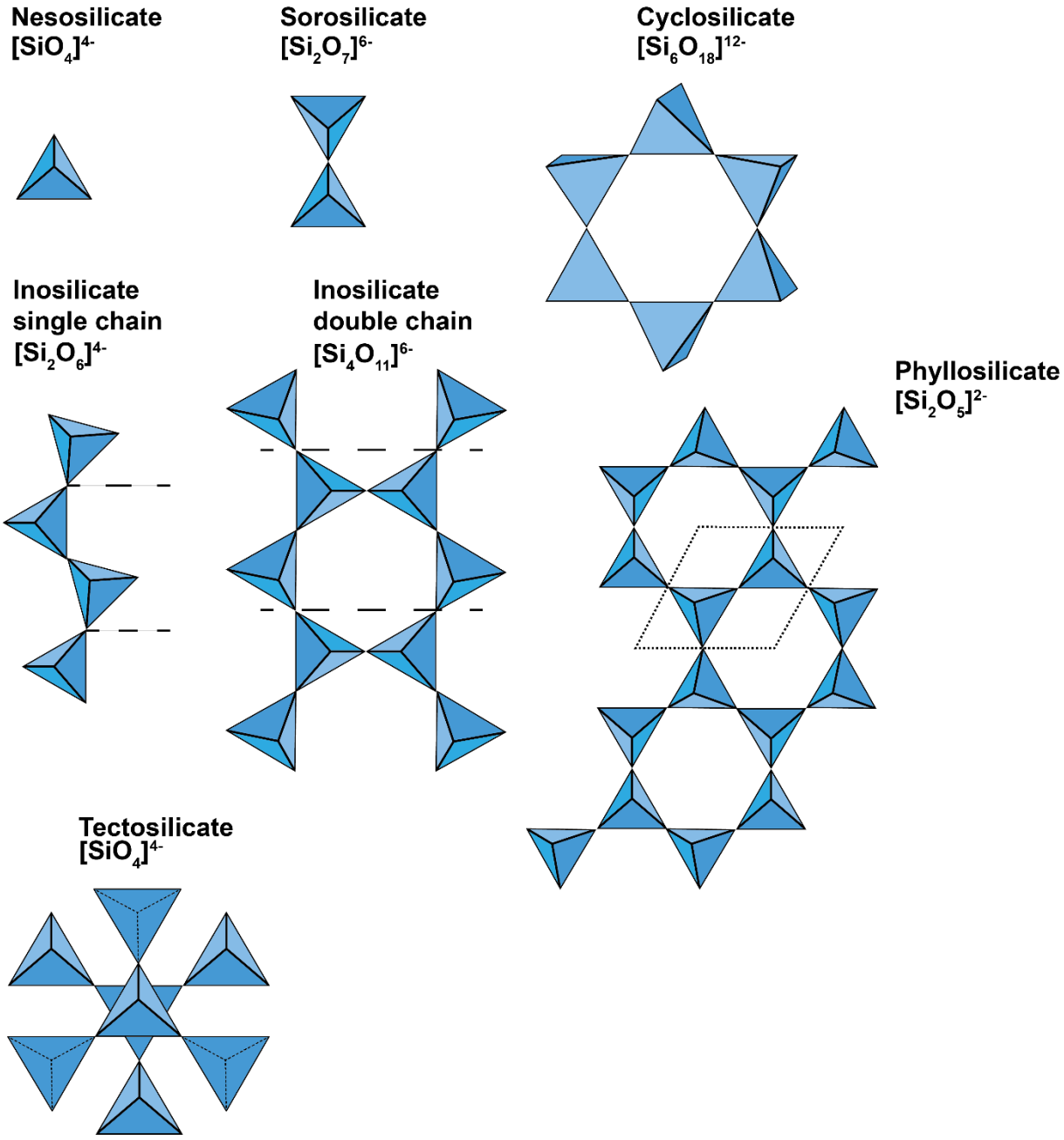

Figure 1.19 Schematic overview of the different classes of silicates consisting of tetrahedral SiO_4 units.

Here, *nesosilicates* (olivine / $[(Mg,Fe)_2(SiO_4)]$) are characterized by isolated tetrahedral units in their crystal structure. In *sorosilicates* (melilite / $[(Ca,Na)_2(Al\ Mg,Fe)(S_2O_7)]$) the silicate anions ($Si_2O_7^{2-}$) contain corner sharing tetrahedrons. If at least three tetrahedra are connected as a closed unit, *cyclosilicate* structures are formed (beryl / $Al_2Be_3(Si_6O_{18})$). An even higher degree of condensation leads to *inosilicates*, which are characterized by infinite

chains of silicate tetrahedra with 1:3 ratio for single (enstatite / $MgSiO_3$) and 4:11 ratio for double chains (tremolite / $Ca_2Mg_5(OH)_2(Si_4O_{11})_2$). If throughout the silicate structure three corners are connected to adjacent tetrahedra the material is classified as a *phyllosilicate*. Many common minerals as talc ($Mg_3Si_4O_{10}(OH)_2$) and kaolinite ($Al_2(OH)_4Si_2O_5$) belong to this class and are characterized by layers of different sizes, with characteristic chemico-physical properties (such as hardness and morphology). A full 4-fold connectivity, i.e. every oxygen atom in a silicate units is connected to SiO_4 unit, leads to the class of *tectosilicates* with three-dimensional structure. A partial substitution of Si^{4+} by Al^{3+} will lead to a negative charge and can be compensated by monovalent cations.

Sodium silicate

A broad interest in the system Na_2O-SiO_2 arises from its technical use for the production of water glass solutions and the manufacturing of acid-resistant enamel frits. Additionally, it can be applied as inorganic binders and builders in washing powders.[97] The structure of sodium metasilicate (Na_2SiO_3) consists of "zweier" single chains running along the [001] direction and can therefore be considered as an inosilicate.

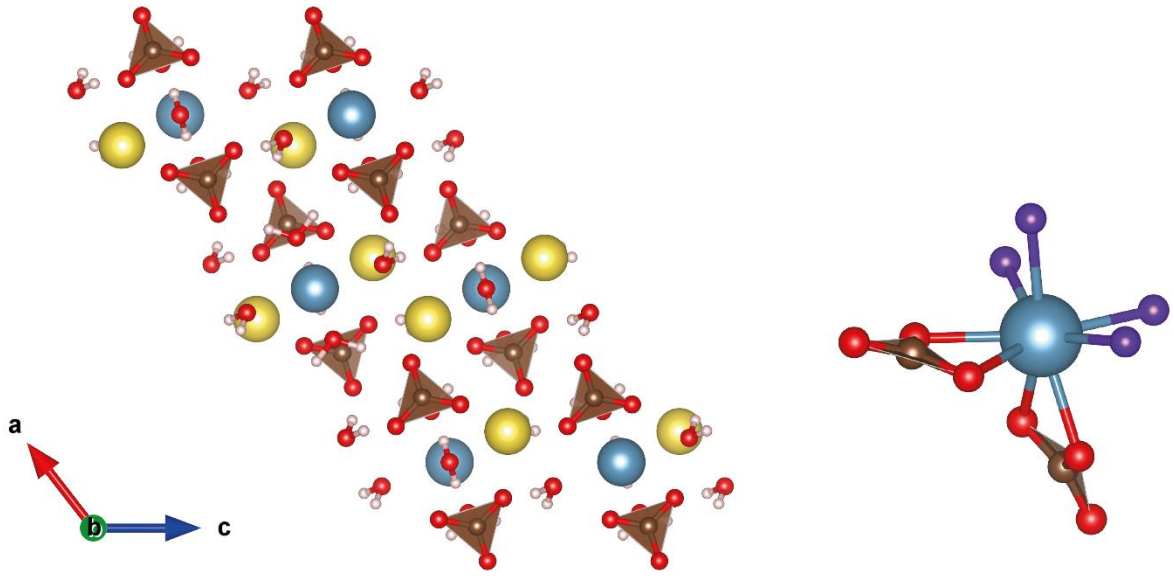

Figure 1.20 Crystal structure of sodium metasilicate projected along the [001] direction and coordination sphere of a Ca^{2+} cation.[98]

composition	$Na_2(SiO_3)$
space group	$Cmc2_1$ (36), Z=4
lattice parameters	a=10.43 Å b=6.02 Å c=4.81 Å

Table 1.7 Crystallographic data of sodium metasilicate. Data taken from ref. [98.]

Calcium metasilicate

The metasilicate of calcium ($CaSiO_3$) is commonly found in nature as wollastonite and can be classified as an inosilicate mineral.[99] Based on its chemical composition (48 % CaO, 51% SiO_2) it has potential applications as a cement additive or replacement for reducing CO_2 emissions in clinker production.[100] There are three known polymorphs of wollastonite, i.e., wollastonite-1T, wollastonite-2M and wollastonite-4A which differ in their periodicity, space groups and structural units. Wollastonite is commonly found in its triclinic form (wollastonite-1T), in which it can be characterized by the space group $P\bar{1}$ with six formula units per unit cell. Its structure consists of infinitely long single chains running along [010] ("dreierketten" $[Si_3O_9]^{6-}$), linked by octahedrally coordinated Ca^{2+} counter ions.

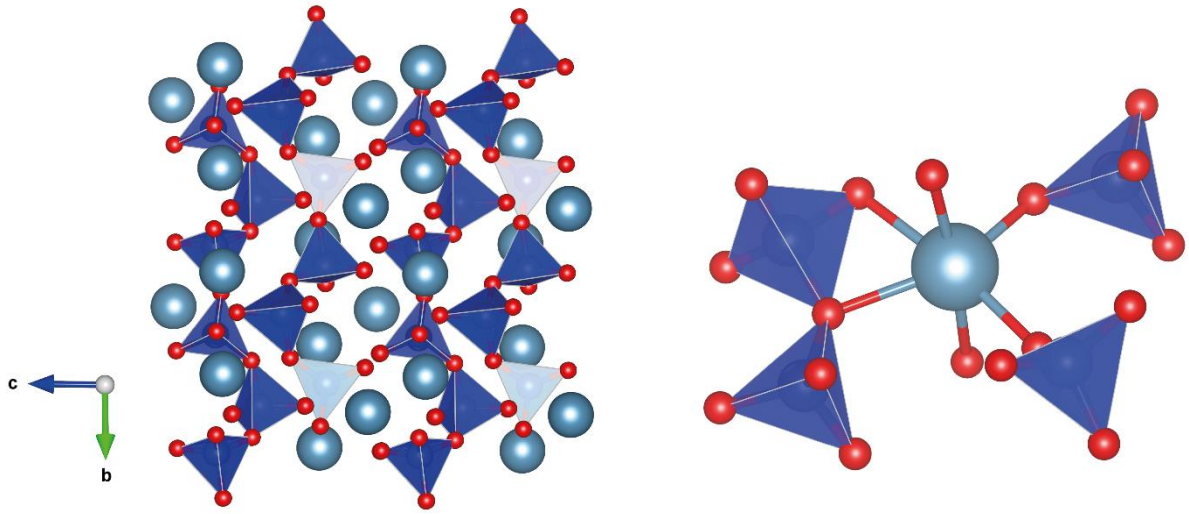

Figure 1.21 Crystal structure of calcium metasilicate projected along the [001] direction and coordination sphere of a Ca^{2+} cation.[101]

composition	$Ca(SiO_3)$
space group	$P\bar{1}$ (2), Z=6
lattice parameters	a=7.94 Å b=7.32 Å c=7.07 Å

Table 1.8 Crystallographic data of sodium metasilicate. Data taken from ref. [101].

Calcium Silicate Hydrate

The family of the calcium silicate hydrate minerals consists of several members. Although rarely found in nature, tobermorite ($Ca_5Si_6O_{16}(OH)_2 \times 7H_2O$) and jennite ($Ca_9[(OH)_4|Si_3O_8OH]_2 \times 6H_2O$) are the most prominent ones, due to ther chemical resemblance to calcium-silicate-hydrate (C-S-H), the glue of cement. [102] The crystal structure of tobermorite can be classified according to difference in basal spacing ranging from 9 Å (riversideite) to 14 Å (plombierite), depending on the degree of hydration.[103] It can be described by a central CaO_2 sheet, connected to silicate "dreierketten" on both sides (Figure 1.22). A similar motif for the silicate chains is encountered in wollastonite.

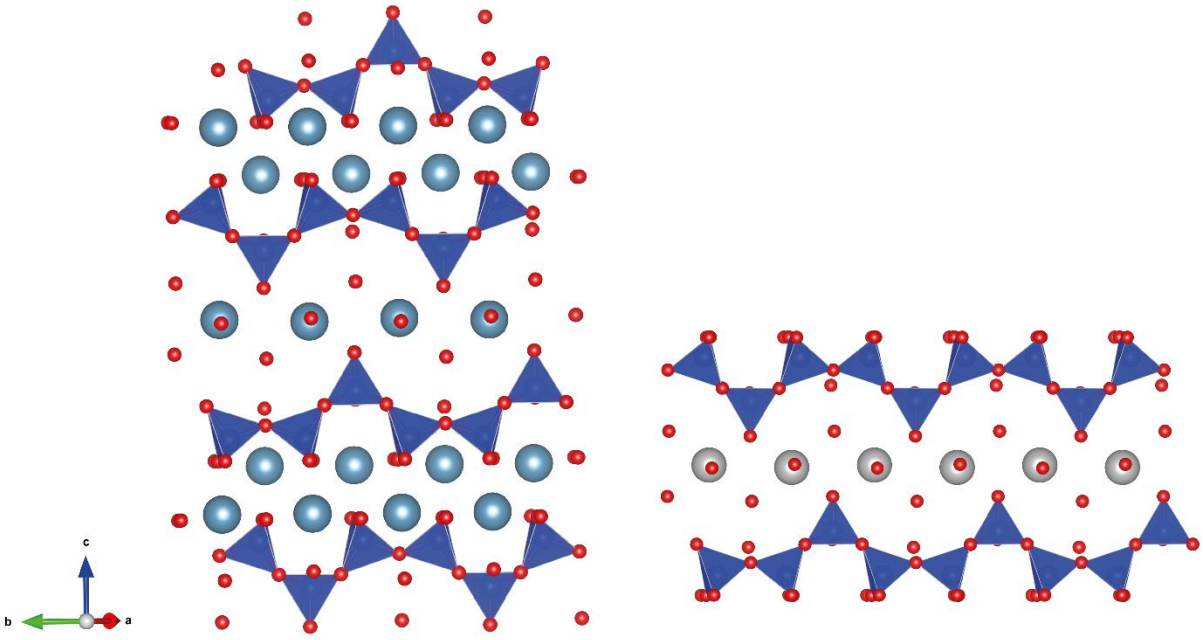

Figure 1.22 Crystal structure of tobermorite projected closely to the [001] direction and dreierketten motif typical for calcium-silicate-hydrate phases.[103]

composition	$Ca_5Si_6O_{16}(OH)_2 \times 7H_2O$
space group	$B11b$ (9), Z=2
lattice parameters	a=6.73 Å b=7.42 Å c=27.98 Å

Table 1.9 Crystallographic and solubility data of sodium metasilicate. Data taken from ref. [103].

1.5.3 Calcium Sulfates

In nature calcium sulfate exists in three pseudopolymorphs, namely gypsum ($CaSO_4 \times 2H_2O$), bassanite ($CaSO_4 \times 0.5H_2O$) and anhydrite ($CaSO_4$). The importance of gypsum in human society arises from its use in construction industry where it is used for gypsum boards, gypsum mortars and as a component in cement.[104,105] The thermodynamically most stable modification in the $CaSO_4$-H_2O system is gypsum, whereas bassanite is metastable at all temperatures. It could be shown by diffraction and vibrational spectroscopy that burning of gypsum is accompanied by dehydration and thus subsequent phase transformation to bassanite and anhydrite.[106]

Anhydrite

The anhydrous crystalline modification in the $CaSO_4$-H_2O system belongs to anhydrite and at least two polymorphs, i.e., β-anhydrite (insoluble) and γ-anhydrite (soluble) are known to exist. Investigation of the thermal decomposition of $CaSO_4 \times 2D_2O$ has shown that gypsum decomposes to a subhydrate and subsequently to γ-anhydrite.[107] The crystal structure shows an arrangement of six-membered channels (Figure 1.23), closely related to the structure of bassanite (*vide infra*).

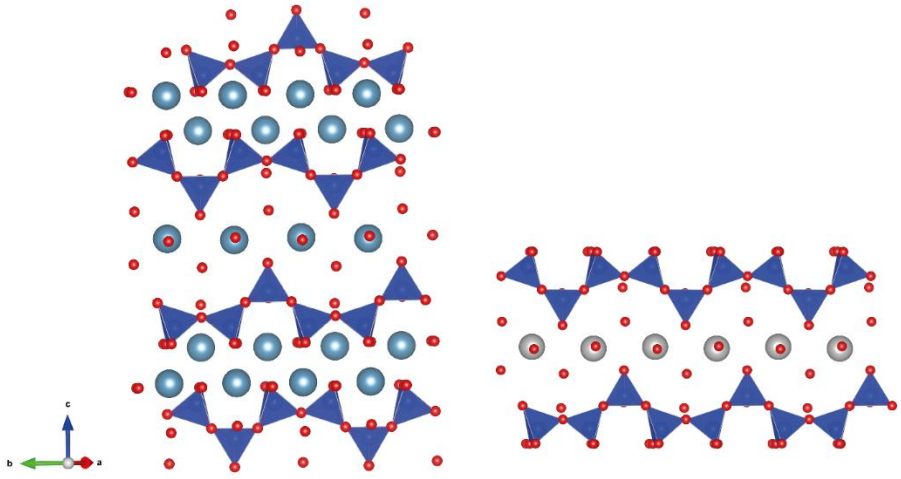

Figure 1.23 Crystal structure of tobermorite projected closely to the [001] direction and dreierketten motif typical for calcium-silicate-hydrate phases

composition	$CaSO_4$
space group	$C222$ (21), Z=6
lattice parameters	a=12.07 Å b=6.97 Å c=6.30 Å

Table 1.10 Crystallographic data of anhydrite. Data taken from ref.[107].

Bassanite

Bassanite is the hemihydrate in the $CaSO_4$-H_2O system and metastable at all temperatures. It has been shown that bassanite plays an important role in the formation of gypsum, during which a homogenous precipitation of bassanite nanoparticles, followed by self-assembly to elongated aggregates and finally a transformation to gypsum could be observed.[108] The structure is built up of $Ca^{2+} - SO_4^{2-}$ chains, running along the [001] direction (Figure 1.24), which leads to the formation of channels with an approximate diameter of 4 Å, which can host structural water and other molecules.[109]

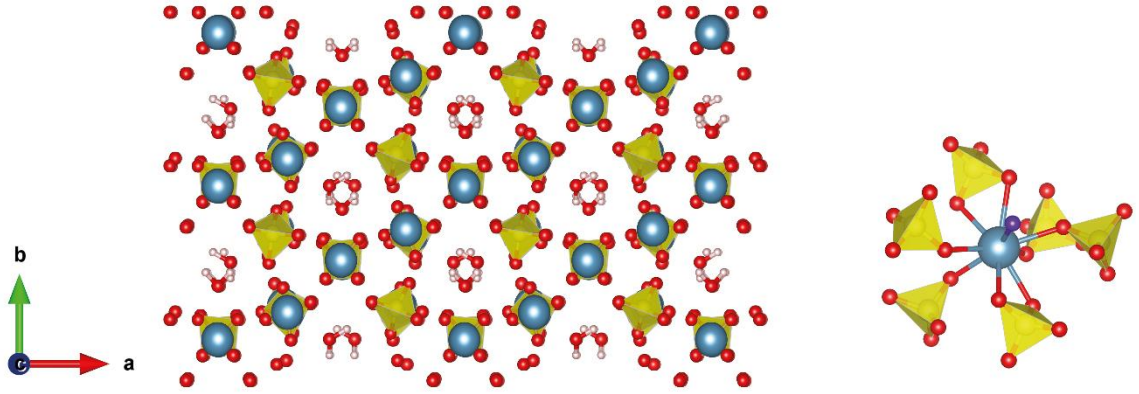

Figure 1.24 Crystal structure of bassanite projected along [001] and coordination sphere of a Ca^{2+} cation.[110]

composition	$CaSO_4 \times 0.5H_2O$
space group	$P3_121$ (152), Z=3
lattice parameters	a=6.937 Å c=6.345 Å

Table 1.11 Crystallographic data of bassnite. Data taken from ref. [110].

Gypsum

The thermodynamically most stable modification at ambient conditions in the $CaSO_4$-H_2O system is gypsum. It has a needle like morphology and its structure is marked by double layers, interconnected due to hydrogen bonding of the water species. Due to this structural arrangement the preferred cleavage is parallel to (010).

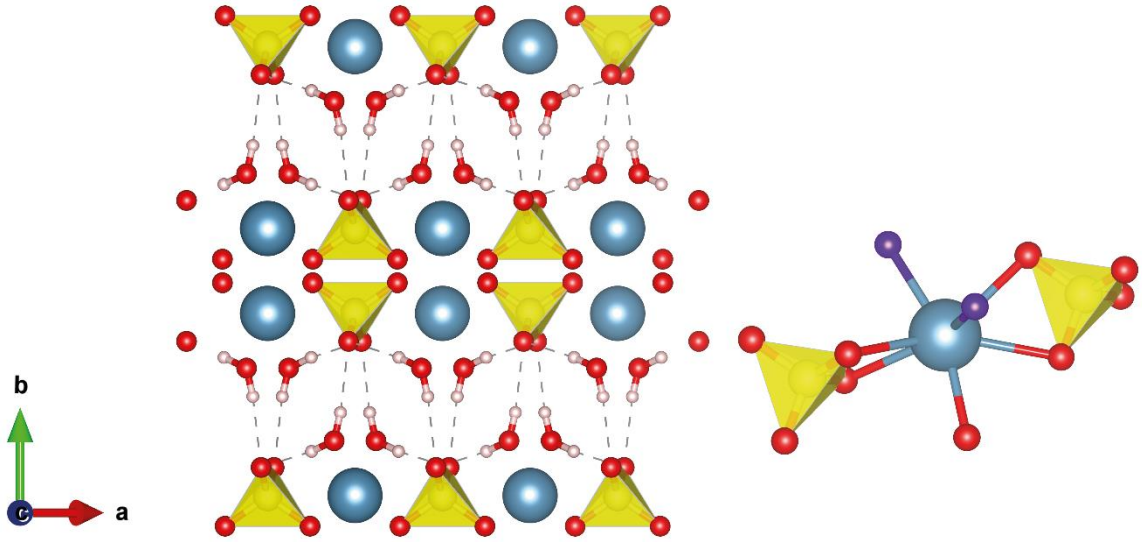

Figure 1.25 Crystal structure of gypsum projected along [001] and coordination sphere of a Ca^{2+} cation.[111]

composition	$CaSO_4$ x $2H_2O$
space group	$P12/c1$ (15), Z=4
lattice parameters	a=6.291 Å b=15.218 Å c=5.681 Å

Table 1.12 Crystallographic data of bassanite. Data taken from ref. [111].

1.5.4 Phosphate Minerals

Phosphates contribute to a wide variety of chemistry and they are of special interest, due to their broad range of industrial applications and their importance in biochemistry and in biomineralization.[112] Metal phosphates are used as corrosion coatings[113], catalysts[114], glasses[115] and have received special attention in recent years due to their use as battery materials.[116] A major part of their structural diversity arises from the different degrees of protonation and the formation of condensated phosphates, all of which share the structural motif of a P-O-P bond. The condensation leads to different type of binding geometries. If a progressive linear linkage by one or two oxygen atoms in the phosphate unit is given, the corresponding anions are called *polyphosphates* $(P_nO_{3n+1})^{(n+2)-}$.[117] For n=2 this will lead to $(P_2O_7)^{2-}$ anions, commonly called *pyrophosphates*. For very large values of n the O/P ratio approaches 3, and the resulting polyanion has a linear chain structure with the formula $(PO_3)^{n-}$, as for example in Kurrol's salt $(NaPO3)_x$. A special case can be found if the condensation occurs in a cyclic manner, which leads to the formation of ring-like anions of the generic formula $(P_nO_{3n})^{n-}$.

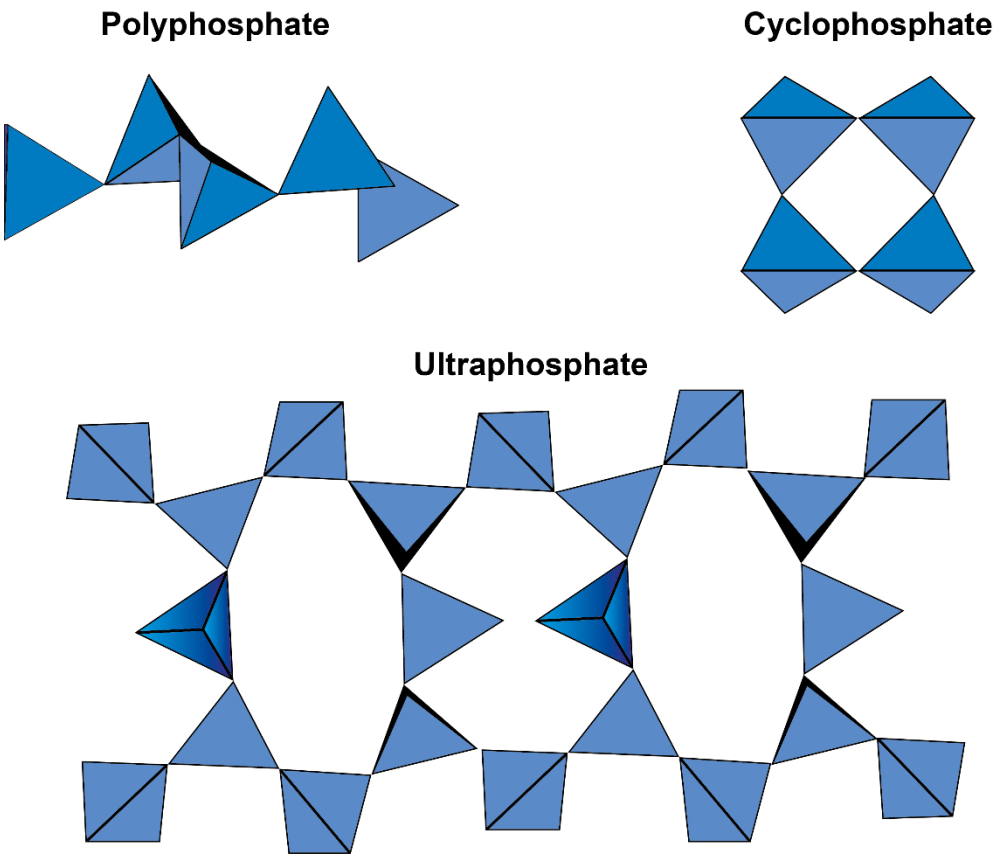

Figure 1.26 Schematic illustration of the different condensed phosphates.

The condensed phosphates containing this structural unit are called *cyclophosphates*. When phosphates share three oxygen atoms with adjacent phosphate groups, anion geometries

including groups, layers, ribbons and networks will be obtained. The resulting phosphates are the so called *ultraphosphates* and have the general formula $\left(P_{(2m+n)}O_{(5m+3n)}\right)^{n-}$. A general illustration for these classes of condensed phosphate is given in Figure 1.26

. **Hopeite**

Many zinc phosphate hydrates are known (i.e., $Zn_3(PO_4)_2 \times 1H_2O$, $Zn_2P_4O_{12} \times 8H_2O$), although the most prominent one remains hopeite ($Zn_3(PO_4)_2 \times 4H_2O$), a rarely occurring natural mineral. Its main applications are in dental cements and in coating technology. Up to three polymorphs (α, β, γ) are known, with slight changes in the hydrogen network. β-hopeite crystallizes in the centrosymmetric space group *Pbnm* with 4 formula units per elemental cell. The structure consists of tetrahedrally coordinated $Zn(O_p)_4$ units, arranged in "Zweier-Einfachkette" chains parallel arranged along [100]. In between layers along [010] direction octahedrally coordinated zinc can be found. The phosphate environment constists of orthophosphates.

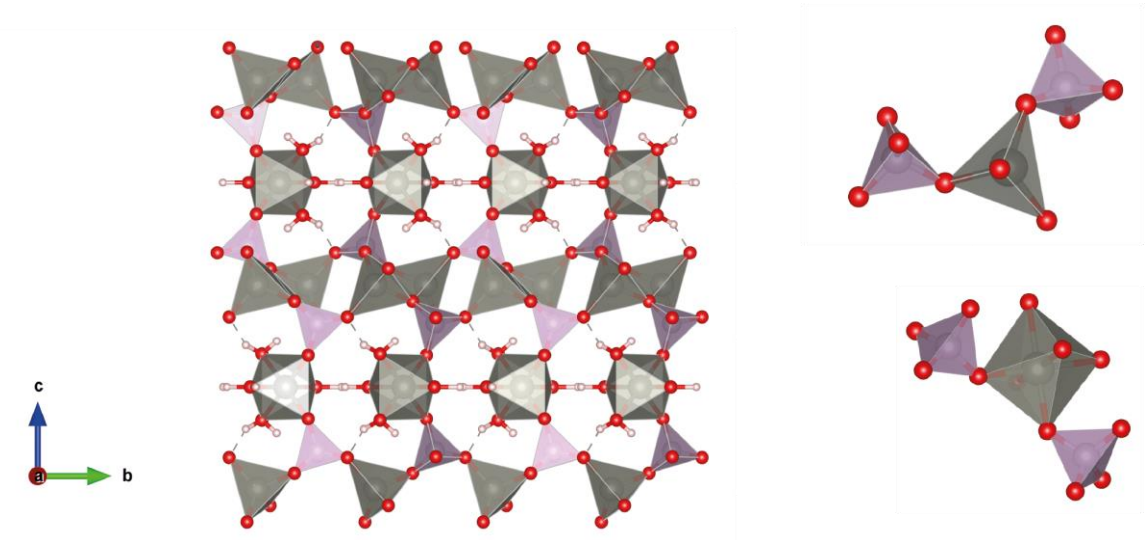

Figure 1.27: Crystal structure of β-hopeite projected along [100] direction. In addition tetrahedral and octahedral environments of zinc positions are shown.[115]

composition	$Zn_3(PO_4)_2$ x H_2O
space group	Pnmb (62), Z=4
lattice parameters	a=10.59 Å b=18.31 Å c=5.03 Å

Table 1.13 Crystallographic data of hopeite. Data taken from [115]

[1] J. J. De Yoreo, P. G. Vekilov, *Rev. Mineral. Geochem.* **2003**, *54*, 57.
[2] V. K. LaMer, R. H. Dinegar, *J. Am. Chem. Soc.* **1950**, *72*, 4847.
[3] S. Karthika, T. K. Radhakrishnan, P. Kalaichelvi, *Cryt. Growth Des.* **2016**, *16*, 6663.
[4] J. De Yoreo, *Nat. Mater.* **2013**, *12*, 284.
[5] R. Becker, W. Döring, *Ann. Phys.* **1935**, *416*, 719.
[6] M. Volmer, A. Weber, *Z. Phys. Chem.* **1926**, *119U*, 277.
[7] J. Frenkel, *J. Chem. Phys.* **1939**, *7*, 538.
[8] R. B. Heady, J. W. Cahn, *J. Chem. Phys.* **1973**, *58*, 896.
[9] M. W. Pitcher, S. V. Ushakov, A. Navrotsky, B. F. Woodfield, G. Li, J. Boerio-Goates, B. M. Tissue, *J. Am. Ceram. Soc.* **2005**, *88*, 160.
[10] A. Navrotsky, *J. Therm. Anal. Calorim.* **1999**, *57*, 653.
[11] J. M. McHale, A. Auroux, A. J. Perrotta, A. Navrotsky, *Science* **1997**, *277*, 788.
[12] W. Ostwald, *Z. Phys. Chem.* **1897**, *22U*, 289.
[13] A. Navrotsky, *Proc. Natl. Acad. Sci. U.S.A.* **2004**, *101*, 12096.
[14] F. Zhang, *J. Phys. Condens. Matter* **2017**, *29*, 443002.
[15] J. Russo, H. Tanaka, *J. Chem. Phys.* **2016**, *145*, 211801.
[16] P. R. ten Wolde, D. Frenkel, *Science* **1997**, *277*, 1975.
[17] O. Gliko, N. Neumaier, W. Pan, I. Haase, M. Fischer, A. Bacher, S. Weinkauf, P. G. Vekilov, *J. Am. Chem. Soc.* **2005**, *127*, 3433.
[18] E. P. Favvas, A. Ch. Mitropoulos, *J. Eng. Sci. Tech. Rev.*
[19] P. G. Vekilov, *Nanoscale* **2010**, *2*, 2346.
[20] H. Fang, M. F. Hagan, W. B. Rogers, *PNAS* **2020**, *117*, 27927.
[21] N. Krautwurst, L. Nicoleau, M. Dietzsch, I. Lieberwirth, C. Labbez, A. Fernandez-Martinez, A. E. S. Van Driessche, B. Barton, S. Leukel, W. Tremel, *Chem. Mater.* **2018**, *30*, 2895.
[22] S. E. Wolf, J. Leiterer, V. Pipich, R. Barrea, F. Emmerling, W. Tremel, *J. Am. Chem. Soc.* **2011**, *133*, 12642.
[23] A. S. Schenk, H. Zope, Y.-Y. Kim, A. Kros, N. A. J. M. Sommerdijk, F. C. Meldrum, *Faraday Discuss.* **2013**, *159*, 327.
[24] C. N. R. Rao, *Mater. Sci. Eng. B* **1993**, *18*, 1.
[25] P. Baláž, M. Achimovičová, M. Baláž, P. Billik, Z. Cherkezova-Zheleva, J. M. Criado, F. Delogu, E. Dutková, E. Gaffet, F. J. Gotor, R. Kumar, I. Mitov, T. Rojac, M. Senna, A. Streletskii, K. Wieczorek-Ciurowa, *Chem. Soc. Rev.* **2013**, *42*, 7571.
[26] L. Takacs, *Chem. Soc. Rev.* **2013**, *42*, 7649.
[27] M. Senna, *Solid State Ion.* **1993**, *63–65*, 3.
[28] V. Šepelák, I. Bergmann, A. Feldhoff, P. Heitjans, F. Krumeich, D. Menzel, F. J. Litterst, S. J. Campbell, K. D. Becker, *J. Phys. Chem. C* **2007**, *111*, 5026.
[29] V. V. Boldyrev, *J. Mater. Sci* **2004**, *39*, 5117.
[30] A. Krusenbaum, S. Grätz, S. Bimmermann, S. Hutsch, L. Borchardt, *RSC Adv.* **2020**, *10*, 25509.
[31] J. G. Hernández, K. J. Ardila-Fierro, D. Crawford, S. L. James, C. Bolm, *Green Chem.* **2017**, *19*, 2620.
[32] S. Głowniak, B. Szczęśniak, J. Choma, M. Jaroniec, *Mater. Today.* **2021**, *46*, 109.
[33] S. Rosenkranz, S. Breitung-Faes, A. Kwade, *Powder Techol.* **2011**, *212*, 224.
[34] D. L. Zhang, *Prog. Mater. Sci.* **2004**, *49*, 537.
[35] R. Weichert, K. Schönert, *J. Mech. Phys. Solids* **1978**, *26*, 151.
[36] P. A. Thiessen, K. Meyer, G. Heinicke, In *Grundlagen der Tribochemie*, Akademie-Verlag, Berlin, **1967**.
[37] C. Suryanarayana, *Prog. Mater. Sci.* **2001**, *46*, 1.

[38] M. Maslyk, S. Bach, W. Li, S. I. Shylin, M. Panthöfer, B. Barton, V. Ksenofontov, K. Xu, B. Meermann, U. Kolb, J. Schmedt auf der Günne, W. Tremel, *J. Phys. Chem. C* **2021**, *125*, 2636.
[39] S. Leukel, M. Panthöfer, M. Mondeshki, G. Kieslich, Y. Wu, N. Krautwurst, W. Tremel, *Chem. Mater.* **2018**, *30*, 6040.
[40] C. Costa, In *Materials for Construction and Civil Engineering* (Eds.: Gonçalves, M. C.; Margarido, F.), Springer International Publishing, Cham, **2015**, pp. 1–52.
[41] K. Wingo, *J. Vet. Dent.* **2018**, *35*, 18.
[42] J. J. Biernacki, J. W. Bullard, G. Sant, K. Brown, F. P. Glasser, S. Jones, T. Ley, R. Livingston, L. Nicoleau, J. Olek, F. Sanchez, R. Shahsavari, P. E. Stutzman, K. Sobolev, T. Prater, *J. Am. Ceram. Soc.* **2017**, *100*, 2746.
[43] H. F. W. Taylor, *Cement chemistry*, 2nd ed., T. Telford, London, **1997**.
[44] R. Benedix, *Bauchemie: Einführung in die Chemie für Bauingenieure*, 2., überarb. Aufl., Teubner, Stuttgart, **2003**.
[45] E. Tajuelo Rodriguez, I. G. Richardson, L. Black, E. Boehm-Courjault, A. Nonat, J. Skibsted, *Adv. Appl. Ceram.* **2015**, *114*, 362.
[46] M.-C. Schlegel, A. Sarfraz, U. Müller, U. Panne, F. Emmerling, *Angew. Chem. Int. Ed.* **2012**, *51*, 4993.
[47] Q. Hu, M. Aboustait, T. Kim, M. T. Ley, J. W. Bullard, G. Scherer, J. C. Hanan, V. Rose, R. Winarski, J. Gelb, *Cem. Concr. Res.* **2016**, *89*, 14.
[48] L. L. Y. Chang, R. A. Howie, J. Zussman, *Non-silicates: Sulphates, Carbonates, Phosphates, Halides (Rock-Forming Minerals)*, Second Edition., Geological Society of London, **1995**.
[49] Y. Mimran, *Sedimentology* **1977**, *24*, 333.
[50] K. Kelts, K. J. Hsü, In *Lakes: Chemistry, Geology, Physics* (Ed.: Lerman, A.), Springer, New York, NY, **1978**, pp. 295–323.
[51] V. Bonavetti, H. Donza, G. Menéndez, O. Cabrera, E. F. Irassar, *Cem. Concr. Res.* **2003**, *33*, 865.
[52] J. S. Han, S. Y. Jung, D. S. Kang, Y. B. Seo, *ACS Sustainable Chem. Eng.* **2020**, *8*, 8994.
[53] A. Borrego-Sánchez, R. Sánchez-Espejo, B. Albertini, N. Passerini, P. Cerezo, C. Viseras, C. I. Sainz-Díaz, *Pharmaceutics* **2019**, *11*, 533.
[54] F. C. Meldrum, *Int. Mater. Rev.* **2003**, *48*, 187.
[55] H. A. Lowenstam, S. Weiner, *On Biomineralization*, Oxford University Press, New York, **1989**.
[56] J. D. Currey, *J. Zool.* **1976**, *180*, 445.
[57] J. Aizenberg, A. Tkachenko, S. Weiner, L. Addadi, G. Hendler, *Nature* **2001**, *412*, 819.
[58] N. H. C. Sparks, S. Mann, D. A. Bazylinski, D. R. Lovley, H. W. Jannasch, R. B. Frankel, *Earth Planet. Sci. Let.* **1990**, *98*, 14.
[59] M. S. Reddy, *Front. Microbiol.* **2013**, *4*, 314.
[60] R. Chang, S. Kim, S. Lee, S. Choi, M. Kim, Y. Park, *Front. Energy. Res.* **2017**, *5*, 17.
[61] M. Albéric, L. Bertinetti, Z. Zou, P. Fratzl, W. Habraken, Y. Politi, *Adv. Sci.* **2018**, *5*, 1701000.
[62] K. Sawada, *Pure Appl. Chem.* **1997**, *69*, 921.
[63] S. Leukel, M. Panthöfer, M. Mondeshki, G. Kieslich, Y. Wu, N. Krautwurst, W. Tremel, *J. Am. Chem. Soc.* **2018**, *140*, 14638.
[64] A. E. Morandeau, C. E. White, *Chem. Mater.* **2015**, *27*, 6625.
[65] S. Bentov, S. Weil, L. Glazer, A. Sagi, A. Berman, *J. Struct. Biol.* **2010**, *171*, 207.
[66] J. Ihli, W. C. Wong, E. H. Noel, Y.-Y. Kim, A. N. Kulak, H. K. Christenson, M. J. Duer, F. C. Meldrum, *Nat Commun* **2014**, *5*, 3169.
[67] P. Opitz, M. P. Asta, A. Fernandez-Martinez, M. Panthöfer, A. Kabelitz, F. Emmerling, M. Mondeshki, W. Tremel, *Cryst. Growth Des.* **2020**, *20*, 6831.

[68] P. Opitz, L. Besch, M. Panthöfer, A. Kabelitz, R. E. Unger, F. Emmerling, M. Mondeshki, W. Tremel, *Adv. Funct. Mater.* **2021**, *31*, 2007830.
[69] F. Lippmann, *Sedimentary Carbonate Minerals*, Springer-Verlag, Berlin Heidelberg, **1973**.
[70] G. Van Tendeloo, H. R. Wenk, R. Gronsky, *Phys. Chem. Minerals* **1985**, *12*, 333.
[71] H. Sitepu, B. H. O'Connor, D. Li, *J Appl Cryst* **2005**, *38*, 158.
[72] L. N. Plummer, E. Busenberg, *Geochim. Comocim. Acta* **1982**, *46*, 1011.
[73] S. Frisia, A. Borsato, I. J. Fairchild, F. McDermott, E. M. Selmo, *J. Sediment. Res.* **2002**, *72*, 687.
[74] N. Nassif, N. Pinna, N. Gehrke, M. Antonietti, C. Jäger, H. Cölfen, *Proc. Natl. Acad. Sci. U.S.A.* **2005**, *102*, 12653.
[75] M. Tucker, V. Paul. Wright, *Carbonate Sedimentology*, Wiley-Blackwell, **1990**.
[76] R. A. Berner, *Geochim. Cosmochim. Acta.* **1975**, *39*, 489.
[77] P. Németh, E. Mugnaioli, M. Gemmi, G. Czuppon, A. Demény, C. Spötl, *Sci. Adv.* **2018**, *4*, 6178.
[78] J. P. R. De Villiers, *Am. Min.* **1971**, *56*, 758.
[79] J. D. Rodriguez-Blanco, S. Shaw, P. Bots, T. Roncal-Herrero, L. G. Benning, *Geochim. Cosmochim. Acta* **2014**, *127*, 204.
[80] T. Ito, *J. Mineral. Petrol. Econ. Geol.* **1993**, 485.
[81] M. I. Bird, A. R. Chivas, C. J. Radnell, H. R. Burton, *Palaeogeor., Palaeoclimatol. Palaeoecol.* **1991**, *84*, 109.
[82] H. Catherine, W. Skinner, G. W. Osbaldiston, A. N. Wilner, *Am. Min.* **1977**, *62*, 273.
[83] L. A. J. Garvie, *Am. Min.* **2003**, *88*, 1879.
[84] H. Hull, A. G. Turnbull, *Geochim. Cosmochim. Acta.* **1973**, *37*, 685.
[85] M. Neumann, M. Epple, *Eur. J. Inorg. Chem.* **2007**, *2007*, 1953.
[86] G. Zhang, C. Verdugo-Escamilla, D. Choquesillo-Lazarte, J. M. García-Ruiz, *Nat Commun* **2018**, *9*, 5221.
[87] H. Effenberger, *Monatsh. Chem.* **1981**, *112*, 899.
[88] D. Kralj, L. Brečević, *Colloids Surf. A Physicochem.* **1995**, *96*, 287.
[89] A. N. Zaitsev, J. Keller, J. Spratt, E. N. Perova, A. Kearsley, *Canad. Mineral.* **2008**, *46*, 843.
[90] A. N. Zaitsev, J. Keller, *Lithos* **2006**, *91*, 191.
[91] P. N. Gavryushkin, V. G. Thomas, N. B. Bolotina, V. V. Bakakin, A. V. Golovin, Y. V. Seryotkin, D. A. Fursenko, K. D. Litasov, *Cryst. Growth. Des.* **2016**, *16*, 1893.
[92] J. L. Bischoff, D. B. Herbst, R. J. Rosenbauer, *Geochim. Cosmochim. Acta.* **1991**, *55*, 1743.
[93] M. Getenet, J. M. García-Ruiz, C. Verdugo-Escamilla, I. Guerra-Tschuschke, *Crystals* **2020**, *10*, 467.
[94] B. Dickens, W. E. Brown, *Inorg. Chem.* **1969**, *8*, 2093.
[95] M. Fleischer, *J. Chem. Educ.* **1954**, *31*, 446.
[96] F. Liebau, *Structural Chemistry of Silicates*, Springer Berlin Heidelberg, Berlin, Heidelberg, **1985**.
[97] V. Kahlenberg, *CHIMIA.* **2010**, *64*, 716.
[98] W. S. McDonald, D. W. J. Cruickshank, *Acta Cryst* **1967**, *22*, 37.
[99] N. I. Demidenko, L. I. Podzorova, V. S. Rozanova, V. A. Skorokhodov, V. Ya. Shevchenko, *Glass and Ceramics* **2001**, *58*, 308.
[100] S. K. Saxena, M. Kumar, D. S. Chundawat, N. B. Singh, *Materials Today: Proceedings* **2020**, *29*, 733.
[101] S. Milani, D. Comboni, P. Lotti, P. Fumagalli, L. Ziberna, J. Maurice, M. Hanfland, M. Merlini, *Minerals* **2021**, *11*, 652.
[102] W. Kunther, S. Ferreiro, J. Skibsted, *J. Mater. Chem. A* **2017**, *5*, 17401.

[103] E. Bonaccorsi, S. Merlino, A. R. Kampf, *J. Am. Chem. Soc.* **2005**, *88*, 505.
[104] A. E. Charola, J. Pühringer, M. Steiger, *Environ. Geol.* **2007**, *52*, 339.
[105] B. Tian, M. D. Cohen, *Cem. Concr. Res.* **2000**, *30*, 117.
[106] T. Schmid, R. Jungnickel, P. Dariz, *Minerals* **2020**, *10*, 115.
[107] C. Bezou, A. Nonat, J.-C. Mutin, A. N. Christensen, M. S. Lehmann, *J. Solid State Chem.* **1995**, *117*, 165.
[108] A. E. S. Van Driessche, L. G. Benning, J. D. Rodriguez-Blanco, M. Ossorio, P. Bots, J. M. García-Ruiz, *Science* **2012**, *336*, 69.
[109] D. Freyer, W. Voigt, *Monatsh. Chem.* **2003**, *134*, 693.
[110] W. Abdel, *Cryst. Mater.* **1993**, *205*, 99.
[111] B. F. Pedersen, D. Semmingsen, *Acta Cryst. B* **1982**, *38*, 1074.
[112] J. D. Toner, D. C. Catling, *Proc. Natl. Acad. Sci. U.S.A.* **2020**, *117*, 883.
[113] L. Kwiatkowski, *Surf. Eng.* **2004**, *20*, 292.
[114] S. Kanai, I. Nagahara, Y. Kita, K. Kamata, M. Hara, *Chem. Sci.* **2017**, *8*, 3146.
[115] R. K. Brow, *J. Non-Cryst. Solids* **2000**, *263–264*, 1.
[116] J. Ling, C. Karuppiah, S. G. Krishnan, M. V. Reddy, I. I. Misnon, M. H. Ab Rahim, C.-C. Yang, R. Jose, *Energy Fuels* **2021**, *35*, 10428.
[117] A. Durif, *Crystal Chemistry of Condensed Phosphates*, Springer US, Boston, MA, **1995**

2

Understanding the Stability and Recrystallization Behavior of Ball-Milled Amorphous Zinc Phosphate

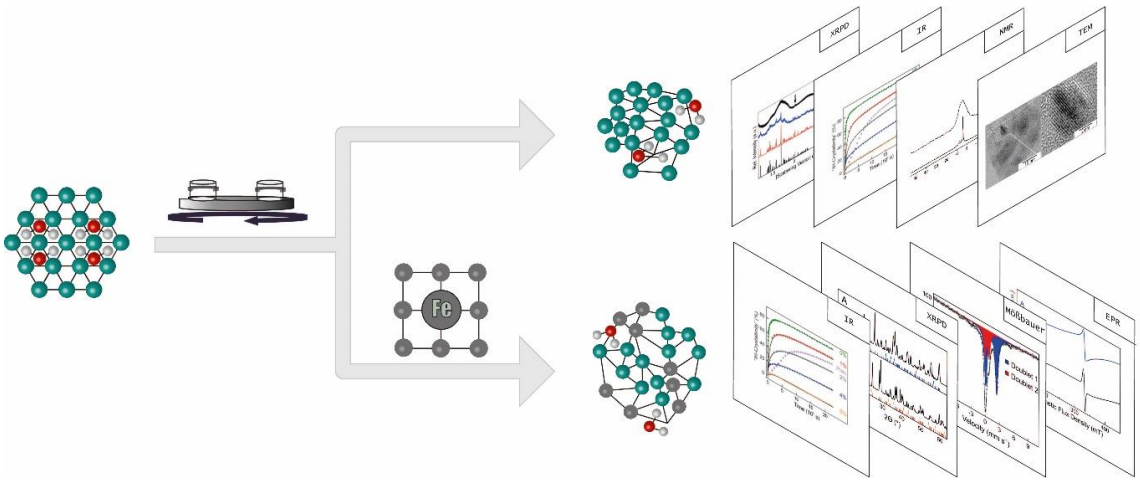

Amorphous zinc phosphate $Zn_3(PO_4)_2$, an important anti-corrosive pigment, was prepared by balling milling hopeite, $Zn_3(PO_4)_2 \times 4H_2O$. The ball milling tools have a strong impact on the outcome of the reaction as traces of iron may be incorporated into the product. This was modelled in zirconia ball mills with traces of elemental Fe (or ^{57}Fe). Monitoring the reaction spectroscopically revealed major differences in the amorphization and also recrystallization behavior due to changes of the local structure of the impurities.

This chapter contains an adapted reproduction of *Journal of Physical Chemistry C* **2021**, DOI: 10.1021/acs.jpcc.0c09044, reprinted with permission of the American Chemical Society.

Authorship Contribution

Study conception and design	M. Maslyk
	S. Bach
	W. Tremel
	J. Schmedt auf der Günne
Acquisition of data	S. Bach
	M. Maslyk
	W. Li
	S. Shylin
	B. Barton
	K. Xu
	V. Ksenofontov
	B. Meermann
Analysis and interpretation of data	M. Maslyk
	S. Bach
	M. Panthöfer
	S. Shylin
	B. Barton
	K. Xu
	B. Meermann
	V. Ksenofontov
Drafting of manuscript	M. Maslyk
	S. Bach
Critical Revision	W. Tremel
	J. Schmedt auf der Günne
	U. Kolb

2.1 Relevance to doctoral thesis

Hopeite (Zn_3PO_4 x 4 H_2O) is a common natural mineral, which is easily accessible by precipitation reactions and finds industrial relevance in coating technologies and as a dental cement. The latter is achieved by mixing ZnO and H_3PO_4 to a slurry paste, which sets after a certain time. Due to the crystalline bound water in the crystal structure and the underlying phosphate network, a rich polymorphism can be observed in zinc phosphate hydrates. As polymorphism influences physical and chemical properties, control over polymorph selection is of special interest in material science. Previous studies in our research group have shown that hydration and diffusion have a substantial impact in the in stabilization of amorphous phases from bottom-up synthesis. As these phases are characterized by a lack of long-range order and structural coherence, the use of mechanochemistry provides an easy bottom-down approach to amorphous phases. Therefore, high energy ball milling was utilized to induce phase transformation in zinc phosphate. An investigation of different milling times and educt ratios had shown that iron impurities from the milling equipment led to an amorphization of the starting compound. To investigate this behavior detail, inert milling equipment (zirconia) was used and the wear of iron simulated by addition of elemental iron powder. In the first step the amorphization of hopeite in respect to different iron ratios was investigated by use of FTIR spectroscopy, DTA/TG analysis, PXRD and NMR spectroscopy. Specific NMR experiments (REDOR) were additionally employed to investigate the observed dehydration of the starting compound. In addition, ^{57}Fe Mößbauer spectroscopy was utilized to check the state of the added iron impurities and gain insight into its effect and localization in the amorphization process. As the crystallization pathways from amorphous phases have been shown to enable access to metastable polymorphs, the thermal and aqueous recrystallization pathways in respect to the impurity ratio were investigated. In general, a new mechanochemical approach to amorphous zinc phosphate from hopeite, by addition of iron impurities could be established. By application of specific spectroscopic and diffraction methods the underlying amorphization process and thermal, as well as aqueous recrystallization could be elucidated

2.2 Introduction

Zinc phosphate $Zn_3(PO_4)_2$ is an important anti-corrosive pigment on metal surfaces, where it acts as anodic inhibitor by forming a dense phosphate surface film.[1–3] In addition, it is used frequently as cement in dentistry for luting permanent metal restorations.[4,5] The formation of the cement is due to non-crystalline zinc phosphate containing small particles of unreacted ZnO. Although no crystalline phosphate is involved in the setting of the cement, its surfaces are modified by small hopeite ($Zn_3(PO_4)_2 \cdot 4\,H_2O$) crystallites, and metastable (crystalline or amorphous) intermediates are assumed to be important during the kinetically controlled hardening.[6] Amorphous zinc phosphate may be thermodynamically stable at the nanoscale due to a crossover in thermodynamic stabilities arising from surface energy,[7] but it is inherently labile and appears to serve, similar to other amorphous phases,[8,9] as a reservoir for the formation of crystalline polymorphs.

Zinc phosphate has also been reported to form protective films on rubbing surfaces.[10] As many other metal phosphates, it adopts a network structure where PO_4^{3-} tetrahedra are interconnected through Zn^{2+} cations.[11–13] The stiffness of the tribofilm is determined by the coordination of the metal atoms.[14,15] By increasing the coordination number of the Zn^{2+} cations under pressure or shear (which may occur during asperity collision), the material may change from an initially open network structure with viscoelastic properties to a more densely packed and therefore stiffer structure.[16] Because of its coordinative flexibility Zn^{2+} can even switch back to four-fold coordination during decompression after having adopted five and six-fold coordination at higher pressure. Therefore, an understanding of the phase transformations (and grain size refinement) of zinc phosphate under pressure or shear is important as it provides insights into its chemical reactivity and structure-property relations.

Zinc phosphate occurs in several degrees of hydration. Among the tetrahydrates, hopeite is the most stable polymorph. Hopeite again has three different polymorphs (α-, β-, and γ-hopeite) that differ only in the orientation of crystal water molecules.[17–20] The related phosphophyllite ($Zn_2Fe(PO_4)_2 \cdot 4\,H_2O$) is an important phase during the formation of corrosion resistant coatings on steel,[1,21,22] and a related basic zinc phosphate (tarbuttite, $Zn_2(PO_4)(OH)$) is formed in phosphate-rich solutions.[23] Zinc hydrogen phosphate trihydrate (ZHPT) forms by slightly changing the formation conditions that are needed to obtain α-hopeite.[17] Stepwise dehydration leads to formation of zinc phosphate dihydrate and finally to anhydrous zinc phosphates.[17,24]

Amorphous zinc phosphate (AZP) can be obtained by fast precipitation from aqueous[25,26] or polyol[27] solution. Phase transformations of metal phosphates (or oxides) by shear occur typically during ball-milling,[30,31] a process central to the processing of nanoparticles.[32–34] Milling generates disorder, amorphization, and defects (e.g., point defects and crystallographic shear (Wadsley defects)). Especially for hydrated or porous compounds, milling can lead to dehydration with a concomitant collapse of ordered linkages between the building blocks.[35–40] Amorphization by ball-milling is a multi-step process where random dislocations are formed in an initial step and impact energy is reduced by rearranging lattice dislocations to clusters.[41-43] By progressively reducing the cluster size, nanopowders containing amorphous/disordered regions with nanocrystalline grains embedded in amorphous grain boundaries are formed. Therefore, the structure of ball-milled nanopowders may be very different from that of nanopowders synthesized by wet chemistry.[44,45] Compounds may appear transiently after short milling times,[45] and materials formed under milling conditions may be metastable at ambient temperature and pressure, because they exist in thermodynamic equilibrium only at high temperature or/and pressure. Polymorphic transformations depend on the dynamical conditions of grinding,[46] but also on the nature (steel, zirconia) of the grinding tools.[4] Metastable phases may be stabilized either by structural distortions induced through the milling process[48] or by incorporating impurities (e.g., Fe^{2+}, Fe^{3+} and Cr^{3+} from steel) into the sample due to the wear and oxidation of the milling media.[49] Despite the surge of studies on high-energy ball-milling,[30-34,41-43,50-52] comparatively little attention has been paid to the effect of impurities and contaminations introduced during the grinding process on the products, their properties and reactivity, in particular considering the importance of ball-milling for the large-scale production of nanoparticles. During the preparation of amorphous zinc phosphate, the recrystallization to hopeite turned out to be very different for materials prepared in stainless steel and zirconia containers (see Figure S 2.1, Supporting Information), although the container had no apparent effect on the amorphization itself. We have pursued and analyzed this abrasion effect by intentionally adding ^{57}Fe impurities to simulate the abrasion effect and to understand the effect of Fe on the metastability of zinc phosphate and its inhibited recrystallization at the nanoscale. We show that Fe impurities stabilize amorphous zinc phosphate prepared under shear and inhibit recrystallization of ball-milled amorphous zinc phosphate (BM-AZP). Our results provide insight into reactions in protective films on rubbing surfaces or during battery cycling and give and theoretical guidance for the preparation of amorphous phosphates and oxides.

2.3 Experimental section

Synthesis of Hopeite. Hopeite was synthesized by mixing 300 mM of $Zn(NO_3)_2$ solution ($Zn(NO_3)_2 \cdot 6\,H_2O$ in Milli-Q water, >98%, Sigma-Aldrich) and 200 mM of Na_3PO_4 solution (>96%, Sigma-Aldrich). The mixture was stirred for 1 week at room temperature, centrifuged (9000 rpm), and dried by re-suspending in ethanol p. A. (≥99.5%, Sigma-Aldrich), centrifuging again, and finally drying under dynamic vacuum for 3 d.

Amorphous Zinc Phosphate (AZP) Nanoparticles. AZP nanoparticles were prepared by direct precipitation from solution.[26] $Zn(NO_3)_2 \cdot 2\,H_2O$ (> 98%, Sigma-Aldrich) (10 mL) (solution 1), and Na_3PO_4 (> 96%, Sigma-Aldrich) were dissolved in deionized water (10 mL) (solution 2, both at ambient temperature), and solution 1 was stirred with 400 rpm in a beaker while solution 2 was added. To instantly separate the precipitated solids from solution the mixture was centrifuged (9000 rpm, 5 min) immediately. Subsequently, the solid was re-suspended in and centrifuged from acetone p.A. (≥ 99.5 %, Sigma-Aldrich) three times to remove adsorbed water. The solid was dried at room temperature under dynamic vacuum ($p = 3 \times 10^{-3}$ mbar) for two days.

Amorphous Zinc Phosphate by Ball Milling (BM-AZP) of Hopeite. 800 mg of hopeite were dispersed in reagent-grade ethanol (m=7.1 g) in order to dissipate heat, pressure, and friction during milling. The dispersions were treated with a planetary ball mill (Retsch PM100) in jars made of stainless steel (for different time intervals). 81 g of stainless steel grinding balls (5 mm diameter) were used. The number of revolutions was set to 600 min^{-1}

In addition, ZrO_2 grinding balls and jars were used (to lower the contamination of the samples caused by abrasion of the grinding tools because of their hardness). 15 g of grinding balls (1 mm diameter) were used (planetary ball mill PULVERISETTE 7 classic, Fritsch). The number of revolutions was set to 600 min^{-1} (BM-AZP-Zr). The reaction was carried out as well with different amounts of iron powder (>99.99%, Chempur, Alfa Aesar, -22 mesh) (0 to 80 mg, mass ratio Fe to hopeite ζ=0–10%) in order to quantify the effect of iron on the amorphization process and properties of the final products (BM-AZP-Fe). The maximum reaction time amounts to 360 minutes as no further changes in the X-ray profiles of the products were observed after this time.

Semi-Crystalline Zinc Phosphate (semi-CZP). To gain further insight in the crystallization pathways the ball milling reaction was interrupted at several points of the mechanochemical reaction. The isolated product intermediate is semi-crystalline zinc phosphate (semi-CZP). Fe-doped samples have the designation semi-CZP-Fe, undoped samples the designation semi-CZP-Zr.

Amorphization Kinetics. Depending on the milling time, samples varied in their crystallinity as determined by quantitative Fourier transform infrared spectroscopy (FT-IR) and powder X-ray diffraction (PXRD). For IR spectroscopy, the splitting of the asymmetric stretch of the phosphate group (occurring in crystalline hopeite) was analyzed. The IR measurements were calibrated with standards containing physical mixtures of crystalline hopeite and AZP with different ratios of the two components (Figure S 2.2, Supporting Information). The crystallinity of the samples could be evaluated quantitatively at any point during the transformation from the band splitting.

Crystallization Kinetics in Water. The reactivity of the amorphous products was examined by recrystallization in water. The reactions were monitored IR spectroscopically. The measurements were carried out on an ATR crystal of a Fourier transform infrared spectrometer by adding Milli-Q water. Spectra were recorded every 80 s and analyzed quantitatively using a MATLAB script. The splitting of the asymmetric stretching mode of the phosphate group is an indicator for the crystallinity. The phosphate band of crystalline zinc phosphate is split, whereas the band of amorphous zinc phosphate is non-split/broadened. As the (same area of the) sample is located constantly in the beam path of the evanescent wave, the fluctuations are low and the crystallization kinetics are determined without bias. For detailed information concerning X-ray synchrotron powder diffraction and NMR spectroscopy see Supporting Information (Experimental).[53-55]

2.4 Results and discussion

Phase-pure hopeite with particle sizes in the µm range was synthesized by precipitation from aqueous solutions of $Zn(NO_3)_2$ and Na_3PO_4. Phase identity was confirmed by PXRD and IR spectroscopy (Figure S 2.3, Supporting Information). All phases prepared and studied in this work are summarized in Figure 2.1.

Amorphization Kinetics. Amorphous zinc phosphate BM-AZP-Zr was prepared by treating crystalline hopeite in a planetary ball mill (zirconia balls). The amorphization was complete after 340 min of milling, as indicated by a broad non-split phosphate band in the

FT-IR spectrum (Figure 2.2A). The band splitting occurs only in crystalline hopeite due to factor group splitting and site symmetry. The reaction rate was determined by taken "snap shots" (interrupting the milling process after given time intervals, taking samples and recording their FT-IR spectra *ex situ*)[56,57] The band splitting is a measure for the progress of the amorphization reaction (Figure 2.2B). The "IR-crystallinity" reflects the local (short-range) order within the sample, whereas diffraction data (reflection width and profile) provide information concerning crystallite size, long-range order ("X-ray-crystallinity") and strain.

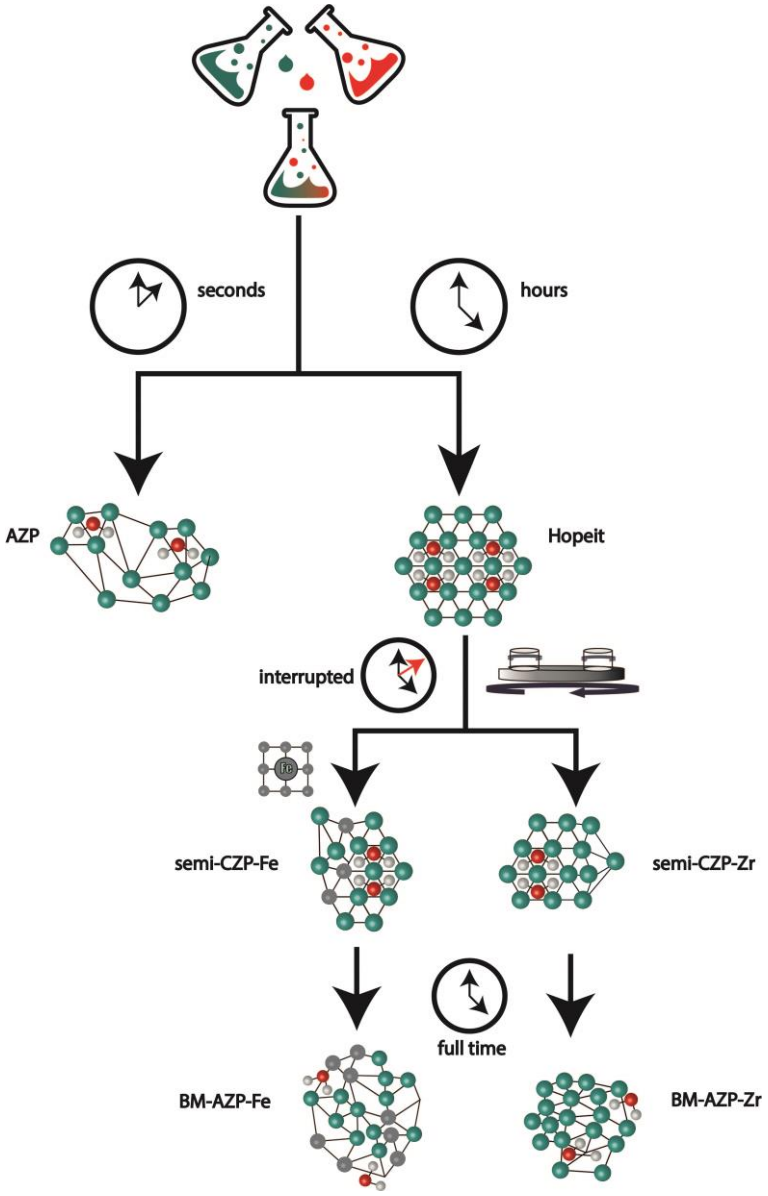

Figure 2.1 Overview of the products prepared during this study. The samples with the abbreviation semi-CZP were obtained by interrupting the ball milling at certain time intervals. Samples designated as BM-AZP were studied after the mechanochemical reaction was complete (340 min). The annotations Fe and Zr correspond to samples obtained in the absence or presence of iron "impurities".

The progress of the milling reaction in the presence of iron impurities (BM-AZP-Fe, ζ=2%, Figure S 2.4, Supporting Information) was similar. The transformation from hopeite to BM-AZP-Fe (in the presence of iron impurities) was monitored by XRD as well. The diffractograms in Figure 2.3 show sharp intensities in the diffraction pattern of hopeite after 2 min of milling (red trace). The pronounced reflection broadening after 62 min (blue trace) indicates the loss of crystallinity, and after 340 min (black trace, measured with high-energy synchrotron radiation) the amorphization was complete as demonstrated by the absence of reflections in the X-ray diffractogram. The most intense reflection of Fe appears at 11.72° in 2Θ (indicated by the black arrow in Figure 2.3A).

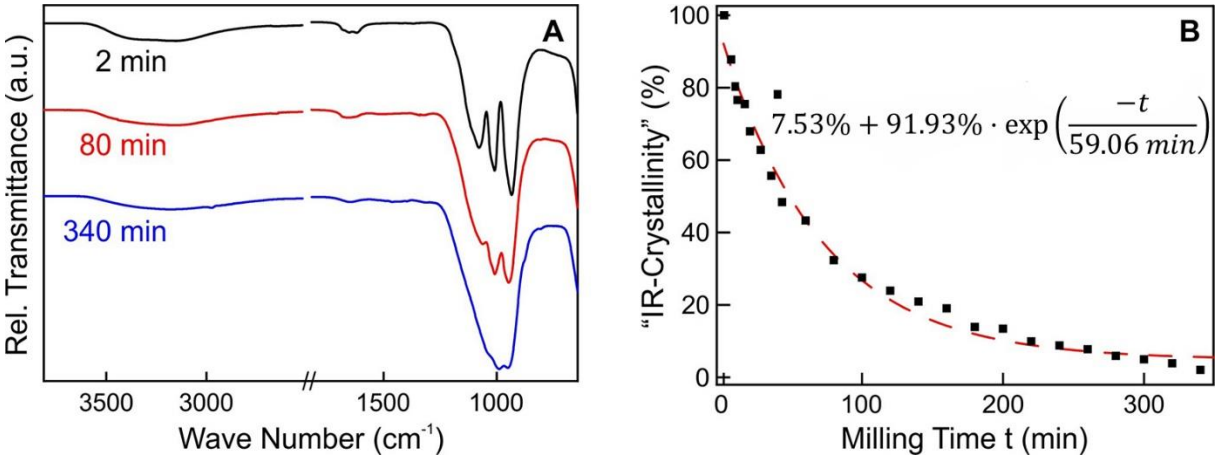

Figure 2.2 (A) IR spectra of $Zn_3(PO_4)_2 \times 4\ H_2O$ (hopeite) after different process (milling) times of 2, 80, and 340 min in the absence of Fe impurities. The bands centered around 1000 cm^{-1} correspond to the stretching modes of the PO_4^{3-} groups. The bands of crystalline hopeite are split because of lattice symmetry constraints. (B) Amorphization kinetics derived by quantitative analysis of the IR spectra (normalized to the phosphate).

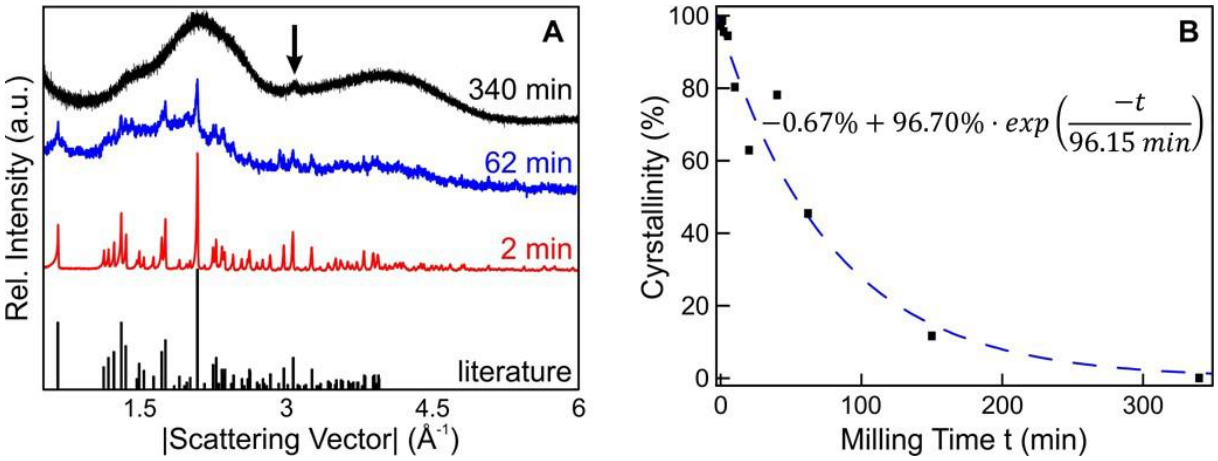

Figure 2.3 (A) X-ray diffractograms of hopeite in the presence of Fe impurities (ζ=2%) after different milling times. The sample of BM-AZP-Fe (340 min) was measured with high-intensity synchrotron radiation and set to 0% of crystallinity for zinc phosphate. The black arrow indicates the most intense reflection of elemental α-Fe. The corresponding literature cif-file was taken from Liebau et.al[18] (B) Amorphization kinetics derived by quantitative analysis of the intensity profiles using the PONKCS approach.[58]

Mössbauer spectroscopy indicated a 7% content of "unreacted" α-Fe (Figure 2.8C). Thus, we conclude that no other crystalline FeO_x or ZnO_x phases were present in BM-AZP-Fe. Using the PONKCS approach, the kinetics of the transition from the crystalline to the amorphous state was monitored by quantitative analysis of the intensity profiles (Figure 2.3B).[58] IR spectroscopy and XRD show an exponential decay for crystalline hopeite with similar decay constants. The kinetics of the transition from the crystalline to the amorphous state in presence of iron impurities was monitored again by quantitative analysis of the band splitting in the IR spectra.[56,57] Experiments with different amounts of iron showed no recognizable effect of iron on the reaction (Table S 2.1, Supporting Information). The amorphization kinetics follow an exponential decay. It is very similar to that of the reaction in the absence of Fe, regardless of the concentration of Fe impurities, i.e., there is no effect of Fe on the amorphization process itself.

Composition of Amorphous Products. The composition of the final amorphous products was characterized by EDX, ICP-MS, and ICP-OES (Table S 2.2, Supporting Information). An average Zn:P ratio of 3.0:2.0 was found. Different initial iron "impurity" concentrations were observed in subsequent analyses with a deviation of ±3%, although a distinction between iron incorporated in and iron physically mixed with the amorphous material was not possible. EDX showed Fe "impurities" to be distributed homogeneously within the samples. The water of hydration in BM-AZP-Zr corresponds (according to thermogravimetric analysis) to an average formula $Zn_3(PO_4)_2 \cdot 2.1\ H_2O$ (Figure S 2.5, Supporting Information). This suggests that water of hydration (coordinated to Zn^{2+} with hydrogen bonding to PO_4^{3-} anions) is essential for the degree of crystallinity in this hydrated system. Due to mechanical treatment loss of water in the crystal structure is observed which leads to a collapse of the crystal structure of the underlying hydrate. The amorphization of crystalline hydrates represents an important group of solid-state transformations in general.[59] Crystallization of anhydrous compounds requires large structural rearrangements and therefore is inhibited.[26,59-64]

The BM-AZP-Zr crystallites have a plate-like morphology with diameters between 500 nm and 3 µm (Figure S 2.6A, Supporting Information). At higher magnification the plates are of agglomerates of nearly spherical particles with diameters of 50-150 nm (Figure S 2.6B, Supporting Information). As synthetic hopeite contains micro-plates with diameters in the µm range (Figure S 2.6C, Supporting Information)., a possible explanation for this contrast between the original plates and plate-like morphologies after milling could be due to a

process in which smaller particles are formed and followed by an aggregation due to a reduction in surface energy.

In order to monitor the amorphization, TEM images of zinc phosphate with 20% of "IR-crystallinity" (Figure 2.4) were taken. A low radiation dose was applied to minimize side effects by amorphization due to radiation damage. The TEM images showed mostly amorphous material, TEM contrast is caused by density fluctuations in the amorphous material. Crystalline regions with diameters < 10 nm are embedded in amorphous bulk material, i.e. BM-AZP-Zr can be viewed as a nanocrystalline-reinforced *amorphous matrix* composite (analogous to a glass ceramic). The amorphization starts at the raw edges under mechanical treatment. Different distances of lattice planes are observed, all corresponding to the characteristic reflections of hopeite in X-ray or electron diffraction. The amorphization proceeds under non-equilibrium conditions. Therefore, it is not surprising that no preferred growing direction is observed as for a growing crystal under equilibrium conditions. Furthermore, mechanochemical amorphization does not lead to uniform particles as observed during a precipitation process. A distribution of particles with different sized and morphology is formed.

Different solid-state ^{31}P and ^{1}H NMR experiments were performed to investigate the effects of structural water on the amorphization and recrystallization mechanism. To prevent a partial invisibility of the NMR resonance by paramagnetic Fe impurities introduced by ball-milling, ball milling was done with zirconia vessels and balls: ball milling produced BM-AZP-Zr; semi-CZP-Zr was obtained *via* interrupted crystallization. Several peaks in the ^{31}P MAS NMR spectrum (Figure 2.5) can be assigned on the basis of previous studies of hopeite,[26] and zinc orthophosphates.[27-29] The sharp resonance of semi-CZP-Zr was assigned to hopeite $Zn_3(PO_4)_2 \cdot 4H_2O$-Zr. The broad line width of BM-AZP-Zr is typical for amorphous zinc orthophosphate[27] (Figure 2.5). These spectra are compatible with BM-AZP-Zr particles which are amorphous. They are incompatible with heterogeneous models containing remnants of crystalline hopeite, i.e. the relative amount of crystalline hopeite is below the detection limit of the NMR experiment.

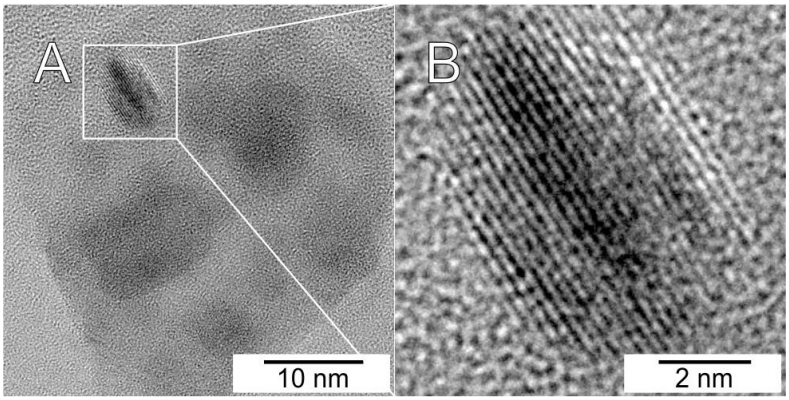

Figure 2.4 (A) TEM image of ball milled hopeite with 20% "IR crystallinity". (B) HRTEM image shows that crystalline regions smaller than 10 nm are embedded in an amorphous matrix.

An interesting question that remains is whether ball-milling causes a partial dehydration which is reversed upon crystallization of BM-AZP-Zr. NMR can be used to identify dehydrated products by the chemical shift, relaxation fingerprint and $^{31}P\{^{1}H\}$-REDOR experiments. $^{31}P\{^{1}H\}$-REDOR experiments are sensitive to the spatial proximity between ^{31}P and ^{1}H from structural water; the absence of a $^{31}P\{^{1}H\}$-REDOR effect would be evidence for the lack of H atoms in BM-AZP-Zr. However, the REDOR experiments clearly show that ball-milling does not produce anhydrous zinc phosphate (e.g. $Zn_3(PO_4)_2$). This is in agreement with the finding of relaxation times T_1 of about 1 min for BM-AZP-Zr and semi-CZP-Zr, while $Zn_3(PO_4)_2$ is expected to show much longer relaxation times (>1000 s) (compare to ref. 27). The strength of the magnetic dipole-dipole interactions between ^{31}P and ^{1}H is reflected in the effective dipole-dipole coupling constant[65] ν_{dip} which was obtained from a fit of the initial regime of the REDOR curves to a simulated curve describing an isolated two-spin system (Figure S 2.7 and S 2.8, Supporting Information). The effective coupling constants for the main peaks of BM-AZP-Zr and semi-CZP-Zr are -1004 and -954 Hz, respectively, and agree within the error limits (~5-10%).

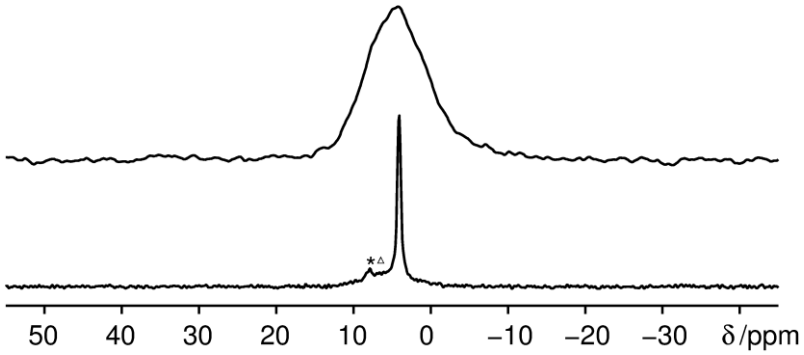

Figure 2.5 ^{31}P MAS NMR spectra of BM-AZP-Zr (top) and semi-CZP-Zr (bottom) obtained at a sample spinning frequency of 12.5 kHz. The asterisk and the hollow triangle indicate the weak signals from $Zn_3(PO_4)_2 \cdot 2H_2O$ and an unknown side phase, respectively.

This finding indicates that the amount of structural water was not reduced significantly during ball milling. Minor amounts of side phases are apparent by weak resonances at 6.0 and 7.8 ppm besides the dominant peak at 4.1 ppm in semi-CZP-Zr. The peak at 7.8 ppm was assigned to $Zn_3(PO_4)_2 \cdot 2H_2O$ on the basis of the isotropic chemical shift and the observed non-zero $^{31}P\{^1H\}$-REDOR effect (Table 2.1). An implication of this observation is that small amount of structural water is released during ball-milling and not reabsorbed during recrystallization.

Table 2.1 NMR results for BM-AZP and semi-CZP samples (chemical shift conventions as in ref. 55, obtained from a non-linear least square fit of slow-spinning MAS NMR spectra (Figure S 2.9, Supporting Information) and data for crystalline reference compounds.

Substance	δ_{iso}/ppm	δ_{aniso}/ppm	η	δ_{xx}/ppm	δ_{yy}/ppm	δ_{zz}/ppm	T_1/s
BM-AZP-Zr	4.4	28	0.91	-22.3	3.1	32.4	59±2
semi-CZP-Zr	4.1	32	0.91	-26.5	2.7	36.1	60±1
α-$Zn_3(PO_4)_2 \cdot 4H_2O$[28]	4.52						
β-$Zn_3(PO_4)_2 \cdot 4H_2O$[28]	4.34						
$Zn_3(PO_4)_2 \cdot 2H_2O$[29]	8.0						
α-$Zn_3(PO_4)_2$[27]	3.9	-36	0.86	37.0	6.4	-31.7	
β-$Zn_3(PO_4)_2$[27]	7.6	20	0.62	-8.7	3.8	27.7	
	2.8	-12	0.92	14.4	3.3	9.2	

To study the incorporation of Fe into BM-AZP, the corresponding particles were characterized by ^{31}P MAS NMR (Figure S 2.10 and S 2.11, Supporting Information). Only a single ^{31}P resonance can be resolved which has a significantly shorter relaxation time T_1 of 0.7 s (isotropic peak) than the same peak in BM-AZP-Zr (59 ± 2 s, Table 2.1). This behavior is ascribed to a paramagnetic relaxation enhancement. The lack of a slow relaxing component indicates that Fe is present throughout the particles and not only at the surface.

Crystallization Kinetics in Water. BM-AZP-Zr contains much less structural water than hopeite. Therefore, recrystallization to hopeite requires an aqueous solution or atmospheric moisture because water (i) is a structural building block and (ii) acts as a mineralizer that increases the mobility of the structural building blocks.[67] A plausible explanation for this behavior is the much lower activation energy for surface diffusion compared to solid state diffusion.[68] In fact, crystalline hopeite was obtained after short reaction times (approx.

1 min) by re-suspending BM-AZP-Zr in water. Moreover, the reaction rate of amorphous zinc phosphate (AZP) prepared by precipitation [26] and of BM-AZP-Fe was very different.

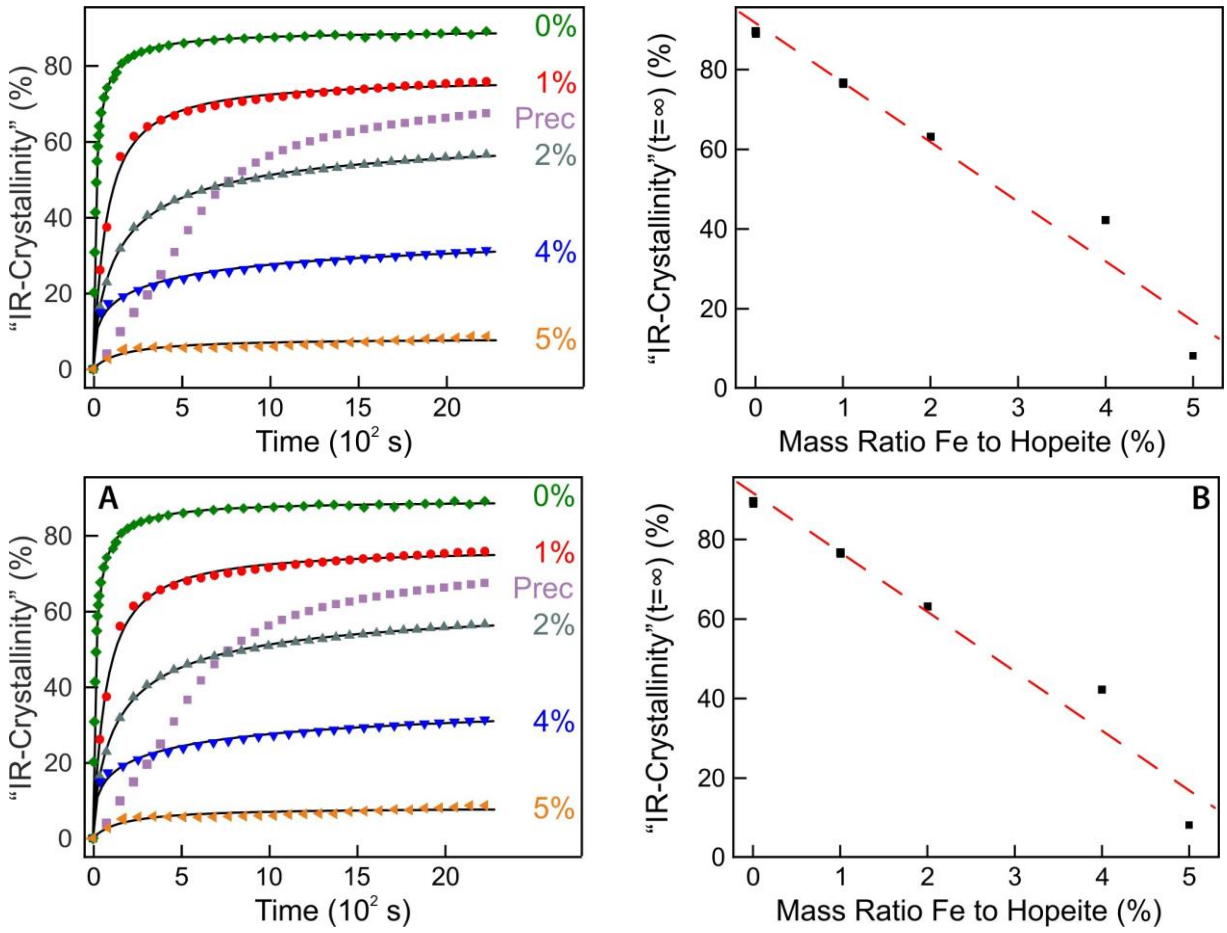

Figure 2.6 (A) Crystallization kinetics of BM-AZP-Zr with different amounts of iron (mass ratio ζ in %) during milling (black lines represent Langmuir plots). (B)"IR-Crystallinity" at saturation limits according to a Langmuir plot.

Figure 2.6 displays the crystallization kinetics of mechanochemically prepared BM-AZP-Zr/Fe (BM-AZP-Zr) with different amounts of Fe added) and of AZP (reference compound) as determined by quantitative *in situ* IR spectroscopy. The crystallization of AZP can be described by an Avrami-type kinetics,[69-73] i.e., the transformation rates are low at the beginning and at the end of the transformation, but rapid in between. This leads to a sigmoidal curve (a double logarithmic plot is shown in Figure S 2.12, Supporting Information) representing the reaction rate. The initial slow rate corresponds to the time required for the formation of a sufficient number of nuclei of the new phase. The transformation is rapid during the intermediate period in which the nuclei grow into particles while the initial phase is consumed and nuclei continue to form. Once the

transformation is close to completion there is only a small amount of starting material left, and the transformation slows down again. The formed particles touch each another and new grain boundaries form that inhibit further growth. In essence, nucleation and growth following an Avrami-type kinetics are indicative of an autocatalytic recrystallization. A non-linear least-squares fit of this evolution to the Avrami form[69-72] $s = 1-\exp(-[k(t-t_0)]^n)$ yielded the best results for $t_0 = 0$ (indicating that crystallization starts instantaneously). Values of 1.17 for the exponent n and 2.67×10^{-4} s^{-1} for the Avrami constant k were obtained.[60,68,71] The fit is satisfactory for longer reaction times and for the manner, in which the curve saturates. This is in part due to the data reduction at large reaction times and the correlation of the parameters. The large values of n suggest that the process is not diffusion-controlled and that nucleation might continue even through the growth phase.[69-73] BM-AZP-Zr synthesized in the absence of Fe is unstable with respect to crystallization in water. After only 2 min more than 80% of the sample transformed to hopeite. The reaction profile showed a Langmuir-like behavior. This suggests that the crystallization proceeds *via* adsorption/desorption of water to distinct surface sites S capable of binding the H_2O adsorbate. Subsequently, the transformation occurs to crystalline hopeite. This reaction involves an surface complex with adsorbed H_2O(ads) having an associated equilibrium constant K_e. According to this mechanism the reaction approaches a "saturation" limit for longer reaction times. In the presence of iron "impurities" the recrystallization slowed down significantly with increasing Fe content, and a major portion of the sample remained amorphous. With 40 mg of Fe used during milling (ζ=5%), the "IR-crystallinity" only increased to 10% even after 2 days. 80 mg (ζ=10%) of iron used during ball milling suppressed the crystallization of BM-AZP-Fe completely, even after dispersing for 2 months in water. In the absence of water, BM-AZP-Zr and AZP are stable (even at 300 °C) for several months, i.e., water acts as a mineralizer enhancing the mobility of the surface ions. Therefore, we assume that the transformation of both materials to hopeite occurs *via* a dissolution-recrystallization process. We attribute the differences in the reactivity of BM-AZP-Zr and AZP to their different compositions and local structures, in particular to differences of the hydration networks. BM-AZP-Fe particles have an inhomogeneous and plate-like appearance. The plates are composed of smaller coalesced nanoparticles (reduction of surface energy). The abrasion of Fe, which was simulated here by intentionally adding Fe particles to the mill-charge, leads to the local incorporation of Fe^{2+} or Fe^{3+} ions into the AZP structure. The Fe impurities are assumed to be incorporated preferentially from the surface sites (unsaturated). Surface-bound Fe^{2+} is oxidized to Fe^{3+}

easily. As Fe^{2+} and Fe^{3+} are more oxophilic than Zn^{2+}, local hydrated $[Fe(H_2O)_x]^{2+}$ and $[Fe(H_2O)_x]^{3+}$ sites will form, and Fe^{3+}-bound water prevents further migration of the water molecules that are required for structural rearrangement and crystallization. In addition, $[Fe(H_2O)_6]^{3+}$ is strongly acidic (pK_a=3.05)[74] and therefore can protonate phosphate groups, thereby acting as crystallization inhibitor.

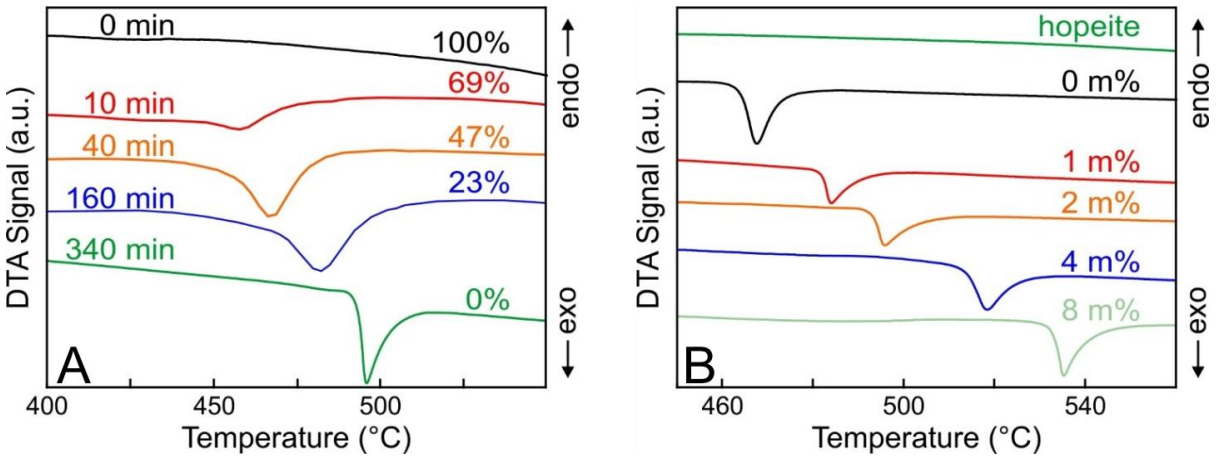

Figure 2.7 (A) DTA traces of hopeite milled with 2 m% of Fe for different milling durations (displayed on the left) corresponding to different degrees of "IR-crystallinity" (displayed on the right). (B) DTA traces of hopeite and its milling end products (BM-AZP-Fe) with different amounts of Fe during the milling reaction (mass %).

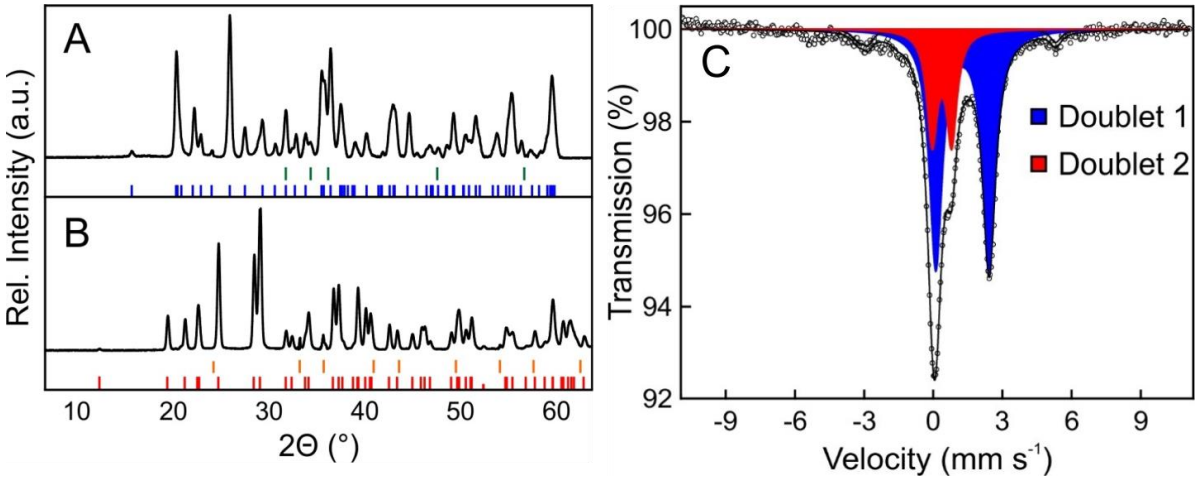

Figure 2.8 (A) X-ray diffractogram of γ-$Zn_{3-x}Fe_x(PO_4)_2$ formed by heating a sample BM-AZP-Fe in the presence of 16 mg ^{57}Fe (ζ=2%) at 700°C under argon. (in blue: literature reflections of γ-$Zn_3(PO_4)_2$, in green: literature reflections of ZnO. (B) Heating up on air leads to α-$Zn_3(PO_4)_2$ (red ticks) containing α-Fe_2O_3 impurities (orange ticks). (C) ^{57}Fe Mössbauer spectrum of BM-AZP-Fe synthesized with 2 m% of ^{57}Fe. Besides two doublets with intensity contributions of 65 and 28% there is a small sextet (contribution 7%) corresponding to trace amounts of unreacted elementary Fe.

Thermal stability. Thermal analysis (TGA) showed that BM-AZP-Zr (ζ=0, no Fe) loses structural water continuously upon heating but remains non-crystalline up to 468 °C (see Figure S 2.5, Supporting Information). Even after annealing at 350°C for 5 d under argon, BM-AZP-Zr remained amorphous. Quantitative analysis of the TGA data yielded a composition $Zn_3(PO_4)_2 \cdot 0.2\ H_2O$ after annealing BM-AZP-Zr at 350°C. Milling increases the portion of BM-AZP-Zr. As a result, the intensity of the exothermic signal increases as well. In addition, the transformation temperature, i.e., the inertness of the balled-milled product, increased with increasing milling time (Figure 2.7A). The effect of Fe is also evident from the thermally induced crystallization. An increasing Fe content (ζ=8%) led to an increase of the transformation temperature (amorphous-crystalline) from 468 to 535°C (Figure 2.7B). "Fe-doped" γ-$Zn_{3-x}Fe_x(PO_4)_2$ was formed upon annealing BM-AZP-Fe under Ar (Figure 2.8A). γ-$Zn_{3-x}M_x(PO_4)_2$ has been reported to form a solid solution with divalent transition metals (ζ > 5 mol%),[21,75-77] where the Zn^{2+} ions at the tetrahedral sites are replaced. Excess Zn^{2+} may phase separate as ZnO. In fact, weak reflections of zincite (ZnO) were observed in the X-ray diffractogram. γ-$Zn_3(PO_4)_2$ is one of the rare examples, where Zn^{2+} occurs in both, tetrahedral and octahedral sites. Calvo et al.[19] reported that the "doping metal" occupies the octahedral position because Zn^{2+} prefers a tetrahedral rather than an octahedral coordination. Annealing of BM-AZP-Fe in air led to the formation of α-$Zn_3(PO_4)_2$ containing α-Fe_2O_3 impurities as a side phase, as shown by X-ray diffraction, Mössbauer spectroscopy, and magnetic susceptibility measurements (Figures 2.8 and 2.9).

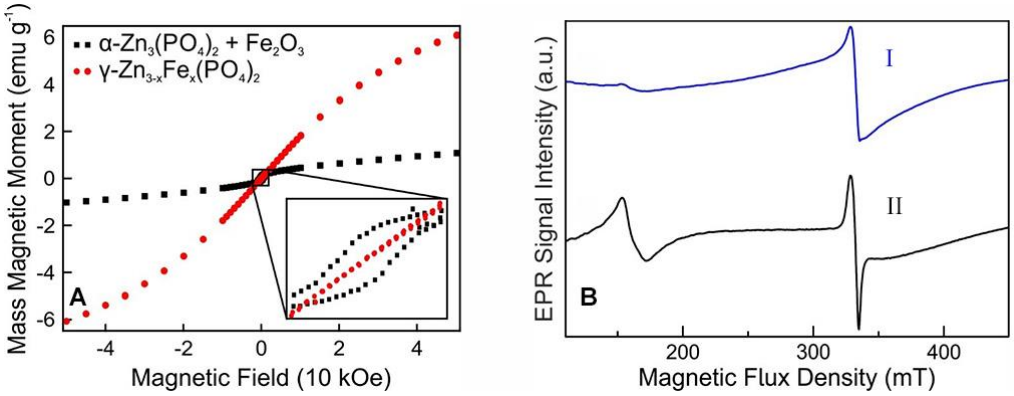

Figure 2.9 (A) Hysteresis loops (5 K) for BM-AZP-Fe , ball-milled in the presence of 2 mol% ^{57}Fe after annealing at 700°C under Ar (red spheres) and in air (black squares).(B) EPR spectra of BM-AZP-Fe (synthesized with 16 mg of ^{57}Fe) at room temperature (I) and cooled with N_2 (II).

The hopeite crystal structure contains two different zinc sites with tetrahedral and octahedral coordination in a ratio of 2:1. The Zn^{2+} cations on the tetrahedral sites are coordinated by four oxygen atoms of different phosphate groups, while the environment of the octahedral sites consists of oxygen atoms of two different water molecules and four

different phosphate groups. The Mössbauer spectra of BM-AZP-Fe (2% ^{57}Fe, Figure 2.8C) show three iron signals with contributions of 65% (doublet 1) 28% (doublet 2) and 7% (sextet) (Table 2.2). The weak sextet (7%) corresponds to traces of non-reacted elementary ^{57}Fe. The strong (65%) doublet 1 corresponds to high-spin Fe^{2+}, doublet 2 with intermediate intensity (28%) corresponds to high-spin Fe^{3+}. Based on the small difference (~4%) between ionic radii[78] of Fe^{2+} (0.63 Å) and Zn^{2+} (0.60 Å) in tetrahedral coordination we assign doublet 1 to Fe^{2+} ions in tetrahedral (surface-near) coordination in amorphous BM-AZP-Fe. Doublet 2 is assigned to hydrated $[Fe(H_2O)_x]^{3+}$ surface sites rather than to a discrete iron hydroxide phase. Mössbauer measurements at liquid nitrogen temperature support this conclusion. During annealing (at 400 and 700°C, respectively), doublet 2 vanished and a new doublet (doublet 3) appeared (Figure S 2.13, Supporting Information). Doublet 3 of BM-AZP-Fe (after annealing) shows the presence of high-spin Fe^{2+} in tetrahedral sites of the γ-$Zn_3(PO_4)_2$ structure. Doublet 1 (after annealing) corresponds to surface Fe^{2+} in non-crystalline BM-AZP-Fe. The Fe^{3+} species in BM-AZP-Fe (before annealing) contribute to doublet 2 (after annealing) compatible with Fe^{3+} species with surface-bound water ($[Fe(H_2O)_x]^{3+}$ or OH^- groups. The decrease of the intensity of doublet 1 after annealing at 700 °C is due to crystallization (loss of surface sites, Figure S 2.13, Supporting Information).

Table 2.2. Hyperfine parameters of ^{57}Fe in Fe substituted $Zn_{3-x}Fe_x(PO_4)_2nH_2O$

signal	isomer shift / mm s^{-1}	quadrupole splitting / mm s^{-1}	species	amount / %
BM-AZP-Fe (2 m% ^{57}Fe)				
1	1.315(3)	2.744(5)	Fe^{2+}, hs	65(1)
2	0.532(9)	0.73(1)	Fe^{3+}, hs	28(1)
BM-AZP-Fe (2 m% ^{57}Fe, 400 °C for 5d, Ar)				
1	1.195(3)	2.58(2)	Fe^{2+}, hs	45(3)
3	1.221(3)	1.92(1)	Fe^{2+}, hs	55(3)
BM-AZP-Fe (2 m% ^{57}Fe, 700 °C for 5d, Ar) ($\gamma - Zn_{3-x}Fe_x(PO_4)_2$				
1	1.100(1)	2.81(2)	Fe^{2+}, hs	14(2)
3	1.253(2)	1.905(4)	Fe^{2+}, hs	86(2)
BM-AZP-Fe (2 m% ^{57}Fe, 700 °C for 5d, on air) ($\alpha - Zn_3(PO_4)_2$				
4	0.344(1)	0,410(1)	Fe^{3+}, hs	100

At an annealing temperature of 700°C γ-$Zn_{3-x}Fe_x(PO_4)_2$ was formed in higher, at 400°C in lower amounts. Annealing in air lead to the formation of α-$Zn_3(PO_4)_2$ with small (5%) amounts of superparamagnetic hematite (by oxidation and phase separation from γ-$Zn_{3-x}Fe_x(PO_4)_2$), as shown by PXRD (Figure 2.8A) and Mössbauer spectroscopy (Figure 2.8B). The Mössbauer spectrum showed only hs-Fe^{3+} in octahedral coordination, compatible with the formation of hematite (α-Fe_2O_3, Figure S 2.14, Supporting Information). Furthermore, this was supported by a collective magnetization at 5 K, observed in the magnetic susceptibility and magnetization measurements (Figure 2.8A). Solid solutions of γ-$Zn_{3-x}Fe_x(PO_4)_2$ with Fe^{2+} species replacing Zn^{2+} in the γ-$Zn_3(PO_4)_2$ crystal structure showed paramagnetic behavior. As iron is present in in BM-AZP-Fe as Fe^{2+} and Fe^{3+}, EPR spectroscopy was carried out to examine if the presence of Fe^{3+} is associated with compensating Zn^{2+} vacancies ("hole doping") or leads to free unpaired electrons or radicals (Figure 9, right) We observed several signals at $g\approx4.0$ with a temperature-dependent signature, which are comparable with the results for Fe-substituted ZnO ($Zn_{1-x}Fe_xO$).[79] The transitions are spin forbidden ($\Delta m_s=2$) and attributed to the presence of isolated Fe^{3+} ions ($^6S_{5/2}$, $S=5/2$) with uncoupled Fe^{3+} species near-by, leading to a ferromagnetic coupling over a small area. A weaker signal at $g\approx2.0$ (a so-called half-field signal) is due to the coupling of spin functions and an associated violation of the selection rules. The EPR signal of the Fe^{2+} ions cannot be resolved due to the small value of spin lattice relaxation time, and a full analysis of the EPR signal is too complex. Still, these results indicate that the presence of free unpaired electrons or radicals can be ruled out[79-81] in BM-AZP-Fe.

2.5 Conclusions

We have shown that metastable amorphous zinc phosphate can be prepared by ball-milling of hopeite. The metastable product is stabilized by incorporation of Fe impurities due to wear of the milling media (stainless steel balls). Abrasion from milling tools was simulated by addition of pure ^{57}Fe. The amorphization process and its kinetics were monitored by X-ray powder diffraction with high-intensity synchrotron radiation and quantitative IR spectroscopy. Thermal analysis revealed the release of Zn^{2+} coordinated water to be a key step during the formation of amorphous zinc phosphate (BM-AZP) by ball-milling. Solid state NMR results indicated BM-AZP and AZP to follow different crystallization pathways. Quantitative IR spectroscopy proved useful for the *in situ* determination of the re-crystallization kinetics of BM-AZP in water. The recrystallization of BM-AZP formed in the absence of Fe followed a classical Avrami behavior. However, Fe impurities inhibited the recrystallization of BM-AZP-Fe to hopeite tremendously. The thermally induced

crystallization of BM-AZP to $Zn_3(PO_4)_2$ was shifted by up to 65 °C to higher temperatures for BM-AZP-Fe in the presence of Fe impurities (ζ=5%) under Ar.

^{57}Fe Mössbauer spectroscopy probed the local environment of the Fe centers and provided insight into the mechanically induced changes on a local atomic scale. The inhibition of crystallization of metastable BM-AZP was increased by Fe doping. Fe^{2+} and Fe^{3+} are incorporated on the tetrahedral and octahedral sites of the underlying γ-$Zn_3(PO_4)_2$ crystal structure. Annealing of the resulting γ-$Zn_{3-x}Fe_x(PO_4)_2$ in air lead to the oxidation of Fe and to the formation of α-$Zn_3(PO_4)_2$ containing α-Fe_2O_3 impurities, as shown by Mössbauer spectroscopy and magnetic susceptibility measurements. EPR studies showed the incorporation of Fe^{3+} in γ-$Zn_{3-x}Fe_x(PO_4)_2$ to be coupled with the formation of Zn^{2+} vacancies. Fe^{3+} defect surface sites bind water strongly because of their higher oxophilicity (Pearson hardness) compared to Fe^{2+} and Zn^{2+}. As a result, hydrated $[Fe(H_2O)_x]^{3+}$ surface complexes are formed, which prevent surface migration of Fe^{3+}-bound water that is required for structural rearrangement and crystallization.

Our findings shed not only light on the amorphization mechanism of $Zn_3(PO_4)_2$ in stainless steel ball mills at the molecular scale, but also on the formation of corrosion resistant coatings on steel used for phosphate conversion coatings or protective films on rubbing surfaces. They highlight how the reactivity of the amorphous material is determined by impurities associated with the preparation under shear. Furthermore, our results provide insight and theoretical guidance for the preparation of amorphous phosphates and oxides.

2.6 References

[1] Etzrodt, G. Pigments, Inorganic, chapter 5, Anticorrosive Pigments, in Ullmann's Encyclopedia of Industrial Chemistry. Wiley-VCH, 7th Ed., 2011.

[2] Wenig, D.; Jokiel, P.; Uebleis, A.; Boehni, H. Corrosion and protection characteristics of zinc and manganese phosphate coatings. *Surf. Coatings Technol*. **1997**, *88*, 147–156.

[3] Del Amo, B.; Romagnoli, R.; Vetere, V. F.; Hernández, L. S. Study of the anticorrosive properties of zinc phosphate in vinyl paints. *Prog. Org. Coat.* **1998**, *33*, 28–35.

[4] Pameijer, C. H. A Review of Luting Agents, *Int. J. Dent*. **2012**, *752861*, 1–7.

[5] Hill, E. E.; Lott, J. A clinically focused discussion of luting materials. *Austr. Dent. J.* **2011**, *56*, Suppl. 67–76.

[6] Davidson, C. L. Luting Cement, the Stronghold or the Weak Link in Ceramic Restorations? *Adv. Eng. Mater*. **2001**, *3*, 763–767.

[7] Navrotsky, A. Energetics of nanoparticle oxides: interplay between surface energy and polymorphism. *Geochem. Trans*. **2003**, *4*, 34−37.

[8] Dove, P. M.; Han, S.; Wallace, A. F.; DeYoreo, J. J. Kinetics of amorphous silica dissolution and the paradox of the silica polymorphs. *Proc. Natl Acad. Sci U.S.A*. **2008**, *105*, 9903–9908.

[9] Leukel, S.; Panthöfer, M.; Mondeshki, M.; Kieslich, G.; Wu, Y.; Krautwurst, N.; Tremel, W. Trapping Amorphous Intermediates of Metal Carbonates. *J. Am. Chem. Soc.* **2018**, *140*, 14638-14646.

[10] Shakhvorostov, D.; Nicholls, M. A.; Norton, P. H.; M.H. Müser, M. H. Mechanical properties of zinc and calcium phosphates. Structural insights and relevance to anti-wear functionality. *Eur. Phys. J. B* **2010**, *76*, 347–352.

[11] Brow, R. K. The structure of simple phosphate glasses. *J. Non-Cryst. Solids* **2000**, *263–264*, 1–28.

[12] Schüth, F. Non-siliceous mesostructured and mesoporous materials. *Chem. Mater*. **2001**, 13, 3184–3195.

[13] Cheetham, A. K.; Rao, C. N. R.; Feller, R. K. Structural diversity and chemical trends in hybrid inorganic–organic framework materials. *Chem. Commun*. **2006**, 4780–4795.

[14] Mosey, N. J.; Müser, M. H.; Woo, T. K. Molecular Mechanisms for the Functionality of Lubricant Additives. *Science* **2005**, 307, 1612–1615.

[15] Shakhvorostov, D.; Müser, M.H.; Mosey, N. J.; Song, Y.; Norton, P. R. Correlating cation coordination, stiffness, phase transition pressures, and smart materials behavior in metal phosphates. *Phys. Rev. B* **2009**, *79*, 094107.

[16] Pawlak, Z.; Yarlagadda, P. K.; Hargreaves, D.; Frost, R. L.; Rauckyte, T.; Zak, S *J. Achiev. Mater. Manufact. Eng*. **2009**, *33*, 35–40.

[17] Herschke, L.; Enkelmann, V.; Lieberwirth, I.; Wegner, G. The Role of Hydrogen Bonding in the Crystal Structures of Zinc Phosphate Hydrates. *Chem. Eur. J.* **2004**, *10*, 2795-2803.

[18] Liebau, F. Zur Kristallstruktur des Hopeits, $Zn_3[PO_4]_2 \times 4\,H_2O$. Acta Cryst. **1965**. 18, 352-354.

[19] Calvo, C. The Crystal Structure of α-$Zn_3(PO_4)_2 \times 4\,H_zO$ *Can. J. Chem*. **1965**, *43*, 436−445.

[20] Whitaker, A. The Crystal Structure of Hopeite, $Zn_3(PO_4)_2 \times 4\,H_zO$. *Acta Cryst.* **1975**, *B31*, 2026-2035.

[21] Thomas, I. M.; Weller, M. T. Synthesis, structure and thermal properties of phosphophyllite, $Zn_2Fe(PO_4)_2{\cdot}4H_2O$. ***J. Mater. Chem.*** **1992**, ***2,*** 1123–1126.

[22] Sankara Narayanan, T. S. N. Surface Pretreatment by Phosphate Conversion Coatings: A Review. *Rev. Adv. Mater. Sci.* **2005**, *9*, 130-177.
[23] Cocco, G.; Fanfani, L.; Zanazzi, P. F. The crystal structure of tarbuttite, $Zn_2(OH)PO_4$. *Z. Kristallogr*. **1966**, *123*, 321–329.
[24] Yuan, A.-Q.; Wu, J.; Huang, Z.-Y.; Zhou, Z.-G.; Wen, Y. X.; Tong, Z.-F. *Chin. J. Chem*. **2007**, *25*, 857−862.
[25] Jung, S.-H.; Oh, E.; Shim, D.; Park, D, H.; Cho, S.; Lee, B. R.; Jeong, Y. U.; Lee, K.-H.; Jeong, S.-H. Sonochemical Synthesis of Amorphous Zinc Phosphate Nanospheres. *Bull. Korean Chem. Soc*. **2009,** *30*, 2280–2282.
[26] Bach, S.; Panthöfer, M.; Dietzsch, M.; Meffert, R.; Emmerling, F.; Ribeiro Celinski, V.; Schmedt auf der Günne, J.; Tremel, W. Thermally Highly Stable Amorphous Zinc Phosphate Nanoparticles as Intermediates During the Formation of Hopeite. *J. Am. Chem. Soc.* **2015**, *137*, 2285–2294.
[27] Roming, M.; Feldmann, C.; Avadhut, Y. S.; Schmedt auf der Günne, J. Characterization of Noncrystalline Nanomaterials: NMR of Zinc Phosphate as a Case Study *Chem. Mater*. **2008**, *20,* 5787−5795.
[28] Herschke, L.; Rottstege, J.; Lieberwirth, I.; Wegner, G. J. Zinc phosphate as versatile material for potential biomedical applications *Mater. Sci: Mater Med* **2006**, *17*, 81-94.
[29] Crosby, R. C.; Haw, J. F.; Lewis, D. H. High temperature solid-state nuclear magnetic resonance using a poly(amide-imide) spinning system *Anal. Chem.* **1988**, *24*, 2695-2699.
[30] Šepelák, V.; Bégin-Colin, S.; Le Caër, G. Transformations in oxides induced by high-energy ball-milling. Dalton Trans. **2012**, *41*, 11927–11948.
[31] Šepelák, V.; Düvel, A.; Wilkening, M.; Becker, K. D.; Heitjahns, P. Mechanochemical reactions and syntheses of oxides. Chem. Soc. Rev. **2013**, *42*, 7507–7520.
[32] Baláž, P. Mechanochemistry in Nanoscience and Minerals Engineering, Springer-Verlag: Berlin, Germany, 2008.
[33] Willart, J. F.; Descamps, M. Solid State Amorphization of Pharmaceuticals. *Mol. Pharmaceutics* **2008**, *5*, 905–920.
[34] High-Energy Ball Milling, **Mechanochemical Processing of Nanopowders.** Sopicka-Lizer, M., Ed., Wooshead Publishing, Cambridge 2010.
[35] Ziadeh, M.; Chwalka, B.; Kalo, H.; Schütz, M. R.; Breu, J. simple approach for producing high aspect ratio fluorohectorite nanoplatelets utilizing a stirred media mill (ball mill). *J. Clay Miner.* **2012**, *47*, 341–353.
[36] Bennett, T. D.; Cao, S.; Tan, J. C.; Keen, D. A.; Bithell, E. G.; Beldon, P. J. Facile Mechanosynthesis of Amorphous Zeolitic Imidazolate. Frameworks *J. Am. Chem. Soc.* **2011**, *133*, 14546**–**14549.
[37] Cao, S.; Bennett, T. D.; Keen, D. A.; Goodwind, A. L.; Cheetham, A. K. Amorphization of the prototypical zeolitic imidazolate framework ZIF-8 by ball-milling. *Chem. Commun.* **2012**, *48*, 7805–7807.
[38] Bennett, T. D.; Saines, P. J.; Keen, D. A.; Tan, J.-C.; Cheetham, A. K. Ball-Milling-Induced Amorphization of Zeolitic Imidazolate Frameworks (ZIFs) for the Irreversible Trapping of Iodine. *Chem. Eur. J*. **2013**, *19*, 7049–7055.
[39] Lock, N.; Christensen, M.; Kepert, C. J.; Iversen, B. B. Effect of gas pressure on negative thermal expansion in MOF-5. *Chem.Commun*. **2013**, *49*, 789–791.
[40] Bennett, T. D.; Cheetham, A. K. Amorphous Metal−Organic Frameworks. *Acc. Chem. Res*. **2014**, *47*, 1555−1562.
[41] James, S. L.; Adams, C. J.; Bolm, C.; Braga, D.; Collier, P.; Friščić, T., Grepioni, F.; Harris, K. D. M.; Hyett, G.; Jones, W.; Krebs, A.; Mack, J.; Maini, L.; Orpen, A. G.; Parkin, I. P.; Shearouse, W. C.; Steed, J. W.; Waddel, D. C. Mechanochemistry: opportunities for new and cleaner synthesis. *Chem. Soc. Rev*. **2012**, *41*, 413–447.

[42] Boldyrev, V. V. Mechanochemistry and mechanical activation of solids. *Russ. Chem. Rev*. **2006**, *75*, 177–189.
[43] Li, Q.J-J, Sheng, H., Ma, E. Strengthening in multi-principal element alloys with local-chemical-order roughened dislocation pathways. *Nature Commun.* **2019**, *10*, 3563
[44] Šepelák, V.; Bergmann, I.; Indris, S.; Feldhoff, A.; Heitjans, P.; Becker, K. D. Mechanically induced processes in spinel oxides followed by spectroscopic methods, in Experimental and Theoretical Studies in Modern Mechanochemistry, ed. F. Delogu and G. Mulas, Transworld Research Network, Kerala **2010**, 191**–**206.
[45] Bégin-Colin, S.; Le Caër, G.; Mocellin, A.; Zandona, M. Polymorphic transformations of titania induced by ball milling. *Philos. Mag. Lett*. **1994**, *69*, 1–7.
[46] Bégin-Colin, S.; Le Caër, G.; Zandona, M.; Bouzy, E.; Malaman, B. Influence of the nature of milling media on phase transformations induced by grinding in some oxides. *J. Alloys Compd*. **1995**, *227*, 157–166.
[47] Boldyrev, V. V.; Lyakhov, N. Z.; Pavlyukhin, Yu. T.; Boldyreva, E. V.; Ivanov, E. Yu.; Avvakumov, E. G. Achievements and prospects in mechanochemistry. *Sov. Sci. Rev. B. Chem*. **1990**, *14*, 105–161.
[48] Gateshki, M.; Petkov, V.; Williams, G.; Pradhan, S. K.; Ren, Y. Atomic-scale structure of nanocrystalline ZrO_2 prepared by high-energy ball milling *Phys. Rev. B* **2005**, 71, 224107.
[49] Štefanić, G.; Musić, S.; Gajović, A. Structural and microstructural changes in monoclinic ZrO_2 during the ball-milling with stainless steel assembly. *Mater. Res. Bull*. **2006**, *41*, 764–777.
[50] Friščić, T.; Halasz, I.; Beldon, P. J.; Belenguer, A. M.; Adams, F.; Kimber, S. A. J.; Honkimäki, V.; Dinnebier, R. E. Real-time and in situ monitoring of mechanochemical milling reactions. *Nat. Chem.* **2013**, *5*, 66–73.
[51] Halasz, I.; Kimber, S. A. J.; Beldon, P. J.; Belenguer, A. M.; Adams, F.; Honkimäki, V.; Nightingale, R. C.; Dinnebier, R. E.; Friščić, T. In situ and real-time monitoring of mechanochemical milling reactions using synchrotron X-ray diffraction. *Nat. Protocols* **2013**, *8*, 1718–1729.
[52] Batzdorf, L.; Fischer, F.; Wilke, M.; Wenzel, K. J.; Emmerling, F. Direct in situ investigation of milling reactions using combined X-ray diffraction and Raman spectroscopy. *Angew. Chem. Int. Ed.* **2015**, 54, 1799–1802.
[53] Cheary, R.W.; Coelho, A. A fundamental parameters approach to X-ray line-profile fitting. *J. Appl. Cryst*. **1992**, *25*, 109–121.
[54] Coelho, A. *TOPAS Academic V5;* Coelho Software: Brisbane, Australia, 2007.
[55] Harris, R. K.; Becker, E. D.; Cabral de Meneses, S. M.; Granger, P.; Hoffman, R. E.; Zilm, K. W. Further conventions for NMR shielding and chemical shifts (IUPAC Recommendations 2008). *Pure Appl. Chem.* **2009**, *80*, 59–84.
[56] Pawlig, O.; Schellenschläger, V.; Lutz, H. D.; Trettin, R. Vibrational analysis of iron and zinc phosphate conversion coating constituents. *Spectrochim. Acta A Mol. Biomol. Spectrosc.* **2001**, *57*, 581–590.
[57] Zedler, L.; Hager, M. D.; Schubert, U. S.; Harrington, M. J.; Schmitt, M.; Popp, J.; Dietzek, B. Monitoring the chemistry of self-healing by vibrational spectroscopy – current state and perspectives. *Mater. Today* **2014**, *2*, 57–69.
[58] Scarlett, N. V. Y.; Madsen, I. C. Quantification of phases with partial or no known crystal structures. *Powder Diffraction* **2006**, *21*, 278–284.
[59] Willart, J. F.; Descamps, M. Solid State Amorphization of Pharmaceuticals. *Mol. Pharma ceutics* **2008**, *5*, 905–920.
[60] Wang, H.; Xu, B.; Smith, P.; Davies, M.; DeSilva, L.; Wingate, C. Kinetic modelling of gibbsite dehydration/amorphization in the temperature range 823–923 K. *J. Phys. Chem. Solids* **2006**, *67*, 2567–2582.

[61] Brantut, N.; Schubnel, A.; Rouzaud, J.-N.; Brunet, F.; Shimamoto, T. High-velocity frictional properties of a clay-bearing fault gouge and implications for earthquake mechanics *J. Geophys. Res.* **2008**, *113*, B10401
[62] Wolf, S. E.; Leiterer, J.; Kappl, M.; Emmerling, F.; Tremel, W. New insights into the nucleation process of calcium carbonate by contact-less *in situ* scattering techniques using the levitating drop method**.** *J. Am. Chem. Soc*. 2008, *130*, 12342–12347
[63] Bach, S.; Panthöfer, M.; Bienert, R.; Emmerling, F.; Tremel, W. The Role of Water during the Crystallization of Amorphous Cobalt Phosphate Nanoparticles. *Cryst. Growth Des.* **2016**, *16*, 4232−4239
[64] Leukel, S.; Tremel, W. Water controlled crystallization of $CaCO_3$, $SrCO_3$ and $MnCO_3$ from amorphous precursors. *Crystal Growth Des.* **2018**, *18*, 4662-4670
[65] Schmedt auf der Günne, J. *J. Magn. Reson*. **2003**, *165*, 18–32
[66] Bak, M.; Rasmussen, J. T.; Nielsen, N. C. SIMPSON: a general simulation program for solid state NMR spectroscopy. *J. Magn. Reson.* **2000**, *147*, 296–330.
[67] Schäfer, H. The Present Situation of Solid State Chemistry. *Angew. Chem.* **1971**, *83*, 35–42.
[68] Bartz, M.; Küther, J.; Vaughan, G.B.M.; Seshadri, R.; Tremel, W. Crystallization of $SrCO_3$ on a self-assembled monolayer substrate: An *in-situ* synchrotron X-ray study. *J. Mater. Chem.* **2001**, *11*, 503–506.
[69] Avrami, M. Kinetics of Phase Change. II. Transformation-Time Relations for Random Distribution of Nuclei. *J. Chem. Phys*. **1940**, *8*, 212–224.
[70] Avrami, M. Kinetics of Phase Change. III. Granulation, Phase Change, and Microstructure. *J. Chem. Phys*. **1941**, *9*, 177–184.
[71] Johnson, W. A.; Mehl, R. F. Reaction kinetics in processes of nucleation and growth. *Trans. AIME* **1939**, *135*, 416–458.
[72] Liu, F.; Sommer, F.; Bos, C.; Mittemeijer, E. J. Analysis of solid state phase transformation kinetics: models and recipes. *Int. Mater. Rev*. **2007**, *52*, 193–212.
[73] Holleman A. F.; Wiberg. N. Anorganische Chemie, chapter 14, Die Eisengruppe.De Gruyter, 103. Auflage
[74] Baran, E. J.; Nord, A. G.; Diemann, E. Electronic spectra and cationic distribution in the system $(Mg_{1-x}Co_x)_3(PO_4)_2$. *J. Phys. Chem. Solids* **1989**, *50*, 983–984.
[75] Sørensen, M. B.; Hazell, R. G.; Bentien, A.; Bond, A. D.; Jensen, T. R. Two new cobalt–zinc orthophosphate monohydrates, hydrothermal synthesis, crystal structures and thermal investigation. *Dalton Trans.* **2005**, *3*, 598–606.
[76] Xu, C.; Li, Y. D.; Huang, Y.; Yu, Y. M.; Seo, H. J. Luminescence characteristics and site-occupancy of Eu^{2+}- and Eu^{3+}-doped $MgZn_2(PO_4)_2$ phosphors. *J. Mater. Chem.* **2012**, *22*, 5419–5426.
[77] Shannon, R. D., Revised Effective Ionic Radii and Systematic Studies of Interatomic Distances in Halides and Chalcogenides. *Acta Crystallogr*. **1976**, *A32*, 751-767.
[78] Tong, T.; Zhang, J.; Tian, B.; Chen, F.; He, D. Preparation of Fe^{3+}-doped TiO_2 catalysts by controlled hydrolysis of titanium alkoxide and study on their photocatalytic activity for methyl orange degradation. *J. Hazard. Mater.* **2008**, *155*, 572–579.
[79] Karmakar, D.; Mandal, S. K.; Kadam, R. M.; Paulose, P. L.; Rajarajan, A. K.; Nath, T. K.; Das, A. K.; Dasgupta, I.; Das, G. *P.* Ferromagnetism in Fe-doped ZnO nanocrystals: Experiment and theory *Phys. Rev. B* **2007**, *75*, 144404.
[80] Grätzel, M.; Howe, R. F. Electron Paramagnetic Resonance Studies of Doped TiO_2 Colloids. *J. Phys. Chem.* **1990**, *94*, 2566–2572.

2.7 Supporting information

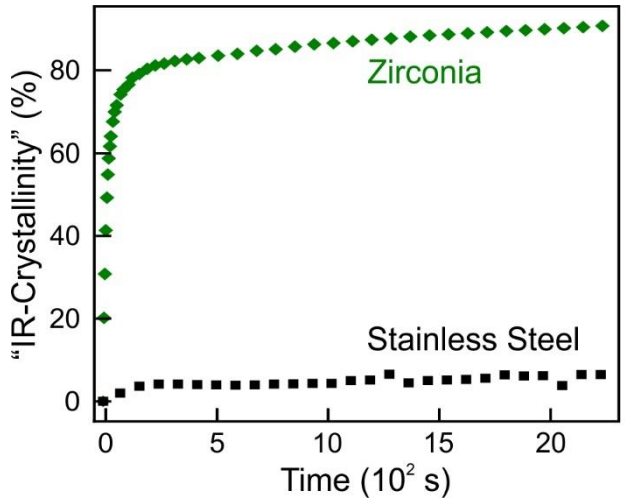

Figure S2.1. Recrystallization of amorphized zinc phosphate hydrate in the presence of water measured by IR spectroscopy. The products of the amorphization process show large differences in their recrystallization kinetics depending on the grinding material (stainless steel vs. zirconia).

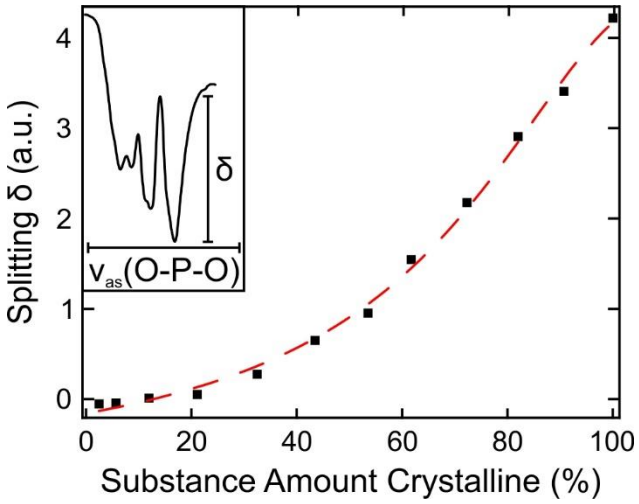

Figure S2.2 Standards for quantification: Mixtures of crystalline and amorphous phases of zinc phosphate hydrate and the resulting splitting δ of the asymmetric phosphate stretching mode (see inset).

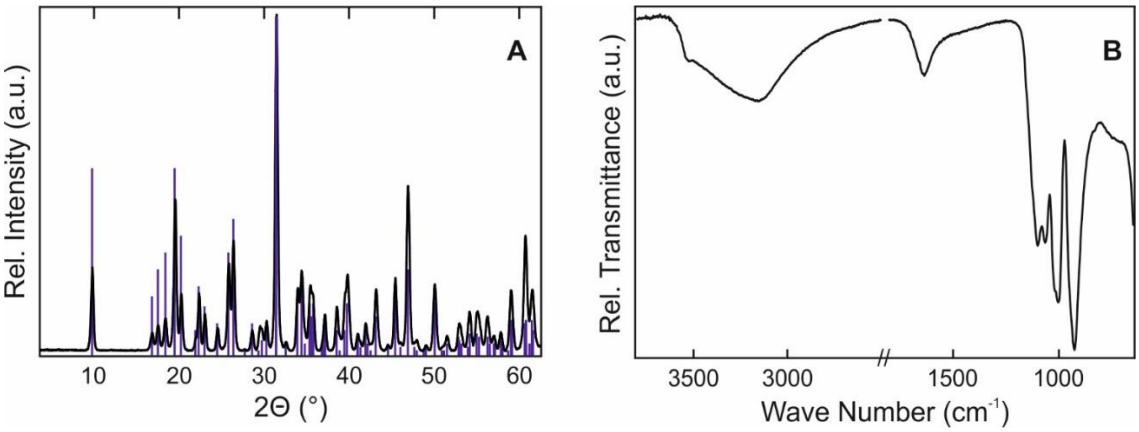

Figure S2.3 (A) Powder XRD of hopeite synthesized by mixing $Zn(NO_3)_2$ and Na_3PO_4. The XRD pattern was measured with CuKα radiation. Blue bars represent the literature reflections of hopeite.[1] (B) IR spectrum of hopeite.

.

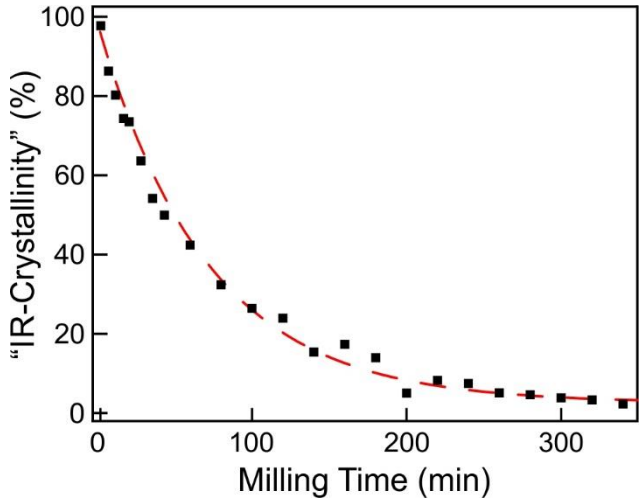

Figure S2.4 Amorphization kinetics derived from a quantitative analysis of the respective IR spectra after different milling times for $Zn_3(PO_4)_2 \times 4\ H_2O$ in the presence of Fe impurities (2 mol %).

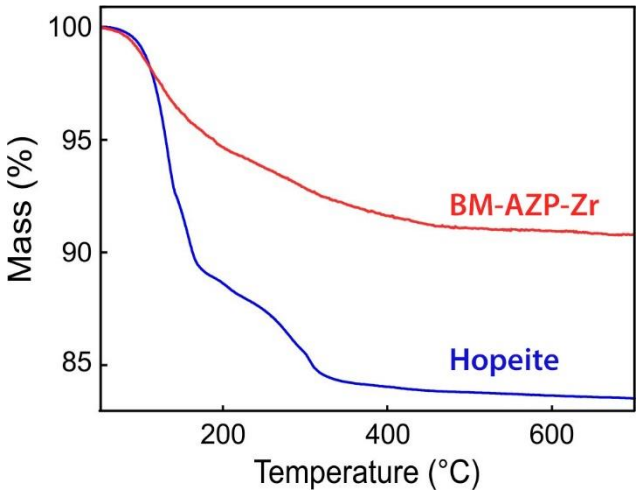

Figure S2.5 TGA traces of BM–AZP–Zr showing the continuous loss of mass upon heating (red line). In contrast, hopeite loses its structural water in defined steps and contains a higher amount of structural water.

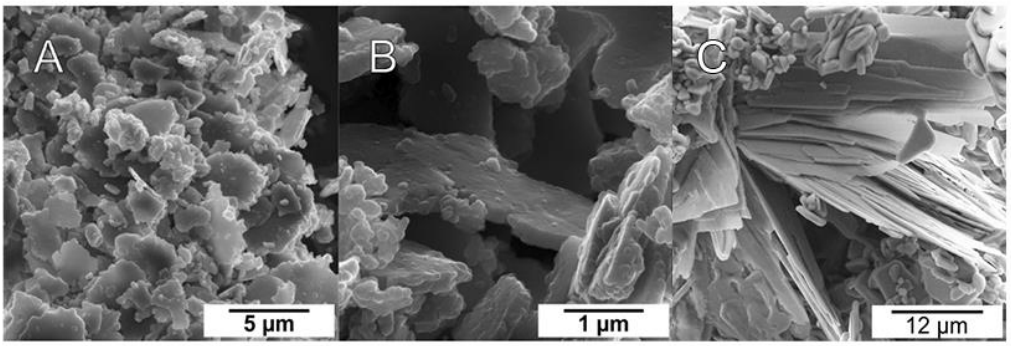

Figure S2.6 SEM images of BM-AZP-Zr at different magnifications (A and B) and synthesized Hopeit (C).

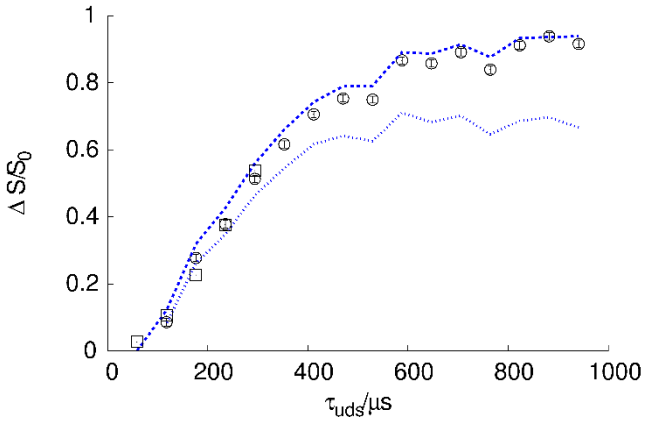

Figure S2.7 $^{31}P\{^{1}H\}$-REDOR curve of BM-AZP-Zr (hollow spheres with error bars) along with fitted data with ν_{dip} = -1004 Hz (hollow squares), upper (dashed line) and lower (dotted line) error margins. Experimental data is obtained with a sample spinning frequency of 12.5 kHz. The τ_{uds} is the universal dephasing time. The S_0 is the reference signal, ΔS is the difference between S_0 and the dephased echo signal.

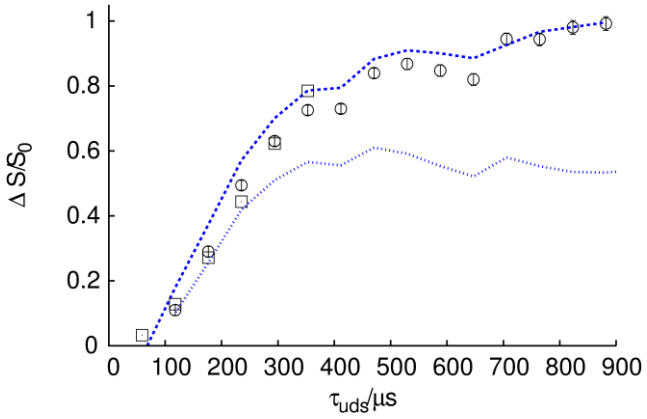

Figure S2.8 $^{31}P\{^{1}H\}$-REDOR curve of the sharp signal at 4 ppm for semi-crystalline zinc phosphate semi-CZP-Zr (hollow spheres with error bars) along with fitted data with ν_{dip} = -954 Hz (hollow squares), upper (dashed line) and lower (dotted line) error margins. Experimental data is obtained with a sample spinning frequency of 12.5 kHz. The τ_{uds} is the universal dephasing time. The S_0 is the reference signal, ΔS is the difference between S_0 and the dephased echo signal.

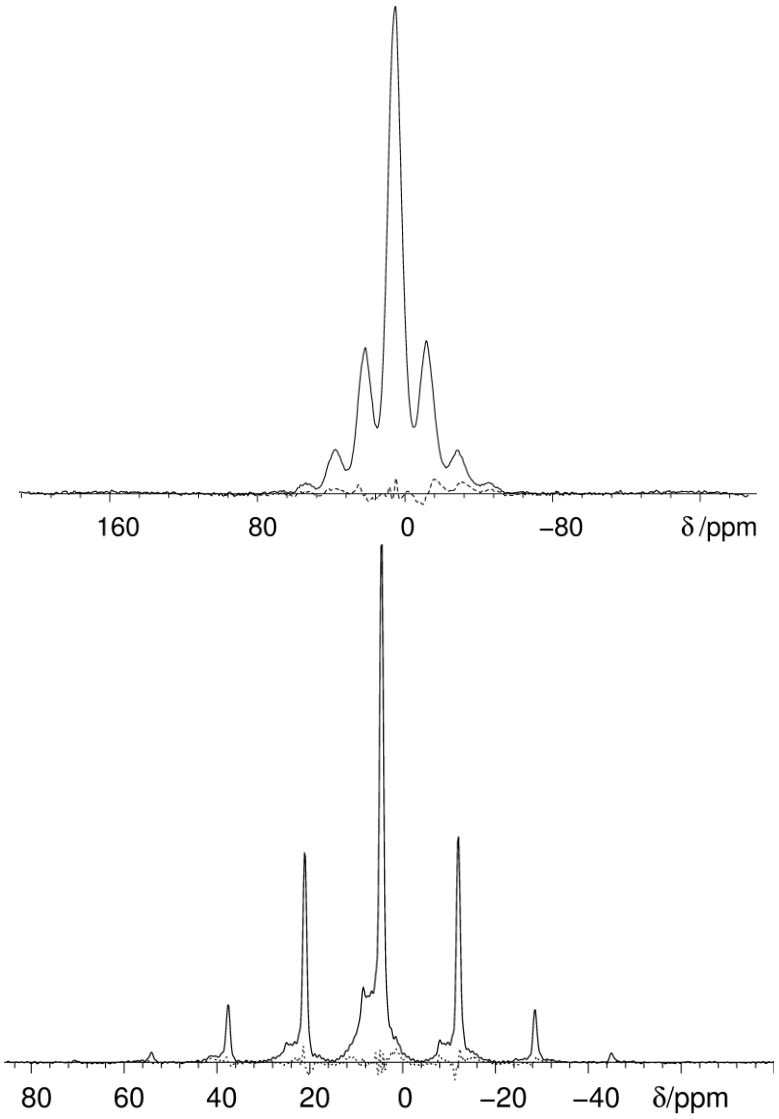

Figure S2.9 ^{1}H decoupled ^{31}P MAS spectra (solid line) for BM-AZP-Zr (top) and semi-crystalline zinc phosphate semi-CZP-Zr (bottom) at a sample spinning frequency of 2 kHz, compared with the residual intensity (dashed line) subtracted with SIMPSON simulated pattern. The simulated data are documented in Table 1. Impurities: δ_{iso} 6.0 ppm.

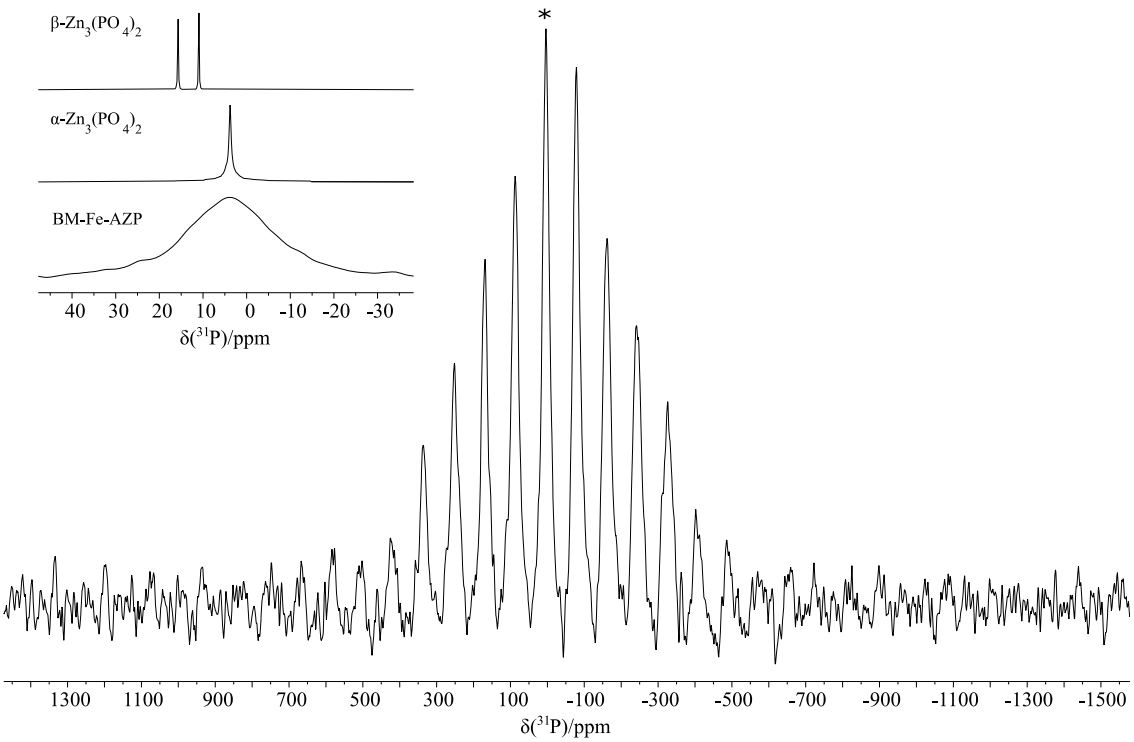

Figure S2.10 The ^{31}P MAS NMR spectrum of BM-AZP-Fe, and the comparison of it to the spectra of α-$Zn_3(PO_4)_2$ and β-$Zn_3(PO_4)_2$ (stack plot shown in the insert). All spectra were measured with spinning frequency of 10 kHz. The peak marked with asterisk is the isotropic chemical shift (4.4 ppm).

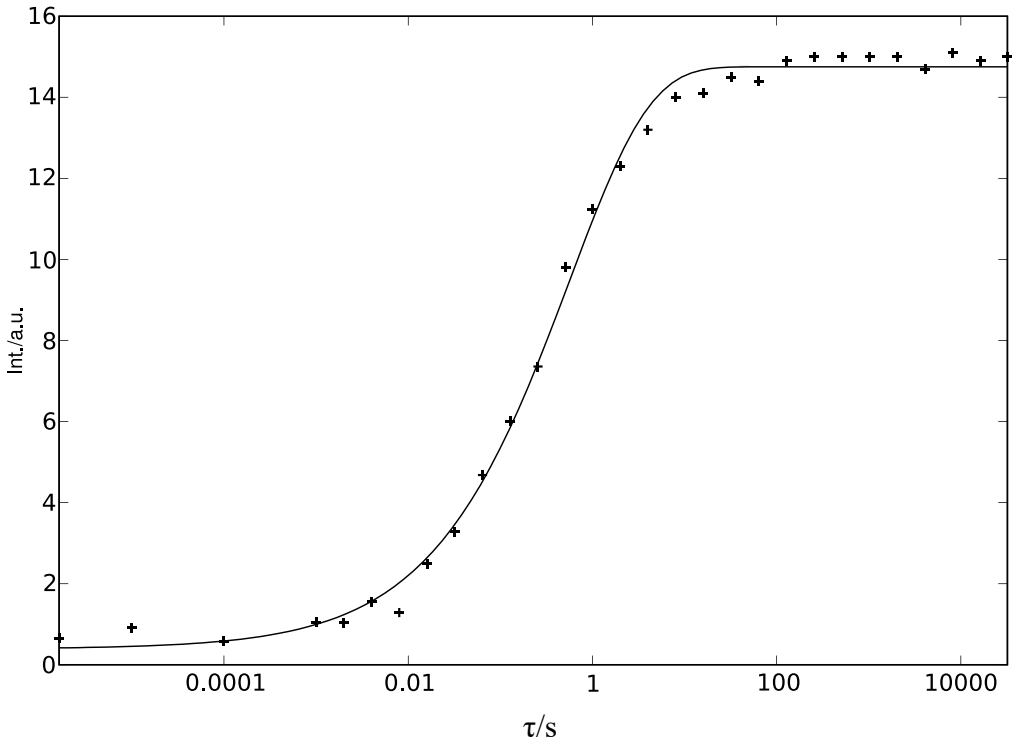

Figure S2.11 Fitting of the relaxation time T_1 of BM-AZP-Fe .The peak intensities of the isotropic chemical shift and the neighboring 6 spinning side bands were included. The relaxation time T_1 was calculated to be 0.53 ± 0.04 s.

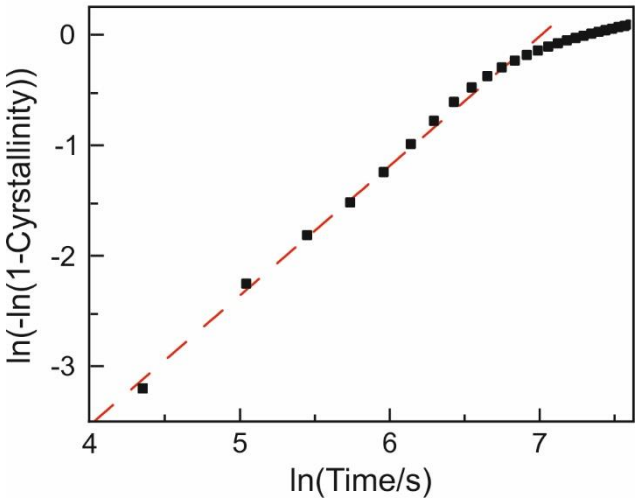

Figure S2.12 Double logarithmic plot of the recrystallization kinetic of AZP showing the Avrami mechanism.

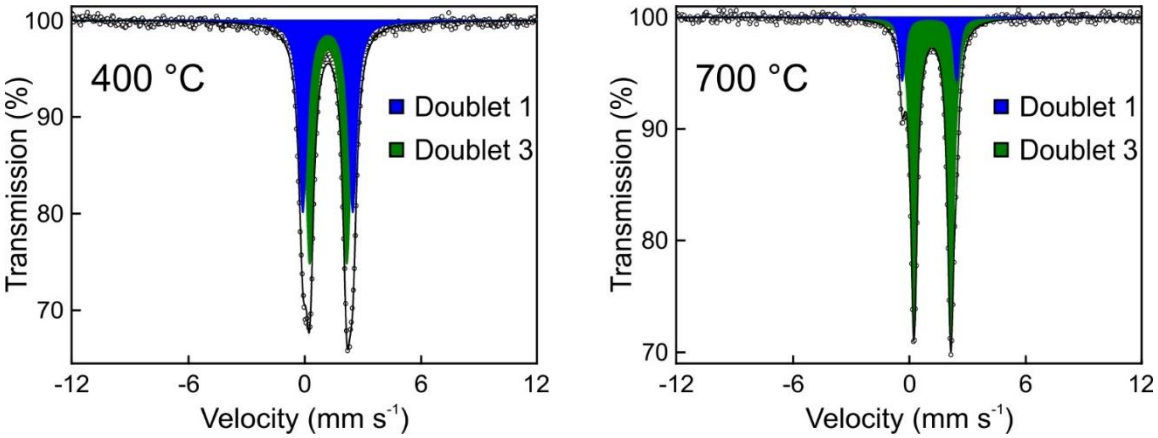

Figure S2.13 Mössbauer spectra of BM-AZP (2 m% ^{57}Fe) after annealing at 400 °C and 700 °C for 5 d under argon. The signal of BM-AZP (doublet 1) disappears at elevated temperatures, the signal of γ-$Zn_{3-x}Fe_x(PO_4)_2$.(doublet 3) appears and grows.

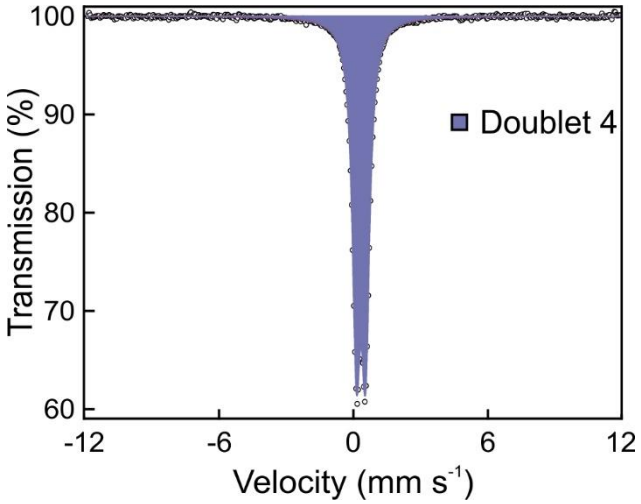

Figure S2.14 Mössbauer spectrum of BM-AZP (2 m% ^{57}Fe) after annealing at 700 °C for 5 d in air. Only the signal of α-Fe_2O_3 (doublet 4) was observed.

Table S2.1 Milling reactions with different amounts of added Fe.

Amount of Fe used during milling / mol%	Milling time until complete amorphization[a] / min	"IR-crystallinity" after 60 min of milling / %
0	340	56.8
1	320	59.2
2	340	59.6
4	360	57.8
5	320	56.5
10	340	59.0

[a] determined by quantitative ATR-IR spectroscopy

Table S2.2. Elemental quantification of BM-AZP in the absence of iron impurities by ICP-MS, ICP-OES, EDX after a milling time of 340 minutes

ICP-MS	^{64}Zn	^{69}Zn	^{31}P
mean conc. / µg L^{-1}	570.7±7.0	580.7±4.7	179.4±1.4
mean conc. / µmol L^{-1}	8.73±0.11	8.88±0.07	5.79±0.04
ratio			3.00:1.97
ICP-OES	Zn	P	
mean conc. / µg L^{-1}	2440	790	
mean conc. / µmol L^{-1}	37.3	25.5	
ratio			3.0:2.1
EDX	Zn K	P K	
at %	15.78	10.73	
ratio		3.0:2.0	

Section S1 – Experimental Details

X-ray Diffraction. High resolution synchrotron powder diffraction data for the final mech-AZP were collected using beamline 11-BM at the Advanced Photon Source (APS), Argonne National Laboratory using an average wavelength of 0.413664 Å. Discrete detectors covering an angular range from -6 to 16° 2Θ are scanned over a 34° 2Θ range, with data points collected every 0.001° 2Θ and scan speed of 0.01°/s. The 11-BM instrument uses x-ray optics with two platinum-striped mirrors and a double-crystal Si(111) monochromator, where the second crystal has an adjustable sagittal bend.[2] Ion chambers monitor incident flux. A vertical Huber 480 goniometer, equipped with a Heidenhain encoder, positions an analyzer system comprised of twelve perfect Si(111) analyzers and twelve Oxford-Danfysik $LaCl_3$ scintillators, with a spacing of 2° 2Θ. Analyzer orientation can be adjusted individually on two axes. A three-axis translation stage holds the sample mounting and allows it to be spun, typically at ~5400 rpm (90 Hz). A Mitsubishi robotic arm is used to mount and dismount samples on the diffractometer.[3] An Oxford Cryosystems Cryostream Plus device allows sample temperatures to be controlled over the range 80-500 K when the robot is used. The diffractometer is controlled via EPICS.[4] Data were collected while continually scanning the diffractometer 2Θ arm. A mixture of NIST standard reference materials, Si (SRM 640c) and Al_2O_3 (SRM 676) is used to calibrate the instrument, where the Si lattice constant determines the wavelength for each detector. Corrections are applied for detector sensitivity, 2Θ offset, small differences in wavelength between detectors, and the source intensity, as noted by the ion chamber before merging the data into a single set of intensities evenly spaced in 2Θ.[5-8]

Experimental Details Nuclear Magnetic Resonance Spectroscopy

The solid state NMR spectra were obtained at 7.05 T on a Bruker Avance II NMR spectrometer equipped with a home-built transmission line 4 mm McKay probe head at a ^1H frequency of 300.13 MHz. The chemical shifts of ^1H are reported using the δ scale, relative to 1% tetramethylsilane (TMS) in $CDCl_3$ on a deshielding scale. The chemical shifts of ^{31}P are reported relative to 85% H_3PO_4. For the ^{31}P measurements, the ^1H resonance of 1% tetramethylsilane in $CDCl_3$ served as an external secondary reference using the Ξ-values as reported by the IUPAC.[9] The sample spinning frequency was 12.5 kHz for rotational echo double resonance (REDOR), 2 kHz for chemical shift anisotropy (CSA) analysis and 10 kHz for the single pulsed spectra stack plots.

The deconvolution of signals as well as spin-lattice relaxation (T_1) and peak area analysis were assisted by the program Deconv2Dxy.[10] The SIMPSON[11] simulations of the CSA patterns and the $^{31}P\{^{1}H\}$-REDOR curves were achieved with a home written tcl-script implemented with non-linear least square fitting. The REDOR curve was plotted on the universal dephasing scale,[12] and the error limits of the REDOR curves were calculated according to the reference 13.

References

[1] Liebau, F. Zur Kristallstruktur des Hopeits, $Zn_3[PO_4]_2 \times 4\,H_2O$. Acta Cryst. **1965**. 18, 352-354.

[2] Wang, J.; Toby, B. H.; Lee, L. P.; Ribaud, L.; Antao, S.; Kurtz, C.; Ramanathan, M.; von Dreele, R. B.; Beno, M. A. A dedicated powder diffraction beamline at the Advanced Photon Source: Commissioning and early operational results. *Rev. Sci. Instr.* **2008**, *79*, 085105.

[3] Lee, P. L.; Shu, D.; Ramanathan, M.; Preissner, C.; Wang, J.; Beno, M. A.; von Dreele, R. B.; Ribaud, L.; Kurtz, C.; Antao, S. M.; Jiao, X.; Toby, B. H. A twelve-analyzer detector system for high-resolution powder diffraction. *J. Synchr. Rad.* **2008**, *15*, 427-432.

[4] Dalesio, L. R.; Hill, J. O.; Kraimer, M.; Lewis, S.; Murray, D.; Hunt, S.; Watson, W.; Clausen, M.; Dalesio, J. The Experimental Physics and Industrial Control-System Architecture - Past, Present, and Future, *Nucl. Instr. Meth. Phys. Res. Sect. A* **1994**, *352*, 179-184.

[5] Lee, P. L.; Shu, D.; Ramanathan, M.; Preissner, C.; Wang, J.; Beno, M. A.; Von Dreele, R. B.; Ribaud, L.; Kurtz, C.; Antao, S. M.; Jiao, X.; Toby, B. H. A twelve-analyzer detector system for high-resolution powder diffraction, *J. Synchr. Rad*. **2008**, *15*, 427-432.

[6] Preissner, C.; Shu, D.; Toby, B. H.; Lee, P.; Wang, J.; Kline, D.; Goetze, K. The sample-changing robot for the 11-BM high-throughput powder diffraction beamline," *Nucl. Instr. Meth. Phys. Res. Sect. A* **2009**, *42*, 990.

[7] Wang, J.; Toby, B. H.; Lee, P. L.; Ribaud, L.; Antao, S.; Kurtz, C.; Ramanathan, M.; Von Dreele, R. B.; Beno, M. A., A dedicated powder diffraction beamline at the Advanced Photon Source: Commissioning and early operation results. *Rev. Sci. Instr*. **2008**, *79*, 085105.

[8] Lagarec, K.; Rancourt, D. G. Mössbauer Spectra of Solid Solutions Processed Using the Voigt Function. *Nucl. Instrum. Methods Phys. Res., Sect. B* **1997**, *129*, 266–280.

[9] Harris, R. K.; Becker, E. D.; Cabral de Menezes, S. M.; Granger, P.; Hoffman, R. E.; Zilm, K. W. Further conventions for NMR shielding and chemical shifts (IUPAC Recommendations 2008). *Pure Appl. Chem*. **2009**, *80*, 59–84.

[10] D. Jardón-Álvarez, J. Schmedt auf der Günne, Reduction of the temperature gradient in laser assisted high temperature MAS NMR. *Solid State Nucl. Magn. Reson.* **2018**, *94*, 26–30.

[11] M. Bak, J. T. Rasmussen, N. C. Nielsen, SIMPSON: A General Simulation Program for Solid-State NMR Spectroscopy. *J. Magn. Reson.* **2000**, *147*, 296–330.

[12] M. Roming, C. Feldmann, Y.S. Avadhut, J. Schmedt auf der Günne, Characterization of Noncrystalline Nanomaterials: NMR of Zinc Phosphate as a Case Study. *Chem. Mater.*, **2008**, 20, 5787-5795.

[13] V.R. Celinski, J. Weber, J. Schmedt auf der Günne, C-REDOR curves of extended spin systems. *Solid State Nucl. Magn. Reson.*, **2013**, *49-50*, 12—22.

3

Multistep crystallization pathways in the ambient temperature synthesis of a new alkali activated binder

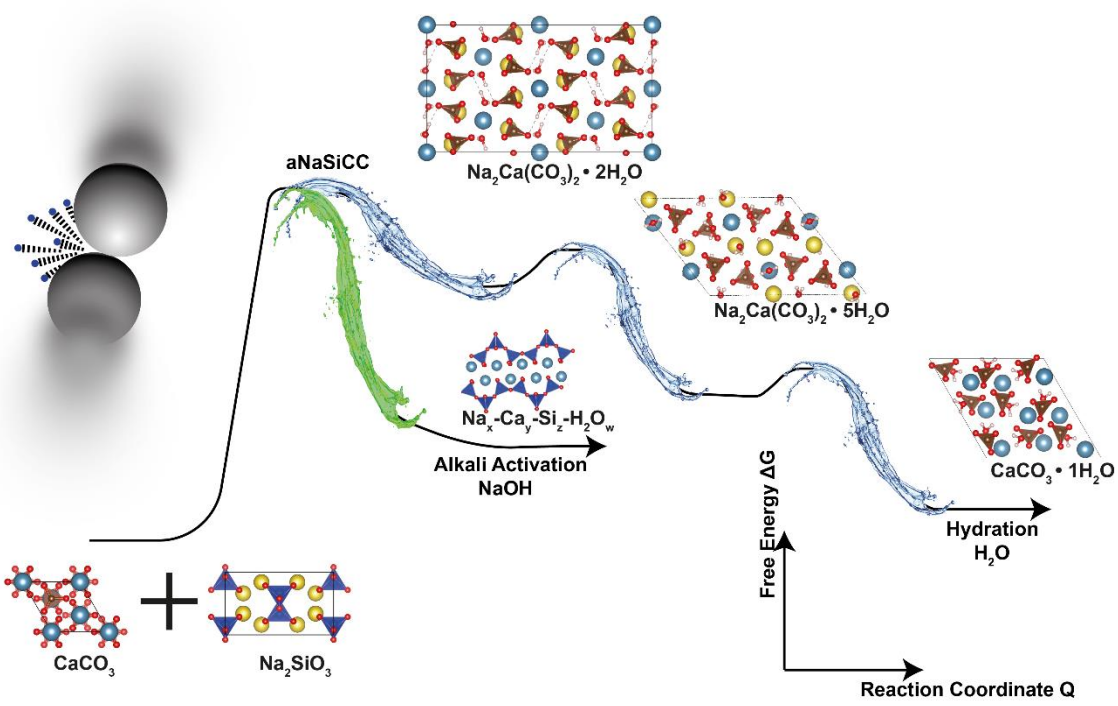

Ball milling of calcite and sodium metasilicate lead to the formation of "activated" amorphous sodium calcium silicate carbonate (aNaSiCC). Diffusion controlled crystallization of aNaSiCC in water/acetonitrile mixtures induced crystallization via pirssonite and gaylussite to monohydrocalcite. Alkali activation with NaOH lead to the formation of a C-S-H-like phase, enabling the formation of a concrete binder without the need for high-temperature calcination and emission of CO_2.

This chapter contains an adapted reproduction of *Advanced Functional Materials* **2021**, DOI: 10.1002/adfm.202108126 reprinted with permission of Wiley Online Library.

Authorship Contribution

Study conception and design	M. Maslyk W. Tremel
Acquisition of data	M. Maslyk T. Gäb G. Matveeva M. Mondeshki Y. Krysiak
Analysis and interpretation of data	M. Maslyk Y. Krysiak M. Mondeshki P. Opitz
Drafting of manuscript	M. Maslyk
Critical Revision	W. Tremel M. Mondeshki U. Kolb

3.1 Relevance to doctoral thesis

The increasing demand for cement and concrete in construction industry has a significant impact on the annual CO_2 emissions. About 8% of worldwide CO_2 emissions are estimated to arise from cement production. The fundamental production processes in cement production can be summarized as a high temperature synthesis of limestone ($CaCO_3$) and clay minerals (SiO_2) to specific calcium silicate phases. Depending on the clay constituents and the desired cement properties, varying aluminate and ferrite phases are part of the cement as well. In general, two processes are mainly responsible for the CO_2 emissions. To establish high temperatures for the solid-state reaction of burned lime (CaO) and clay (SiO_2) combustion of fossil fuels is needed. In addition, the decomposition of limestone to burned lime produces nearly 0.5g of CO_2 per gram limestone. The close resemblance of burning and rehydration processes in cement production to natural mineralogical analogues can be used to address the reduction of CO_2 emissions. Therefore, the goal of this project can be summarized in the formation of an amorphous precursor by mineralogical constituents, with comparable rehydration behavior to cement clinker. To access a stable precursor high energy ball milling was utilized and the material characterized by means of FTIR spectroscopy, XRPD, NMR spectroscopy, TEM and SEM, as well as PDF analysis. Application of these characterization methods allowed for a detailed view on the reaction between calcium carbonate (limestone) and sodium metasilicate. To further investigate the crystallization pathway, a mixture of water/acetonitrile was employed to kinetically control the recrystallization. Thus, it could be shown that the recrystallization occurs through multiple, metastable intermediates. In addition, a direct comparison with a non-silicate containing reference, has shown that the silicate environment has a fundamental influence on the recrystallization pathway and could also identify a metathesis reaction between calcium carbonate and sodium metasilicate as the driving force for the underlying reaction. Based on theese findings it was concluded that a calcium silicate precursor should result from the amorphization process, possibly allowing for acess to calcium-silicate-hydrate (C - S-H), the “glue of cement”. Indeed, it could be confirmed that the addition of an activiator (sodium hydroxide), leads to a compound similar to C-S-H, thus enabling a new and sustainable synthesis route to cementious materials.

3.2 Introduction

Mitigating the environmental consequences of anthropogenic CO_2 emissions is one of the major challenges of this century. For every ton of cement that is produced, one ton of greenhouse gases is released into the atmosphere, and the production of Portland cement accounts for ~8% of anthropogenic CO_2 release.[1] Portland cements contain ground cement clinker, basically calcium silicates and aluminates, produced from limestone and other components in a high-temperature process with the release of CO_2, and then mixed with a sulfate carrier that serves to control solidification. Promising approaches to offset some of the massive carbon dioxide emissions from cement in clinker production include replacing Portland clinker with non-calcined limestone ($CaCO_3$), a readily available Ca source, or using alkali-activated binders/geopolymers as Si source for cement.[2,3] Alkali-activated binders and geopolymers can be distinguished according to the calcium content in the precursor and the phases of the resulting binder. Low-calcium systems tend to produce binders such as geopolymers, which may contain sodium aluminosilicate hydrate (N-A-S-H) gels, while high-calcium systems form alkali-activated binder containing phases like calcium silicate hydrate (C-S-H) or calcium aluminosilicate hydrate (C-A-S-H) gels.[4,5] Still, the reaction of calcium carbonate in alkali-activated/geopolymer systems,[6] in particular the reaction mechanisms, have rarely been studied. Firdous et al. [7] showed that calcium carbonate reacts partially with sodium silicate solutions by forming a C-S-H phase, which is likely to contain some sodium. Mineral additions in cements as supplementary cementitious materials are known to have accelerating effects on cement hydration.[8,9] They are attributed, among other things, to the distribution of nucleation sites.[10] The use of up to 5%$_{wt}$ limestone in Portland cement as reactive filler material raises the question if amorphous calcium carbonate could be used as an alternative activated precursor as it will alter the dissolution and precipitation reactions, thereby reducing CO_2 emissions.[11] Pure calcium carbonate is the textbook model system to study crystallization from solution at a molecular level. In ambient conditions, calcium carbonate exists in three anhydrous (calcite, aragonite, and vaterite)[12,13] and three hydrous (ikaite, monohydrocalcite, hemicarbonate) polymorphs[14,15,16] and in amorphous forms (ACC).[17] Studies on calcium carbonate, in particular ACC, have witnessed major advances in our comprehension of the early stages of crystallization.[18,19,20,21] Liquid-like precursors to ACC and so-called prenucleation species have been reported depending on the crystallization conditions.[22,23,24,25] Much of our current understanding of ACC comes from biomineral studies. Biogenic ACC has been classified as stable and hydrated (with an approximate composition $CaCO_3$ x H_2O) or

transient and anhydrous,[17] and a stepwise transformation of ACC is assumed although the exact mechanistic pathways remain unclear considering diffusion coefficients, mobility and hydration energy of the divalent ions.[26,27,28] While anhydrous ACC is stable in the presence of water,[24] hydrated ACC crystallizes rapidly, which makes the process difficult to monitor.[29,30,31,32] The crystallization of hydrated ACC may be slowed down by (i) reducing the water concentration or (ii) with matrix materials. Silica as "inert" matrix prevents ACC crystallization. Silica-coatings prepared by mixing $CaCl_2$ with Na_2CO_3/Na_2SiO_3 stabilize $CaCO_3$ prenucleation clusters[33] or retard ACC nucleation by setting a barrier to water diffusion.[34,35] This allowed monitoring the polymorphic transformations of ACC. Crystallization experiments conducted in the absence of silica showed a conversion to calcite *via* vaterite and aragonite, while encapsulation in a silica matrix[36] containing a mixture of different silicate species due to its preparation in diluted "water glass", induced marked changes in the temporal evolution of the polymorphic fractions.[37] This work investigates the formal metathesis reaction of solid calcium carbonate with solid sodium metasilicate at room temperature and its significance for geopolymer/alkali-activated binders using an amorphous solid solution of $CaCO_3$ and Na_2SiO_3 as an "activated precursor". To this end, the reactants, $CaCO_3$ and Na_2SiO_3, were ball-milled into a reactive amorphous form in which the components of the desired product are mixed at the molecular level. This milling process allows an industrial scale implementation while potentially reducing undesired emission of CO_2,in combination with conventional production processes. Furthermore, it is shown that by deliberate retardation of the crystallization process, a stepwise transformation can be traced via metastable phases. Solid state reactions are typically very slow and require long reactions times and high temperatures, because the transport lengths of the reacting species are in the order of micrometers, while the diffusion coefficients typically range from 10^{-12} to 10^{-16} cm^2/s.[38] Diffusional control can be circumvented by reducing transport distances to molecular dimensions by dispersing the components at a molecular level or increasing defect concentrations.[39,40,41] This statistical "frozen" mixture of starting materials as an activated sprecursor was generated mechanochemically.[42] Different from solid state reactions, where diffusion is intristically slow, and solution reactions, where diffusion is fast, water/acetonitrile mixtures were used to retard the crystallization process and to enable structural reordering.[43] Our approach experimentally mimics the "simulated annealing" concept, which has been employed for predicting inorganic solids and their crystal structures[44] and allows to explore the energy landscape of a reaction system by controlling supersaturation *via* solvent concentration.

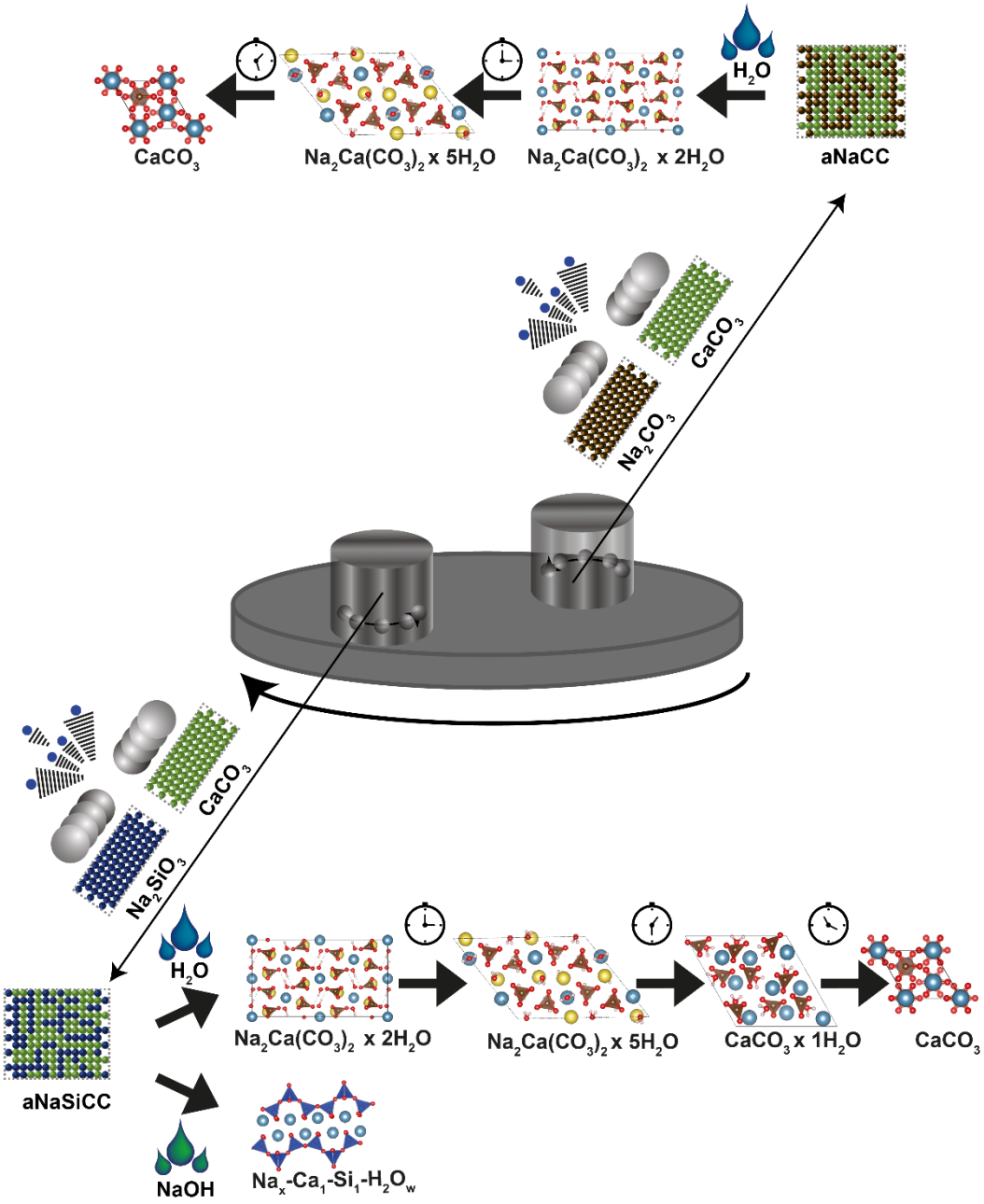

Figure 3.1. Overview of the mechanochemical preparation of the amorphous intermediates of $CaCO_3$ and $NaCO_3$ (aNaCC) or $CaCO_3$ and $NaSiO_3$ (aNaSiCC) and the reaction paths of the setting reactions of aNaCC and aNaSiCC with water. The hydration reaction of aNaCC with H_2O leads to the crystallization of calcite (top).The reaction of aNaSiCC on the carbonate reaction branch leads to monohydrocalcite ($CaCO_3$ x H_2O), on the silicate reaction branch after NaOH activation to the formation of C-S-H (bottom).

This allows to follow the reaction pathway analytically and structurally through a number of intermediates in order to mechanistically understand the formation of alkali-activated binders. X-ray powder diffraction (XRD) and total scattering, transmission electron microscopy (TEM) combined with automated diffraction tomography (ADT), Fourier transform infrared spectroscopy (FTIR), and multinuclear magic angle spinning (MAS) nuclear magnetic resonance (NMR) spectroscopy were used to elucidate the reaction

kinetics and phase evolution and local structure at the primary stages of the reaction for crystalline and especially non-crystalline intermediates. The sequence of events is outlined in Figure 3.1. In a first "activation" step, calcium carbonate and sodium metasilicate were ball-milled to a randomly "frozen" non-equilibrium intermediate, sodium calcium carbonate/silicate (aNaSiCC). The corresponding reaction of calcium carbonate with Na_2CO_3 (the carbon analogue of Na_2SiO_3) yielded amorphous sodium calcium carbonate (aNaCC). Reaction of aNaSiCC with water under controlled conditions initiates a cascade of reactions leading to monohydrocalcite ($CaCO_3 \times H_2O$) *via* the metastable intermediates pirssonite ($Na_2Ca(CO_3)_2 \times 2H_2O$) and gaylussite ($Na_2Ca(CO_3)_2 \times 5H_2O$ in the Ca branch. The reaction starting from silicate-free aNaCC leads without incorporation of water only to the formation of calcite. The formation of pirssonite and gaylussite indicates a reorganization of the sodium and calcium cations, thus promoting the formation of a calcium silicate precursor in the Si branch, which likely contains some sodium and reacts to a C-S-H-type phase by activation with NaOH. Ca/Si (C/S) ratios between 0.67 and 1.5 are consistent with a defect *tobermorite* structure.[45] Our findings are a step forward in unravelling the reaction mechanisms involved in the preparation and formation of alkali-activated binders.

3.3 Results and discussion

Synthesis

Mechanochemical Activation. We investigated the mechanochemical activation of calcite with sodium metasilicate (Na_2SiO_3) and sodium carbonate (Na_2CO_3) in a planetary ball mill. Recrystallization in water led to mixed sodium/calcium carbonate hydrates (*vide infra*). This indicates that a high sodium content in calcium carbonate plays a crucial role in recrystallization and hydration. Small amounts (7.5 $\%_w$) of Na_2CO_3 have been shown to induce amorphization of calcite in mechanochemical reactions.[40] As calcium silicate hydrate (C-S-H), the main constituent of hydrated cements, can contain a broad range of Ca/Si ratios[46] we reacted equimolar amounts of $CaCO_3$ with Na_2SiO_3 and its carbon analogue Na_2CO_3 to compare the outcome of the mechanochemical reactions. The presence of only one $CaCO_3/Na_2SiO_3$ (aNaSiCC, Na_2SiO_3 substitution) or two $CaCO_3/Na_2CO_3$ (aNaCC, Na_2CO_3 substitution) modulations in the powder X-ray diffraction patterns of the amorphous products aNaSiCC and aNaCC (Figure 3.2A) and the absence of any electron diffraction spots in TEM (Figure 3.2B) are compatible with a loss of long-range order on the micro- and nanoscale in both products. Fourier-transform infrared (FTIR) spectroscopy

is a useful tool to probe local environments.[47] FTIR spectra of aNaSiCC and aNaCC (Figure 3.2C) show four characteristic carbonate bands (symmetric stretch ν_1 1070 cm^{-1}; out-of-plane deformation ν_2, 865 cm^{-1}; asymmetric stretch ν_3, 1377 cm^{-1}; in-plane-deformation ν_4, 695 and 717 cm^{-1}). The (symmetry forbidden) ν_1 mode, the splitting of the ν_3 and ν_4 modes and the distinct broadening of the vibration bands of the CO_3^{2-} anion are strong indicators for the evolution of the chemical environment due to amorphization.[48] The bands of aNaSiCC are shifted to higher wavenumbers compared to aNaCC. This is most pronounced for the ν_3 mode and in line with the bond energies for the CO_3^{2-} and SiO_3^{2-} anions. The incorporation of silicate in aNaSiCC is marked by a broad band in the range from 1100 to 900 cm^{-1} associated with the symmetric and asymmetric stretching modes of the Si-O-Si (1050 cm^{-1}) and Si-O^- (950 cm^{-1}) units.[49,50] Structural information about the short-range order in amorphous aNaSiCC was obtained by solid-state (ss) MAS-NMR.[51]A comparison of the ^{13}C NMR spectra of calcite (δ = 168.2 ppm, FWHM= 30 Hz), aNaCC (δ = 169.4 ppm, FWHM = 340 Hz), and aNaSiCC (δ = 170.16 ppm, FWHM = 334 Hz) (Figure 3.2D) shows a slight shift and distinct broadening of the CO_3^{2-} signals in aNaSiCC and aNaCC compared to calcite. While the C-O length in calcite is 1.25 Å[52], shorter distances of 1.18 Å are observed in Na_2CO_3.[53] This leads to stronger deshielding and thus a slight downfield shift of 2.2 ppm compared to the ^{13}C NMR shifts of calcite (168.5 ppm) and sodium carbonate (170.7ppm). A previous study found that the amorphization of calcite is complete with only 7% sodium carbonate.[40] It is accompanied by signal broadening without a change in the ^{13}C carbonate shift. Higher amounts of Na_2CO_3 lead to a slight change of ~1 ppm in the ^{13}C shift (signal at 169.5 ppm for aNaCC). This average ^{13}C shift (between the ^{13}C shifts of Na_2CO_3 and calcite) may be due to a statistical distribution of Na^+ and Ca^{2+} cations around the CO_3^{2-} counter ion, resulting in a decrease in the average C-O length, in agreement with the differences in experimental FTIR data (*vide supra*). Surprisingly, a comparable ^{13}C shift was found in aNaSiCC as in pure Na_2CO_3 (170.5 ppm), implying that the local electronic environment of the CO_3^{2-} carbon atom in aNaSiCC and crystalline Na_2CO_3 is virtually identical even in the disordered state. This indicates an association of Na^+ and CO_3^{2-} ions or the charge compensation of Ca^{2+} and SiO_3^{2-} ions, which will be addressed in more detail below.

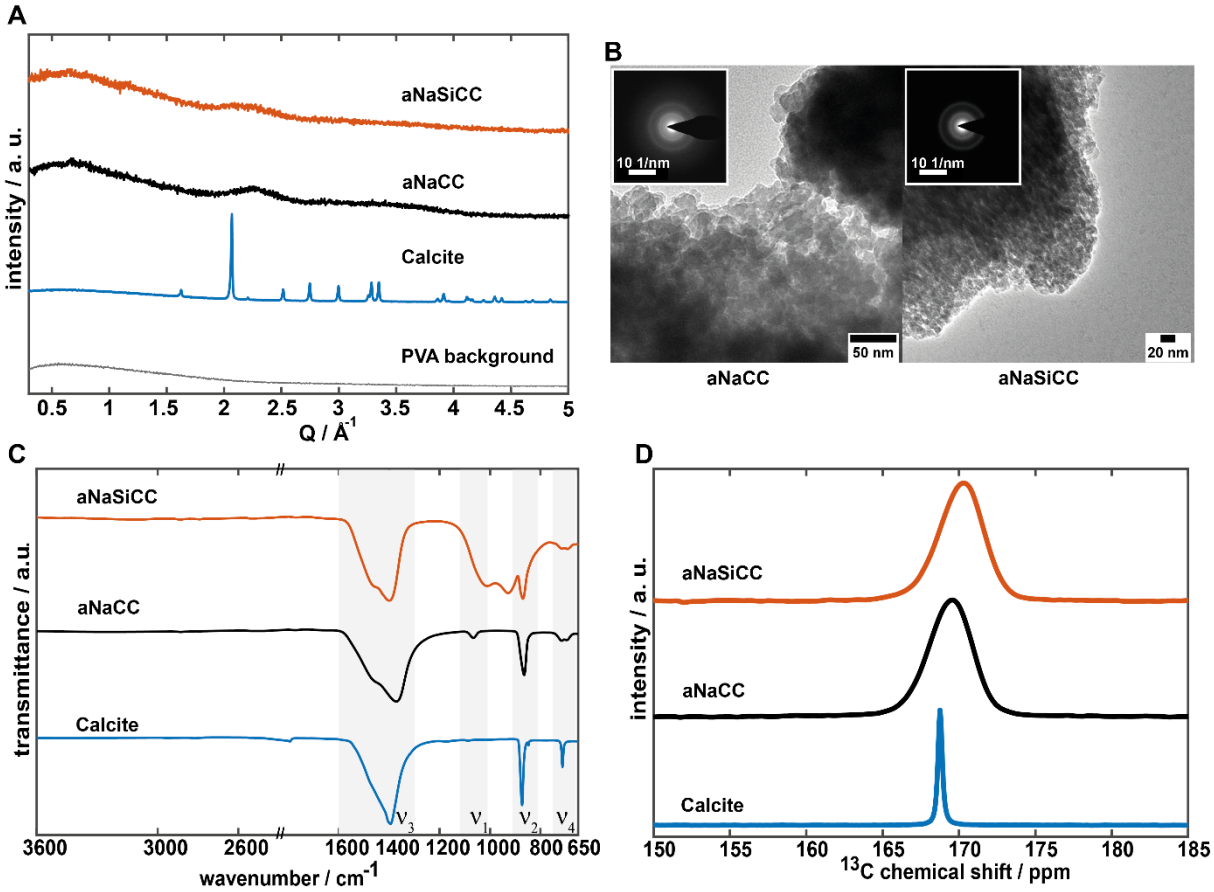

Figure 3.2. (A) PXRD diffractograms after full amorphization (grey line: PVA background; blue line: Calcite black line: aNaSiCC; red line: aNaCC). (B) TEM images and SAED pattern of aNaSiCC and aNaCC after complete amorphization. Insets show the corresponding SAED patterns. (C) IR spectra of calcite (blue line), aNaSiCC (red line), and aNaCC (black line). (D) ^{13}C NMR spectra of calcite (blue line), aNaCC (black line), aNaSiCC (red line).

Kinetics of Mechanochemical Activation Reaction. In addition to the structure of the amorphous intermediates aNaCC and aNaSiCC, the formation mechanism during the milling reaction is of special interest. Since diffraction methods cannot provide meaningful information for amorphous products, the vibrational signatures of the carbonate groups and their ^{13}C NMR resonance signals were used as local probes. Changes in the local environments during the amorphization of aNaSiCC and aNaCC were monitored by taking "snap shots" of the products, i.e., interrupting the milling at specified time intervals and recording FTIR and ^{13}C-NMR spectra *ex situ*. The evolution of the FTIR spectra was monitored semiquantitatively using Lambert – Beer's law $A = -log_{10}(T)$.(Figure 3.3A) The broadening and the shift of the ν_2 bands (inset Figure 3.3A) were used to follow the transition from calcite (ν_2 = 873 cm^{-1}) to the amorphous phases (ν_2 = 861 cm^{-1} for aNaSiCC; ν_2 = 858 cm^{-1} for aNaCC) using a bimodal Pseudo-Voigt function. After 450 minutes of grinding, the samples were X-ray amorphous as no changes occurred in the FTIR spectra and the diffractograms were free of reflections. Thus, the crystallinity at this time

was set to "0%". By comparing the intensities from the respective fits with the v_2 mode of calcite (100% at t = 0) we observed an exponential loss of crystallinity (Figure 3.3A). The amorphization for aNaCC was faster than of NaSiCC. It was nearly complete after 300 min, whereas the amorphization for sodium silicate required a full run of 450 min. This could be monitored from the change in the Na environment during milling by ^{23}Na MAS NMR (Figure 3.3B). Its quadrupole moment (I = 3/2) makes ^{23}Na a suitable probe for changes in the local electronic environment. Still, the interpretation of the spectra is more complex due to the additional second-order quadrupole interactions.[54,55] NMR spectra of amorphous systems are characterized by broad resonances lacking the characteristic quadrupole pattern. The ^{23}Na spectrum of sodium metasilicate (Figure 3.3B, blue spectrum at t = 0) shows only one signal at 16.3 ppm with a FWHM of 600 Hz, which indicates a slightly distorted trigonal bypiramidal environment with an average Na-O distance of 2.37 Å.[56] Due to the high symmetry the quadrupole coupling constant is relatively low leading to a sharp resonance. For Na_2CO_3 (Figure 3.3B, red spectrum at t=0) one sharp signal at 3.8 ppm with a FWHM of 530 Hz and one broadened signal at -21.3 ppm with a FWHM of 2100 Hz appear because of the different sodium sites in Na_2CO_3.[57]

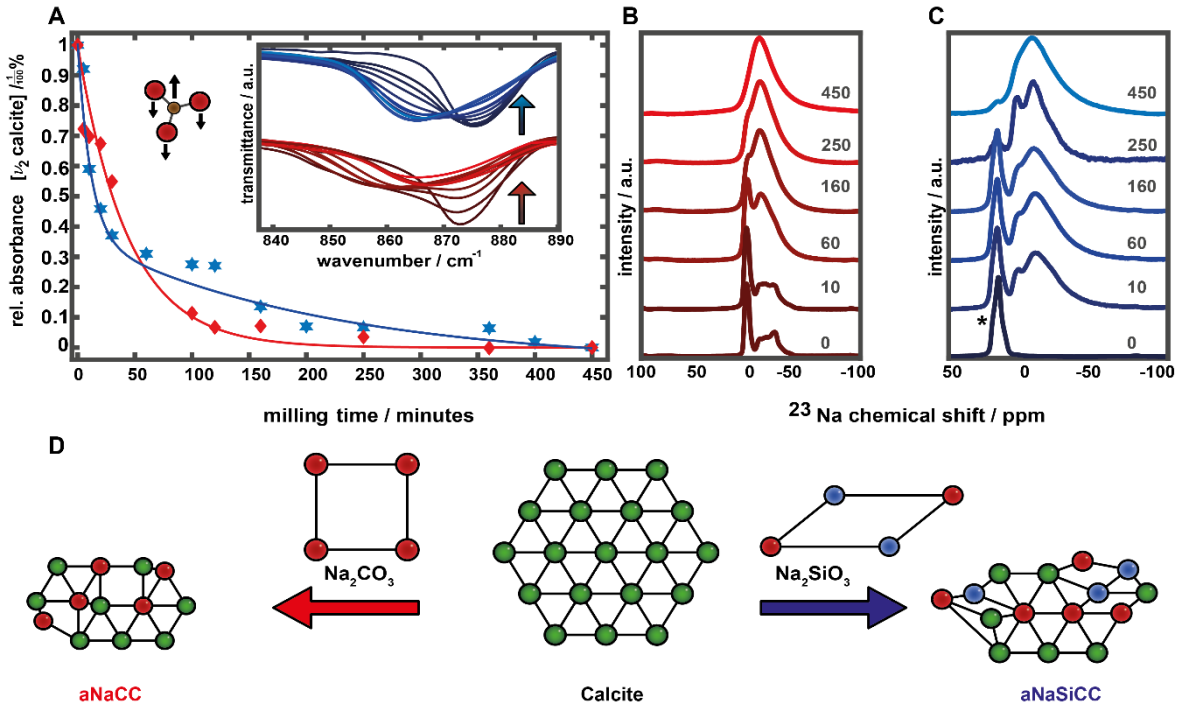

Figure 3.3. (A) Exponential fits to the FTIR spectra for the amorphization of aNaCC (red line) and aNaSiCC (blue line) obtained by infrared spectroscopy. The inset shows the evolution of the v_2 band (narrow: dark blue /dark red, broad: light blue /light red). (B,C) Time-dependent ^{23}Na MAS NMR signal after different milling times (red: aNaCC; blue: aNaSiCC) (D) Scheme illustrating how incorporation of sodium and silicate ions lead to disorder and eventually to a lack of long-range order.

While the narrow line is associated with a highly symmetric octahedral coordination (CN 6), the broadened signal originates from a ninefold coordination of sodium (CN 9). A decrease in Na-O bond lengths is correlated with a high-field shift occurring for mean distances of 2.35 Å in octahedral and 2.70 Å in ninefold coordination of sodium carbonate.[58] The amorphization of Na_2SiO_3 is a process associated with the generation of new sodium sites due to Na^+ transfer from silicate to carbonate environments. After 10 minutes of milling two new broad resonances at -10.2 and 2.5 ppm appear in addition to the sharp 16.3 ppm signal (*) of Na_2SiO_3 in the ^{23}Na NMR spectrum due to two new disordered sodium environments. These two peaks slowly merge into one signal at -8.1 ppm after 160 minutes of milling while no significant change is detected for the resonance at 16.3 ppm. The intensity of the latter drops down sharply after 250 minutes of milling to be replaced by two sodium signals at -8.0 and 3.5 ppm due to the evolution of a new environment. Complete amorphization is observed after 450 minutes of grinding (a broad signal at -6.5 ppm with FWHM of 2600 Hz) with only traces of the original sodium environment from sodium metasilicate remaining. This is in harmony with fits to the IR spectra that show a delayed amorphization for the silicate sample. The amorphization of Na_2CO_3 is also a stepwise process associated with the sites of lower and then of higher symmetry. No changes are visible in the ^{23}Na NMR spectrum during the first 10 minutes of grinding. A spectrum recorded after 60 minutes of milling clearly showed a loss of local order for the nine-coordinate sodium. The amorphization of the octahedrally coordinated sodium which is related with broadening of the resonance at ca. 3.8 ppm requires about 150 minutes of milling. During the last step two resonances merge into one broad peak with a maximum at -6.5 ppm and a FWHM of 2900 Hz. The comparable FWHM and chemical shifts of the ^{23}Na spectra for aNaSiCC and aNaCC indicate that the amorphization is caused by disorder resulting from the incorporation of sodium cations into the calcium carbonate structure, as ionic radii of Na^+ and Ca^{2+} are similar (Ca^{2+}: 1.06 Å; Na^+: 0.98 Å).[59]

Structure of aNaCC and aNaSiCC. The short-range order of aNaSiCC and aNaCC was analyzed using X-ray total scattering. The reduced atomic pair distribution function (PDF) G(r) (Figure 3.4) represents the number of atoms in a spherical shell around a reference atom,[60] i.e., the absence of any maxima beyond 7 Å is compatible with a non-crystalline structure.[61,62] The termination ripples are due to Fourier termination effects resulting from the finite Q range.[60] While for aNaCC a maximum still appears at 6 Å, the PDF of aNaSiCC fades out after ~4.3 Å revealing even less structural coherence. A well-defined peak at 1.28 Å corresponds to the C-O separations of the carbonate units. The deviation to

the reported C-O distances of 1.25 Å in calcite[52] may be attributed to distortions resulting from the incorporation of different ions and deformation due to milling. The peak at 2.4 Å is associated with non-bonding O-O distances of the carbonate groups and a superposition of first Ca-O and Na-O atom pairs (Figure S3.1B,D).[63] The sharp maximum at 1.64 Å in aNaSiCC is associated with typical bond lengths of the tetrahedral SiO_4 units,[64] showing the incorporation of silicate groups in the amorphous intermediate. The difference in peak height for the signal at 2.34 Å and a small shoulder for aNaSiCC at 2.62 Å show different Ca-O and Na-O environments, as no silicate contributions are expected here. More pronounced differences at ~3.4 Å and 4.1 Å represent superpositions of several atom pairs, i.e., M-M, M-Si, M-C (M = Na, Ca) (Figure S3.1A,C).. As no sharp maximum appears in the region around 3.1 Å which is associated with interconnected SiO_4 units (Figure S3.1D). [65] it is assumed that only a broad distribution of Si-O-Si pairs is present in aNaSiCC with no preference for structural order as in crystalline silicates.

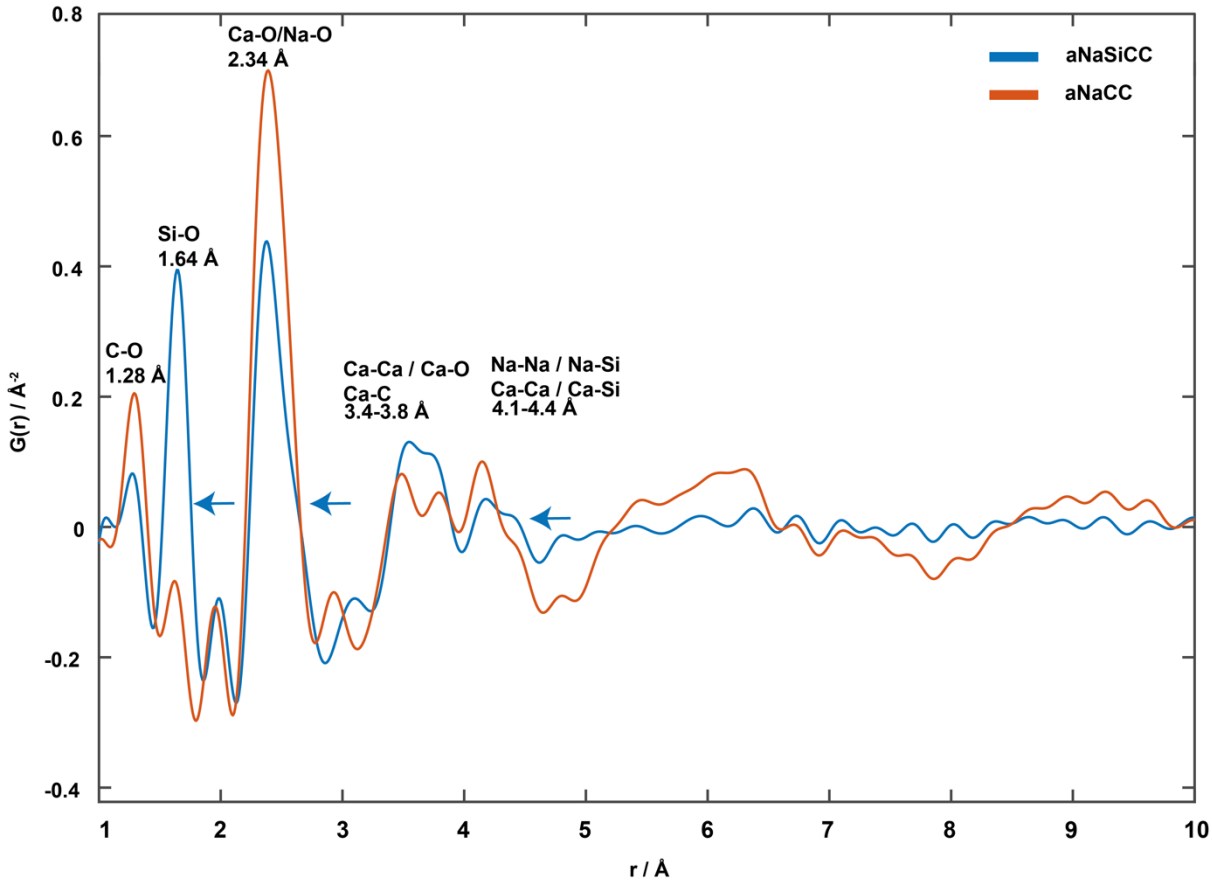

Figure 3.4. Reduced pair distribution function of aNaSiCC and aNaCC in the range from 1 to 10 Å. Blue arrows mark significant differences between aNaSiCC and aNaCC.

Hydration reaction

Carbonate Products. The effect of silicate on the reactivity of the sodium-calcium carbonate system was investigated in temperature- and water-induced reactions. Water in acetonitrile mixtures were used to control hydration kinetics by slowing down the reaction and mimic the reaction cascade illusttared in Figure 3.5.[43,66] Since the hydration rate depends on the water concentration, different water/acetonitrile mixtures were used to simulate the individual reaction steps starting from the amorphous precursors. They are referred to as the first, second and third hydration steps (corresponding to 5 %v, 10 %v and pure water, respectively). Crystallization of aNaCC in a 5%$_v$ H_2O/CH_3CN mixture led to the formation of pirssonite ($Na_2Ca(CO_3)_2 \times 2H_2O$) in an initial step, indicated by a pronounced splitting or broadening of the valence mode of the carbonate group (asymmetric stretch (ν_3): 1480 and 1390 cm^{-1}; symmetric stretch (ν_1): 1068 cm^{-1}) (Figure 3.5A).[67] Two additional signals at 3210 and 3064 cm^{-1} show the formation of O-H groups. For intermediate water concentrations (10%$_v$ H_2O/CH_3CN mixture) a sharp signal emerges at 1400 cm^{-1} (ν_3 mode), while the band at 1060 cm^{-1} (ν_1 mode) vanishes. Additional bands at 3325, 3257 and 2936 cm^{-1} (the regime characteristic for O-H vibrations) are compatible with the formation of gaylussite ($Na_2Ca(CO_3)_2 \times 5H_2O$).[68] For low and intermediate water concentrations (5%$_v$ and 10%$_v$ H_2O/CH_3CN) the recrystallization of aNaSiCC and aNaCC lead to similar results. However, when the recrystallization of aNaCC is carried out in an excess of water (or pure water) it proceeds directly to calcite, indicated by a single ν_3 band at 1410 cm^{-1} and a pronounced in-plane-deformation band (ν_4) at 714 cm^{-1}.[48] In contrast, the reaction of aNaSiCC in pure water leads to a product lacking the ν_4 band in the region of 700 cm^{-1}, whose IR spectrum exhibits a slight shoulder at 764 cm^{-1} and a sharp band at 3235 cm^{-1} (characteristic of O-H groups not involved in strong hydrogen bonding). Despite the absence of a characteristic splitting of this ν_3 vibration this is compatible with the formation of monohydrocalcite ($Ca(CO_3) \times H_2O$).[15,48] A magnified view of the IR spectra and a detailed assignment of the infrared modes are given in the Supporting Information.(Figure S3.2,Table S3.1). A detailed analysis of the changes in the silicate environment, based on ^{29}Si NMR and FTIR spectra, is given in the Supporting Information (Figure S3.3, Table S3.2).

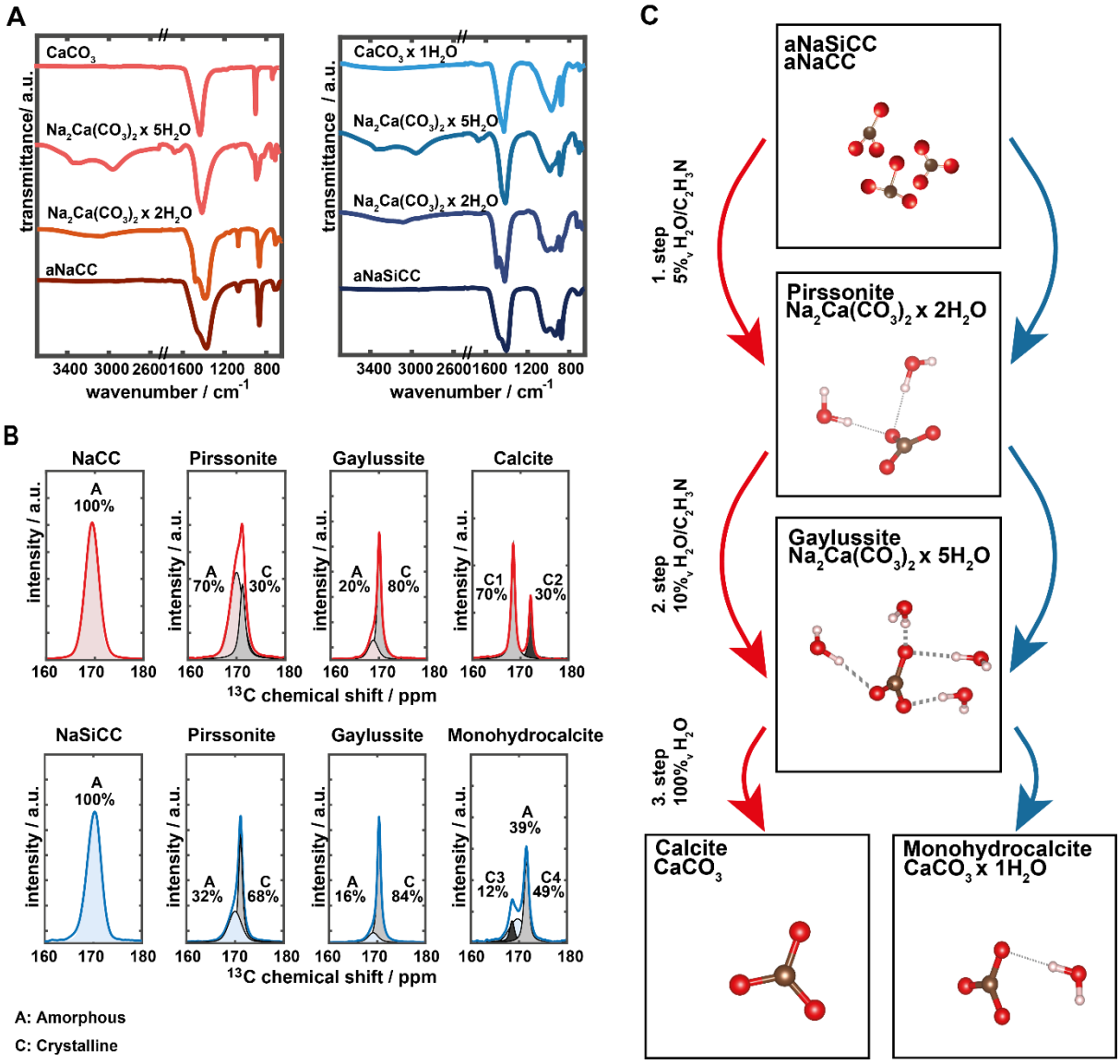

Figure 3.5. (A, B) Evolution of the FTIR and ^{13}C SP MAS-NMR spectra of aNaCC and aNaSiCC upon reaction with H_2O/CH_3CN mixtures. Red spectra represent products obtained from aNaCC, blue spectra correspond to products obtained from aNaSiCC. Kinetic control of the reactions was achieved with variable concentration of water. Low concentrations ($5\%_v$ H_2O/CH_3CN) lead to the formation of pirssonite ($Na_2Ca(CO_3)_2 \times 2H_2O$), intermediate concentrations ($10\%_v$ H_2O/CH_3CN) to the formation of gaylussite ($Na_2Ca(CO_3)_2 \times 5H_2O$). High concentrations of water lead to the formation of calcite for aNaCC, whereas monohydrocalcite was formed for NaSiCC. (C) Characteristic environments for the carbonate groups in the structures of aNaCC and aNaSiCC:pirssonite, gaylussite, monohydrocalcite and calcite. The amorphous phases aNaSiCC and aNaCC are assumed to contain a superposition of different carbonate environments with different point symmetries.

Different stages of the reaction were characterized by ^{13}C single pulse- (SP) (Figure 3.5B) and ^{13}C cross-polarization (CP) MAS NMR spectroscopy (Figure S3.4, S3.5, S3.6). The single pulse experiments were recorded with a long recycle delay to ensure complete relaxation and to facilitate quantitation. A single broad resonance was observed for aNaSiCC (chemical shift 170.16 ppm; FWHM 334 Hz) and aNaCC (chemical shift 169.4, FWHM 340 Hz) compatible with a broad distribution of different carbonate environments (*vide supra*).

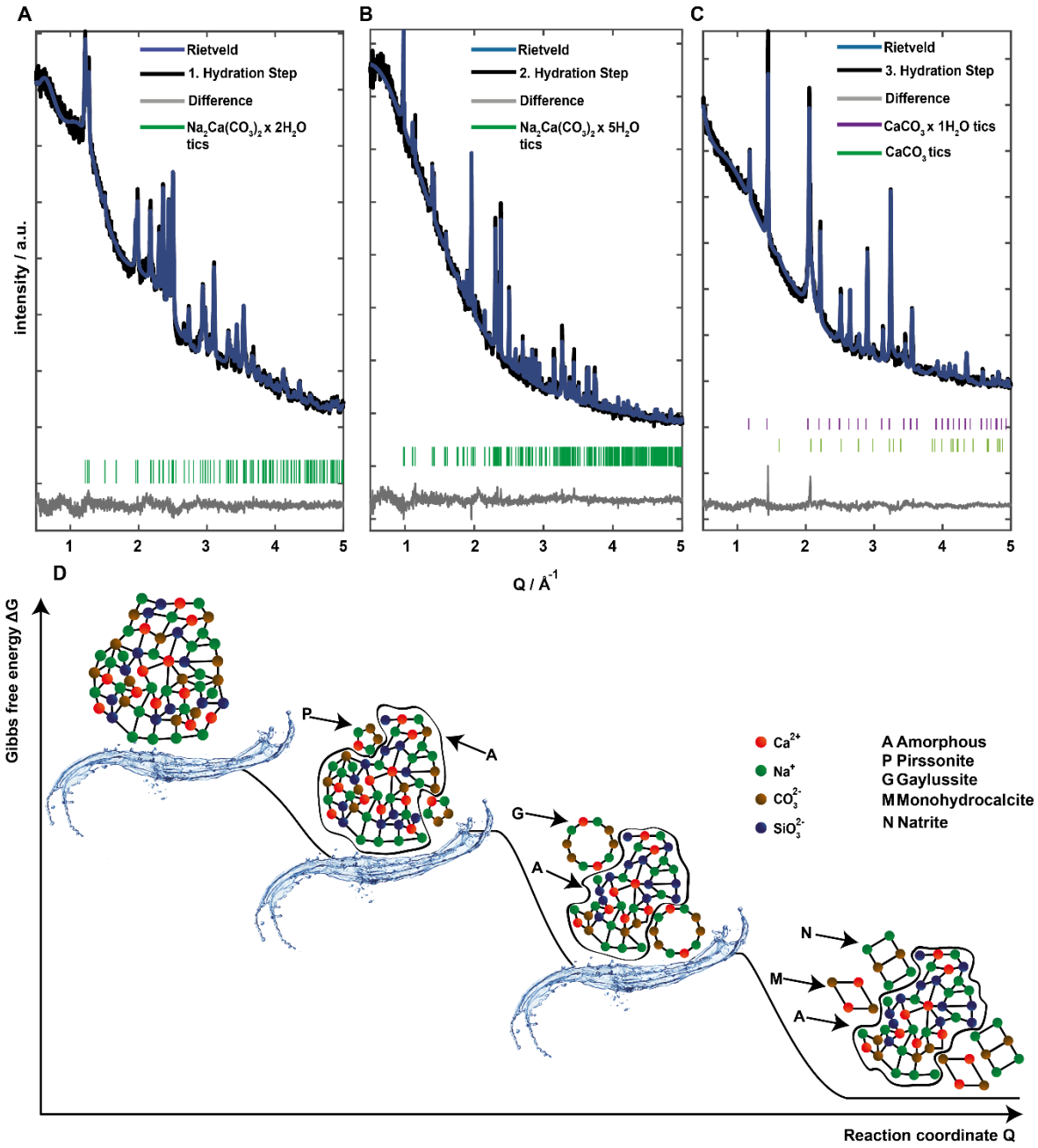

Figure 3.6. X-ray powder diffractograms showing the phase evolution during the hydration reaction of and aNaSiCC prepared by ball-milling. Kinetic control was achieved by lowering the water concentration with CH_3CN. Black lines show the experimental patterns, colored lines the Rietveld refinement. Gray line show the difference patterns, and green ticks indicate the calculated reflection positions of pirssonite (A), gaylussite (B) and monohydrocalcite (C).). (D) Schematic energy landscape for the hydration reaction of aNaSiCC via pirssonite and gaylussite to monohydrocalcite and natrite (γ-Na_2CO_3).

Incipient hydration led to less symmetric and narrower profiles. According to the results of FTIR and NMR spectroscopy, two different chemical environments are present. The minimum signal approach allows to subdivide the spectra into an amorphous and crystalline part. A sharp resonance at 171.2 ppm, which was assigned to crystalline pirssonite, appeared in the ^{13}C-NMR spectra of aNaCC (FWHM 134 Hz) and aNaSiCC (98 Hz) during the reaction with 5%$_v$ H_2O/CH_3CN. A signal at 170.4 ppm for aNaCC (FWHM 93Hz) and

aNaSiCC (FWHM 83 Hz) was observed for the second reaction step (10%$_v$ H_2O/CH_3CN) corresponding to gaylussite. A sharp resonance at 171.5 ppm (C2, FWHM 114 Hz) for the hydration reaction of aNaSiCC is compatible with the formation of monohydrocalcite[48] for the third reaction step (hydration in pure water), while the sharp resonance for the corresponding reaction of aNaCC at 168.4 ppm (C1, FWHM 81 Hz) is characteristic for calcite. In addition to calcite, a second crystalline environment was found at 172 ppm (C2, FWHM 90 Hz) in aNaCC, which is attributed to Na_2CO_3 (*vide infra*). A similar behavior was observed in aNaSiCC, where an additional amorphous phase at ~170 ppm was observed (Figure 3.5A). A resonance at 168.4 ppm (C3) is attributed to calcite, which is likely to be formed from metastable monohydrocalcite (C4). The evolution of crystalline phases due to hydration was confirmed by PXRD (Figure 3.6).

Sharp reflections formed with proceeding hydration (besides an X-ray amorphous background), which fitted none of the typical $CaCO_3$ polymorphs (i.e., vaterite, aragonite, calcite, monohydrocalcite). Pirssonite and gaylussite were identified as reaction products for the hydration of both, aNaCC and aNaSiCC, by Rietveld refinement.[69] using the *TOPAS* software package.[70] It was not possible to index the PXRD data of the last hydration step in aNaSiCC due to possible multiphasic mixture and broadened reflections. Therefore, three-dimensional electron diffraction (3D ED) was invoked because it allows structural analysis of crystals down to the nanoscale. The three-dimensional reconstruction of the 3D ED data, taken from a nanocrystal with ill-defined morphology (Figure S3.7), led to a trigonal unit cell (a = 6.129(6) Å, c = 7.443(3) Å, space group $P3_121/P3_221$, Z = 3) of $CaCO_3$ x H_2O. The relative thick crystal absorbed almost all of the weak superstructure reflections. Still, it was possible to obtain the first order in section *hk*3 (Figure 3.7). Nevertheless, by considering the dynamical scattering[71] it was first possible to obtain an inversion twinning and second to identify and refine the hydrogen position of the water molecule (R_{obs} = 9.87%, Table S3.5). Thus, it was clearly confirmed that the reflections in the PXRD diffractogram originate from monohydrocalcite[15] and an additional phase identified as natrite (γ-Na_2CO_3) by FTIR and ^{23}Na MAS NMR (Figure S3.8, S3.9 and S3.10) This allowed to elucidate the reaction pathway outlined in Figure 3.6D for the hydration reactions of aNaSiCC and aNaCC (Figure S3.11).

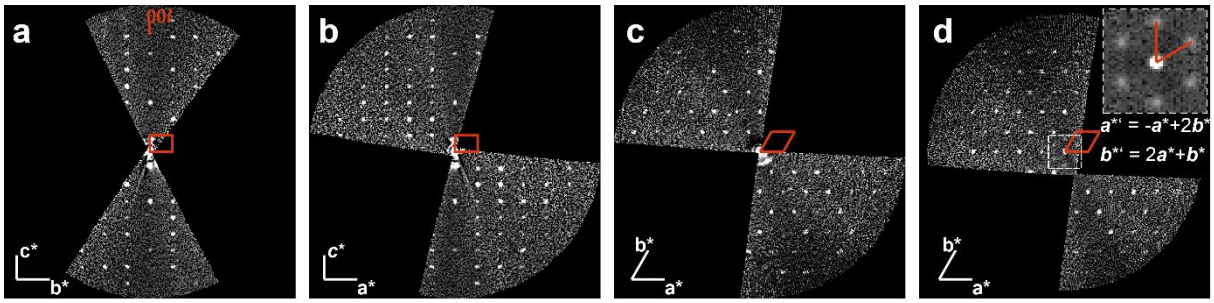

Figure 3.7. Reconstructed sections 0*kl*, *h*0*l*, 0*kl* and 3*kl* (a-d) of monohydrocalcite recorded with 3D ED at -176 °C. Weak superstructure reflections in section *3kl* are enlarged for clarity.

In summary, an amorphous precursor without long range order is formed in an "activation step" by ball-milling $CaCO_3$ and soda (Na_2CO_3) or $CaCO_3$ and sodium metasilicate (Na_2SiO_3). The presence of the ionic constituents in "molecular" dispersion allowed for reduced transport distances during crystallization and low activated reactions which are needed for kinetic control in the hydration process. A 100 mg quantity of the intermediates (aNaSiCC or aNaCC respectively) dissolved in 5 mL of a 5%$_v$ water/acetonitrile mixture formally corresponds to a concentration of 400 mg/mL. Due to the 1:1 ratio of the components in the milling procedure, the average molar masses for aNaSiCC and aNaCC are 222 g/mol and 206 g/mol, respectively. Assuming complete dissolution of aNaSiCC and aNaCC as a first approximation for simplicity, we obtain concentrations in the range of ~1.9 mol/l and local ionic strengths in the range of ~13, i.e., the solubility limits would be by far exceeded. Therefore, high local concentrations of Na^+, Ca^{2+} and CO_3^{2-} ions lead to the formation of metastable pirssonite and gaylussite during hydration.[68,72] The hydration reaction starts with the dissolution of aNaSiCC close to the particle surface (Figure 3.8B) and subsequent transport close to crystal surfaces respectively. This leads to high saturation levels of Na^+, Ca^{2+} and CO_3^{2-} ions (Figure 3.8C) and leads to new amorphous and crystalline environments by reversible dissolution/recrystallization processes (Figure 3.8D), indicated by differences in the proton signals and the relaxation times $T_{1\rho}^H$ in ^{13}C CP experiments due to differences in ^{13}C-^1H separations and ^1H mobility.(Figure S3.4, S3.5, S3.6, S3.12 and Table S3.3, S3.4). The reorganization of the silicate network is assumed to lead to differences observed in the TGA traces of aNaSiCC and aNaCC (Figure S3.13). Thermally induced crystallization of aNaCC and aNaSiCC show the reaction to nyerereite ($Na_2Ca(CO_3)_2$) and Na_2CaSiO_4 (Figure S3.14). The emergence of distinct morphologies in close proximity to amorphous domains was observed in TEM (Figure S3.15) and SEM (Figure S3.16), but electron diffraction experiments proved difficult due to the beam

sensitivity of the material, showing emerging changes in morphology and diffraction patterns (Figure S3.17). For rapid hydration (pure water), gaylussite transformed to calcite (for aNaCC, Figure S3.18) or monohydrocalcite (for aNaSiCC, Figure 3.8E, F). As Na_2CO_3 precipitates despite of its high solubility (30.7g Na_2CO_3/100g H_2O) (Figure S3.8) it is assumed to leach out after gaylussite formation from small cavities of the product, which hinders dissolution due to confinement (Figure S3.9, S3.10). Monohydrocalcite forms only from aNaSiCC, while calcite forms from aNaCC. This suggests that the silica environment has a directing effect on recrystallization and, similar to small amounts of foreign ions (Mg^{2+}, PO_4^{3-}) or macromolecules[73] affect polymorph selection of and local order in $CaCO_3$.[74]

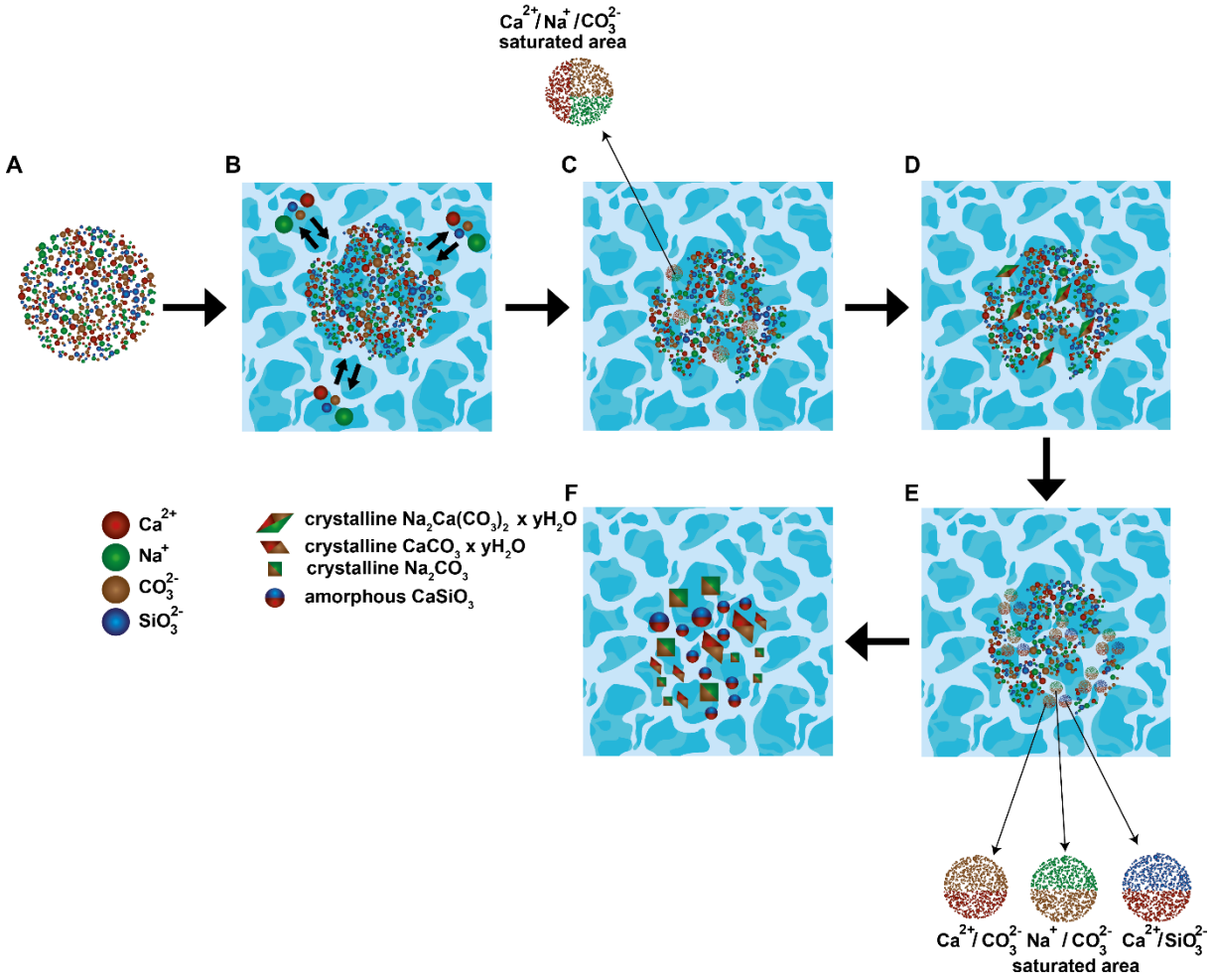

Figure 3.8. Possible hydration mechanism for aNaSiCC. (a) The amorphous activated precursor is brought into contact with a water/acetonitrile mixture. (b) Surface dissolution leads to areas of high supersaturation and partial reorganization. (c) Crystallization occurs in the areas of high supersaturation. High local concentrations and slow diffusion lead to metastable pirssonite ($Na_2Ca(CO_3)_2 \times 2H_2O$) initially and to gaylussite ($Na_2Ca(CO_3)_2 \times 5H_2O$) for longer reaction times. (d) Long contact with water leads to phase separation and formation of areas with high sodium/carbonate, calcium/carbonate and calcium/silicate concentrations, (e) leading to a mixture of Na_2CO_3, $CaCO_3 \times H_2O$ and non-crystalline Ca,(Na)SiO_3.

In nature, silicate in cystoliths is known to stabilize biogenic ACC.[75] Likewise, silicate has been used synthetically as passive "coating" to stabilize ACC,[34,35] while slow ion diffusion in silica gels[76,77] and the associated concentration gradients lead to the formation of monohydrocalcite even in the absence of Mg^{2+} cations. Multi-textured, self-organized monohydrocalcite was formed by temperature-controlled precipitation of $CaCO_3$ in silica.[78] In aNaSiCC, Na^+ and silicate ions are intimately mixed with $CaCO_3$ at a molecular scale. As monohydrocalcite was formed regardless of the hydration reaction, its formation may be related to a retarded crystallization process, similar to a coating of ACC by silicate, associated with the formation of non-crystalline calcium silicates (Figure S3.3).

Alkali-activation of aNaSiCC

aNaCC and aNaSiCC were activated with sodium hydroxide (Figure 3.9).[79] No changes were observed by FTIR for aNaCC (except the formation of small amounts of portlandite), but striking changes occurred in the silicate and carbonate characteristics for aNaSiCC. The decrease of the carbonate/silicate ratio compared to aNaSiCC and the occurrence of a vibration at 953 cm^{-1} which is attributed to a Q2 environment[80] strikingly resembles the C-S-H formation in coprecipitation experiments (Figure 3.9B).[81] In contrast to aNaSiCC, the X-ray powder diffractogram of the NaOH-activated sample showed reflections at 0.60, 2.06, and 2.26 Å, typical for C-S-H phases (Figure 3.9C). The reflection at the lowest Q value corresponds to the basal spacing and thus indicates 3D order.[82,83] Sheet- and fibril-like morphologies as in tobermorite were observed in TEM (Figure 3.9D). [84,85] The ^{29}Si MAS NMR spectrum showed two sharp resonances at -80.43 ppm (FWHM: 182 Hz) and -85.56 ppm (FWHM: 163 Hz) compatible with Q^1, Q^2 and Q^2b environments.[86,87] due to dreierketten silicate chains (Figure 3.9E). X-ray total scattering provided additional insight into the short-range order. A comparison of the reduced pair distribution function between aNaSiCC and NaOH-activated aNaSiCC shows pair correlations in the range of up to 30 Å, indicative of a medium-range order in the C-S-H-like phase (Figure 3.9F). Similar as in aNaSiCC, the maxima at 1.2 Å, 1.6 Å and 2.4 Å correspond to C-O, Si-O and M-O pairs,[88] where the C-O distance shows a slight shift to lower *r* values. Differences in peak profiles and intensities are linked to differences in the short-range order, i.e., the atom coordination numbers. In contrast to the amorphous aNaSiCC, a peak now occurs at 3.1 Å that correlates with a Si-Si pair, which can be attributed to Si-Si separations associated with the corner-sharing tetrahedra in the Dreierketten silicate structure. A comparison of aNaSiCC, as a starting material to CSH, with a reference of amorphous calcium silicate (aCS, Figure S3.19)before and after activation shows similar pair distribution functions for the starting materials, as well as the obtained C-S-H phases. A distinct difference is the pronounced pair-pair distance at 1.28 Å resulting from the included carbonate groups in aNaSiCC and alkali activated aNaSiCC. The sharp peak at 3.72 Å is attributed to the Ca-Si pair from the silica chain, which is adjacent to the central Ca-O layer. This separation becomes smaller in carbonated C-S-H, which was attributed to decalcification.[89] The material described here does not show such a behavior, although being carbonate-rich. This implies a new pathway to a C-S-H-like material by mechanochemical activation without preceding calcination of the calcium source. A previous study has shown that the activation of calcium carbonate with sodium silicate solutions leads to a mixture of C-S-H with high contents of

crystalline calcium carbonates results from a variety of dissolution and recrystallization processes.[7] The mechanochemical approach allows a new chemical approach, which is due to the different arrangement of the "molecular" building blocks in the activated amorphous precursor phase.

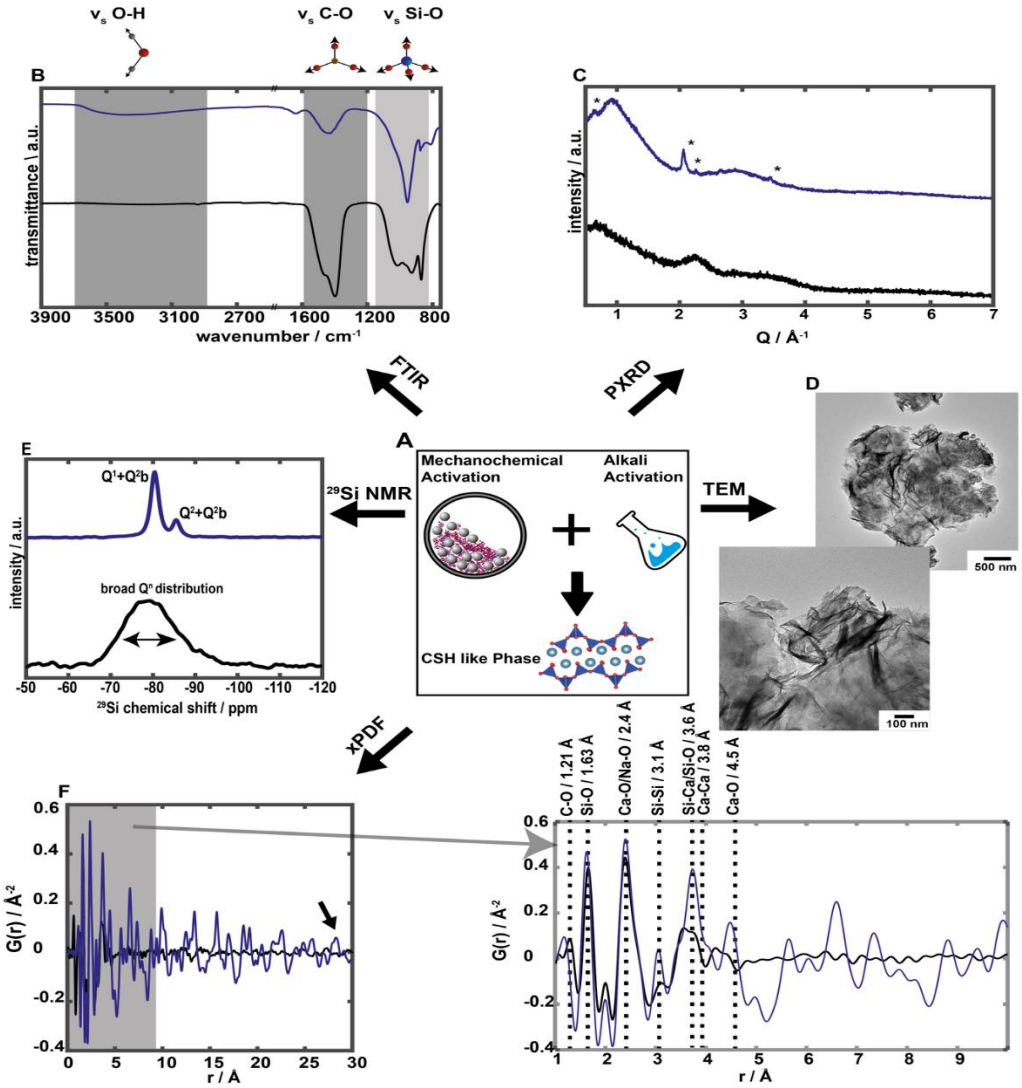

Figure 3.9. Preparation of the activated precursor aNaSiCC and structural characterization of aNaSiCC and NaOH-activated products. (A) Mechanochemical activation of $CaCO_3/Na_2CO_3$ and $CaCO_3/Na_2SiO_3$ mixtures by ball milling and chemical activation with sodium hydroxide. (B) FTIR spectra of aNaSiCC (black line) and NaOH-activated product (blue line). (C) X-ray powder diffractograms of aNaSiCC (black line) and NaOH-activated product (blue line) showing the virtually amorphous structure of the activated aNaSiCC precursor. The reflections at 0.60, 2.06, and 2.26 $Å^{-1}$ for the NaOH-activated product are typical for C-S-H phases. The reflection at 0.60 $Å^{-1}$ corresponds to the basal C-S-H spacing and indicates 3D order. (D) TEM image of NaOH-activated aNaSiCC with foil-like and fibrillary morphologies (E) ^{29}Si MAS NMR spectra of aNaSiCC (black line) and NaOH-activated product (blue line) with two sharp resonances at -80.43 ppm (FWHM: 182 Hz) and -85.56 ppm (FWHM: 163 Hz) indicating Q^1, Q^2 and Q^2b environments due to dreierketten silicate chains. The spectrum of aNaSiCC (black line) shows only one broad signal due to disorder. (F) Reduced pair distribution functions of aNaSiCC (black line) and NaOH-activated aNaSiCC (blue line). The PDF of aNaSiCC fades out beyond 4 Å. The NaOH-activated product shows pronounced signals up to 30 Å compatible with a C-S-H related structure having distinct silicate environments and medium range order.

3.4 Conclusion

Making alternative binders from available and cheap natural raw materials such as calcium carbonate or geopolymers/alkali activated binders is an environmentally friendly solution for sustainable development of building materials. Many natural raw materials contain several mineral phases often including calcium carbonates which define their reactivity. We have studied the salt metathesis reaction of calcium carbonate ($CaCO_3$) with solid sodium silicate (Na_2SiO_3) and its role for geopolymer/alkali-activated binders. High-temperature treatment and the associated CO_2 emissions can be avoided by a grinding activation step. The formation of the cement paste and the hydration reactions proceed *via* a complex cascade of non-equilibrium reactions before reaching thermodynamic equilibrium. An amorphous intermediate (aNaSiCC) of $CaCO_3$ and Na_2SiO_3 containing the ionic constituents in "molecular" dispersion is prepared in the ball-milling activation step. This allows for molecular transport pathways during hydration reactions and extremely low activated reactions, because the precipitation of solids from liquids, which is nucleation limited and kinetically controlled, and solid state transformations, which are diffusion limited and thermodynamically controlled, have almost equal weighting. Elementary steps of the hydration reaction could be resolved by a combination of FTIR and multinuclear MAS-NMR spectroscopy with automated electron diffraction tomography.

Ball milling typically leads to reactive defect-rich structures with poorly defined crystal domains that elude structural analysis using conventional diffraction methods. We show here that despite the challenges in the structure analysis of poorly crystalline nanomaterials, even fine structural details can be elucidated with 3D electron diffraction.

A multistep cascade of hydration reactions occurs starting from the amorphous aNaSiCC precursor *via* pirssonite ($Na_2Ca(CO_3)_2 \times 2H_2O$) and gaylussite ($Na_2Ca(CO_3)_2 \times 5H_2O$) to monohydrocalcite. Activation of aNaSiCC with a NaOH lead to a phase with structural similarity to C-S-H. The formation of pirssonite and gaylussite suggests that alkali metals are removed from the binder in water and promote the formation of a C-S-H phase containing some sodium. The used C/S ratio of ~ 1 is compatible with a defect *tobermorite* structure. Our results outline a possibility for cement production without CO_2 emissions at ambient temperature. High-temperature treatment and the associated CO_2 emissions can be circumvented by a simple grinding activation step. As grinding is a standard technique in the cement industry, this might allow industrial scale implementation. Limestone can be prepared by directly dissolving CO_2 from flue gas in water in a pressure separation plant

followed by injection for mineral storage.[90] Thus, our approach could even open up a possibility to produce cement by CO_2 fixation instead of CO_2 emissions.

3.5 Experimental section

Materials. Calcite (98%, Socal 31, Solvay), sodium carbonate (anhydrous 99.5%, Alfa Aesar), calcium carbonate-^{13}C (99 atom % ^{13}C, isotec), sodium metasilicate (~18 mesh, Alfa Aesar) cyclohexane (analytical reagent grade, Fisher Chemicals), calcium hydroxide (95%, Alfa Aesar), silica fumed powder (0.007µm, Sigma Aldrich) ethanol (absolute 99.8+%, Fisher Chemicals), acetonitrile (for HPLC, gradient grade, 99.9 %, Honeywell Riedel-de Haën) and doubly-deionized water (resistivity > 18mΩ cm).

Synthesis

Synthesis of amorphous sodium calcium carbonate (aNaSiCC). Sodium carbonate (0.257 g, 2.4 mmol) was treated with calcium carbonate (0.243 l g, 2.4 mmol) in a planetary ball mill (Pulverisette 7 Classic, Fritsch). The starting materials and 9 mL of cyclohexane were transferred together with 7.5 grams of grinding balls (about 2000 balls, 1 mm diameter, ZrO_2) into ZrO_2 grinding jars. The mixture was milled for 15 h at 720 rpm. To avoid overheating, alternate 10 minutes of grinding and then a 10 min rest phase was used. Therefore, 450 min of ball milling results in a reaction time of 900 min. Afterward, the cyclohexane was removed with a pipette. The product was dispersed in ethanol, separated from the grinding balls by decantation, then isolated by centrifugation and dried *in vacuo*.

Synthesis of amorphous sodium silicate calcium carbonate (aNaCC). Sodium metasilicate (0.243 g, 2.29 mmol) was treated with calcium carbonate (0.257 l g, 2.57 mmol) in a planetary ball mill (Pulverisette 7 Classic, Fritsch). The starting materials and 10 mL of cyclohexane were transferred together with 3.65 grams of grinding balls (about 1100 balls, 1 mm diameter, ZrO_2) into ZrO_2 grinding jars. The mixture was milled for 15 h at 720 rpm. To avoid overheating, intermittent grinding (10 min of grinding /10 min rest phase) was used. Therefore, 450 min of ball milling corresponds to a reaction time of 900 min. Cyclohexane was removed with a pipette after the reaction. The product was dispersed in ethanol, separated from the grinding balls by decantation, then isolated by centrifugation and dried *in vacuo* .

Synthesis of amorphous calcium silicate (aCS) Calcium hydroxide (0.277g, 3.7 mmol) was treated with fumed silica powder (0.233g, 3.7 mmol) in a planetary ball mill. (Pulverisette 7 Classic, Fritsch). The starting materials and 9 mL of cyclohexane were

transferred together with 7.5 grams of grinding balls (about 2000 balls, 1 mm diameter, ZrO_2) into ZrO_2 grinding jars. The mixture was milled for 3 h at 720 rpm. To avoid overheating, alternate 10 minutes of grinding and then a 10 min rest phase was used. Therefore, 180 min of ball milling results in a reaction time of 360 min. Afterward, the cyclohexane was removed with a pipette. The product was dispersed in ethanol, separated from the grinding balls by decantation, then isolated by centrifugation and dried *in vacuo*

Crystallization experiments. Crystallization experiments were carried out by adding 100 mg of aNaSiCC or aNaCC to solutions of 5%v or 10%v acetonitrile in water or pure water (resulting in concentrations of 20 mg/mL). To monitor crystallization *ex situ* at a given time 1 mL of the dispersion was transferred to a microreaction vessel containing 0.5 mL of acetone. After centrifugation, the liquid phase was decanted, washed with acetone again and dried *in vacuo*.

Characterization

X-ray Powder Diffraction. X-ray diffractograms were recorded with a STOE Stadi P equipped with a Mythen 1k detector using Mo $K\alpha_1$ radiation (λ=0.7093 Å). The dry samples were prepared between polyvinyl acetate foils in perfluoroether (Fomblin Y, Aldrich). The measurements were performed in the 2θ range from 2° to 45° with a step size of 0.015° (continuous scan, 150 s/deg). Crystalline phases were identified with the PDF-2 database using Bruker AXS.

ATR-FTIR Spectroscopy. Attenuated total reflection (ATR) FTIR spectra were recorded on a Nicolet iS10 spectrometer (Thermo scientific) in the frequency range from 550 to 4000 cm^{-1} with a resolution of 1.4 cm^{-1} per data point.

Solid-State NMR Spectroscopy. All solid state NMR spectra were recorded on a Bruker Advance 400 DSX NMR spectrometer (Bruker BioSpin GmbH, Rheinstteten, Germany operated by Topspin 1.3, 2007, patchlevel 8) at a ^{1}H frequency of 399.87 MHz, ^{13}C frequency of 100.55 MHz and ^{31}P frequency of 161.87 MHz. A commercial 3 channel 4 mm Bruker probe head at 10 kHz magic angle spinning (MAS) was used for all experiments. The ^{1}H NMR spectra and ^{1}H background corrected spectra were recorded averaging 32 transients with 8 s recycle delay. For all solid-state ^{13}C cross-polarization (CP) magic angle spinning (MAS) NMR experiments, an initial 90° pulse with 4.0 μs length and 5 s recycle delay were used. A ramped CP pulse (from 64 to 100%) with duration of 20 μs, 50 μs, 100 μs, 200 μs, 500 μs, 1 ms, 2 ms, 3 ms, 5 ms and 7 ms was used for recording the

CP build-up curves. Two pulse phase modulation (TPPM) ^{1}H decoupling scheme was used while acquiring the ^{13}C signal. 512 transients were averaged for the CP experiments. The spectra were baseline-corrected, and a broadening of 60 Hz was applied. Quantitative ^{13}C single pulse excitation experiments allowing full relaxation were recorded by averaging 16 transients with a recycle delay of 2200 s and TPPM heteronuclear decoupling. Spectral deconvolution was performed using self-written MatLab scripts (version 2017b).

Thermal Analysis. Coupled thermogravimetry-differential thermal analysis (TG-DTA) was carried out on a Netzsch STA 449 F3 Jupiter device. About 10 mg of the sample was heated in an alumina cup in argon atmosphere from 50 to 650 °C at a heating rate of 10 K/min.

Transmission Electron Microscopy (TEM) Imaging and simple diffraction measurements were acquired on a FEI Tecnai G" Spirit microscope operating at 120 kV (LaB_6 filament), equipped with a Gatan US1000 CCD-camera (16-bit, 2048 x 2048 pixels). Samples were prepared by placing one drop (15 µl) of a diluted nanoparticle dispersion in ethanol on a carbon-coated copper grid and letting it dry at room temperature. 3D ED measurement of monohydrocalcite was carried out with a transmission electron microscope (TEM) FEI Tecnai F30 S-TWIN equipped with a field emission gun (300 kV). The powdered sample was dispersed in ethanol using an ultrasonic bath and sprayed on carbon-coated copper grid using an ultra sound sonifier[91] TEM images and electron diffraction (ED) patterns were acquired with a Gatan UltraScan4000 CCD camera (16-bit, 4096 x 4096 pixel) at hardware-binning of 4. Scanning transmission electron microscopy (STEM) images were collected by a FISCHIONE high-angular annular dark field (HAADF) detector and acquired by Emispec ES Vision software. Three-dimensional electron diffraction data were collected using the acquisition module Fast-ADT (FADT) developed for FEI and JEOL microscopes[92]A condenser aperture of 10 µm and mild illumination settings (gun lens 8, spot size 6) were used in order to produce a semi-parallel beam of 520 nm in diameter (0.12 $e^-/Å^2s$). Crystal position tracking was performed in microprobe STEM mode. For tilt experiments acquisitions were performed with a Gatan cryo-transfer tomography holder. Prior to the measurements the sample and the stage were cooled under cryogenic conditions. The ED data were collected on both TEMs with electron beam precession (precession electron diffraction, PED) to improve reflection intensity integration quality.[93,94] PED was performed using a Digistar unit developed by NanoMEGAS SPRL. The precession angle was kept at 1.0°. The PETS2.0 software package was used for 3D electron diffraction data processing.[95] Difference Fourier mapping and least-squares (dynamical) refinement were

performed with the software JANA2006.[96] U_{iso} of the atomic sites C1, O1, O2 and O3 were kept to be the same.

X-Ray Total Scattering for Pair Distribution Function Analysis. To obtain structural information about the short range order X-ray total scattering for pair distribution function (PDF) analysis was performed with data acquired from Beamline 11-ID-B of the Advanced Photon Source (APS, Argonne, Il). An incident photon energy of 58.6 keV (λ = 0.2115 Å) was used, and the samples were measured in transmission through a 3 mm polyimide (Kapton) capillary with a sample-to-detector distance of 158 mm. The scattering patterns were measured using an amorphous Si Perkin Elmer detector system (2048 x 2048 pixels, 200 × 200 μm^2 pixel size). To calibrate the sample-to-detector distance, tilt and pitch relative to the incident beam path a CeO_2 standard was used for calibration. The obtained two-dimensional scattering data was integrated from 0.5 to 24 $Å^{-1}$ in GSAS-II to produce on-dimensional scattering profiles.[97] PDFgetX3 was used to process the experimental total scattering data.[98]

Corrections such as background subtraction (by measuring the empty Kapton tube), contributions from incoherent scattering and corrections for nonlinear detector efficiency or normalization by the average atomic scattering cross section of the sample were applied using this software. The stoichiometric compositions of the amorphous materials, $Na_2Ca(CO_3)_2$ in aNaCC and $Na_2Ca(SiO_3)(CO_3)$ in aNaSiCC, were used for data normalization.

3.6 References

[1] R. Andrew, *Earth Syst. Sci. Data*, **2018**, *10* 195-217.
[2] E. Gartner, H. Hirao, *Cem. Concr. Res*., **2015**,*78*, 126-142.
[3] J. L.Provis, *Cem. Concr. Res*., **2018**,*114*, 40-48.
[4] X. Ouyang, D.A. Koleva, G. Ye, K. v. Breugel, *Mater. Struct.,* **2017**, *50*, 213.
[5] H.Niu, M. Abdulkareem, H. Sreenivasan, A.M. Kantola, J. Havukainen, M. Horttanaien, V.-V. Telkki, P. Kinnunen, M. Illikainen, *Miner. Eng.*, **2020**, *157*, 106535.
[6] D. E. Ortega-Zavala, J. L. Santana-Carrillo, O. Burciaga-Díaz, J. I. Escalante-García, *Cem. Concr. Res.,* **2019**, *120*, 267-278.
[7] R. Firdous, T. Hirsch, D. Klimm, B. Lothenbach, D. Stephan, *Miner. Eng.,* **2021**, *165*, 106849.
[8] W. A. Gutteridge, J. A. Dalziel, *Cem. Concr. Res.,* **1990**, *20*, 778-782.
[9] M. Cyr, P. Lawrence, E. Ringot, *Cem. Concr. Res.,* **2005**, *35*, 719-730.
[10] E. Berodier, K. Scrivener, *J. Am. Ceram. Soc.,* **2014**, *97*, 3764-3773.
[11] T. Matschei, B. Lothenbach, F. P. Glasser, *Cem. Concr. Res.*, **2007**, *37*, 551-558.
[12] F. C. Meldrum, *Int. Mater. Rev.*, **2003**, *48*, 187-224.
[13] J. W. Morse, R. S. Arvidson, A. Lüttge, *Chem. Rev.*, **2007**, *107*, 342-381.
[14] K.-F. Hesse, H. Küppers, *Z. Kristallogr.*, **1983**, *163*, 227-231.
[15] H. Effenberger, *Monatsh. Chem.*, **1981**, *112*, 899-909.
[16] Z. Zou, W. J. E. M. Habraken, G. Matveeva, A. C. S. Jensen, L. Bertinetti, M. A. Hood, C-Y Sun, P. U. P. A. Gilbert, I. Polishchuk, B. Pokroy, J. Mahamid, Y. Pliti, S. Weiner, P. Werner, S. Bette, R. Dinnebier, U. Kolb, E. Zolotoyabko, P. Fratzl, *Science*, **2019**, *363*, 396-400.
[17] L. Addadi, S. Raz, S.Weiner, *Adv. Mater.,* **2003**, *15*, 959-970.
[18] D. Gebauer, M. Kellermeier, J. D. Gale, L. Bergström, H. Cölfen, *Chem. Soc. Rev.,,* **2014***, 43,* 2348-2371.
[19] J. J. D. Yoreo, P. U. P. A. Gilbert, N. A. J. M. Sommerdijk, R. L. Penn, S. Whitelam, D. Joester, H. Zhang, J. D. Rimer, A. Navrotsky, J. F. Banfield, A. F. Wallace, F. M. Michel, F. C. Meldrum. H. Cölfen, P. M. Dove, *Science*, **2015**, *349*, 1-9.
[20] N. T. K. Thanh, N. Maclean, S. Mahiddine, *Chem. Rev.,* **2014**, *114*, 7610-7630.
[21] J. Lee, J. Yang, S. G. Kwon, T. Hyeon, *Nat. Rev. Mat.*, **2016**, *1*, 16034.
[22] L. B. Gower, D. J. Odom, *J. Cryst. Growth.,* **2010***, 4*, 719-734.
[23] D. Gebauer, A. Völkel, H. Cölfen, *Science*, **2008**, *322*, 1819-1822.
[24] S. E. Wolf, J. Leiterer, M. Kappl, F. Emmerling, W. Tremel, *J. Am. Chem. Soc.*, **2008**, *130*, 12342-12347.
[25] S. E. Wolf, J. Leiterer, V. Pipich, R. Barrea, F. Emmerling, W. Tremel, *J. Am. Chem. Soc.,* **2011**, *133*, 12642-12649.
[26] Y. U. T. Gong, C. E. Killian, I. C. Olson, N. P. Appathurai, A. L. Amasino, M. C. Martin, L. J. Holt, F. H. Wilt, P. U. P. A. Gilbert, *Proc. Natl. Acad. Sci. U.S.A.,* **2012**, *109*, 6088-6093.
[27] D. J. Tobler, J. D. Rodriguez-Blanco, K. Dideriksen, N. Bovet, K. K. Sand, S. L. S. Stipp, *Adv. Funct. Mater.*, **2015**, *25*, 3081-3090.
[28] C. Günther, A. Becker, G. Wolf, M. Epple, *Z. Anorg. Allg. Chem.*, **2005**, *631*, 2830-2835.
[29] D. Pontoni, J. Bolze, N. Dingenouts, T. Narayanan, M. Ballauff, *J. Phys. Chem. B.*, **2003**, *107*, 5123-5125.
[30] J.-D. Rodriguez-Blanco, S. Shaw, L. G. Benning, *Nanoscale*, **2011**, *3*, 265-271.
[31] P. Bots, L. G. Benning. J.-D. Rodriguez-Blanco, T. Roncal-Herrero, S. Shaw, *Cryst. Growth. Des.*, **2012**, *12*, 3806-3814.

[32] M. Dietzsch, I. Andrusenko, R. Branscheid, F. Emmerling, U. Kolb, W. Tremel, *Z. Kristallogr.*, **2016**, *232*, 255-265.
[33] M. Kellermeier, D. Gebauer, E. Melero-García, M. Drechsler, Y. Talon, L. Kienie, H. Cölfen, J. M. García-Ruiz, W. Kunz, *Adv. Funct. Mat.*, **2012**, *22*, 4301-4311.
[34] J. Ihli, W. C. Wong, E. H. Noel, Y-Y. Kim, A. N. Kulark, H. K. Christenson, M. J. Duer, F. C. Meldrum, *Nat. Comm.*, **2014**, *5*, 3169.
[35] M. Kellermeier, E. Melero-Garcia, F. Glaab, R. Klein, M. Drechsler,R. Rachel, J. M. Garcia-Ruiz, W. Kunz, *J. Am. Chem. Soc.*, **2010**, *132*, 17859-17866.
[36] S. Sjöberg, *J. Non-Cryst. Solids*, **1996**,*196*, 51-57.
[37] M. Kellermeier, F. Glaab, R. Klein, E. Melero-García, W. Kunz, J. M. García-Ruiz, *Nanoscale*, **2013**, *5*, 7054-7065.
[38] H. Schäfer, *Angew. Chem. Int. Ed.*, **1971**, *10*, 43-50.
[39] A. Stein, S. W. Keller, T. E. Mallouk, *Science*, **1993**, *259*, 1558-1564.
[40] S. Leukel, M. Panthöfer, M. Mondeshki, G. Kieslich, Y. Wu, N. Krautwurst, W. Tremel, *Chem. Mater*, **2018**, *30*, 6040-6052.
[41] P. Opitz, M. P. Asta, A. Fernandez-Martinez, M. Panthöfer, A. Kabelitz, F. Emmerling, M. Mondeshki, W. Tremel, *Cryst- Growth Des.*, **2020**, *10*, 6831-6846.
[42] S. R. Bauers, S. R. Wood, K. M. Ø. Jensen, A. B. Blichfeld, B. B. Iversen, S. J. L. Billinge, D. C. Johnson, *J. Am. Chem. Soc.*, **2015**, *137*, 9652-9658. .
[43] S. Leukel, W. Tremel, *Cryst. Growth Des.*,**2018**, *18*, 4662-4670
[44] S. Kirkpatrick, C. D. Gelatt, Jr., M. P. Vecchi, *Science*, **1983**, *220*, 671-680.
[45] D. A. Kulik, *Cem. Conc. Res.*, **2011**, *41*, 477-495.
[46] I. G. Richardson, *Cem. Conc. Res.,* **2008**, *38*, 137-158.
[47] L. Zedler, M. Hager, U. Schubert, M. J. Harrington, M. Schmitt, J. Popp, B. Dietzek, *Mater. Today*, **2014**, *17*, 57-69.
[48] H. Nebel, M. Neumann, C. Mayer, M. Epple, *Inorg. Chem.,* **2008**, *47*, 7874-7879.
[49] H. Liu, S. Ho Hahn, M. Ren, M. Thiruvillamalai, T. M. Gross, J. Du, A. C. T. v. Duin, S. H. Kim, *J. Am. Ceram. Soc.*, **2020**, *103*, 3575-3589.
[50] E. Dowty, *Phys. Chem. Min.*, **1987**, *14*, 80-93.
[51] H. Eckert, *J. Sol-Gel Sci. Technol.*, **2018**, *88*, 263-295
[52] H. Sitepu, B. H. O'Connor, D. Li, *J. Appl. Crystallogr.*, **2005**, *38*, 158-167.
[53] Ž. Čančarevič, J. C. Schön, M. Jansen, *Z. anorg. Allg. Chem.*, **2006**, *632*, 1437-1448.
[54] A. R. Jones, R. Winter, G. N. Greaves, I. H. Smith, *J. Phys. Chem. B.*, **2005**, *49*, 23154-23161.
[55] H. Koller, G. Engelhardt, A. O. M. Kentgens, J. Sauer, *J. Phys. Chem.*, **2002**, *6*, 1544-1551.
[56] W. S. McDonald, D. W. J. Crucikshank, *Acta Cryst.*, **1967**, *22*, 37-43.
[57] M. Dusek, G. Chapuis, M. Meyer, V. Petricek, *Acta Crystallogr. B.,***2003**, *B59*, 337-352.
[58] A. M. George, S. Sen, J. F. Stebbins, *Solid State Nucl. Magn. Reson.*, **1997**, *10*, 9-17.
[59] V. M. Goldschmidt, *Sci. Nat.*, **1926**, *14*, 477-485.
[60] T. Egami, S. J. Billinge, *Underneath the Bragg Peaks*. London: Pergamon, 2003.
[61] H.-W. Wang, L. L Daemen, M. C. Cheshire, M. K Kidder, A. G. Stack, L. F. Allard, J. Neuefeind, D. Olds, J. Liu, K. Page, *Chem. Comm.*, **2017**, *20*, 2942-2945.
[62] J. Huang, J. D. Blakemore, D. Fazi, O. Kokhan, N. D. Schley, R. H. Crabtree, G. W. Brudvig, D. M. Tiede, *Phys. Chem. Chem. Phys.*, **2014**, *5*, 1814-1819.
[63] H-W. Wang, L. L. Daemen, M. C.Cheshire, M. K. Kidder, A. G. Stack, L. F. Allard, J. Neuefeind, D. Olds, J. Lie, K. Page, *Chen. Comm.*, **2017**, *20*, 2942-2945
[64] M. G. Tucker, M. T. Dove, D. A. Keen, *J. Phys.: Condens. Matter*; **2000**, *12*, 425-430.

[65] S. Bae, H. Jee, H. Suh, M. Kanematsu, A. Shiro, A. Machida, T. Watanuki, S. Morooka, G. Geng, H. Suzuki, *Constr. Build. Mater*, **2020**, *237*, 117714.
[66] F. Manoli, E. Dalas, *J. Cryst. Growth*, **2000**, *218*, 359-364.
[67] H. H. Adler, P. F. Kerr, *Am. Min.*, **1963**, 839-853.
[68] C. R. Bury, R. Redd, *J. Chem. Soc.*, **1933**, *0*, 1160-1162
[69] H. M. Rietveld, *Z. Kristallogr.*, **2010**, 12, 545-547
[70] A. A. Coelho, *J. Appl. Cryst.*, **2018**, *51*, 210-218.
[71] L. Palatinus, P. Brázda, P. Boullay, O. Perez, M. Klementová, S. Petit, V. Eigner, M. Zaarour, S. Mintova, *Science*, **2017**, *355*, 166-169
[72] F. E. Littman, H. J. Gaspari, *Ind. Eng. Chem. Res*, **1956**, *, 48*, 408-410.
[73] M. Balz, H.A. Therese, J. Li, J.S. Gutmann, M. Kappl, L. Nasdala, W. Hofmeister, H.-J. Butt, W. Tremel, *Adv. Funct. Mater*., **2005**, *15*, 683-688.
[74] . F. Natalio, T. Coralles, M. Panthöfer, I. Lieberwirth, D. Schollmeyer, W.E.G. Müller, M. Kappl, H.-J. Butt, W. Tremel, *Science* **2013**, *339*, 1298-1302.
[75] A. Gal, S. Weiner, L. Addadi, *J. Am. Chem. Soc.*, **2010**, *132*, 13208-13211.
[76] G. Zhang, J. M. Delgado-López, D. Choquesillo-Lazarte, J. M. García-Ruiz, *CrystEngComm.*, **2013**, *15*, 6526-6532.
[77] J. W. McCauley, R. Roy, *Am. Min.*, **1974**, *59*, 947-963.
[78] G. Zhang, C. Verdugo-Escamilla, D. Choquesillo-Lazarte, J. M. García-Ruiz, *Nat. Comm.*, **2018**, *9,* 5221
[79] F. Pacheco-Torgal, J. Castro-Gomes, S. Jalali; *Constr. Build. Mater.,***2008**, *22*, 1315-1322.
[80] P. Yu, R. J. Kirkpatrick, B. Poe, P. F. McMilan, X. Cong, *J. Am. Ceram. Soc.*, **1999**, *82*, 742-748.
[81] S. Steiner, B. Lothenbach, T. Proske, A. Borgschulte, F. Winnefeld, *Cem. Conc. Res.*, **2020**, *135*, 106116.
[82] E. T. Rodriguez, K. Garbev, D. Merz, L. Black, I. G. Richardson, *Cem. Conc. Res.*, **2017**, *93*, 45-56.
[83] K. Garbev, G. Beuchle, M. Bornefeld, L. Black, P. Stemmermann, *J. Am. Ceram. Soc.*, **2008**, *91*, 3005-3014.
[84] I. G. Richardson; *Cem. Conc. Res.*, **2004**, *34*, 1733-1777.
[85] H. Li, T. Du, H. Xiao, Q. Zhang, *J. Am. Ceram. Soc.*, **2017**, *100*, 3227-3238.
[86] X. Cong, J. Kirkpatrick; *Adv. Cem. Based. Mater.*, **1996**, *3*, 144-156.
[87] I. G. Richardson, J. Skibstedt, L. Black, R. J. Kirkpatrick, *Adv. Cem. Res,* **2010**, *22*, 233-24.,
[88] S. Grangeon, A. Fernandez-Martinez, A. Baronnet, N. Marty, A. Poulain, E. Elkaïm, Cédric Roosz, G. P. Henocq, F. Claret, *J. Appl. Cryst.*, **2017**, *50*, 14-21.
[89] A. E. Morandeau, C. E. White, *J. Mater. Chem. A.*, **2015**, *16*, 8597-8605.
[90] S. Ó. Snæbjörnsdóttir, B. Sigfússon, C. Marieni, D. Goldberg, S. R. Gislason, E. H. Oelkers, *Nat. Rev. Earth Environ*. **2020**, *1*, 90-102
[91] E. Mugnaioli, T. Gorelik, U. Kolb, *Ultramicroscopy,* **2009**, *109*, 758-765
[92] S. Plana-Ruiz, Y. Krysiak, J. Portillo, E. Alig, S. Estradé, F. Peiró, U. Kolb, *Ultramicroscopy,* **2020**, *211*, 112951
[93] R. Vincent, P. A. Midgley, *Ultramicroscopy*, **1994**, *53*, 271-282
[94] E. Mugnaioli, U. Kolb, *Ultramicroscopy,* **2009**, *109*, 758-765
[95] L. Palatinus, P. Brázda, M. Jelínek, J. Hrdá, G. Steciuk, M. Klementová, *Acta Cryst. B*, **2019**, *75*, 512-522
[96] V. *Petříček, M. Dušek*, L. Palatinus, Z. Krisallogr., **2014**, 229, 345-352
[97] B. H. Toby, R. B. Von Dreele, J. *Appl. Cryst.*, **2012**, *46*, 544-549.
[98] P. Juhás, T. Davis, C. L. Farrow, S. J. L. Billinge, *J. Appl. Cryst.*, **2013**, *46*, 560-566.

3.7 Supporting information

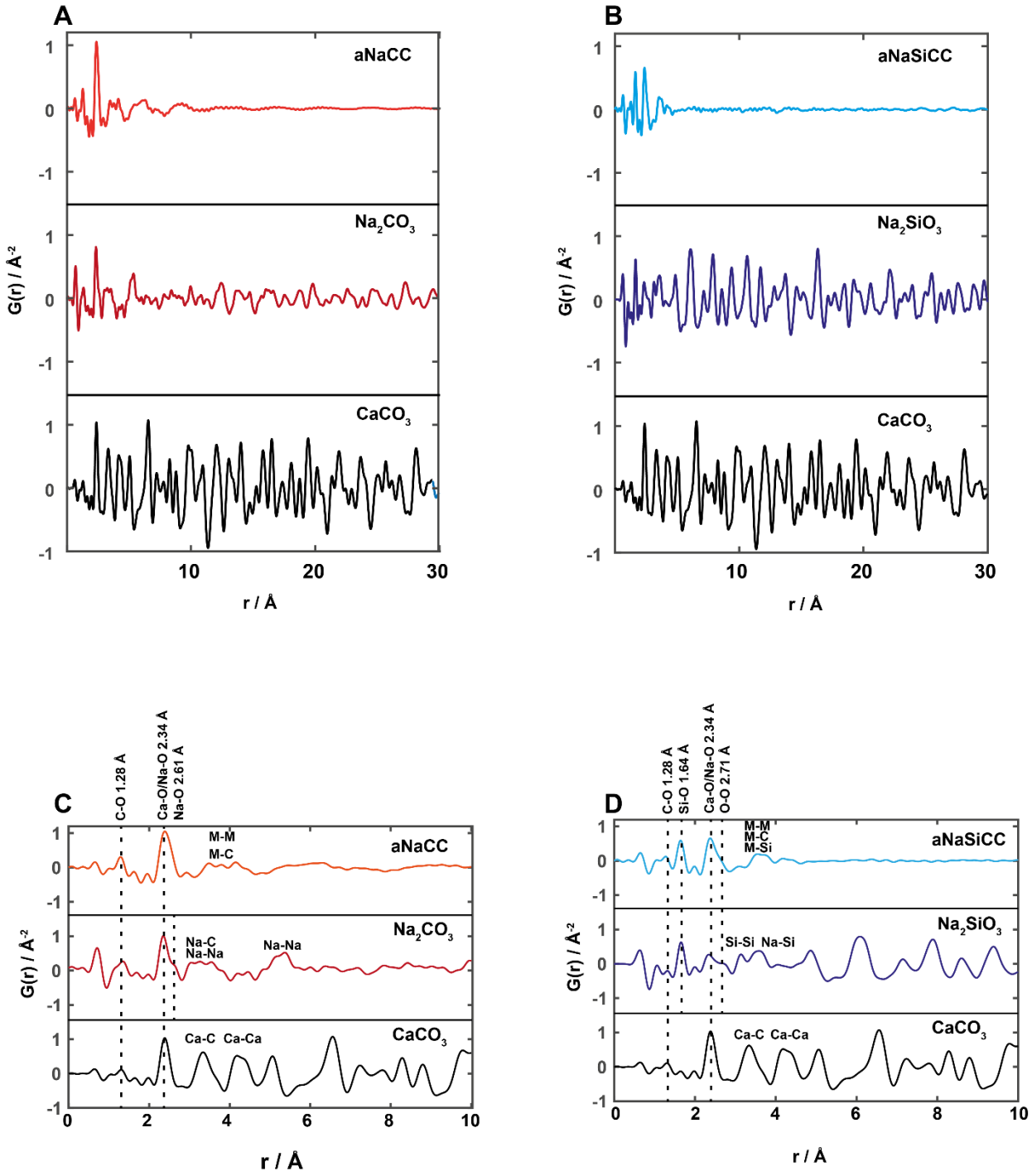

Figure S3.1. Reduced pair distribution functions in the range from 0 to 30 Å (A, B) of amorphous aNaCC (red line) and aNiSiCC (blue line) resulting from the starting materials $CaCO_3/Na_2CO_3$ and $CaCO_3/Na_2SiO_3$ by ball-milling. The range between 0 and 10 Å for aNaCC (red line) and aNiSiCC (blue line) and the starting materials $CaCO_3/Na_2CO_3$ and $CaCO_3/Na_2SiO_3$ is shown in C and D.

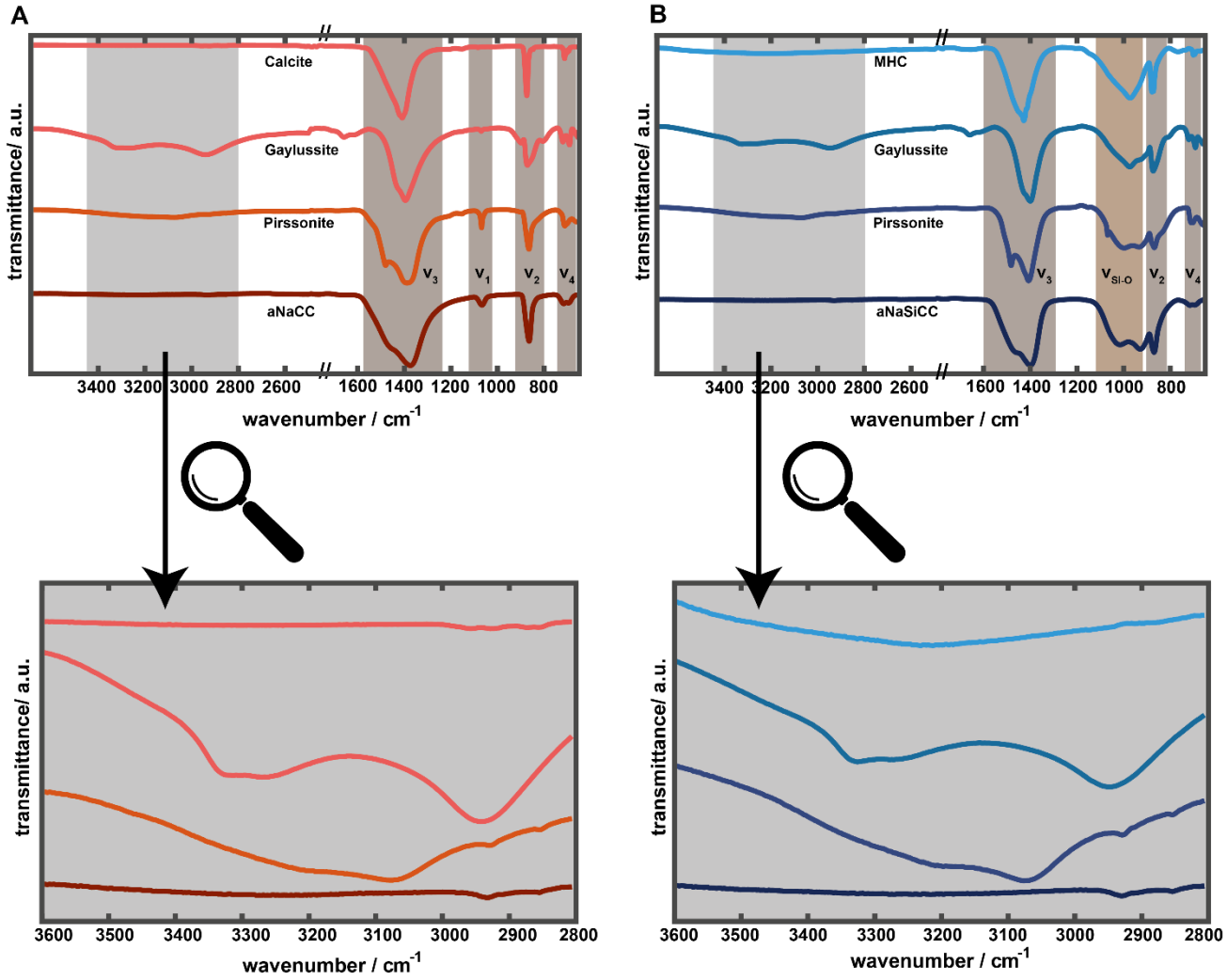

Figure S3.2. Evolution of the FTIR spectra for the products of the hydration reaction of the activated intermediates aNaCC (A) and aNaSiCC (B). The magnified spectra show the valence oscillations of the hydroxyl groups with hydrogen bonds. In the range of occur 2800 cm^{-1} to 3000 cm^{-1} more weak bands appear, which are due to the C-H valence vibrations of the dispersion medium cyclohexane during the milling reaction and the acetonitrile/water mixture for the controlled hydration end reaction. Spectra (drawn in red) show products of the hydration reaction of aNaCC. Spectra (drawn in blue) show products of the hydration reaction of aNaCC. The color depth encodes the time course of the reactions.

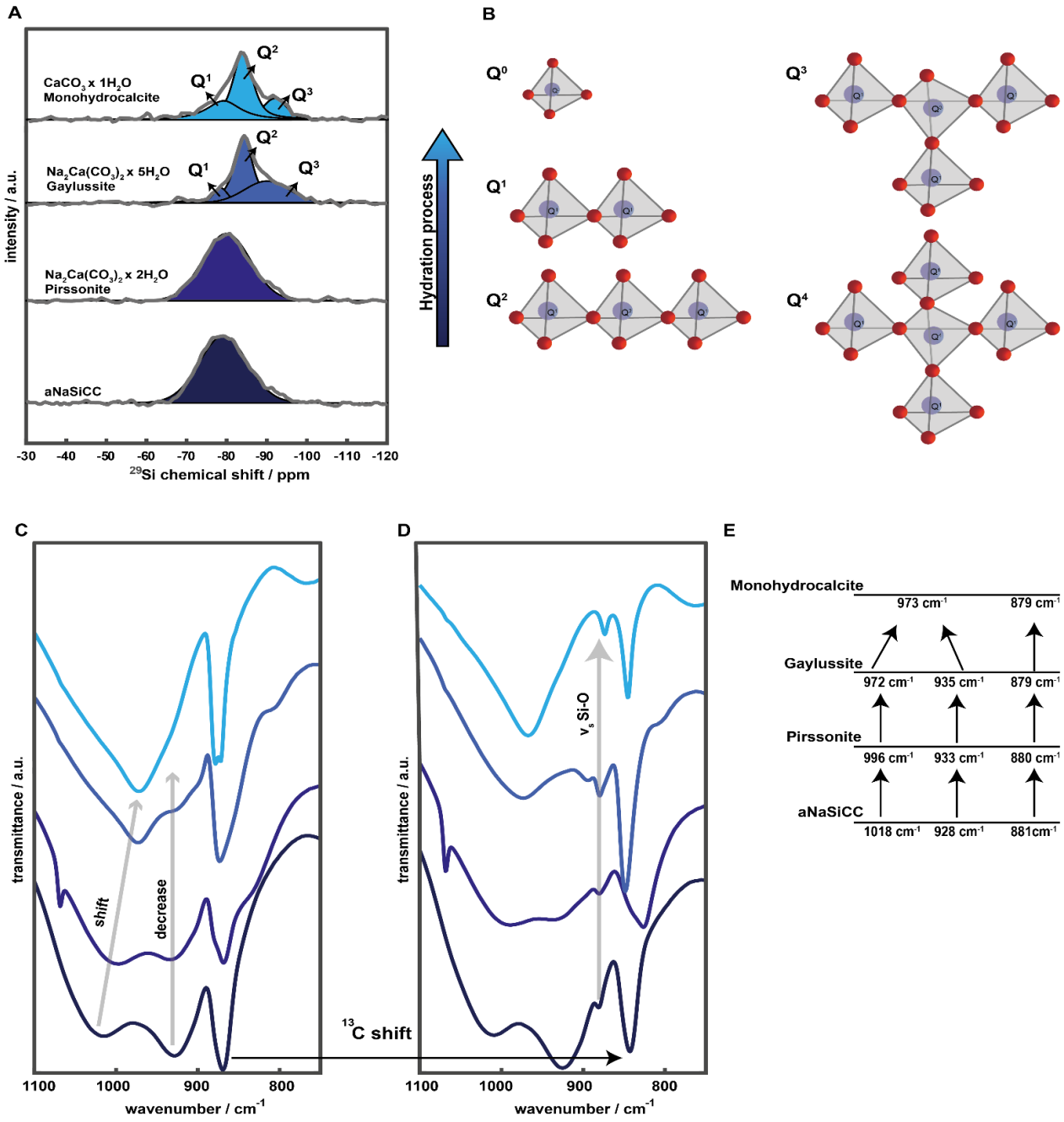

Figure S3.3. ^{29}Si NMR and FTIR spectra showing the progress of the hydration reaction of the activated intermediate aNaSiCC (indicated by the color depth from dark blue to light blue). (A) ^{29}Si NMR spectra, (B) silicate environments, and (C, D) FTIR spectra showing the Si-O vibrational modes in the spectral region between 700 and 1100 cm^{-1}. The FTIR spectra shown in (C) were recorded for the hydration reaction of aNaSiCC, the spectra shown in (D) were recorded for the hydration steps with ^{13}C enriched aNaSiCC. A summary for the shift in wavenumber changes is given in (E).

Change of the silicate environment

Crystalline sodium metasilicate shows three vibrational modes in the region from 1200 to 800 cm^{-1} (at 1034, 968 and 897 cm^{-1}).[1] They are associated with corner-sharing $[-O-(SiO)_2-O-]_n$ tetrahedral chains.[2] The ^{29}Si resonance of this so-called Q^2 environment hast a chemical shift of -78 ppm (FWHM 111 Hz).[3] Due to the carbonate environment of the materials the v_2 mode of the carbonate ions (which typically appear at ~870 cm^{-1}) may overlap with the silicate modes.[4]

The following hydration steps were used to distinguish between carbonate and silicate ^{13}C enriched samples of aNaSiCC (100%). In inharmonic oscillator approximation the enrichment should lead to a shift to lower wavenumbers for the carbonate signal due to the higher reduced mass of ^{13}C. In all ^{13}C enriched samples we observed a shift of the wavenumber by ~0.98, corresponding to the reduced mass resulting from the ^{13}C enrichment. In addition, all spectra of ^{13}C enriched aNaSiCC show a mode at ~880 cm^{-1} which is assigned to vibrational modes of the silicate groups. In summary, the hydration reaction of aNaSiCC to monohydrocalcite appears in the region from 800 to 1100 cm^{-1} as shown in the scheme in (E).

From vibrational spectroscopy studies of alkali and alkaline earth silicates it was shown that the frequencies of the v(Si-O) stretching vibrations depend on the type and number of bridging oxygen atoms of the silicate groups. Higher frequencies are associated with higher connectivity, hence the signals at ~1020, 930, and 880 cm^{-1} are assigned to species Q^1, Q^2, and Q^3, respectively.[5], [6],[7] These assignments are compatible with the ^{29}Si MAS NMR spectra. After the mechanochemical reaction, a broad distribution centered at -79 ppm (FWHM 1.24 kHz) appears for the ^{29}Si environment in aNaSiCC, corresponding to a Q^2 environment. Based on the signal width this resonance is likely to be a superposition of signals due to different silicate environments. In the hydration reaction of aNaSiCC to monohydrocalcite the ^{29}Si environment becomes more asymmetric, indicated by the appearance of a pronounced Q^2 and Q^1 environment and a decrease of the Q^3 signal.

The mechanochemical reaction leads to a molecular-scale mixing, with a breakup and recondensation of the silicate groups. The silicate environment changes strongly after adding water. Since sodium-calcium double carbonate hydrates recrystallize from aNaSiCC, the sodium cations must be in close proximity to calcium cations and carbonate anions. Therefore, for charge balance reasons, areas from which sodium has diffused away must be compensated by calcium or hydronium ions. Spectroscopic studies have shown that substitution of calcium in sodium silicate glasses leads to a pronounced change in the stretching vibration at ~1050 cm^{-1}, which is similar to the change of the signal at 1018 cm^{-1} in aNaSiCC to 973 cm^{-1} in the third hydration step.[8] In agreement with the "molecular site model," Na^+ ions are expected to prefer Q^3 sites due to their larger combined radii, in

contrast to Ca^{2+}, which would prefer Q^2 sites.[9] This is compatible with a distinct signal at ~-84 ppm (FWHM 416 Hz) in the ^{29}Si MAS NMR spectra in the Q^2 range typical for calcium silicates such as wollastonite and pseudowollastonite[10] and different from signals found in sodium silicates.[10],[11],[12]

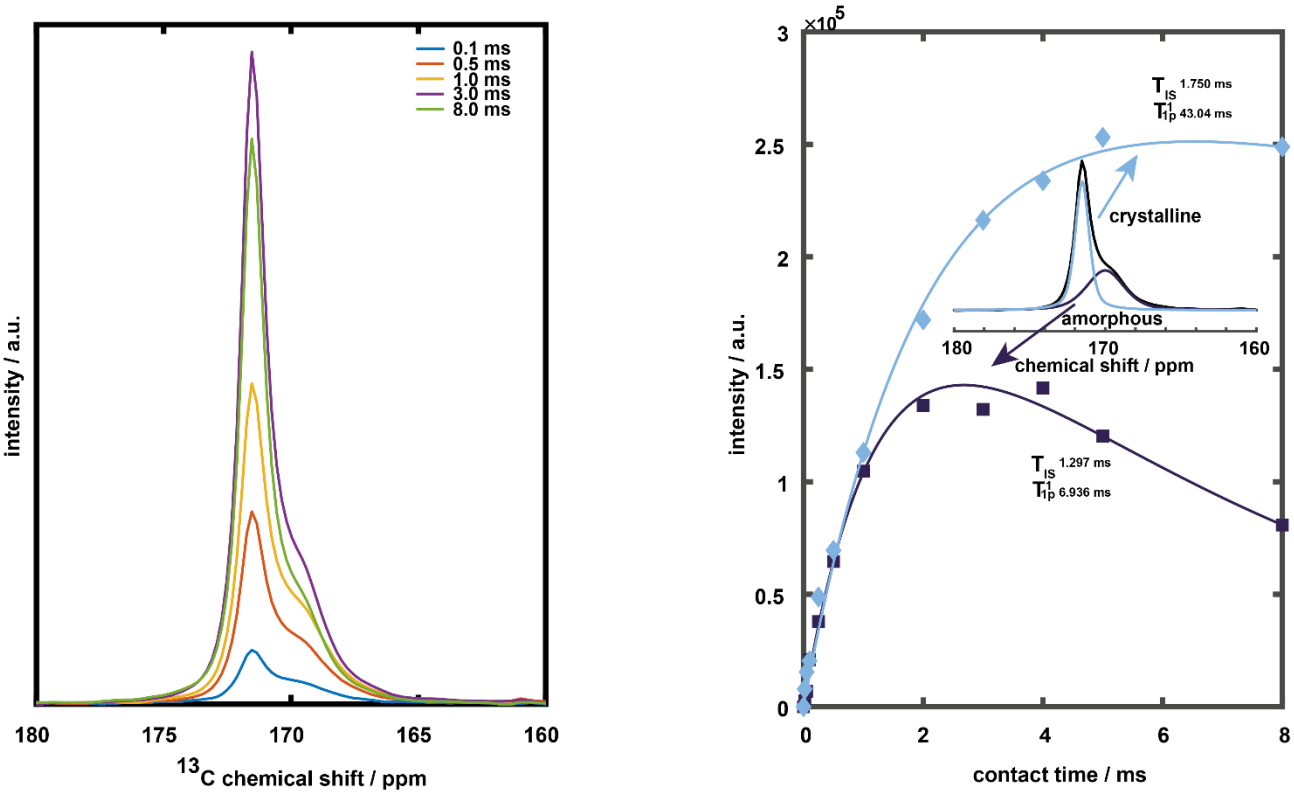

Figure S3.4. ^{1}H-^{13}C CP MAS spectra recorded for 0.1, 0.5, 1.0, 3.0 and 8.0 ms contact time for the third hydration step of aNaCC (treatment with deionized water) which results in the formation of monohydrocalcite. The spectra were deconvoluted into an amorphous and crystalline part using a Pseudo-Voigt profile function. The area was plotted as a function of cross-polarization time from which the CP build up curves of both environments were extracted.

.

The experimental CP curves in Figure S3.4 were deconvoluted into two signals, corresponding to the amorphous and crystalline environments of aNaCC. A comparison of the ^{13}C SP and ^{1}H-^{13}C CP spectra shows that the crystalline environments in the ^{13}C spectra can be attributed to signals at 171.2 ppm (pirssonite), 170.4 ppm (gaylussite) and 171.6 ppm (monohydrocalcite). The evaluate the differences between the hydration reactions of aNaSiCC and aNaCC the areas of the deconvoluted signals were integrated and plotted against the contact time. A "classical" I-S approach was used to fit the CP build-up curves. The signal intensity arises from a transfer of magnetization from the abundant (^{1}H) nuclei to rare (^{13}C) nuclei which depends on the strength of ^{1}H-^{13}C dipole-dipole couplings. The coupling depends on (i) the distance between coupled pairs ($\propto 1/r^3$), (ii) the number of protons and (iii) the mobility of the functional groups. The reader is directed to the review by Kolodziejski and Klinowski [13] for a detailed explanation of the parameters. The best fits in the examined systems were obtained with eq. S1:

$$I(t) = I_0 \left(1 + \frac{T_{IS}}{T_{1\rho}^{H}}\right)^{-1} \left[\exp\left(\frac{-t}{T_{1\rho}^{H}}\right) - \exp\left(\frac{-t}{T_{IS}}\right)\right] \qquad \text{(S1)}$$

Here T_{IS} and $T_{1\rho}^{H}$ are the CP time constant and ^{1}H relaxation time constant in the rotating frame.

A comparison of the data in Table S3.3 and Table S3.4 allows several conclusions about the hydration reaction:

1. The T_{IS} (increasing $1/T_{is}$) values for monohydrocalcite, pirssonite and gaylussite decrease regardless of the amorphous or crystalline nature. The strength of the dipole-dipole coupling depends on the number of protons in the vicinity of the carbonate anion. Since there are five H_2O molecules in the local carbonate environment in the gaylussite, two H_2O molecules in pirssonite and only one in the monohydrocalcite structure, this correlates well with a decrease in the CP rate constant in the order gaylussite > pirssonite > monohydrocalcite.
2. The closest C…H separations in the crystalline phases (calculated from the published crystal structures[14],[15]) correspond to ~3.2 Å for monohydrocalcite, ~2.6 Å for gaylussite and ~2.4 Å for pirssonite. As T_{C-H} is related to a sum over carbon-proton distances $T_{C-H}^{-1} \propto \sum_i d(\text{C-1H}_i)$, in which d(C-1H$_i$) *is* the internuclear distance between the carbonate C and the ith proton in direct vicinity, T_{IS} values should increase from pirssonite to gaylussite to monohydrocalcite.[16] The discrepancy to the observed data due to gaylussite and pirssonite may be related to the broader distribution of water molecules in gaylussite.

3. A comparison of the amorphous and crystalline components in the course of the hydration reaction shows that in pirssonite the $T_{IS'}$ values of the amorphous and crystalline domains are almost identical. However, the amorphous components have significantly higher $T_{1\rho}^{H}$ values. Since the $T_{1\rho}^{H}$ value is a volume property,[17] the large difference between the amorphous and crystalline portions could be due to either phase-separated domains or different mobilities in the amorphous and crystalline environments.

Due to the slower diffusion of water in the water/acetonitrile mixture, the hydration reaction could start in a first step with the formation of surface layers that are already completely infiltrated by water, followed by subsurface layers into which the water from the surface region starts to penetrate. In the second hydration step of the transformation to gaylussite, the differences between the $T_{IS'}$ values in the amorphous and crystalline portions are still dominant, but the differences in $T_{1\rho}^{H}$ are small. Considering the dependence of the dipole-dipole interaction on the $^{1}H...^{13}C$ separations and the number of protons in the immediate vicinity of the carbonate anions, the amorphous environment could be characterized by shorter distances (and thus stronger interactions) between carbonate anions and water molecules, or alternatively by more water molecules in the neighborhood of the carbonate groups. This would indicate the formation of a strongly hydrated amorphous phase that is structurally different from the developing crystalline phase. The difference in $T_{1\rho}^{H}$ values could indicate different ^{1}H ranges, although less pronounced than in the first hydration step. A similar trend was observed for monohydrocalcite, the final product, although the protons in the amorphous phase showed faster relaxation (in the rotating frame) than in the crystalline phase.

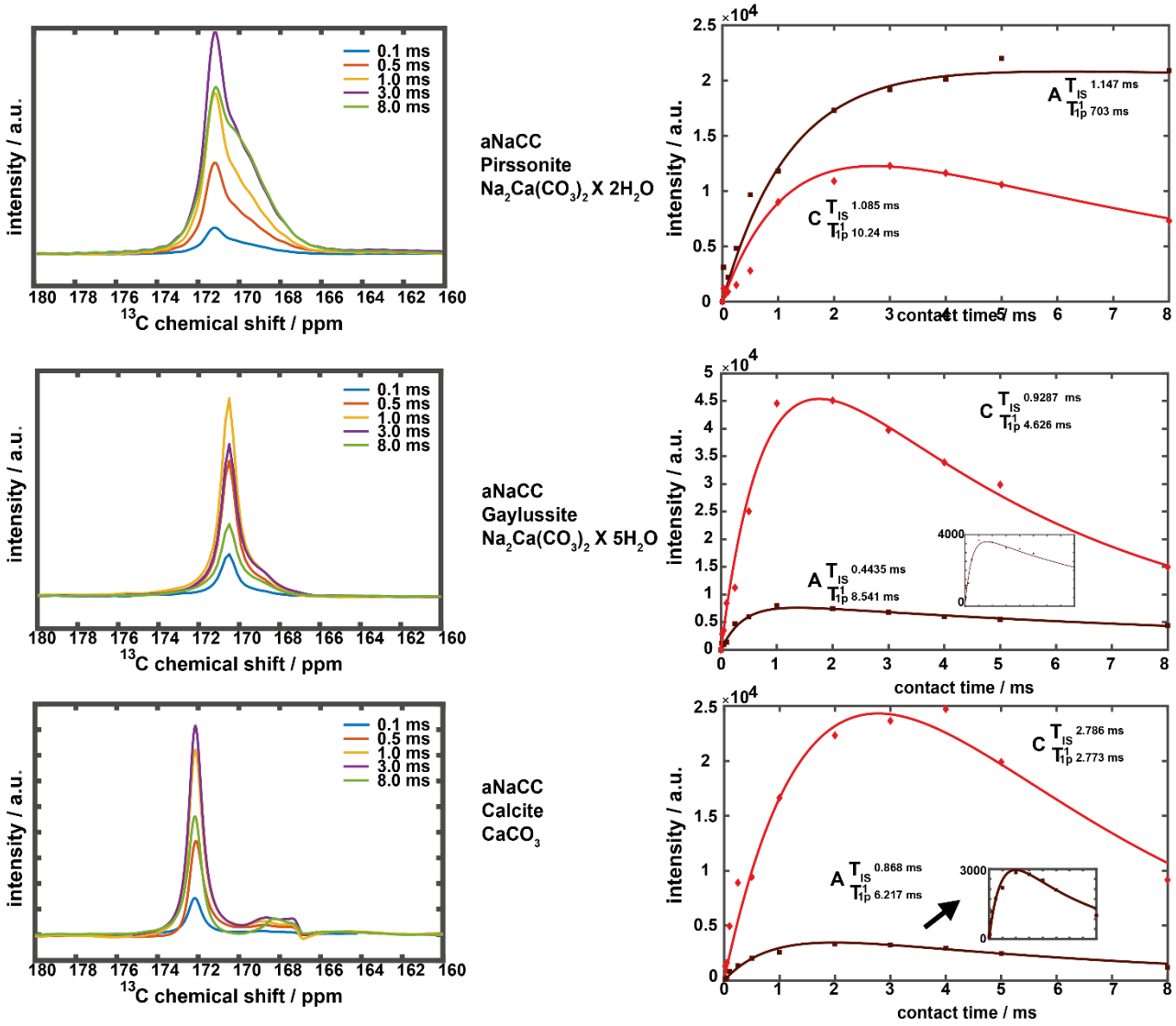

Figure S3.5. Comparison of the ^{1}H-^{13}C CP build up curves for the amorphous and crystalline environments for the individual hydration steps of aNaCC. The dark-coloured lines represent the amorphous part (denoted with A), the red lines represent the crystalline part (denoted C). The fitting was carried out using eq 1 using the classical I-S model

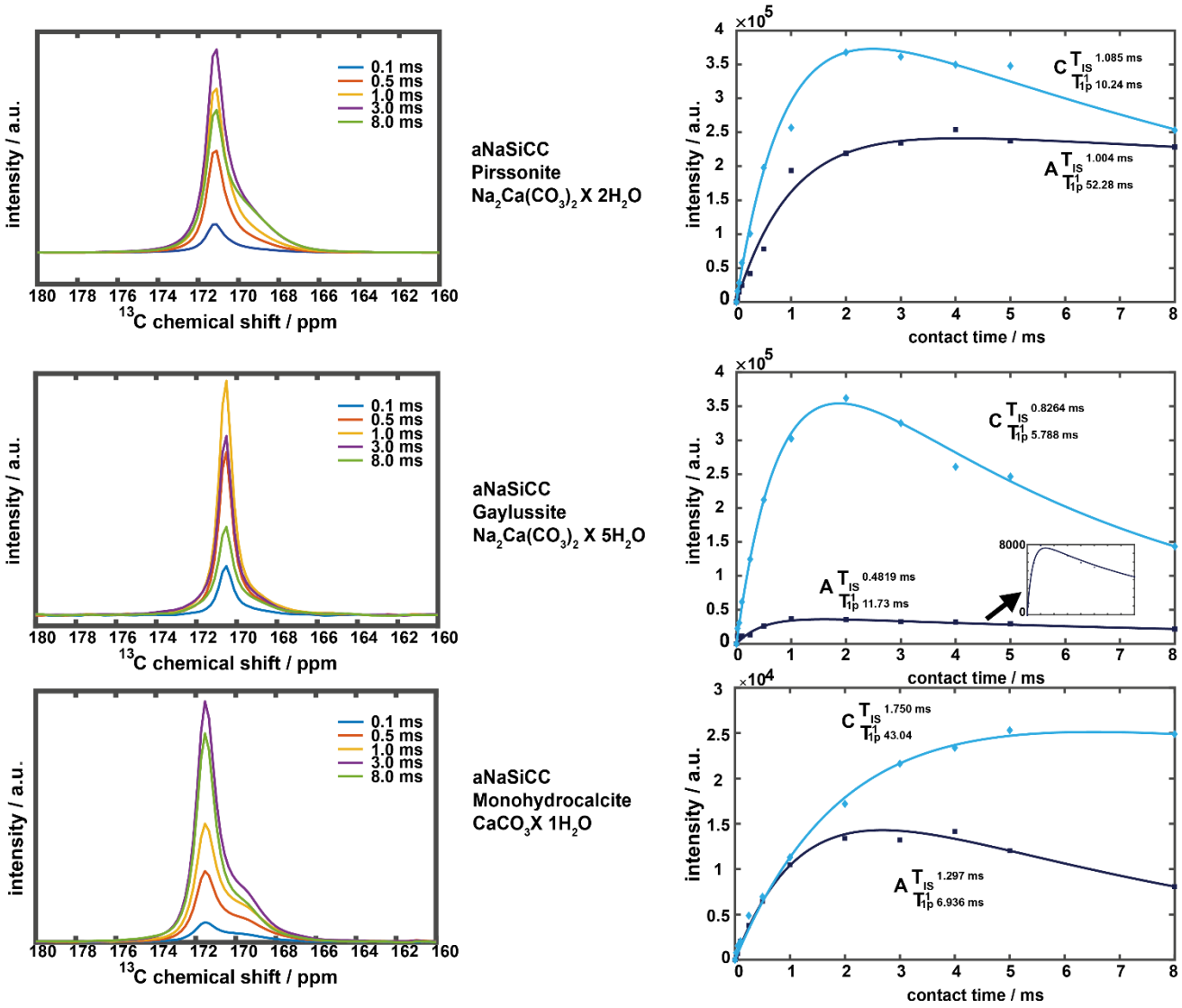

Figure S3.6. Comparison of the ^{1}H-^{13}C CP build up curves for the amorphous and crystalline environments obtained from the different hydration steps of aNaSiCC (blue curves). The dark-colored lines represent the CP build-up curves for the amorphous part (denoted with A), the light-colored lines represent the crystalline part (denoted C). The fitting was carried out using eq 1 using the classical I-S model

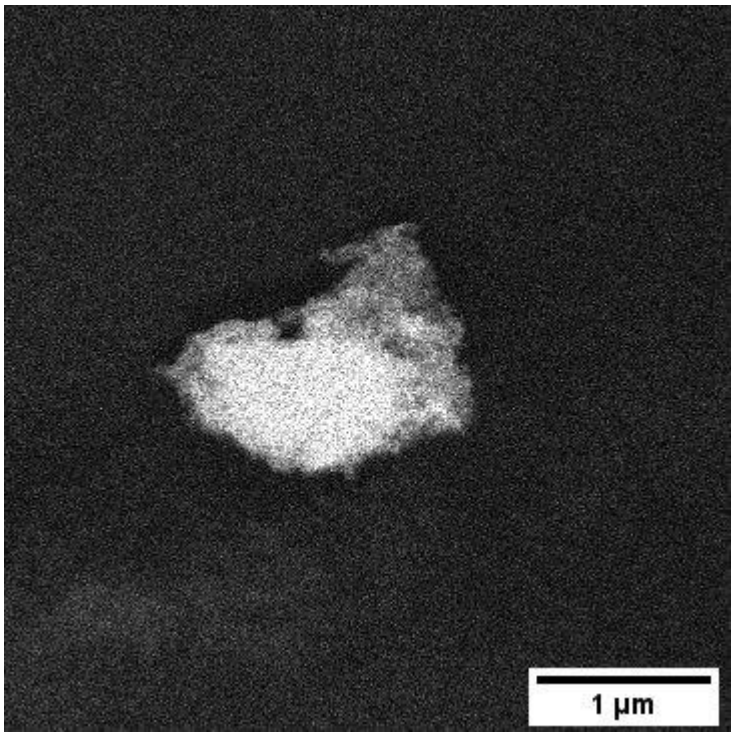

Figure S3.7. Image of the crystal selected for 3D ED measurement.

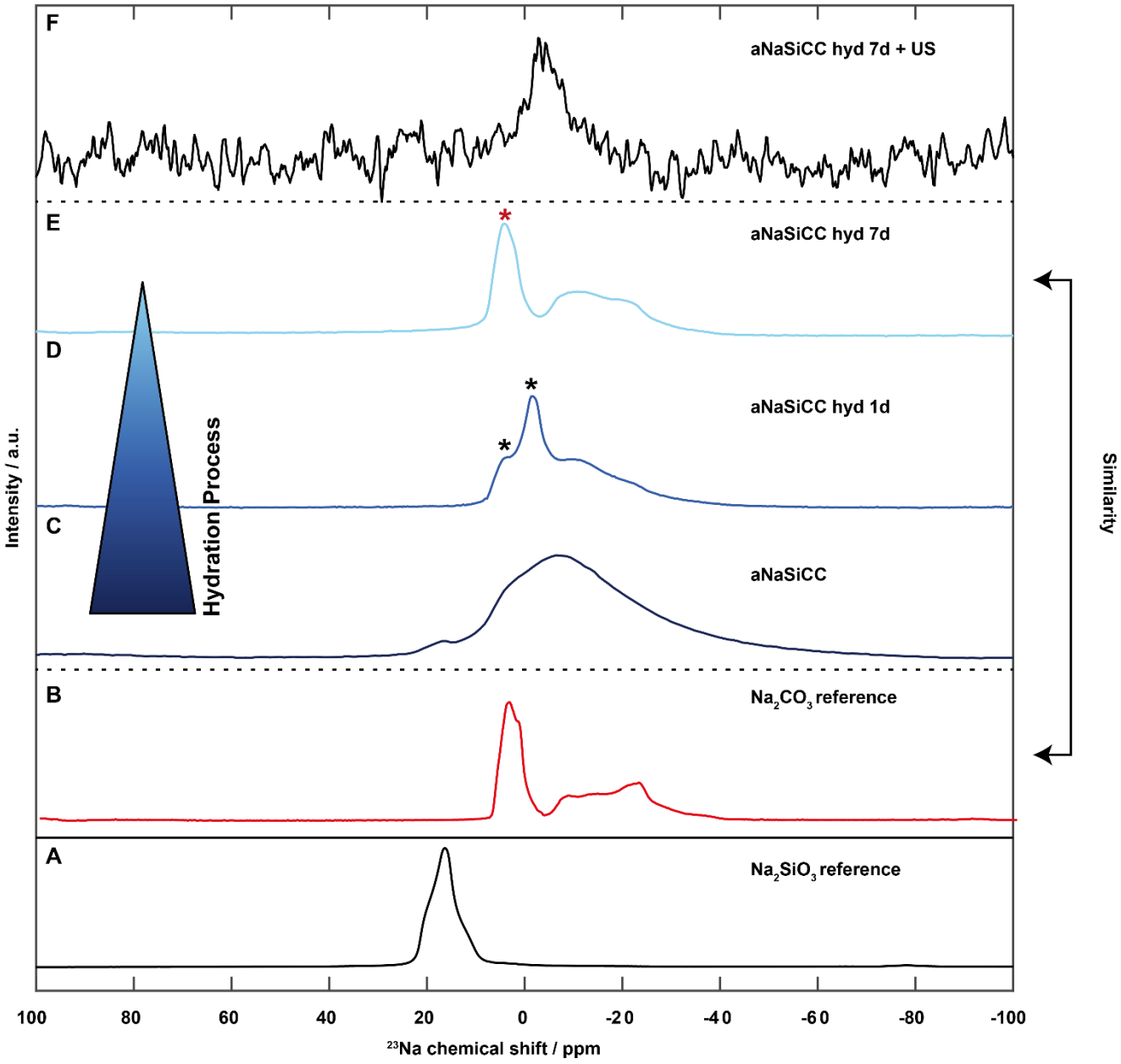

Figure S3.8. ^{23}Na MAS NMR spectra of Na_2SiO_3 (A, black line) and Na_2CO_3 (B, red line) as reference materials and aNaSiCC (C, blue line), and of the hydration products of aNaSiCC after hydration with pure water for 1 d (D), 7 d (E), and 7 d with additional ultrasonication for 1 minute (F). The ^{23}Na spectrum of aNaSiCC hydration with pure water after 7d bears similarity with the ^{23}Na spectrum of Na_2CO_3.

Formation of natrite (γ-Na_2CO_3) by dissolution and recrystallization

FTIR spectra of aNaSiCC and aNaCC after the hydration reaction in excess water indicate the formation of monohydrocalcite[15] and calcite.[4] Only the splitting of the ν_3 mode of monohydrocalcite (formed from aNaSiCC) is absent (Figure S3.9) and for aNaCC two additional modes appear in the ν_4 region at 702 and 694 cm^{-1} (Figure S3.10). Since it has been demonstrated independently by ADT that the hydrate reaction of aNaSiCC produces monohydrocalcite, the missing band splitting may result from a superposition with the bands of another carbonate phase. The modes at 702 and 694 cm^{-1} after the hydration reaction of aNaCC are characteristic of sodium carbonate.[18] Since pirssonite and gaylussite are formed in the hydration reaction of aNaSiCC and aNaCC, the presence of sodium carbonate is not unexpected.

The hydrate reaction of aNaSiCC was studied by ^{23}Na MAS NMR (Figure S3.8). After a reaction time of 1d in water, the sodium environment showed a sharp signal with a shoulder (D,*). A broad signal after 7 d of reaction time is compatible with the 23Na environment of sodium carbonate (E,*). With this information, all phases in the X-ray powder diffractograms could be assigned with Rietveld fits. (Figure S3.9 and S3.10).

The hydrate reactions of aNaSiCC and aNaCC were performed with 100 mg each of aNaSiCC/aNaCC in 5 mL of water. For complete phase separation, this would correspond to ~0.05 g of sodium carbonate, which, however, should be completely dissolved in water (solubility limit ~1.5 g per 5 mL) due to its high solubility (30.7 g Na_2CO_3/100 g H_2O).[19]

Based on the NMR data, the sodium carbonate is encapsulated in small domains near calcite and monohydrocalcite from aNaSiCC and aNaCC, respectively. To dissolve the sodium carbonate, the domains must be separated using an external force (e.g., mechanical stress) to provide sufficient contact with water. After ultrasonication, the material was free of sodium carbonate, as shown by a comparison of the FTIR spectra and Rietveld refinments before and after ultrasonication (Figure S3.9 and S3.10). ^{23}Na MAS NMR of hydrated aNaSiCC after ultrasonic treatment showed only a weak signal at ~-5ppm compatible with surface-bound sodium cations (Figure S3.8 F).

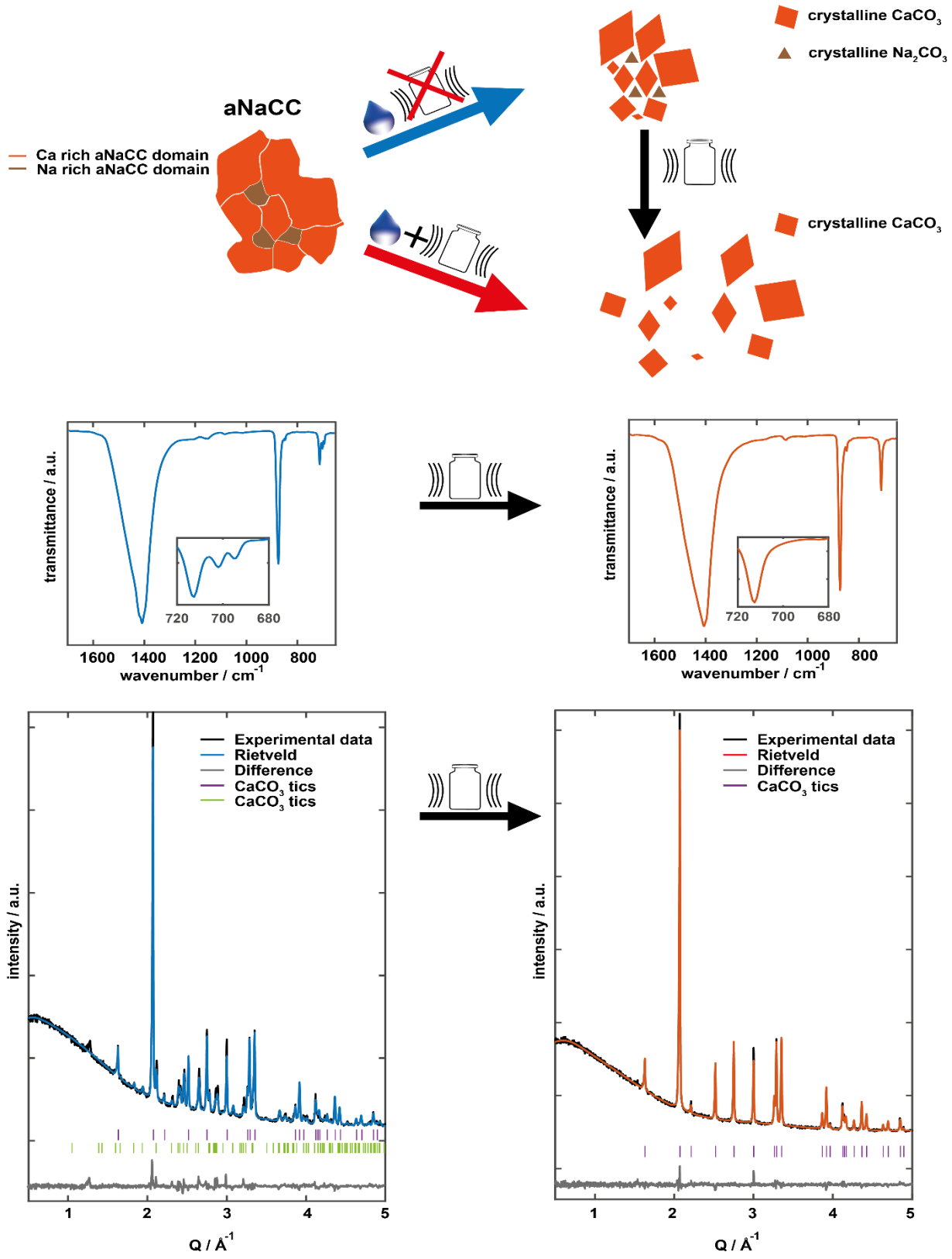

Figure S3.9. FTIR spectra and X-ray powder diffractograms of the hydration products of aNaCC in water without (blue curves) and with (red curves) ultrasonication.

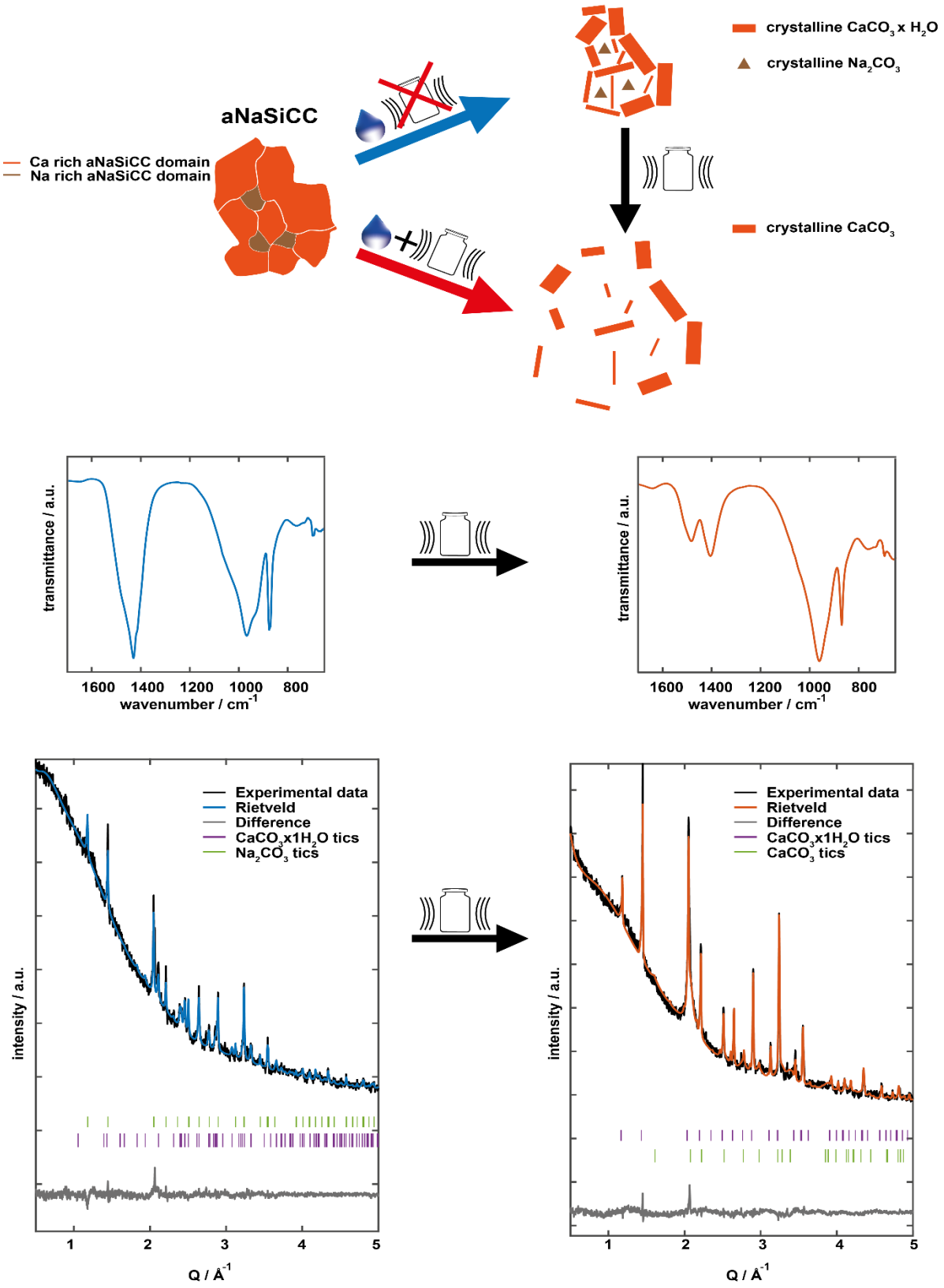

Figure S3.10. FTIR spectra and X-ray powder diffractograms of the hydration products of aNaSiCC in water without (blue curves) and with (red curves) ultrasonication.

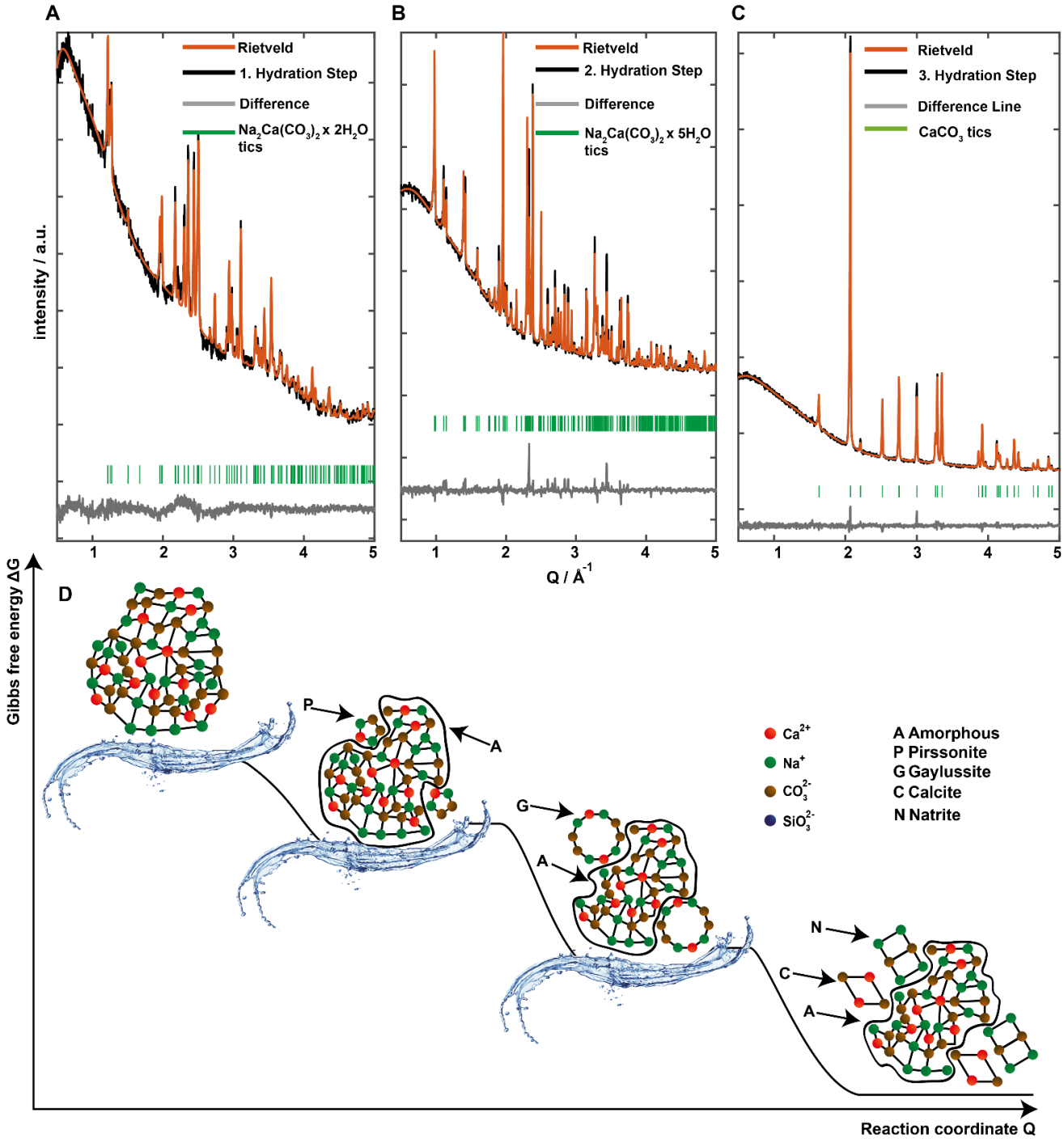

Figure S3.11. X-ray powder diffractograms showing the phase evolution of aNaCC prepared by ball-milling during the hydration reaction with water. Kinetic control was achieved by lowering the water concentration with CH_3CN. Black lines show the experimental patterns, colored lines the Rietveld refinement. Gray line show the difference patterns, and green ticks indicate the calculated reflection positions of pirssonite (A), gaylussite (B) and calcite (C).). The scheme (D) illustrates a simplified reaction model for the hydration reaction.

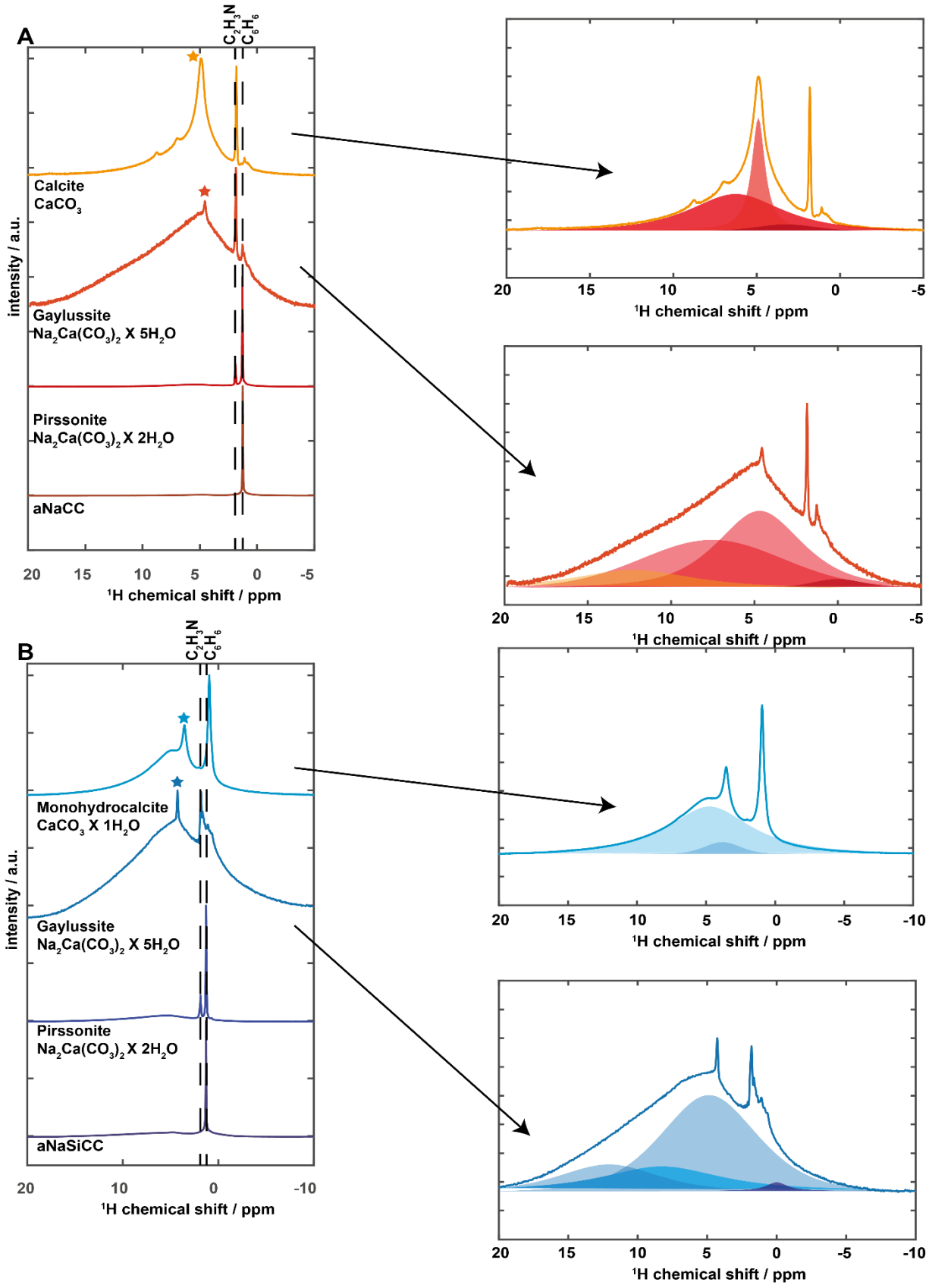

Figure S3.12. ^{1}H NMR spectra for the hydration of aNaCC (A) and aNaSiCC (B).

^{1}H environment measured by NMR

The hydration reaction of aNaCC and aNaSiCC was investigated with ^{1}H MAS NMR spectroscopy using background suppression. The spectra for aNaCC and aNaSiCC show a signal at 1.25 ppm assigned to cyclohexane (milling dispersant). The resonance at 5 ppm is assigned to adsorbed water. After the first hydration step, an additional small signal at 1.9 ppm (corresponding to acetonitrile) appears for aNaCC and aNaSiCC. Due to the use of water/acetonitrile mixtures (to slow the recrystallization process) a part of acetonitrile adheres to the particle surfaces. The crystallization of pirssonite (a dihydrate) is manifested by the increase of the water signal at 5 ppm. The low intensity could be explained by the small amount of crystalline phase during the first hydration step (see main manuscript). With proceeding hydration reaction the intensity of the water signal increases. This may be explained by an increased uptake of water and subsequent reorganization due to longer contact with the water/acetonitrile mixtures. Both cyclohexane and acetonitrile signals are still present although the cyclohexane signal decreases while the acetonitrile signal increases. The ^{1}H spectra for gaylussite in both samples show a distribution of different water/OH^- environments at 0, 4.5, 8.2 and 12.5 ppm. The distinct signals at 0 and 12.5 ppm are assumed to arise from hydroxyl and bicarbonate groups which might result from the recrystallization process of the initially amorphous material.[20,21] In addition to the broad signals arising from the mobility of the water, a sharp signal at ~4.3 ppm (*) can be observed which might be explained by an environment with decreased mobility. The hydration in pure water leads to calcite ($CaCO_3$) in aNaCC and monohydrocalcite in aNaSiCC ($CaCO_3 \cdot H_2O$). Both spectra show environments with a broad signal at ~6.5 ppm. In addition, the intensity of the distinct signal at ~4.3 ppm increases for both samples indicating a progressing evolution of an environment with less mobile water. Since the hydration of aNaSiCC and aNaCC eventually leads to the formation of calcite, it can be expected that only adsorbed water will be present after complete reorganization. The emergence of a less mobile 1H environment could be due to the progressive recrystallization, where water is mainly adsorbed on the surface, resulting in the loss of mobility present in the amorphous phase. This is in good agreement to the observed cross polarization kinetics which indicate the presence of a highly hydrated amorphous phase for the second hydration step (gaylussite) opposed to the amorphous phase in the last hydration step (monohydrocalcite/calcite).

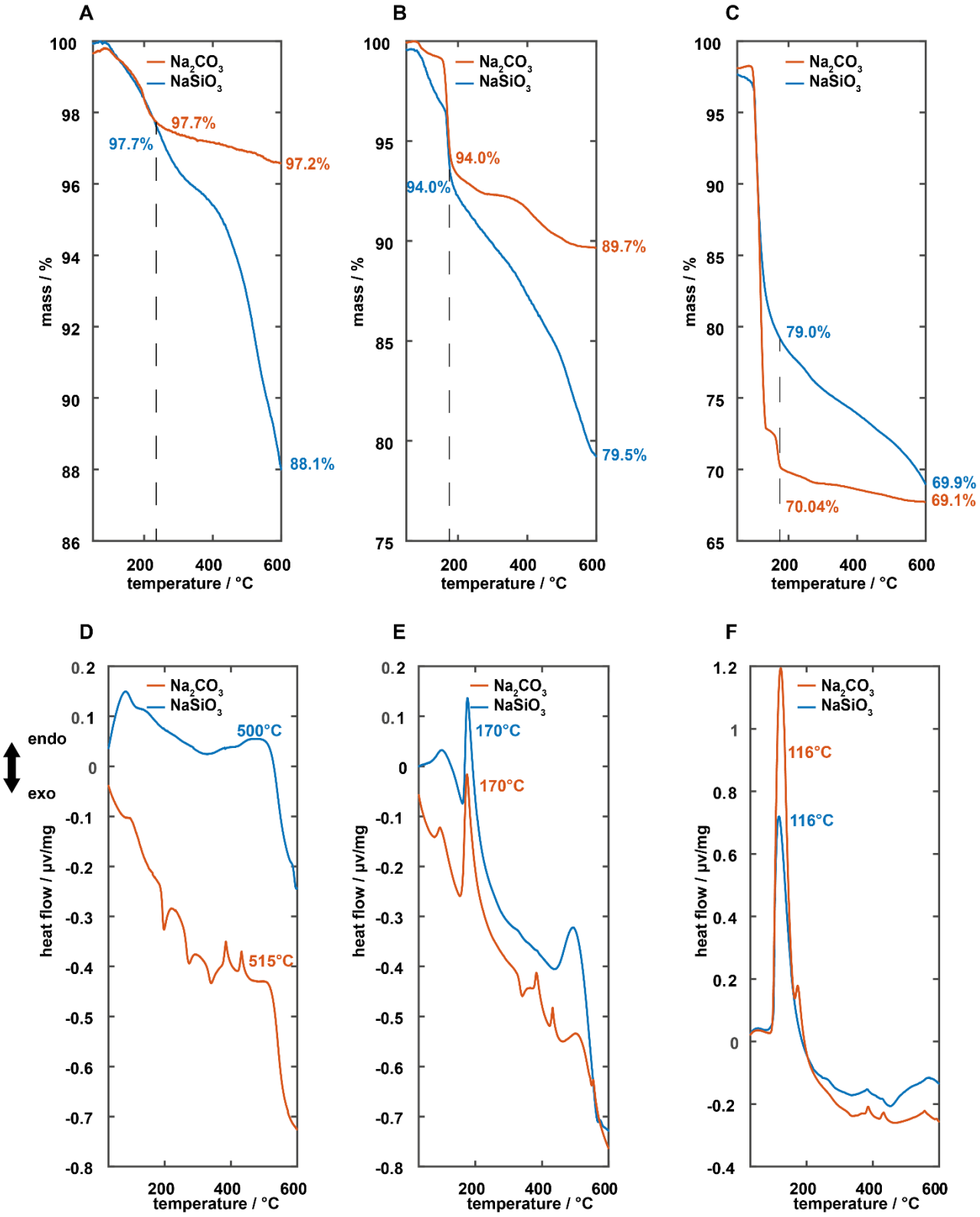

Figure S3.13. TGA (A-C, top) and DTA (D-F, bottom) traces for the hydration reaction of aNaCC and aNaSiCC (A,D) and the hydration intermediates pirssonite (B,E) and gaylussite (C,F). The samples obtained from aNaCC correspond to red lines, the samples from aNaSiCC to blue lines. As the hydration in water leads to different monohydrocalcite and calcite for aNaCC and aNaSiCC respectively, a comparison due to the different chemical composition was omitted.

Mass changes associated with hydration

The individual steps of the hydrate reaction of aNaCC and aNaSiCC were compared by TGA and DTA for the amorphous phase (A,D), pirssonite (B,E) and gaylussite (C,F). As shown by FTIR (Figure S3.2) and ^{1}H NMR (Figure S3.12) cyclohexane molecules are occluded for aNaCC and aNaSiCC. This leads to a mass loss of ~3% (A) below 210° C in aNaCC due to adsorbed water and entrapped cyclohexane. aNaSiCC suffers further mass loss of 11% due to a release of CO_2, while only minor mass changes occur for aNaCC after 210° C. In the DTA profiles exothermic signals at 515° C and 500° C for aNaCC and aNaSiCC (D). correspond to the formation of nyerereite (Figure S3.14, $Na_2Ca(CO_3)_2$)).

In the first hydration step (formation of pirssonite), a mass loss of about 6% (B) occurs at T = 170° C (release of crystal water from $Na_2Ca(CO_3)_2{\cdot}2H_2O$ to $Na_2Ca(CO_3)_2$). The loss of mass nominally corresponds to only partial (20%) dehydration of pirssonite. A mass loss of ~6 % is expected assuming that most of the water corresponds to the crystalline portion of the sample (30 % based on to ^{13}C SP NMR). However, the material contains significant proportions of amorphous phase with minor amounts of water (Figure 4B). Like the non-hydrated amorphous phase, the pirssonite portion in aNaSiCC shows an additional 15% weight loss after 170° C, unlike pirssonite from aNaCC, which shows an additional 4% weight loss. The DTA profiles show an endothermic peak at 170° C for both samples due to the loss of crystal water in pirssonite (E). Additionally, an exothermic signal appears at about 520° C for both samples, as in the amorphous phase which is associated with the phase change to nyerereite. The pirssonite portion in aNaSiCC shows an additional 15% weight loss after 170° C similar as the non-hydrated amorphous phase but unlike pirssonite from aNaCC, which shows an additional 4% weight loss.

In the second hydration step (formation of gaylussite), a weight loss of about 30% for aNaCC and 22% for aNaSiCC occurs at about 185 °C (C), corresponding to a release of crystal water from $Na_2Ca(CO_3)_2{\cdot}5H_2O$. This release of water is associated with an endothermic signal from the DTA trace (F). Complete dehydration corresponds to a weight loss of about 30%.[22] Based on the quantification by ^{13}C SP NMR, 80% of the carbonate environment (main text, Figure 53.B) in the second hydration step can be assigned to a crystalline environment and are thus attributed to gaylussite for the aNaCC sample. As a mass loss of 30% would be expected from a purely crystalline sample of gaylussite, the additional mass loss indicates the formation of a highly hydrated amorphous phase to

account for the additional 6%, experimentally observed. This is consistent with the information from the cross polarization kinetics which suggests a water loss similar as in gaylussite. aNaSiCC shows a weight loss of 22% (nominally 25%) at 185° C. The deviation in mass loss could be related to differences in the amorphous phase, which is presumably a carbonated sodium-calcium silicate.

The silicate-containing aNaSiCC and aNaCC differ in their TGA profiles, as the silicate-containing samples show a higher weight loss compared to the pure carbonate phase. This CO_2 loss is due to either a reaction between silicate and carbonate domains or carbonate decomposition.[23] Loss of bound water (similar as in hydrated calcium silicate gels)[24] might occur in silicate samples as well. Only for gaylussite the mass loss is ~31%, where the decomposition temperature in aNaCC is lower than in aNaSiCC. The silicate environment in aNaSiCC is expected to reorganize (Figure S3.3), and the amorphous carbonized sodium calcium silicate phase should show different thermal behavior than hydrated amorphous aNaCC.

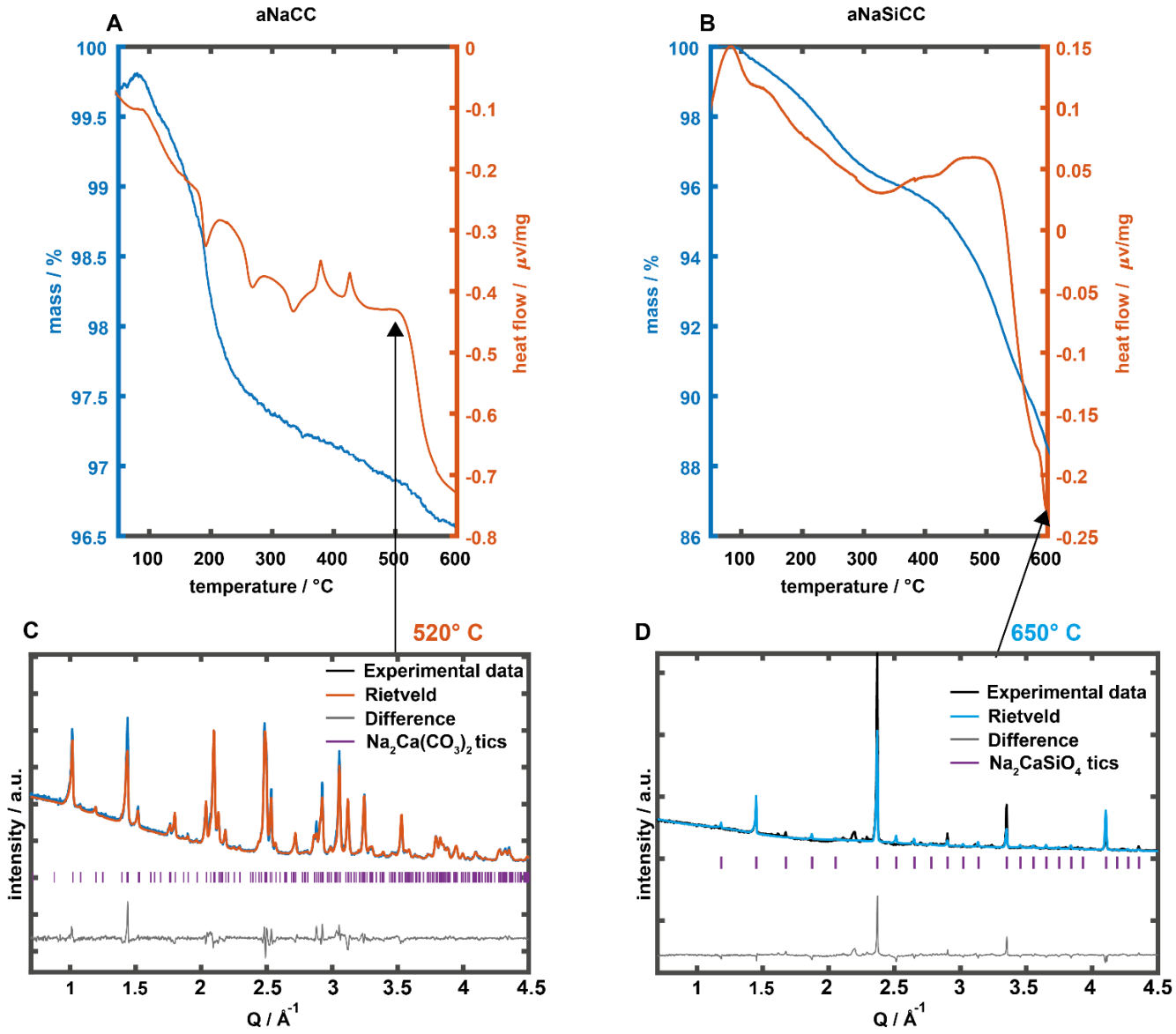

Figure S3.14. TGA (blue curve) and DTA (red curve) traces for aNaCC (A) and aNaSiCC (B) showing the loss of water. The associated phase transitions to crystalline $Na_2Ca(CO_3)_2$ and Na_2CaSiO_4 are demonstrated by the powder diffractograms in (C) and (D).

Thermally induced crystallization

DTA profiles of aNaCC and aNaSiCC show differences upon heating to 520° C. This is attributed to partial crystallization of the amorphous phase to $Na_2Ca(CO_3)_2$. In aNaSiCC the additional silicate environment leads to crystallization to Na_2CaSiO_4 at ~650° C.

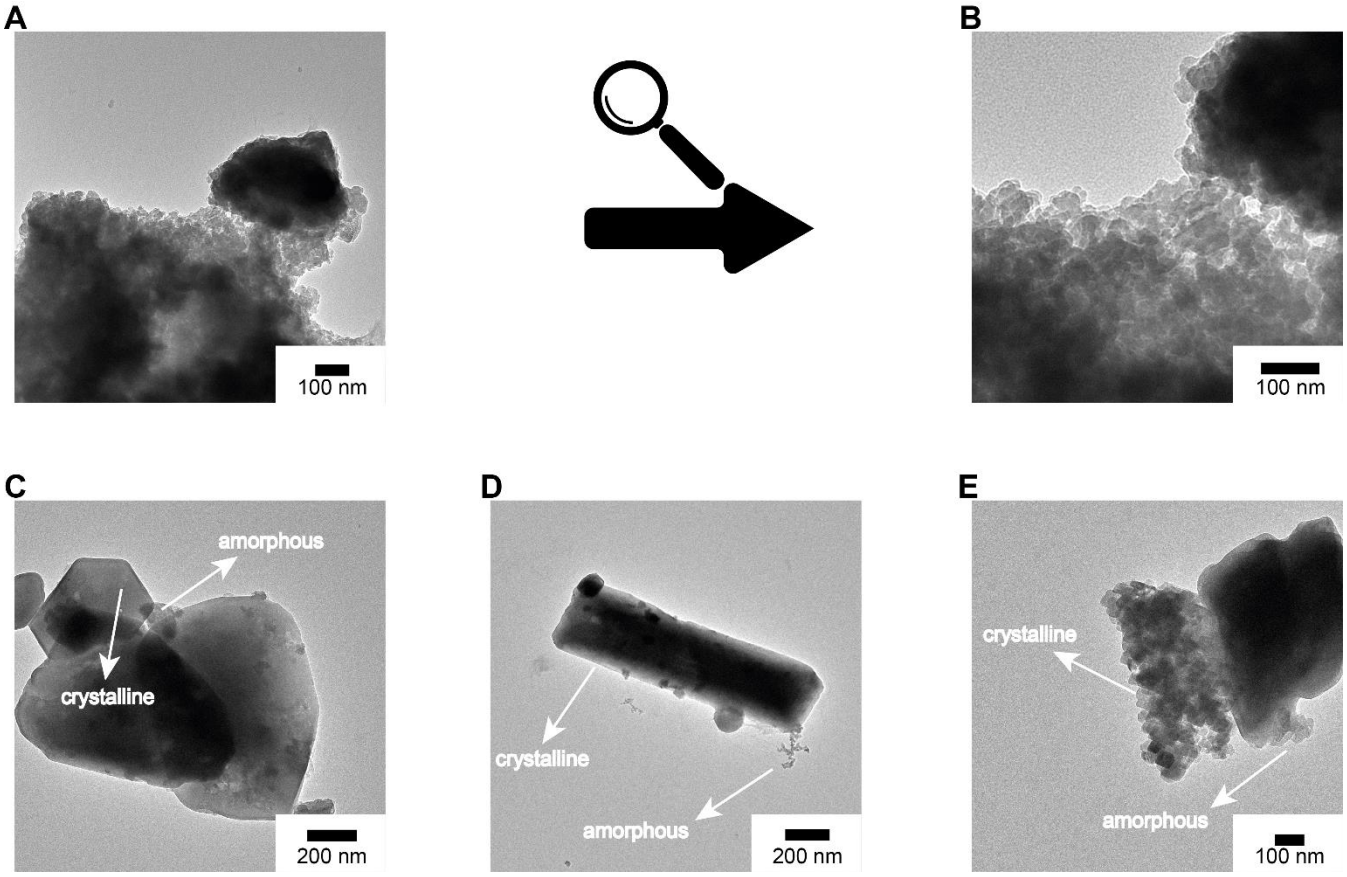

Figure S3.15. TEM images of aNaSiCC showing the presence of small (5-10 nm) agglomerated nanoparticles (A,B). Products of different crystallization steps observed by TEM imaging showing well-defined crystallites with hexagonal (C), rodlike (D), and rhombohedral morphology (E) next to domains without any facets and containing small agglomerates (as in A). The acquisition of diffraction patterns proved impossible due to the beam sensitivity of the samples as shown in Figure S13.

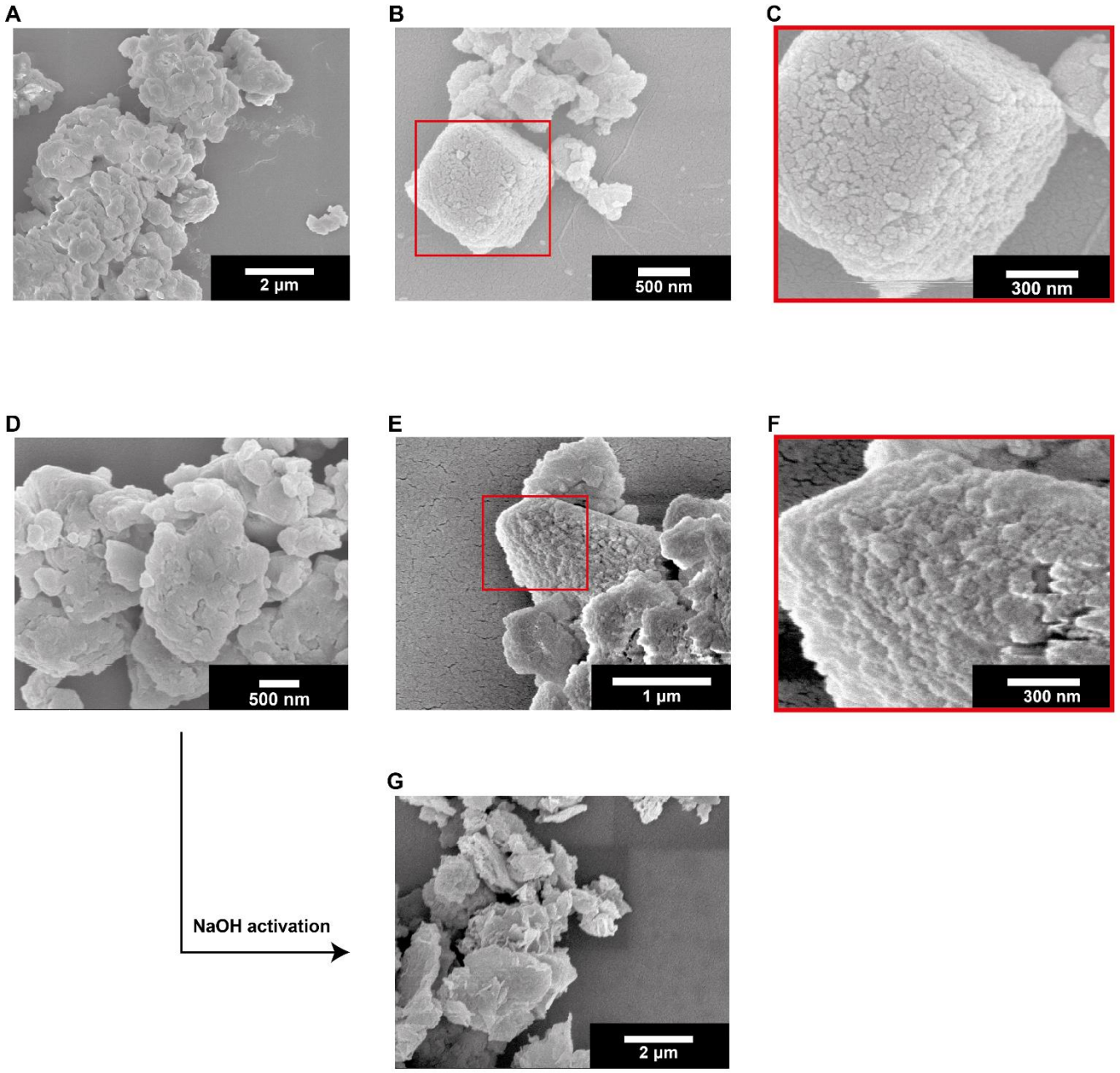

Figure S3.16. SEM images of (A) aNaCC and (B, C) the mesocrystalline products of its hydration reaction in pure water in two different magnifications. SEM images of (D) aNaSiCC and (E, F) its mesocrystalline hydration products in pure water in two different magnifications. (G) SEM image of aNaSiCC after NaOH activation showing plate like morphology.

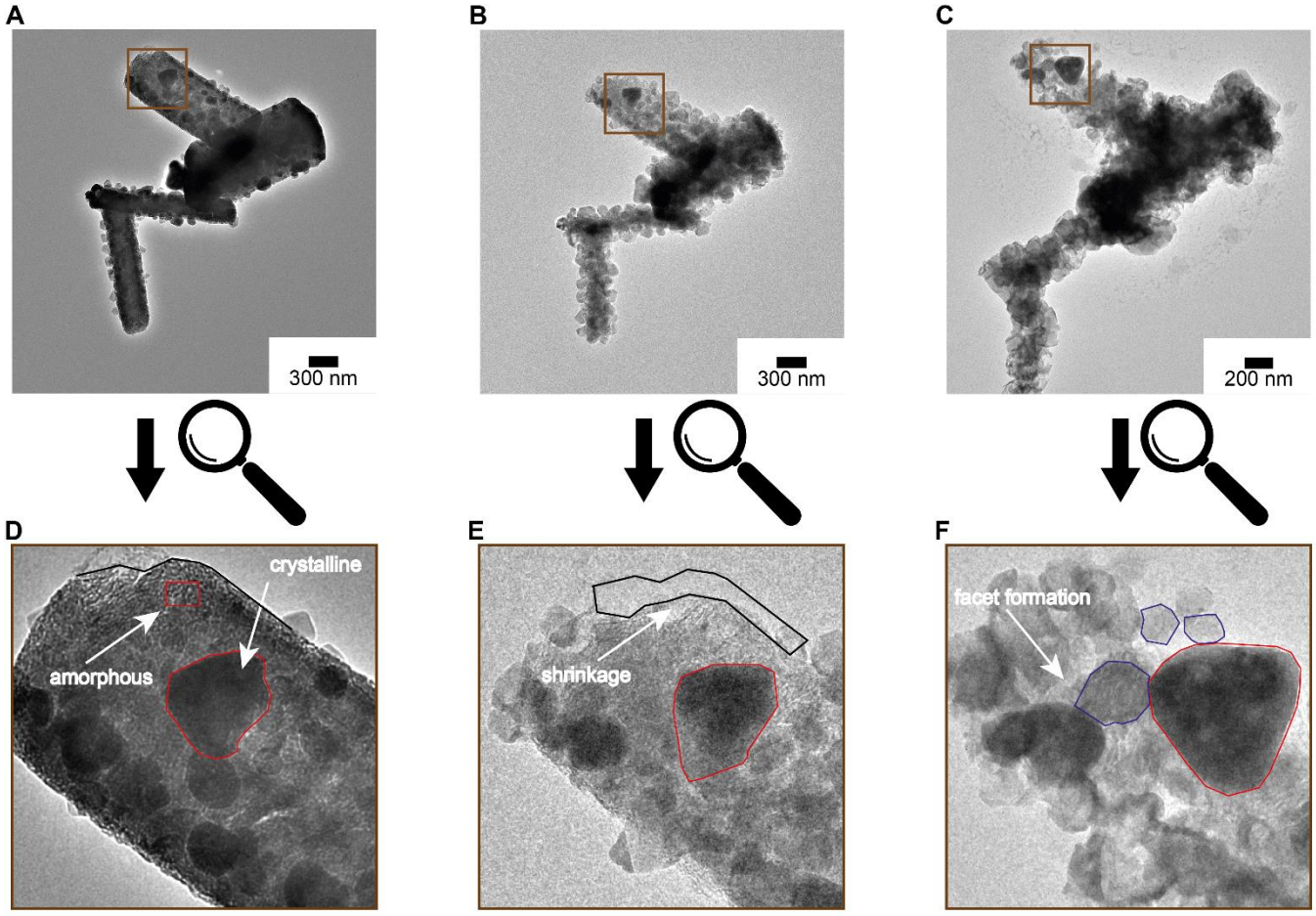

Figure S3.17. TEM images of pirssonite obtained by hydration of aNaSiCC (A, D). Although initially slightly overfocused, amorphous rod-like agglomerates are observed with small crystallites (marked in red) on or within the parent particle (compare scheme and powder diffractograms in Figure S6). Under the electron beam (i.e., after the first image was taken), a phase change occurred (B, E). The rods collapsed and formed new particles with discrete facets (red and blue polyhedral) (B, E). Due to the high crystal water content, water is released to the vacuum environment by the energy of the electron beam and a non-hydrated crystalline phase is formed.

TEM and SEM of products of the hydration reaction and NaOH activation

Agglomerates of nanoparticles with diameters of ~20 nm are formed during milling, since ball milling leads not only to mechanical crystal deformation but also to smaller crystal sizes. (Figure S3.15 A, Figure S3.16 A/D). Changes in crystal morphologies occurred during the hydration water/acetonitrile mixtures leading to the formation of hexagonal, rod-shaped and rhombohedral crystallites on, or within the agglomerates (Figure S3.15 C,D,E). Based on the CP NMR kinetic data spectra we assume that these structures are formed by dissolution /recrystallization on the mesostructured surfaces. The crystallization process ultimately leads to phase separation.

Electron imaging studies showed these changes to occur in dependence of the hydration step (Figure S3.14). New domains formed in some areas (Figure S3.17) because of the radiation sensitivity of the products (release of water in the electron beam under high vacuum conditions). Recording of diffraction patterns could therefore be only conducted under cryogenic conditions in the hydrated samples. The beam sensitivity was also evident in the SEM studies. Figure S16A and D demonstrate that aNaCC and NaSiCC consist of nanoparticle agglomerates. Rhombohedral and prismatic crystallites are formed in the course of the hydration reaction (Figure S3.16B, E). Zoom images (Figure S3.16C, F) show specific agglomeration motifs. Different from the hydration reaction, activation with NaOH leads to the formation of stacked platelets, which frequently occur in C-S-H phases (Figure S3.16G).

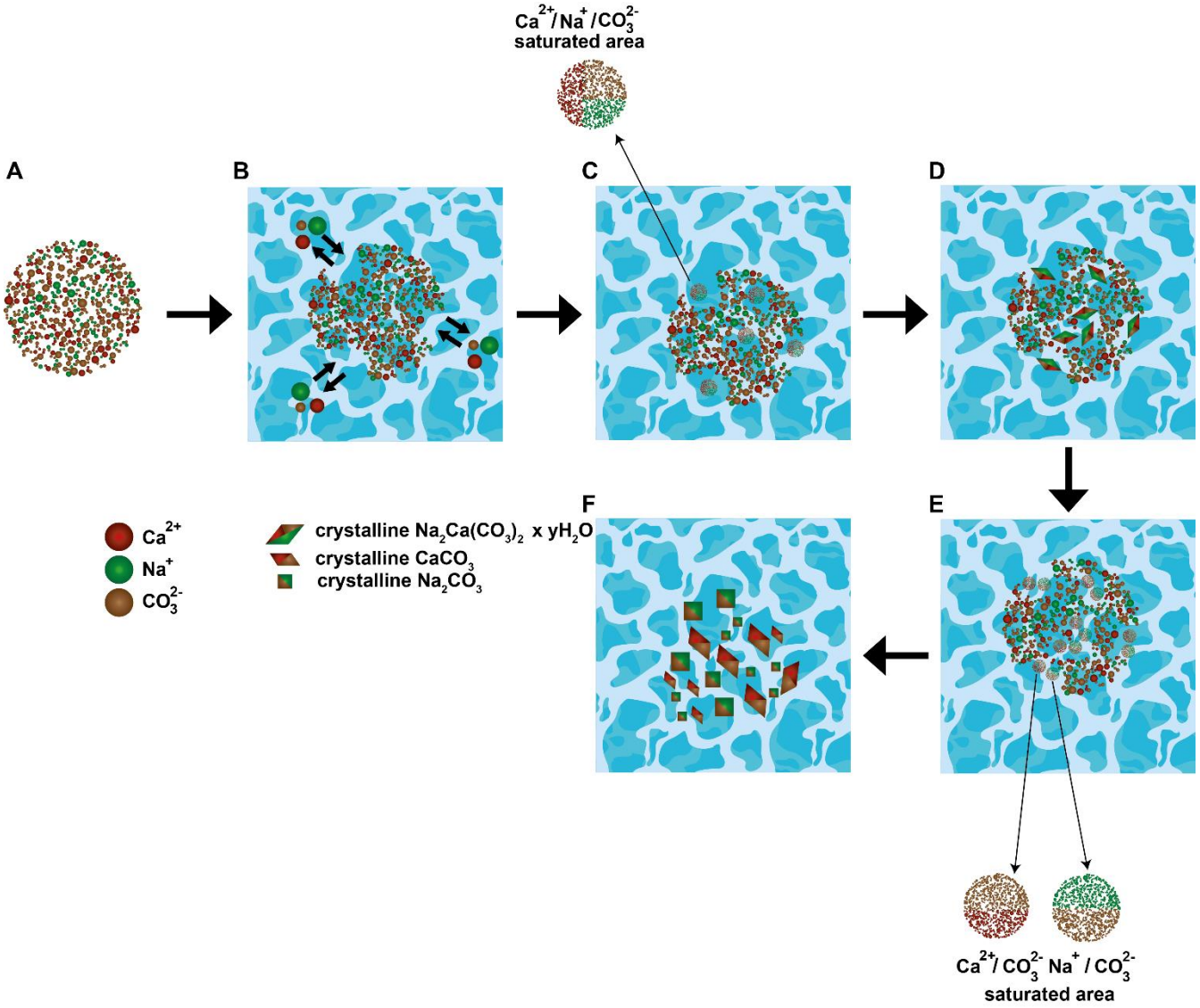

Figure S3.18. Possible hydration mechanism for aNaCC. In a first step, amorphous aNaCC (A) is brought into contact with a water/acetonitrile mixture. (B) Dissolution of aNaCC in the surface layer leads to areas of high supersaturation and partial reorganization. (C) Recrystallization occurs in the areas of high supersaturation. High local concentrations and slow diffusion lead to crystallization of metastable pirssonite ($Na_2Ca(CO_3)_2$ X $2H_2O$) and, after a longer reaction time, to the formation of gaylussite ($Na_2Ca(CO_3)_2$ X $5H_2O$). (D) Prolonged contact with water leads to phase separation and thus to areas with high sodium carbonate and calcium carbonate concentrations, (E) which crystallize in the final step as a mixture of from Na_2CO_3 and $CaCO_3$ X H_2O.

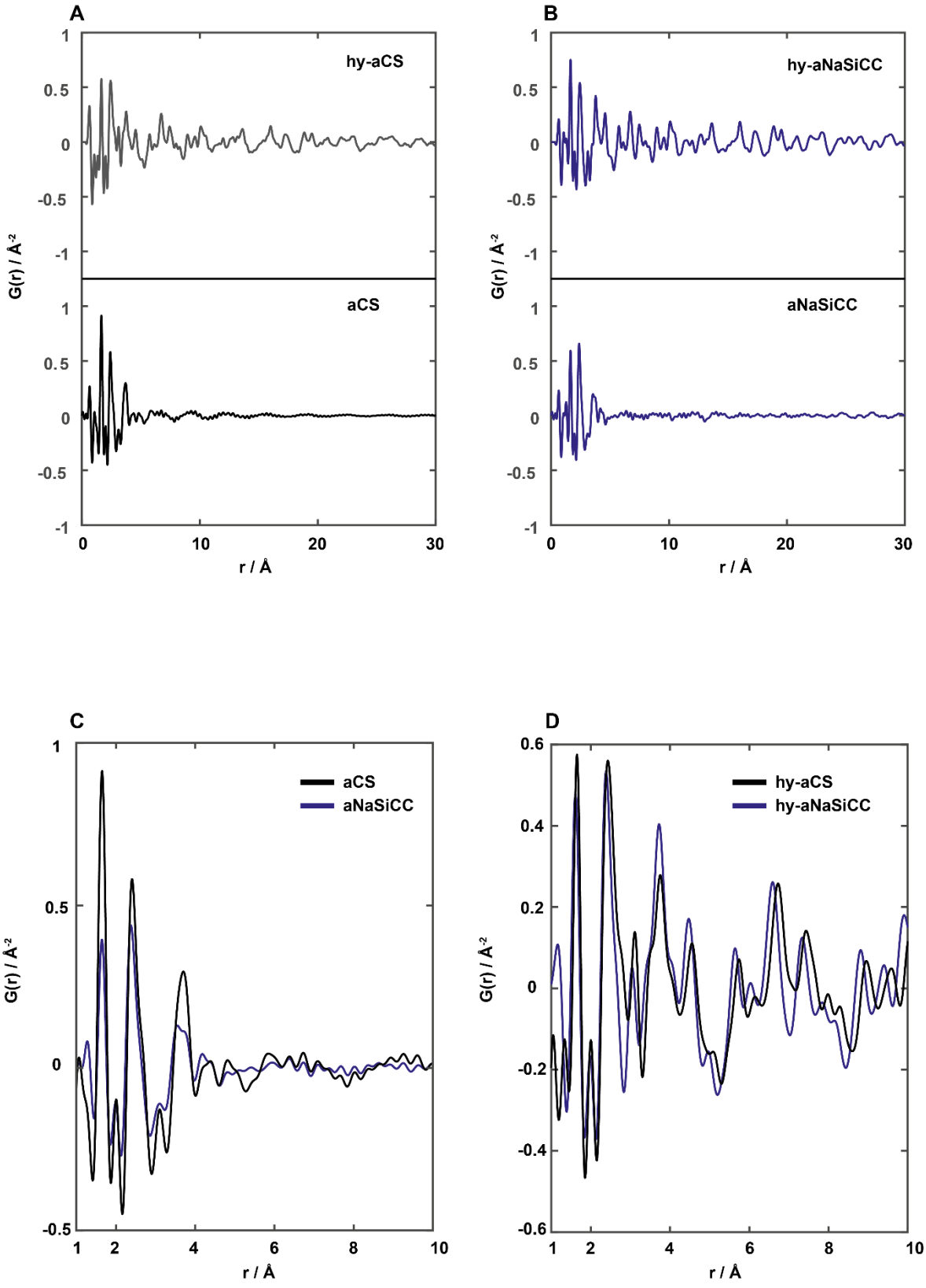

Figure S3.19. Reduced pair distribution functions of amorphous calcium silicate (black line) and aNiSiCC (blue line) and their hydration products hy-aCS and hy-aNaSiCC with C-S-H-like components in the range from 0 to 30 Å (A, B) and in the range from 0 to 10 Å (C, D).

Local structure of conventional C-S-H and alkali activated aNaSiCC

A conventional calcium silicate system was investigated to compare aNaSiCC and alkali-activated aNaSiCC. Amorphous calcium silicate (aCS), analogous to aNaSiCC, was prepared by grinding $Ca(OH)_2$ and SiO_2. The non-crystalline structure is revealed by a virtually featureless reduced atom pair distribution function G(R) above 5 Å (Figure S3.19). G(R) of aNaSiCC, different from that of aCS, has a maximum at 1.3 Å, which can be attributed to the C-O distance of the carbonate groups. In addition, differences in peak heights appear at 1.64, 2.4, and 4.1 Å, which can be attributed to differences in the local coordination of the carbonate building blocks.

After activation with NaOH, the atomic pair distribution functions for aCS and aNaSiCC show peaks up to the 30 Å range, indicating a mid-range order typical of C-S-H. The local region up to 10 Å is very similar for aCS and aNaSiCC after alkali activation. The main difference is the peak at 1.3 Å, which can be assigned to the C-O spacings of the carbonate building blocks and clearly proves that the carbonate groups are still present in the C-S-H-like structure.

Table S3.1. Assignment of the CO_3^{2-} and OH^- vibrational bands of the intermediate phases formed during the individual hydration steps. The columns highlighted in red refer to the reaction products formed by mixing $CaCO_3$ and Na_2CO_3 (referred to as carbonate). The columns highlighted in blue refer to the products formed by reaction of $CaCO_3$ and Na_2SiO_3 (referred to as silicate). The assignments for the silicate bands are given in Figure S2.

Vibrational bands	Amorphous		1. Hydration Step		2. Hydration Step		3. Hydration Step	
	Carbonate aNaCC	Silicate aNaSiCC	Carbonate Pirssonite	Silicate Pirssonite	Carbonate Gaylussite	Silicate Gaylussite	Carbonate MHC	Silicate Calcite
$\nu_1(CO_3^{2-})$	1066	/	1068	1068	/	/	1068 (weak)	/
$\nu_2(CO_3^{2-})$	866	868		868	872	872	878	874
$\nu_3(CO_3^{2-})$	1374	1399	1387	1406	1395	1399	1428	1409
	1426 (shoulder)	1466 (shoulder)	1480	1483	1432 (shoulder)	1428 (shoulder)		
$\nu_4(CO_3^{2-})$	717	716	711	711	721	720	701	713
	690	695			692	692	695	702
								695
$\delta(OH)$	/	/	1660	1660	1662	1662	1668	/
$\nu_s(OH)$	/	/	3074	3075	2940	2942	3200	/
			3217 (shoulder)	3213 (shoulder)	3260	3262		
					3330	3332		

Table S3.2. Assignment of the vibrational bands of the silicate groups and chemical shifts for the products formed in the hydration reaction of aNaSiCC.

Phase	^{29}Si NMR			FTIR	
	chemical shift / ppm	FWHM / ppm	Q^n	wavenumber / cm^{-1}	mode assignment
aNaSiCC	-79.6	14.1	Q^2	881	$\nu_s\ Si-O\ (Q^1)$
				928	$\nu_{as}\ Si-O\ (Q^2)$
				1018	$\nu_{as}\ Si-O\ (Q^3)$
Pirssonite $Na_2Ca(CO_3)_2 \cdot 2H_2O$	-79.9	14.0	Q^2	880	$\nu_{as}\ Si-O\ (Q^1)$
				933	$\nu_{as}\ Si-O\ (Q^2)$
				996	$\nu_{as}\ Si-O\ (Q^3)$
Gaylussite $Na_2Ca(CO_3)_2 \cdot 5H_2O$	-79.1	10	Q^1	879	$\nu_{as}\ Si-O\ (Q^1)$
	-83.9	5.7	Q^2	935	$\nu_{as}\ Si-O\ (Q^2)$
	-92.4	6.7	Q^3	972	$\nu_{as}\ Si-O\ (Q^2)$
Monohydrocalcite $CaCO_3 \cdot 1H_2O$	-78.4	4.1	Q^1	873	$\nu_{as}\ Si-O\ (Q^1)$
	-84.3	5.2	Q^2		
	-91.6	13	Q^3	973	$\nu_{as}\ Si-O\ (Q^2)$

Table S3.3. Parameters for the fits of the CP kinetics for the amorphous products formed in the different hydration steps of aNaCC.

Parameter	Pirssonite		Gaylussite		Monohydrocalcite	
	Amorphous	Crystalline	Amorphous	Crystalline	Amorphous	Crystalline
T_{IS} / ms	1.147	1.085	0.4435	0.9287	0.868	2.786
$T_{1\rho}^{H}$ / ms	703	10.24	8.541	4.626	6.217	2.773

Table S3.4. Parameters for the fits of the CP kinetics for the amorphous products formed in the different hydration steps of aNaSiCC.

Parameter	Pirssonite		Gaylussite		Monohydrocalcite	
	Amorphous	Crystalline	Amorphous	Crystalline	Amorphous	Crystalline
T_{IS} / ms	1.004	1.085	0.4819	0.8264	1.297	1.750
$T_{1\rho}^{H}$ / ms	52.28	10.24	11.73	5.788	6.936	43.04

Table S3.5: 3D ED parameters, residuals and crystallographic data for dynamical refinement of monohydrocalcite.

Monohydrocalcite, $CaCO_3$ X H_2O	
Crystal data	
Crystal system, space group	trigonal, $P3_221$
a (Å), *c* (Å), *V* (Å³)	6.129(6), 7.443(3), 242.1(4)
Z	3
Unit cell content	$Ca_3(CO_3)_3(H_2O)_3$
Data collection	
Radiation type	electrons, 300 kV
Wavelength (Å)	0.01970
Temperature (K)	97
Precession angle (deg.)	0.94
Projected crystal dimension (nm²)	1100x750
Resolution ($Å^{-1}$)	1.2
Tilt step (deg.)	1
No of frames	101
Completeness	100%
Dynamical structure refinement	
U_{iso} of Ca1/O1,O2,O3,C1 (Å²)	0.0073(8)/0.0112(9)
No. of used reflections (obs/all)	1091/2245
Average crystal thickness (nm)	140
Twin fraction [-1 0 0; 0 -1 0; 0 0 -1]	0.17(6)
g_{max}, Sg_{max}(matrix), RSg, Nor	1.3, 0.01, 0.8, 196
R1(obs)/R1(all), wR1(obs)/wR1(all) (%)	9.87/17.38, 11.46/12.90
goodness of fit (obs/all)	1.78/1.43
No. of refined parameters[1]	10+102

[1] Split into the terms of the sum structural parameters and scale factors.

References

[1] D. M. Sanders, W B. Person, L. L. Hench, *Appl. Spectrosc.*, **1974**, *28*, 247-255.
[2] I. Halasz, M. Agarwal, R. Li, N. Miller, *Catal. Letters*, **2007**, *117*, 34-42.
[3] A. R. Jones, R. Winter, G. N. Greaves, I. H. Smith, *J. Phys. Chem. B.*, **2005**, *49*, 23154-23161.
[4] H. Nebel, M. Neumann, C. Mayer, M. Epple, *Inorg. Chem.*, **2008**, *47*, 7874-7879.
[5] T. Furukawa, K. E. Fox, W. B. White; *J Chem. Phys.,* **1981**, *75*, 3226-3237.
[6] L. G. Bäck, S. Ali, S. Karlsson, D. Möncke, E. I. Kamitsos, B. Jonson, *Int. J. Appl. Glass. Sci.*, **2019**, *10*, 349-362.
[7] P. McMillan, *Am. Mineral.*, **1984**, *69*, 622c-644.
[8] G. Hauret, Y. Vaills, Y. Luspin, F. Gervais, B. Coté, *J. Non. Cryst. Solids*, **1994**, *170*, 175-181.
[9] P. McMillan, *Am. Mineral.*, **1984**, *69*, 645-659.
[10] M. R. Hansen, H. J. Jakobsen, J. Skibsted, *Inorg. Chem.*, **2003**, *42*, 2368-2377.
[11] J. F. Stebbins, *J. Non. Cryst. Solids.* **2020***, 6*, 100049.
[12] H. Maekawa, T. Maekawa, K. Kawamura; T. Yokokawa, *J. Non. Cryst. Solid*, **1991**, *127*, 53-64.
[13] W. Kolodziejski, J. Klinowski, *Chem. Rev.* **2002**, *102*, 613-628.
[14] B. Dickens, W. E. Brown, *Inorg. Chem.*, **1969**, *10*, 2093-2103.
[15] H. Effenberger, *Monats. Chem.*, **1981**, *112*, 899-909.
[16] J. Fend, Y. J. Lee, J. D. Kubicki, R. J. Reeder, B. L. Phillips, *Magn. Reson. Chem.*, **2008**, *46*, 408-417.
[17] R. Voelkel, *Angew. Chem. Int. Ed.*, **1988**, *27*, 1468-1483.
[18] M. J. Harris, E. K. H. Salje, *J. Condens. Matter. Phys.*, **1992**, *4*, 4399-4408.
[19] W. M. Haynes, D. R. Lide, T. J. Bruno. CRC Handbook of Chemistry and Physics: A Ready-refererence Book of Chemical and Physical Data. Boca Raton, Florida: CRC Press, 2016.
[20] E. E. Wilson, A. Awonusi, M. D. Morris, D. H. Kohn, M. M. J. Tecklenburg, L. W. Beck, *Biophys. J.*, **2006**, *90*, 3722-3731.
[21] J. Feng, Y. J. Lee, R. J. Reeder, B. L. Phillips, *Am. Min.*, **2006**, *91*, 957-960.
[22] D. R. Johnson, W. A. Robb, *Am. Min.*, **1973**, *58*, 778-784.
[23] J. Ihili, C. Wong, E. H. Noel, Y-Y. Kim, A. N. Kulak, H. Christenson, M. J. Duer, F. C. Meldrum, *Nat. Commun.*, **2014**, *5*, 3169.
[24] E. T. Stepkowska, *J. Therm. Anal. Calorim.*, **2005**, *80*, 727-733

4

A fast and sustainable route to bassanite nanocrystals from gypsum

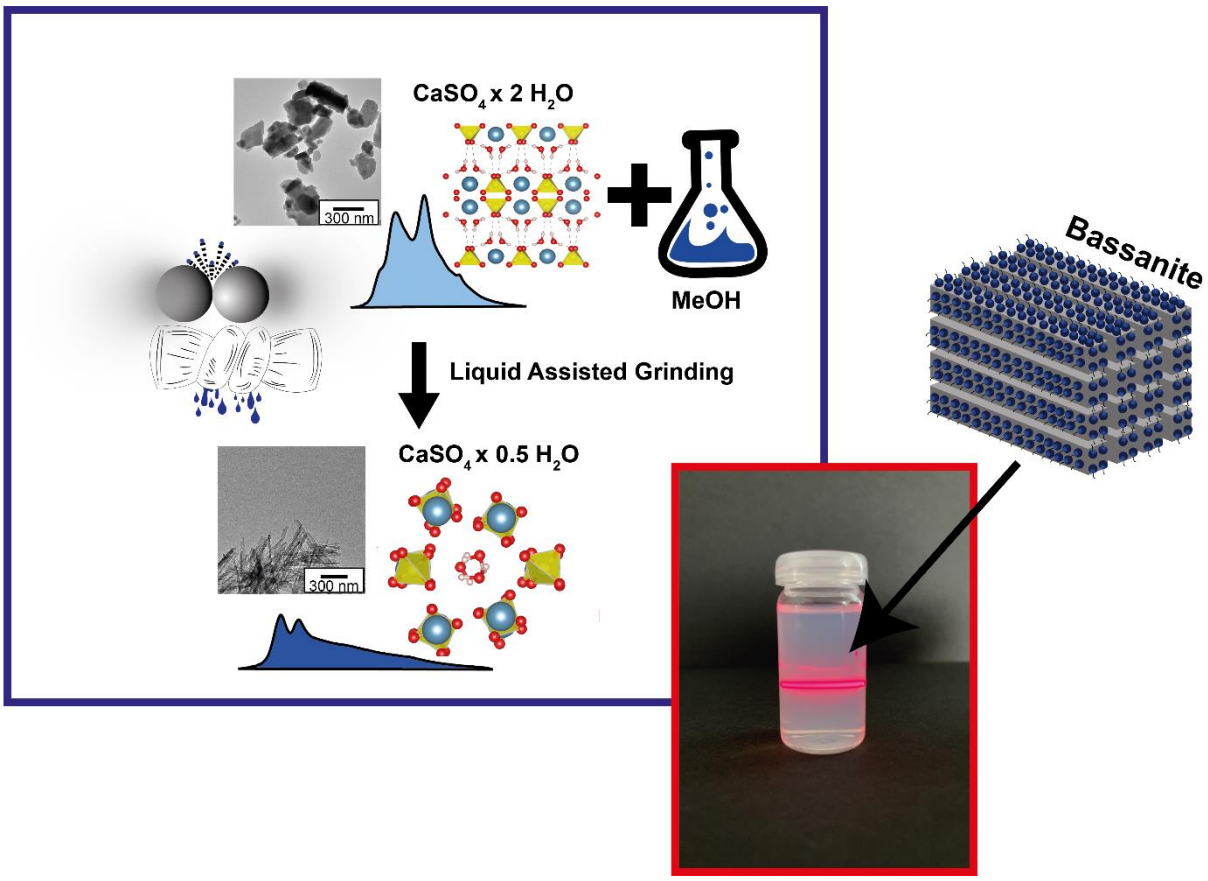

Synopsis

Solvent-assisted ball milling of gypsum leads to the formation of basanite nanocrystals enabling the formation of a binder material without the need for high-temperature calcination and emission of CO_2.

This chapter contains an adapted reproduction of a manuscript accepted in *Advanced Functional Materials*.

Authorship Contribution

Study conception and design	M. Maslyk W. Tremel
Acquisition of data	M. Maslyk Z. Dallos T. Hieke M. Koziol M. Mondeshki
Analysis and interpretation of data	M. Maslyk Z. Dallos
Drafting of manuscript	M. Maslyk
Critical Revision	W. Tremel M. Mondeshki U. Kolb

4.1 Relevance to doctoral thesis

A commonly found mineral in the use of construction industry is *gypsum* ($CaSO_4 \times 2H_2O$), which is mainly used in the form of drywalls (also known as plasterboards). Typically, additional additives as fiber, plasticizer and foaming agents are added to attain specific properties. The tremendous interest in this material arises from its polymorphism, as simple heating processes, up to temperatures around 250° C lead to *bassanite* ($CaSO_4 \times 0.5H_2O$) and anhydrite ($CaSO_4$), which by addition of water can rehydrate to *gypsum.* Although, at first this cycle appears simple, the control in polymorphism is of fundamental interest. Minor changes in the surrounding parameters can already change the stability of the underlying phases. Although the needed temperature is significantly lower comparaed to the burning process in cement manufacture, the drying process is associated with a significant energy demand. As has been shown previously, a specific control in the polymorphism of different minerals can be achieved by use of mechanochemistry. Therefore, this project focused on the access to metastable polymorphs in the calcium sulfate hydrate system. Unlike in previous projects no inorganic impurities have been added, as it could be shown that use of different solvents during ball milling affecs the polymorphism tremendously. By application of several spectroscopic, diffraction and microscopic methods it could be shown that ball milling of *gypsum* in cyclohexane leads to a mixture of *gypsum* and *bassanite*, whereas the use of methanol leads to pure *bassanite*. Thus, the participation of auxiliary solvents in milling reactions for phase transformations could be revealed. In addition it was found that prolonged milling times lead to a stable nanoparticle dispersion. Application of NMR showed that the particles are surface-functionalized with methanol. As the milling procedure is easily scalable and the dispersion is easily mixable with oher organic solvents, this process might find application in industrial processes related to plasterboard manufacturing. In summary it could be shown that ball milling is a feasible approach to polymorph selection in the calcium sulfate hydrate system, depending on the deployed solvents. In addition a simple, scalable route to stable bassanite dispersions was shown to be obtainable by prolonged milling times.

4.2 Introduction

Gypsum ($CaSO_4 \times 2H_2O$, dihydrate) has been used in construction since time immemorial. Today, stucco, screed, plasterboard, putty, and other products for the construction industry are based on this binder.[1] In addition, it is used as a component of cement,[2,3] for 3D printing,[4,5] as fertilizer or as food additive (cleaning of wines, refined sugar, canned vegetables and animal feed).[6] Its biocompatibility allows medical (e.g., plaster bandages, surgical and dental molds, production of toothpaste)[7,8,9] or pharmaceutical (drug delivery) use.[10] When gypsum is heated above ~150°C in the dry state [11] (or at 75 °C in methanol–water solutions),[12] some of the crystal water is removed and $CaSO_4 \times ½\ H_2O$ (hemihydrate) is formed.[13] It is metastable at all temperatures and occurs in nature as the rare mineral bassanite[14] and as a biomineral in some deep-sea medusae.[15] Calcination of gypsum at higher temperatures (> 800°C) yields anhydrite ($CaSO_4$), which is the thermodynamically stable form at higher temperature, where all water of crystallization is removed.[16] The hydration of anhydrite in water is kinetically hindered below 70°C.[17,18] Therefore, anhydrite occurs in water-soluble mineral sediments that are formed by concentration/evaporation from aqueous solutions (evaporites).[19] Anhydrite and bassanite in soils are mainly formed by dehydration of gypsum. Bassanite–anhydrite successions away from the gypsum core show that bassanite is an intermediate in the transformation of gypsum to anhydrite.[20] Calcium sulfate is one of the most abundant minerals on earth, and deposits were found even on Mars.[21] Huge deposits of gypsum and anhydrite occur in nature, and they are mined industrially.[22] Although industrially produced calcium sulfate is colloquially - but incorrectly - referred to as gypsum, it occurs in different hydration states with different physical properties. Chemically, the most common calcium sulfate phase is $CaSO_4 \times ½\ H_2O$ (hemihydrate), one of the world's most widely produced inorganic compounds (worldwide annual consumption ~150 million metric tons).[13] Hemihydrate or so-called plaster of Paris is produced by calcination of gypsum. With water it reacts back to gypsum in a rapid exothermic hydration process,[23] which accounts for the setting and hardening of plaster and cement materials. Therefore, biological systems generate hemihydrate far from chemical equilibrium.[24] The steadily increasing demand for calcium sulfate has put the manufacturing and crystallization processes into the focus of investigations. There is increasing evidence that mineralization proceeds via multi-stage pathways including amorphous precursor phases[25-37] and/or bassanite intermediates[25-31,33]

that convert to gypsum *via* oriented attachment of nanocrystals.[28] Sub-3 nanometer particles have been identified by time-resolved small-angle X-ray scattering (SAXS) as primary species during crystallization,[32] and amorphous calcium sulfate, which can be stabilized by confinement,[38] has been shown to precede bassanite formation.[26,32] All calcium sulfate polymorphs can be prepared selectively by controlling the ratio of water/organic solvent mixtures.[30] The industrial production of bassanite has high added value for a broad range of applications, most of which are based on the reversibility of the dehydration-rehydration reactions of gypsum. From an economic point of view, it is important to achieve dehydration in the shortest possible time with the lowest possible energy input, because raw material costs are very low and energy costs account for the lion's share of this calcination process.[39] The dehydration process is carried out successively during a period of time and depends on a variety of factors, especially the type of calcination, the granulation of the pure raw material, the amount of mineral impurities or other chemical compounds. Calcination temperatures between 100 and 200°C are employed for the building industry. If dehydration is carried out in air furnaces and the energy is produced from fossil fuels, the ecological costs are particularly high. Using solar energy to produce bassanite by calcination of gypsum is one way to improve the carbon footprint.[40] Alternatively, bassanite can be obtained from gypsum by an autoclave process. In contrast to the large-scale production process of β-bassanite, the autoclave reaction favors the conversion of gypsum into α-hemihydrate. This is promising in terms of its material properties and could find industrial applications. [41] To circumvent the high energy consumption and unfavorable continuous operation of the autoclave process, salt/acid or alcohol/water solution processes are pursued as alternative "green" approaches, but they are still operated often only at a laboratory or pilot scale. We report on a new way to produce bassanite from gypsum by solvent-assisted grinding, which allows high energy conservation by bypassing calcination. Depending on grinding time and auxiliary solvent, even stable dispersions of bassanite can be produced. The great advantage of grinding is that scale-up is easily possible.[42] The transformation of gypsum into bassanite was tracked by Fourier transform infrared spectroscopy (FTIR), powder X-ray diffraction (PXRD), transmission (TEM) and scanning electron microscopy (SEM) to gain a mechanistic understanding of the transformation. The analysis revealed that bassanite formation proceeds *via* the reverse pathway to the formation of gypsum from bassanite in solution. ^{1}H nuclear magnetic resonance spectroscopy (^{1}H NMR) and dynamic light scattering (DLS) showed that the stability of the $CaSO_4$ dispersions before and after drying was due to the

facile exchange of crystal water against the auxiliary agent methanol. The good dispersibility of the product allowed the preparation of transparent films and thus may open new avenues for the preparation of $CaSO_4$/polymer composites since both components can be blended in the organic co-solvent.

4.3 Results and discussion

Ball-Milling Reaction

Solvent-assisted ball milling of gypsum was tested with cyclohexane and methanol. Full conversion to bassanite was achieved with the polar auxiliary solvent methanol (ball-milled calcium sulfate, BMCS MeOH) as shown by FTIR, PXRD as well as TEM and SEM. With nonpolar cyclohexane, the conversion was incomplete (ball-milled calcium sulfate cyclohexane, BMCS-CH) (Figure 4.1, Figure S4.1).

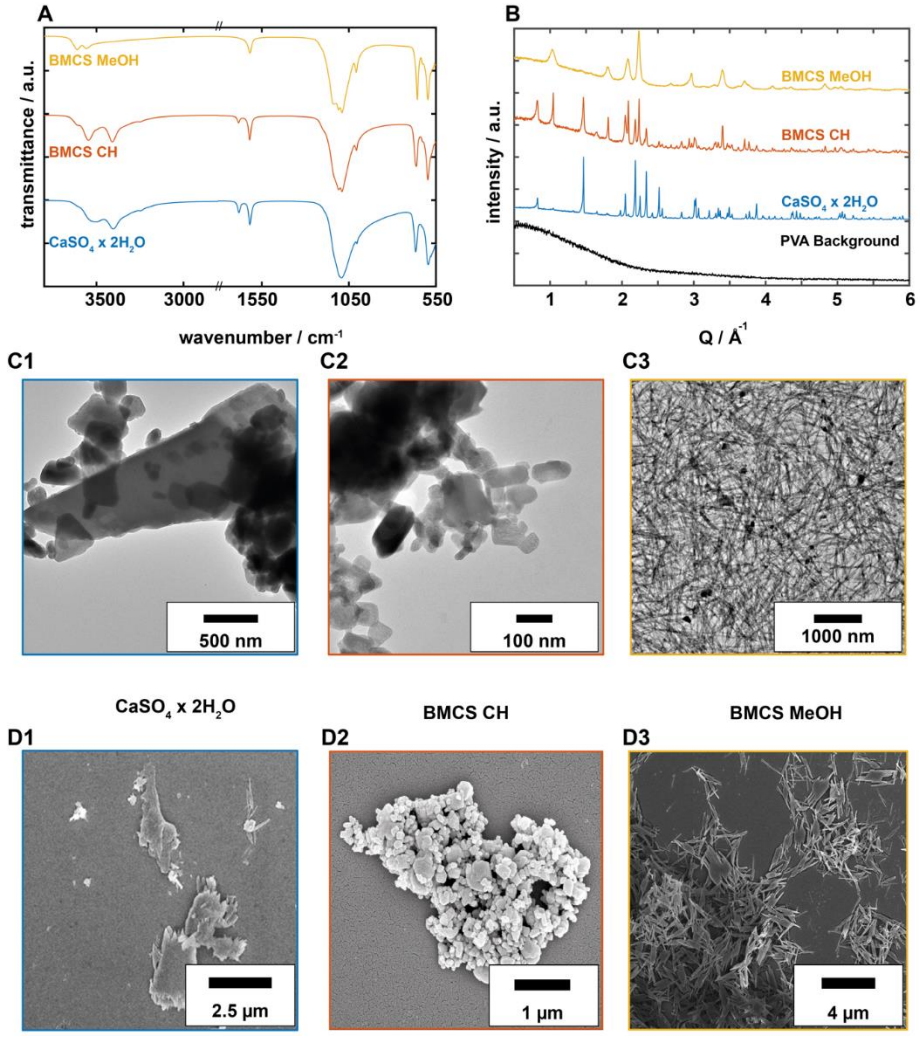

Figure 4.1. (A) Overview FTIR spectra, (B) X-ray diffractograms, (C) TEM and (D) SEM images of pure gypsum ($CaSO_4 \times 2H_2O$, blue lines and squares), gypsum ball-milled with cyclohexane (red lines and squares) and gypsum ball-milled in methanol.

Gypsum crystals have a plate-like morphology and diameters in the micrometer range (Figure 4.1C1, D1). Smaller platelets and nanocrystals with ill-defined morphologies are produced by ball milling in cyclohexane, (Figure 4.1C2, D2). Needle-like nanocrystals were obtained in methanol (Figure 4.1C3, D3). Similar results have been reported for the precipitating $CaSO_4$ from alcoholic solution.[31,43,44]

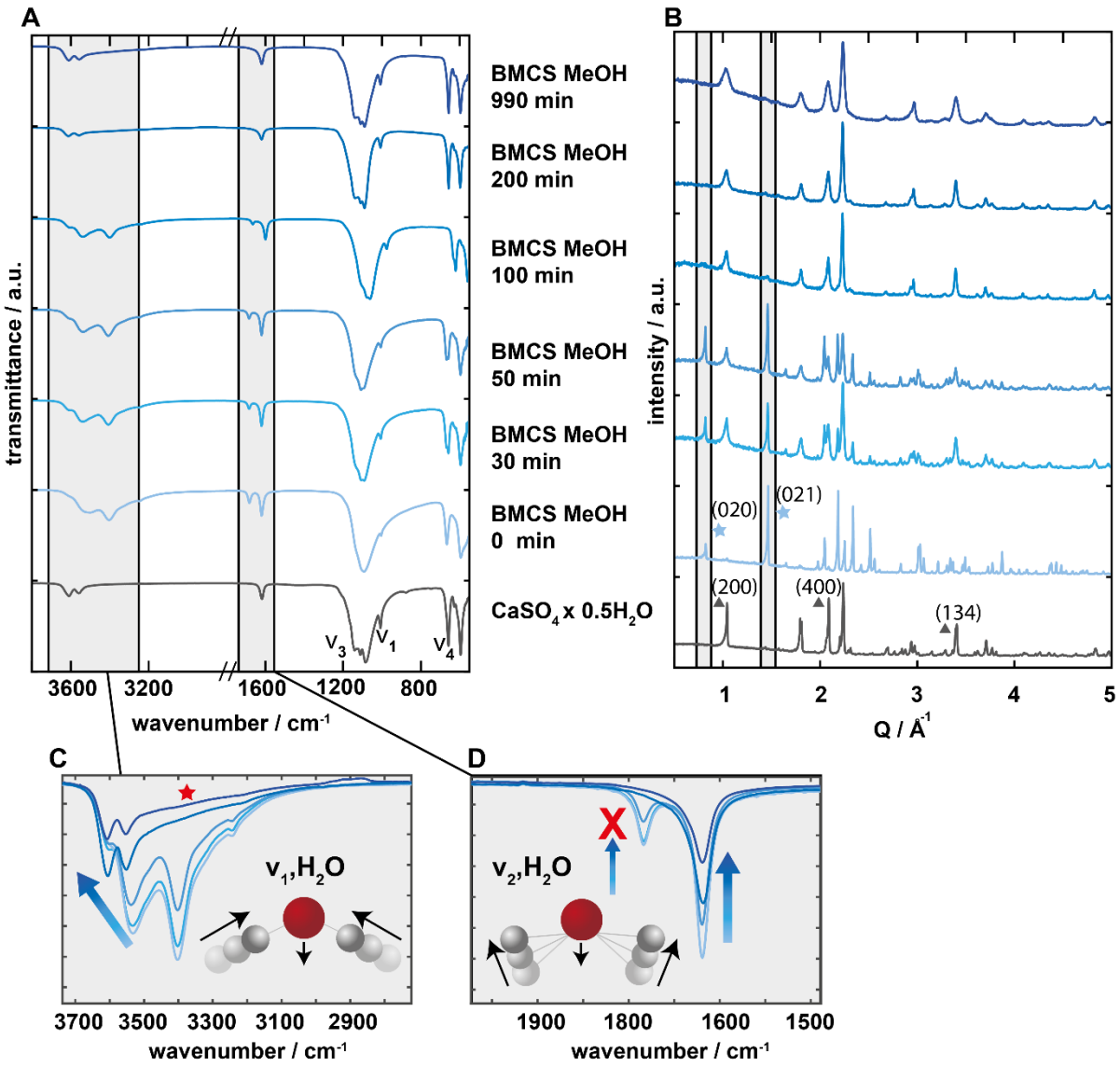

Figure 4.2 Progression of the milling reaction after different reaction times, monitored by (A) FTIR spectroscopy and (B) PXRD. Reflections of bassanite are marked with triangles, reflections of gypsum with stars. The reaction time is coded by the blue color depth. Insets (C, D) show magnified FTIR spectra of the O-H stretching and bending modes.

The kinetics of the grinding reaction were studied by taking "snapshots". Since the kinetics of the grinding reaction is slow, it could be stopped after different time intervals by quenching the hydration reaction with acetone. The quenched intermediates were investigated by FTIR spectroscopy and PXRD. The FTIR spectra show pronounced changes for the O-H stretching (ν_1, H_2O) and bending (ν_2, H_2O) modes of crystal water. A

shoulder at 3604 cm^{-1} in the v_1 region indicates the formation of bassanite, in harmony with the X-ray diffractograms where the 200, 400 and 134 reflections of bassanite appeared after 30 minutes of milling (Figure 4.1B, D). The intensity of the O-H stretching modes (v_3 3509 cm^{-1}, v_1 3399 cm^{-1}) of gypsum decreased, whereas the intensity of the O-H stretches (v_3 3604 cm^{-1}, v_1 3552 cm^{-1}) of bassanite increased. A broad intensity distribution remained between 3500 and 2900 cm^{-1} (Figure 4.2 A,C) compatible with disordered O-H groups due to the occlusion of methanol. The X-ray diffractograms showed a decreasing intensity and a broadening of the 020 and 021 reflections with time. After ~30 minutes of milling the first reflections of bassanite appeared, which broadened slightly after prolonged milling. Only traces of gypsum remained after ~100 minutes and pure bassanite was formed after ~200 minutes. Extending the milling time up to 990 minutes led to the formation a stable dispersion of bassanite nanoparticles. TEM images show the formation of needle-like nanocrystals with diameters of a few nm and lengths of ~100 nm (Figure 4.1C). Different from TEM, which provides static information concerning the structure and aggregation of dry samples, DLS is an ensemble technique that reveals the dynamic behavior of nanocrystals in dispersion (Figure 4.3A, B). DLS revealed the presence of polydisperse bassanite nanoparticles with hydrodynamic radii of $R_{H,1}$ = 165 nm, $R_{H,2}$ = 729 nm, and $R_{H,3}$ = 3.9 µm in methanolic dispersion (Figure 4.3A).

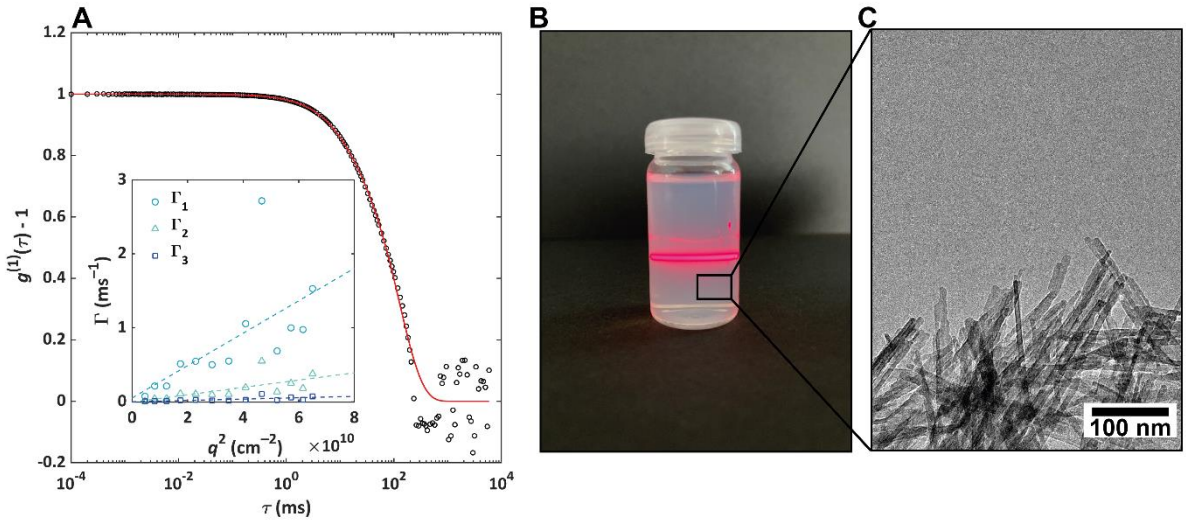

Figure 4.3. (A) Exemplary normalized field correlation function $g^{(1)}(\tau)$ of the nanoparticle dispersion in methanol (black open circles) and fit to a tri-exponential decay (red line). Inset: Γ_{1-3} vs. q^2 reveals at least three diffusing species. (B) Tyndall scattering of a laser beam by bassanite nanoneedles in methanol dispersion. (C) TEM image showing bassanite nanoneedles with lengths of ~ 100 nm.

Solvent Surface Effect

A stable dispersion of bassanite nanoparticles was obtained by extended milling in methanol (990 minutes). It showed an excellent miscibility with organic solvents like ethylene glycol (Figure S2) The molecular interactions responsible for the stability the dispersion were elucidated by ^{1}H liquid and solid state NMR spectroscopy. The ^{1}H ssNMR spectrum of the milled material after centrifugation and subsequent drying of the dispersion was compared with the one of gypsum (as starting material in the mechanochemical reaction) (Figure 4A). Whereas the ^{1}H ssNMR spectrum of gypsum recorded at 10 kHz MAS shows a signal at 4.60 ppm with a full width at half-maximum (fwhm) of 1700 Hz, attributed to the structural water, the ^{1}H resonance detected in the spectrum of the sample milled in methanol (BMCS MeOH) is significantly broadened. After deconvolution the spectrum consists of three signals located at 1.3 ppm (FWHM 2110 Hz), 4.4 ppm (790 Hz) and 4.8 ppm (2670 Hz), which could be assigned to methyl protons as well as two different hydroxyl protons, respectively.The broader and more intense hydroxyl resonance is probably related to structural water in bassanite molecules (presumably in different bassanite polymorphs with respect to the water content). The observed broadening of the resonances of the surface methanol molecules results from reduced dynamics related with stronger proton-proton dipolar couplings which cannot be averaged out by the magic angle spinning at moderate spinning frequencies. To gain resolution due to the fast molecular motion resulting in averaging out of the anisotropic interactions (anisotropy of the chemical shift, dipole-dipole couplings and quadrupole couplings) a variety of ^{1}H solution NMR methods were used to further investigate the bassanite nanoparticles.

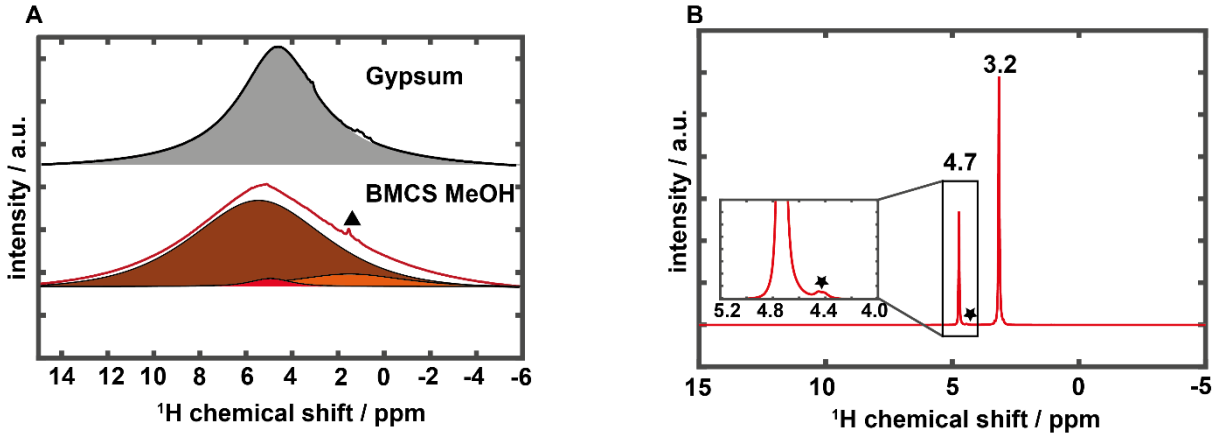

Figure 4.4: Comparison of the ^{1}H solid state NMR spectrum of gypsum and BMCS MeOH showing a broadened signal in BMCS MeOH (A). ^{1}H NMR spectrum of the bassanite dispersion in methanol (B).

The ^{1}H NMR spectrum of bassanite nanoparticles in methanol showed four signals. Two of them (3.2 ppm and 4.7 ppm, Figure 4.4B) correspond to the CH_3 and OH resonances of methanol (Figure S4.3). The other two resonances at 4.4 ppm (Figure 4.4B, *) presumably occur from the water incorporated in the bassanite structure, however, they could also originate from solvent molecules functionalizing the nanoparticle surface in the slow exchange regime. Temperature dependent ^{1}H NMR spectra were recorded, aiming for enhancement of the exchange and changes in the chemical shifts of the solvent hydroxyl group and the signals at 4.4 ppm, until merging (in the fast exchange regime). These experiments did not reveal merging between the signals at 4.4 and 4.7 ppm. The signals at 4.4 ppm however, merge at higher temperatures due to faster particle motion (Figure S4.4). This observation could be explained by an exchange of the water. Thus, we exclude the possibility of the resonance at 4.4 ppm to arise from surface functionalizing solvent hydroxyl groups and attribute it to two different water environments in the bassanite structure. The $CaSO_4$ x 0.5 H_2O nanoparticles were further investigated with ^{1}H NOESY NMR spectroscopy. This NMR experiment probes the through space proton dipole-dipole couplings revealing contacts between dipolar coupled proton species in close proximity, i.e. 4 – 5 Å, as off diagonal peaks. The ^{1}H NOESY NMR spectrum recorded with a mixing time of 1 ms (Figure 4.5A) reveals one broad diagonal and two off-diagonal signals (Figure 5 B). The broad diagonal signal ranging from 4.3 ppm to 5.1 ppm for the OH protons of methanol is related with a distribution of environments and is assumed to arise from the interaction of the hydroxyl protons with different bassanite surface sites. The two clearly visible off-diagonal signals ((4.5 ppm, 4.8 ppm) and (4.4 ppm, 4.7 ppm)) are probably related to the water protons confined in the hexagonal channels in the crystalline structure of bassanite in close proximity to the nanoparticle surface and thus methanolic hydroxyl groups. To confirm this assumption diffusion based NMR experiments were recorded for pure methanol (Figure 4.5C, red lines) and the bassanite dispersion (Figure 5C, black lines) and subsequently overlaid. On one hand the methanol in the dispersion would diffuse more slowly compared to the pure solvent due to exchange with the surface bound methanol. On the other an equivalent diffusion coefficient for the water in the bassanite structure and the surface methanol molecules is expected as the particle movement would be the rate determining step. Indeed, the recorded spectra (Figure 4.5C) show a difference between the D values for pure methanol ($7.9 * 10^{-9}$) and the one in the bassanite dispersion ($1.2 * 10^{-9}$). The observed difference in the diffusion coefficients confirms the functionalization of the nanoparticles by surface bound methanol molecules, which most likely exchange

with the surrounding solvent molecules and are thus the reason for the stability of the dispersion in methanol and other polar solvents. In general, the interaction of methanol molecules with surfaces would lead to a slower diffusion on average as the in this case the solvation shell would also contribute to the hydrodynamic radius of the bassanite particles.

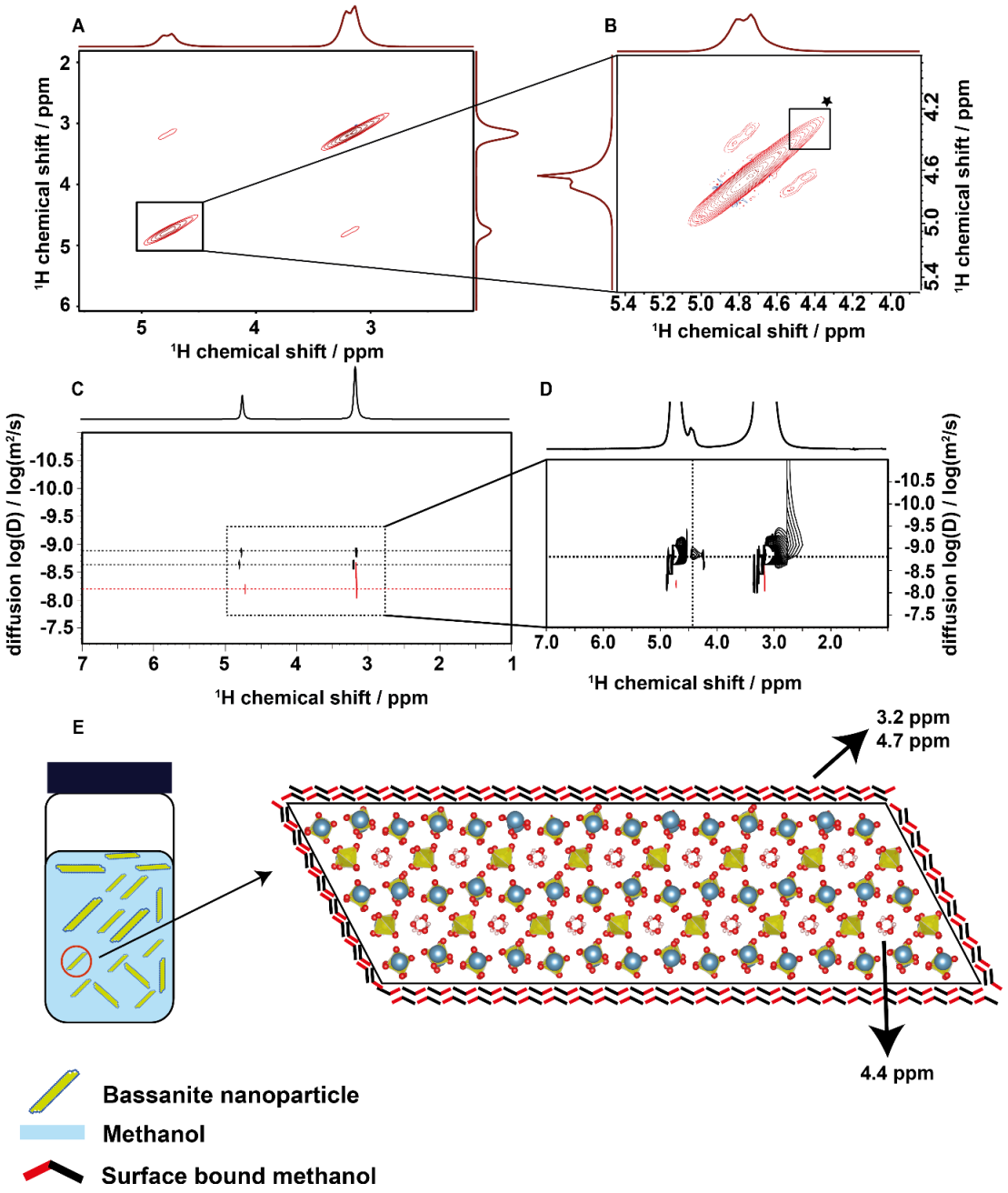

Figure 4.5. (A)^{1}H NOESY NMR spectrum depicting a coupling between the O-H groups of methanol molecules resonating at 4.8 ppm. (B) Magnification of the inset in the ^{1}H NOESY NMR spectrum revealing coupling of the water signal of bassanite at 4.4 ppm with methanol molecules. (C) ^{1}H DOSY spectra of methanol (red) and bassanite dispersion (black). The slower diffusion of methanol molecules in bassanite dispersions indicates a stabilization by surface-bound methanol (D) Magnification of the inset in the ^{1}H DOSY spectrum of methanol (red) and bassanite dispersion (black), revealing the diffusion coefficient of bassanite. (E) Schematic illustration of a bassanite nanoparticle functionalization by methanol molecules viewed along [001] showing the distinct hexagonal channels filled by water molecules.

The DOSY experiments (Figure 4.5D) show that the signals at 4.4 ppm have the same diffusion coefficient as part of the methanol molecules. This confirms the presence of water in bassanite structure. Incorporation of methanol in the basanite pores during the synthesis of the nanoparticles was not confirmed, however, cannot be completely ruled out.In conclusion methanol molecules functionalize the bassanite NP surface and act as ligands stabilizing the NP dispersion in polar organic solvents. The surface functionalization is confirmed by the fact that the ligands have the same diffusion coefficient as the water molecules incorporated in the bassanite structure. The two different off-diagonal resonance signals in the NOESY spectrum could occur from different type of bassanite polymorphs due to differences in the hydration state of bassanite. Potentially, milling in methanol might lead to the formation of subhydrates in the calcium sulfate system or a partial substitution by methanol.

Thermal Stability and Microstructure

Thermal analysis allows to analyze physical changes with time and temperature when bassanite nanocrystals are heated or cooled. The TGA/TGA profile of the bassanite nanocrystals dried from dispersion shows an endothermic mass loss of ~7.9% at ~140 °C (Figure 6A). The transition of $CaSO_4 \times ½\ H_2O$ -> $CaSO_4$ corresponds to a mass loss of 6.3%$_w$ for crystal water. Partial substitution of water by methanol leads to the observed higher mass loss. Based on the analytical information from ^{1}H MAS-NMR that ~20% of the crystal water been replaced by methanol (corresponding to a composition $CaSO_4 \times 0.4\ H_2O \times 0.1\ CH_3OH$) a mass loss of 7.1% is expected H_2O / CH_3OH (4/1), close to the experimental value. PXRD and Rietveld analysis of the product obtained by milling gypsum in methanol showed the formation of bassanite with cell parameters of a = 12.083 Å, b = 6.903 Å and c = 12.683 Å and a crystallite size of ~30 nm (Figure 4.6B). This result seems to contradict the broad distribution obtained with DLS and conventional TEM imaging. However, one must consider that the particle size distribution in a solid bulk sample corresponds only to a limited extent to a model of discrete spherical particles in dispersion (DLS) or individual particles in electron microscopy (TEM). When gypsum was ball-milled in cyclohexane, two DTA signals at 110°C and 150°C with a mass loss of 15% were obtained. Since a mass loss of 20% is expected for pure gypsum, this is compatible with a partial (80%) conversion of gypsum and bassanite (Figure S4.5).

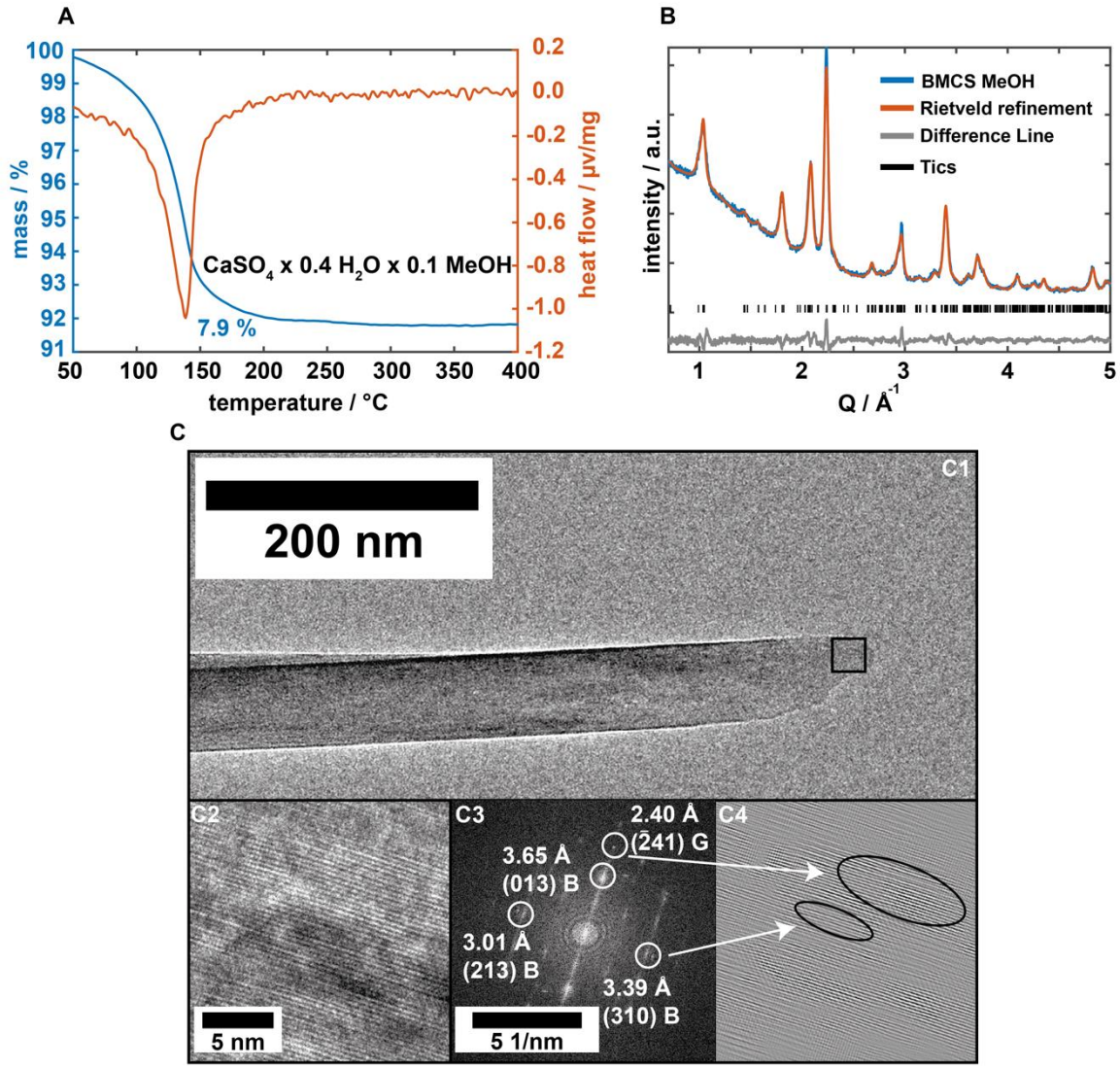

Figure 4.6 (A) TGA (blue line) and DTA traces (red line) for dried bassanite nanocrystals and (B) Rietveld refinement. (C) TEM image (C1) and HRTEM image (C2) of the dried bassanite nanocrystals showing the lattice planes, the reduced Fast-Fourier Transformation [FFT] (C3) and Inverse-Transformed Fourier Transformation [IFFT] (C4).

Figure 4.6C1 shows the TEM image of a single bassanite needle with a length of ~500 nm. A magnified view (Figure 4.6C2) shows a periodic arrangement of lattice planes in the nanocrystal. The Fast-Fourier transform (FFT) was calculated with the Gatan Digital Micrograph Software[45] (Figure 4.6C3) and the electron diffraction pattern was indexed based on the bassanite structure (B). Since the lattice planes were not compatible with a specific zone the needle must consist of several crystalline domains, forming a single needle by oriented attachment.[28] An inverse Fourier transform of the calculated FFT shows dislocations and contrast changes compatible with a non-uniform *d* spacing. Although PXRD and HRTEM show the samples to consist mainly of bassanite, small amounts of anhydrite were found in HRTEM, indicating that mechanochemical dehydration is feasible

by adjusting the milling conditions. Milling of commercial bassanite in methanol and cyclohexane showed indeed the formation of anhydrite (Figure S4.6).

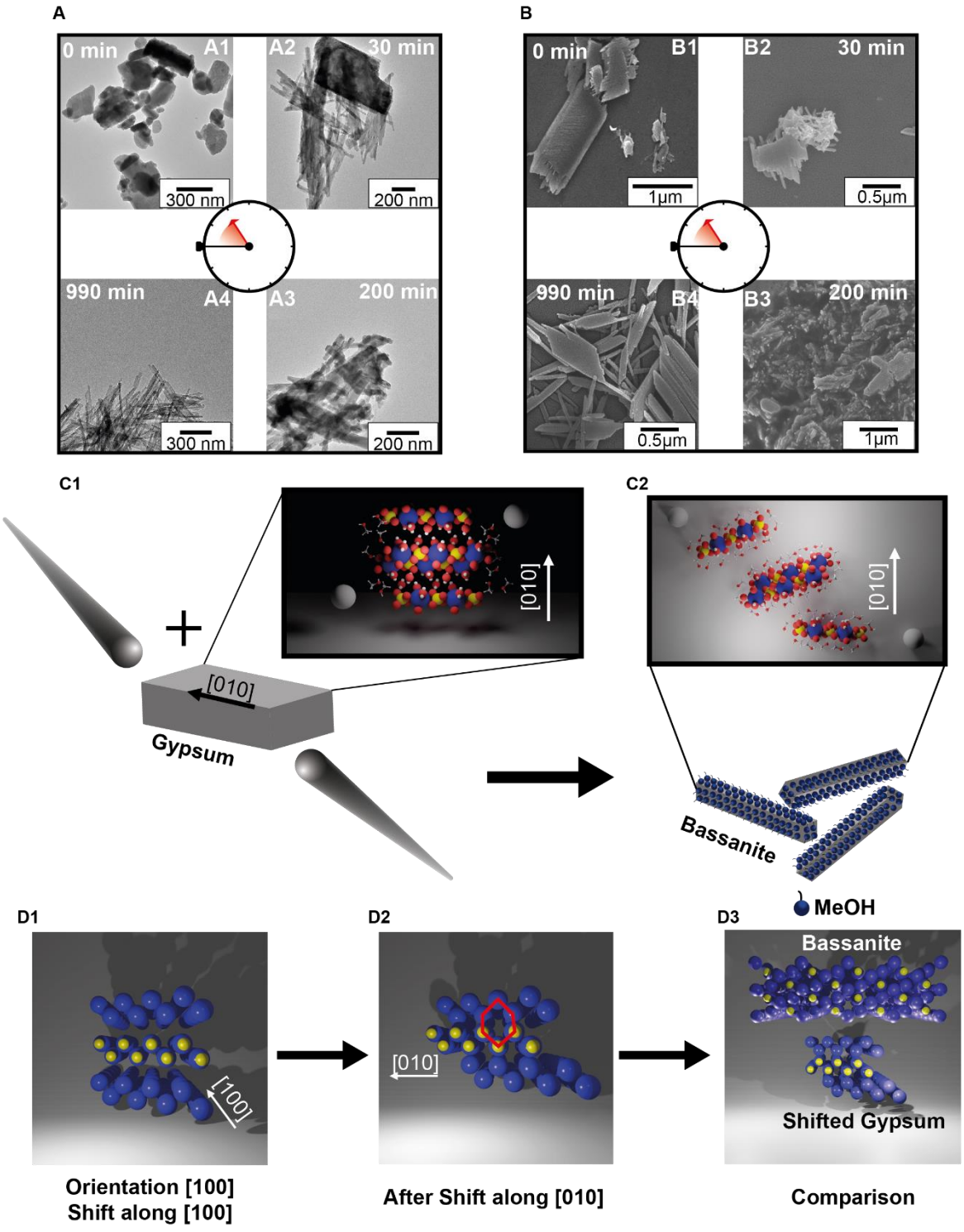

Figure 4.7(A) TEM and (B) SEM images taken after 0, 30 220 and 990 minutes of milling showing the transformation of plate like structures into fine needles. (C1) Schematic sketch of the effect of methanol assisted ball milling. (C2) Sketch of functionalized bassanite nanoparticles, resulting from a cleavage parallel to [010] (D1) View of calcium and sulfur atoms shifted along [100]. (D2) A shearing force parallel to [010] could result in hexagonal channels (red hexagon). (D3) Comparison of gypsum and bassanite along the channel structure

Gypsum to Bassanite Transformation

TEM and SEM "snapshots" were taken at different stages of the milling and crystallization process. For this purpose, the reaction was stopped, aliquots were taken, centrifuged and washed with acetone to prevent further phase transformations. The corresponding samples were then dispersed in acetone and dropped onto a TEM grid or SEM holder respectively. Micrometer-sized platelets were present in the TEM and SEM at the start of the grinding reaction (Figure 6A1 and B1). PXRD showed that bassanite was formed after short reaction time. Crystallites with needle-like and plate-like morphologies were present in TEM and SEM (Figure 4.6A, B 30 minutes). This indicates that the platelets are broken up by shear forces and separated from each other by surface functionalization with methanol. As the crystal structure of gypsum consists of layers, made up of tightly bound Ca^{2+} and SO_4^{2-} ions, which are separated by a hydrogen network made up of water molecules in between these layers, it is assumed that the shear force from the milling is sufficient to cleave these planes parallel to the [010] direction (Figure 7C1). Due to the high polarity, methanol might attach to these surfaces and weaken the hydrogen network. In addition, it plays a fundamental role in stabilizing the resulting bassanite nanoparticles (Figure 7C2). The partial dehydration might result from the generated heat during collisions and the interaction with methanol. The mutual Ca…SO_4 chains in the different polymorphs, make a structural rearrangement easily achievable. A shift in the layers along [100] and [010] leads to hexagonal channels, similar to bassanite. (Figure 7D1 to Figure 7D3). Other than in methanol, grinding in cyclohexane does not lead to the formation of specific morphologies and the transformation to bassanite was incomplete (Figure S7). PXRD and FTIR analysis show that gypsum transformed to bassanite completely with increasing grinding time (~200 minutes). The corresponding TEM and SEM images show needle-like crystallites after 200 min (Figure 4.6A2 and B2). A stable dispersion was obtained for still higher reaction times (~990 min), and the needles had a different aspect ratio (Figure 4.6A3 and B3). The needles were not stable in the electron beam. Rapid imaging was required to prevent radiation-induced dehydration (Figure S4.8). Their formation can be explained by a stepwise reduction in particle size with concomitant stabilization by surface binding of the auxiliary agent methanol. TEM and SEM analysis show that the bassanite nanocrystals assemble into needle-like structures.

Film Casting

Bassanite nanocrystals prepared by ball-milling form clear and stable dispersions in methanol (Figure 4.8A, inset). These dispersions are miscible with a variety of organic solvents (e.g., acetone, different alcohols and ethylene glycol) without any signs of precipitation. This allowed to cast dense nanoparticle films on a glass slide, which form transparent films after drying (Figure 4.8A). Mixing the dispersion with non-polar solvents such as cyclohexane lead phase separation. Adding a few drops of water to the dispersion causes an immediate precipitation of needle-like gypsum nanocrystals (~20 µm in length, Figure 4.7C1, inset).

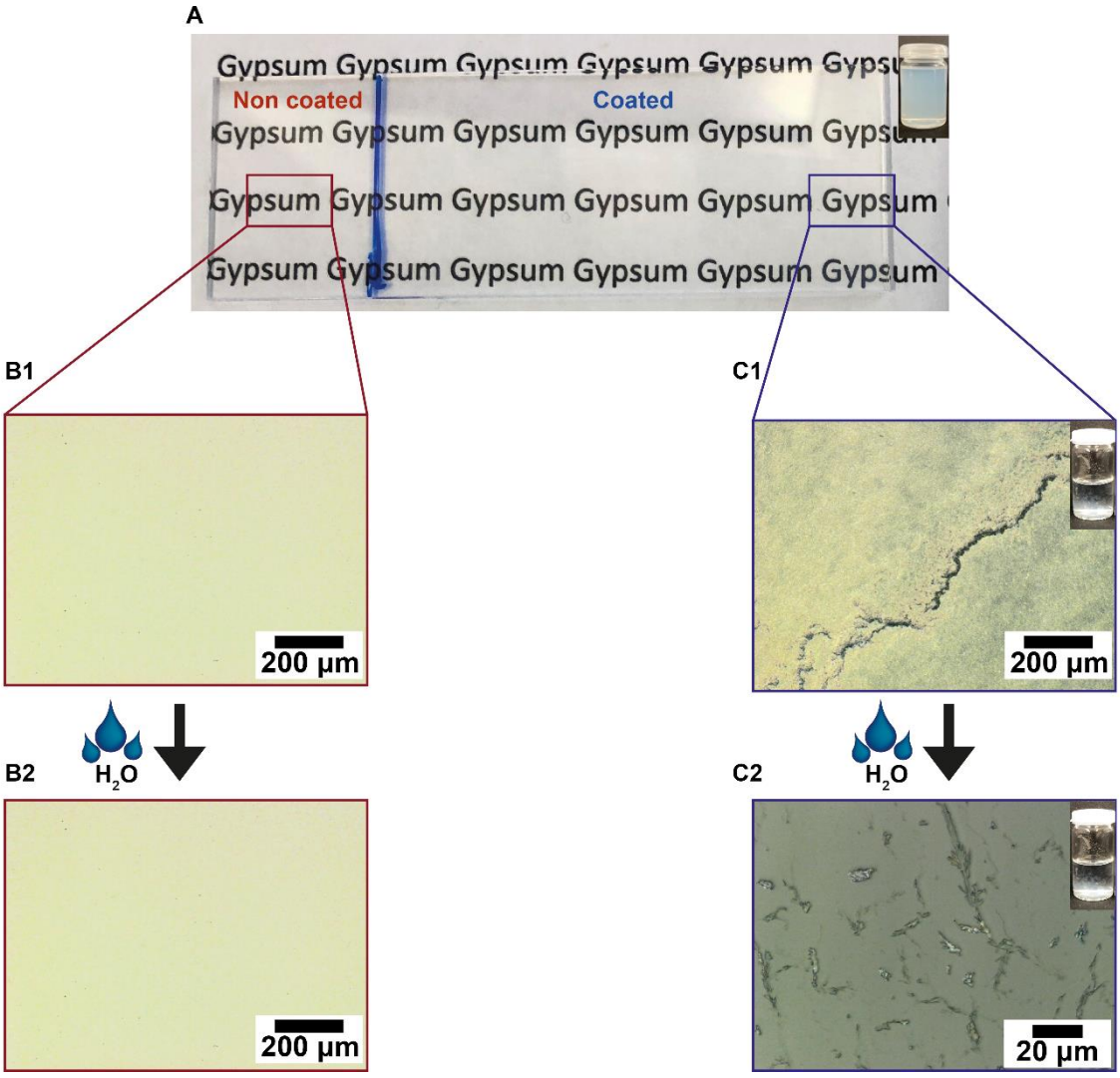

Figure 4.8. (A) Laser microscopy image of dense bassanite nanocrystal film on a glass slide, fabricated from a clear and stable dispersion in methanol (inset) The zoomed image sections (B1, C1) in the red and blue boxes show laser microscopy images of the corresponding areas on the glass slide. Adding a few drops of water lead to immediate precipitation in the dispersion (inset C). After addition of water the non-coated part of the glass slide shows no changes (B2), whereas gypsum crystals form in the coated part (C2).

The stability of the clear dispersions obtained after long milling times allowed to cast dense films on glass slides, which form transparent coatings after drying. This might lead to interesting applications in sensors based on hydration reactions.[46] To assess the feasibility of this approach, a glass slide was dip-coated with the dispersion and examined by laser microscopy after drying (Figure 4.8A). A transparent coating was formed without any perceptible change in the refractive behavior, as shown by the zoomed image sections in the red/blue boxes. Micro sized crystal agglomerates are formed upon contact with water due to the rapid exchange of methanol surface ligands by water, i.e., water leads to rehydration of the methanol-stabilized bassanite nanocrystals and the ensuing formation of gypsum.

4.4 Conclusion

In summary, we devised a new synthesis for bassanite nanoparticles by solvent-assisted ball-milling of gypsum. The milling reaction is complete after only 200 min. The kinetics of the milling reaction were elucidated by making "snapshots" of the reaction by stopping the milling after different time intervals. During milling, gypsum platelets transform to bassanite needles by shear forces. The bassanite nanocrystals are polydisperse with sizes ranging from 20 nm to several hundred nm, and they are separated from each other and stabilized by "surface complexation" with methanol, the ball-milling auxiliary solvent. ^{1}H NMR and FTIR spectroscopy revealed that surface-bound methanol "passivates" the bassanite particles, thereby preventing aggregation and precipitation. They possess needle like morphology. Bassanite nanoparticles prepared by extended ball-milling form long-term stable dispersions in methanol without additional stabilizers and without signs of precipitation. Because of its low boiling point, methanol is easily recovered. Adding water to bassanite dispersions in methanol leads to instant agglomeration, followed by a phase transition to gypsum. The dispersibility in the volatile organic solvent methanol and the elucidation of the crystallization mechanism allow for applications of the bassanite nanocrystals in hybrid materials, e.g., for transparent optical films or as disposable humidity sensors.

The most important advance is that plasterboards from gypsum might be made more efficiently in the future. Every year in Europe, more than 1.5 billion m^2 of interior surface is covered with plasterboards,[47] which are used for partition walls and the cladding of walls, ceilings, roofs or floors, or decorative plaster. To produce plasterboard, manufacturers typically dehydrate the mined gypsum into bassanite in a very time- and

energy-consuming heating process. Our study describes a sustainable way to produce bassanite in a short milling process, thereby eliminating the need for energy-intensive dehydration. Since grinding is a standard process in the construction industry, large-scale implementation seems feasible. Based on the specific properties of our laboratory ball mill an energy consumption of approximately 10 MJ per ton of bassanite would expected, whereas the specific thermal energy consumption for stucco is reported to be 1 GJ/t.[48] Although the energy consumption seems to be higher at first glance, it has to be considered that this calculation is based on a simple upscale multiplication without considering optimization of any parameters. Already the use of containers holding the tenfold amount would lead to an equivalence between calculated laboratory energy consumption and real energy consumption.

4.5 Experimenal section

Materials. Calcium sulfate dihydrate (Sigma-Aldrich), acetone (99.5 %, puriss. p.a., Riedel-de Haën), methanol (HPLC grade, Fisher Chemicals), cyclohexane (analytical reagent grade, Fisher Chemicals),) and doubly-deionized water (resistivity > 18 mΩ cm).

Synthesis of BMCS MeOH. 500 mg of calcium sulfate dihydrate (3,6 mmol) was treated with methanol (9 ml) in a planetary ball mill (pulverisette 7 Classic, Fritsch). The starting materials were transferred together with 7.5 grams of grinding balls (about 2000 balls, 1 mm diameter, ZrO_2) into ZrO_2 grinding jars. The mixture was milled for different time intervals. To avoid overheating 10 min of grinding and a subsequent 10 min rest phase were used. Therefore 200 min of milling correspond to a reaction time of 400 min. Afterwards, decantation and subsequent washing by methanol was used to separate product and ZrO_2 balls.

Synthesis of BMCS CH. 500 mg of calcium sulfate dihydrate (3,6 mmol) was treated with cyclohexane (9 ml) in a planetary ball mill (pulverisette 7 Classic, Fritsch). The starting materials were transferred together with 7.5 grams of grinding balls (about 2000 balls, 1 mm diameter, ZrO_2) into ZrO_2 grinding jars. The mixture was milled for different time intervals. To avoid overheating 10 min of grinding and a subsequent 10 min rest phase were used. Therefore 200 min of milling correspond to a reaction time of 400 min. Afterwards, decantation and subsequent washing by methanol was used to separate product and ZrO_2 balls.

Film fabrication. Transparent calcium sulfate films were prepared by depositing the nanoparticle dispersion on a glass slide and quickly evaporating the solvent in a drying chamber at 80°C.

Characterization.

Transmission electron microscopy. Samples for TEM were prepared by drop-casting 20 µL of the respective sample dispersion on 400 mesh carbon copper grids (Plano GmbH, Wetzlar, Germany). The samples were measured with a FEI Tecnai Spirit TWIN LaB_6 at 120kV equipped with a Gatan US1000 CCD-camera (2048 x 2048 pixels) and a FEI Tecnai F30 S-TWIN at 300 kV equipped with a Gatan US4000 CCD-camera (4096 x 4096 pixels). A 70-µm condenser aperture and standard illumination settings were used for the TEM images acquisition.

Dynamic light scattering. Dusk-free acetone-rinsed quartz glass cuvettes were filled with pre-filtered (syringe filter Millex® AA, pore size: 800 nm, diameter: 25 mm) dispersion solutions. All light scattering experiments were performed on a multi-goniometer ALV-CGS-8F SLS/DLS 5022F, equipped with a Uniphase He/Ne laser (25 mW, 632.8 nm) and an ALV-7004 multi-τ correlator connected to an ALV/high QE APD avalanche photodiode in pseudo-cross-correlation mode (ALV-Laser Vertriebsgesellschaft mbH, Langen, Germany). Temperature control (±0.1 °C) during measurements is assured by a Lauda ultrathermostat RKS C6 (Lauda Dr. Wobser GmbH, Lauda, Königshofen, Germany). The experiments and data acquisition were controlled by an ALV software correlator ALV500/E/EPP-ALV-60X0-WIN 3.0.3.15. Angular dependent measurements were performed in the range of 30 °< θ < 150 ° corresponding to wave vectors of $q = (4\pi\, n \sin(\theta/2)) / \lambda$ with the scattering angle θ, the wavelength λ, and the refractive index n = 1.3288 (for methanol at 20 °C). The recorded intensity correlation functions $g^{(2)}(q, t)$ were converted via Siegert relation $g^{(2)}(\tau) - 1 = \beta + \left|g^{(1)}(\tau)\right|^2$ into the field correlation function $g^{(1)}(\tau)$ with the specific instrument factor β. For polydisperse solutions with diffusing particles of a multitude of sizes, the overall intensity decay resembles a superposition of several exponential decays. Due to a broad sample polydispersity, the recorded amplitude correlation functions $g^{(1)}(\tau)$ were fitted to a tri-exponential decay function of the form $g^{(1)}(q,\tau) = A + B \cdot \exp(-\Gamma_1\tau) + C \cdot \exp(-\Gamma_2\tau) + E \cdot (-\Gamma_3\tau)$ with the decay rates $\Gamma_n = D_n q^2$, the offset A, and the amplitudes B, C, and E.

The diffusion coefficients D_n were converted into hydrodynamic radii using the Stokes-Einstein equation $R_{H,n} = \frac{k_B T}{6\pi\eta D_n}$ with the Boltzmann constant k_B, the temperature T, and the solvent dynamic viscosity η.

IR spectroscopy. ATR-IR spectroscopy was performed at a Nicolet iS10 Spectrometer manufactured by Thermo Scientific. The spectra were recorded in a range from 650 - 4000 cm^{-1} with a resolution of 1.4 cm^{-1} per data point.

Solid state NMR spectroscopy. The ^1H spectra were recorded on a Bruker Advance 400 DSX NMR spectrometer at a ^1H frequency of 399.87 MHz. A commercial 3 channel 4 mm Bruker probe head at 10 kHz magic angle spinning (MAS) averaging 32 scans was used. The spectra were referenced to external adamantine at 1.63 ppm as a secondary reference.

Solution NMR spectroscopy. For these NMR experiments, the samples were synthesized as described above. All ^1H NMR experiments were conducted on a Bruker Avance DRX 400 NMR spectrometer operating at ^1H frequency of 400.31 MHz equipped with 5 mm inverse two channel probe head with z-gradients. The single pulse excitation experiments were recorded using a 30° pulse angle with a recycle delay of 1 s averaging 32 scans. Stimulated echo sequence with bipolar gradient pulses and a longitudinal eddy current delay was used for the ^1H diffusion ordered spectroscopy (DOSY) experiments. The gradient strength was incremented in 16 steps from 2 % to 95 % of the maximum gradient strength. The diffusion time and the gradient pulse length were 100 ms and 2.0 ms with 2 s recycle delay, respectively. After Fourier transformation and baseline correction, the diffusion dimension of the 2D DOSY spectra was processed using the Bruker Topspin 1.3 software package. The diffusion analysis was performed using the Topspin T_1/T_2 relaxation package.

X-ray powder diffraction. X-ray diffractograms were recorded with a STOE Stadi P equipped with a Mythen 1k detector detector using monochromatized MoKα radiation. The sample was attached to polyvinyl acetate films with perfluoroether (Fomblin® Y, Aldrich). The sample was measured in transmission in 0.015° steps (continuous scan, 150 s/°) covering a 2θ range from 1.5° to 43°. Rietveld refinement [49] was performed with Topas Academic v6 using the fundamental parameters approach,[50] based on a structural model for bassanite by Ballirano et al.[51] Crystalline phases were identified according to the PDF-2 data-base [52] using Bruker AXS EVA.[53]

TGA measurements. TGA measurements were carried out on a Netzsch STA 409 PC LUXX in the temperature range from 30 to 400 °C using heating rates of 10 K min^{-1} under air.

Laser microscopy. Laser microscopy images were taken with a Keyence VK 8710 with a wavelength of 658 nm.

4.6 References

[1] J. E. Kogel, M. Society for Mining and Exploration (U. S.)., *Industrial minerals & rocks: commodities, markets, and uses.* (Society for Mining, Metallurgy, and Exploration, Littleton, 2006).

[2] L. Pelletier-Chaignat, F. Winnefeld, B. Lothenbach, G. Le Saout, C. J. Müller, C. Famy, Influence of the calcium sulphate source on the hydration mechanism of Portland cement–calcium sulphoaluminate clinker–calcium sulphate binders. *Cem. Concr. Compos.* **2011**, *33*, 551-561.

[3] J. Bizzozero, C. Gosselin, K. L. Scrivener, Expansion mechanisms in calcium aluminate and sulfoaluminate systems with calcium sulfate. *Cem. Concr. Res.* **2014**, *56*, 190–202.

[4] A. D. Ledingham, J. D. English, S. Akyalcin, B. E. Cozad, J. C. Ontiveros, F. K. Kasper, Accuracy and mechanical properties of orthodontic models printed 3-dimensionally from calcium sulfate before and after various postprinting treatments. *Am. J. Orthod. Dentofac.* **2016**, *150*, 1056–1062.

[5] Z. Zhou, F. Buchanan, C. Mitchell, N. Dunne, Printability of calcium phosphate: Calcium sulfate powders for the application of tissue engineered bone scaffolds using the 3D printing technique. *Mater. Sci. Eng., C* **2014**, *38*, 1–10.

[6] M. Younes, G. Aquilina, L. Castle, K.-H. Engel, P. Fowler, P. Fürst, R. Gürtler, U. Gundert-Remy, T. Husøy, W. Mennes, P. Moldeus, A. Oskarsson, R. Shah, I. Waalkens-Berendsen, D. Wölfle, P. Boon, R. Crebelli, A. Di Domenico, M. Filipic, A. Mortensen, H. Van Loveren, R. Woutersen, A. Giarola, F. Lodi, F. Riolo, M. J. Frutos Fernandez, Re-evaluation of sulphuric acid and its sodium, potassium,calcium and ammonium salts (E 513, 514 (i), 514 (ii), 515 (i), 515 (ii), 516 and 517) as food additive. EFSA J, 2019, 17, 5868.

[7] M. V. Thomas, D. A. Puleo, D. A. Calcium sulfate: Properties and clinical applications. *J. Biomed. Mater. Res. B* **2009**, *88*, 597–610.

[8] N. Sindhura Reddy, S. Sowmya, J. D. Bumgardner, K. P. Chennazhi, R. Biswas, R. Jayakumar, Tetracycline nanoparticles loaded calcium sulfate composite beads for periodontal management. *Biochim. Biophys. Acta* **2014**, *1840*, 2080–2090.

[9] G. Orsini, J. Ricci, A. Scarano, G. Pecora, G. Petrone, G. Iezzi, A. Piattelli, Bone-defect healing with calcium-sulfate particles and cement: An experimental study in rabbit. *J. Biomed. Mater. Res. B* **2004**, *68*, 199–208.

[10] S. J. McConoughey, R. P. Howlin, J. Wiseman, P. Stoodley, J. H. Calhoun, Comparing PMMA and calcium sulfate as carriers for the local delivery of antibiotics to infected surgical sites. *J. Biomed. Mater. Res. B* **2015**, *103*, 870–877.

[11] J. Bensted, S. Prakash, Investigation of the Calcium-Sulphate-Water System by Infrared Spectroscopy. *Nature*, 1968, **219**, 60–61

[12] B. Guan, G. Jiang, Z. Wu, J. Mao and B. Kong, Preparation ofa-Calcium Sulfate Hemihydrate from Calcium SulfateDihydrate in Methanol–Water Solution under Mild Conditions. *J. Am. Ceram. Soc.*, 2011, **94**, 3261–3266

[13] H. Weiss, M. F. Bräu, How Much Water Does Calcined Gypsum Contain? *Angew. Chem. Int. Ed.* **2009**, *48*, 3520-3524.

[14] J. W. Anthony, Handbook of Mineralogy,Vol. V, Mineral Data Publishing, Tucson, 2003.

[15] A. Becker, I. Sötje, C. Paulmann, F. Beckmann, T. Donath, R. Boese, O. Prymak, H. Tiemann, M. Epple, Calcium sulfate hemihydrate is the inorganic mineral in statoliths of Scyphozoan medusae (Cnidaria). *Dalton Trans.* **2005**, 1545–1550.

[16] A. E. S. Van Driessche, T. Stawski, M. Kellermeier, Calcium sulfate precipitation pathways in natural and engineering environments. *Chem. Geol*. **2019**, *530*, 119274.

[17] D. Freyer, W. Voigt, Crystallization and Phase Stability of $CaSO_4$ and $CaSO_4$ - Based Salts. *Monatsh. Chem.* **2003**, *134*, 693–719.
[18] M. Ossorio, A. E. S. van Driessche, P. Pérez, J. M. García-Ruiz, The gypsum–anhydrite paradox revisited. *Chem. Geol.* **2014**, *386*, 16–21.
[19] J. K. Warren, *Evaporites: sedimentology, resources and hydrocarbon* (Springer, Berlin, 2006). Testa, G., Lugli, S. Gypsum–anhydrite transformations in Messinian evaporites of central Tuscany (Italy). *Sediment. Geol.* **2000**, *130*, 249–268.
[20] F. Mees, M. De Dapper, Vertical variations in bassanite distribution patterns in near-surface sediments, southern Egypt. Sediment. Geol. 2005, 181, 225-229.
[21] Y. Langevin, F. Poulet, J.-P. Bibring, B. Schmitt, S. Douté, B. Gondet, Summer evolution of the north polar cap of Mars as observed by OMEGA/Mars Express. *Science* **2005**, *307*, 1581–1584.
[22] F. Wirsching in Ullmanns Enzyklopädie der Technischen Chemie, Vol. 12, Wiley-VCH, Weinheim, 1976.
[23] N. B. Singh, B. Middendorf, Prof. Cryst. Growth Charact. Mater. 2007, 53, 57-??.
[24] W. Huang, E. Ertekin, T. Wang, L. Cruz, M. Dailey, J. DiRuggiero, D. Kisailus, mechanism of water extraction from gypsum rock by desert colonizing microorganisms. Proc. Natl. Acad. Sci. U.S.A. 2020, 202001613.
[25] A. Saha, J. Lee, S. M. Pancera, M. Bräu, A. Kempter, A. Tripathi, A. Bose, New Insights into the Transformation of Calcium Sulfate Hemihydrate to Gypsum Using Time-Resolved Cryogenic Transmission Electron Microscopy. *Langmuir* **2012**, *28*, 11182-11187.
[26] Y.-W. Wang, Y.-Y. Kim, H. K. Christenson, F. C. Meldrum, A new precipitation pathway for calcium sulfate dihydrate (gypsum) *via* amorphous and hemihydrate intermediates. *Chem. Commun.* **2012**, *48*, 504–506
[27] F. Jones, Infrared investigation of barite and gypsum crystallization: Evidence for an amorphous to crystalline transition. *CrystEngComm* **2012**, *14*, 8374–8381.
[28] A. E. S. Van Driessche, L. G. Benning, J. D. Rodriguez-Blanco, M. Ossorio, P. Bots and J. M. García-Ruiz, *Science* **2012**, *336*, 69–72.
[29] Y.-W. Wang and F. C. Meldrum, Additives stabilize calcium sulfate hemihydrate (bassanite) in solution. *J. Mater. Chem.* **2012**, *22*, 22055–22062
[30] U. Tritschler, A. E. S. Van Driessche, A. Kempter, M. Kellermeier, H. Cölfen, Controlling the Selective Formation of Calcium Sulfate Polymorphs at Room Temperature. *Angew. Chem., Int. Ed*. **2015**, *54*, 4083−4086.
[31] U. Tritschler, M. Kellermeier, C. Debus, A. Kempter, H; Cölfen, A Simple Strategy for the Synthesis of Well-Defined Bassanite Nanorods. *CrystEngComm* **2015**, *17*, 3772−3776.
[32] T. M. Stawski, A. E. S. van Driessche, M. Ossorio, J. Diego Rodriguez-Blanco, R. Besselink, L. G. Benning, Formation of Calcium Sulfate through the Aggregation of Sub-3 Nanometre Primary Species. *Nat. Commun*. **2016**, *7*, 11177.
[33] C. Yan, J. Nishida, R. Yuan, M. D. Fayer, Water of Hydration Dynamics in Minerals Gypsum and Bassanite: Ultrafast 2D IR Spectroscopy of Rocks. *J. Am. Chem. Soc*. **2016**, *138*, 9694-9703.
[34] K. He, A. Nie, Y. Yuan, S. M. Ghodsi, B. Song, E. Firlar, J. Lu, Y.-P. Lu, T. Shokuhfar, C. M. Megaridis, R. Shahbazian-Yassar, In Situ Transmission Electron Microscopy Explores a New Nanoscale Pathway for Direct Gypsum Formation in Aqueous Solution. *ACS Appl. Nano Mater.* **2018**, *1*, 5430−5440.
[35] T. M. Stawski, A. E. S. Van Driessche, R. Besselink, E. H. Byrne, P. Raiteri, J. D. Gale, L. G. Benning, The Structure of $CaSO_4$ Nanorods: The Precursor of Gypsum. *J. Phys. Chem. C* **2019**, *123*, 23151−23158.

[36] T. M. Stawski, H. M. Freeman, A. E. S. Van Driessche, J. Hövelmann, R. Besselink, R. Wirth, L. G. Benning, Particle-Mediated Nucleation Pathways Are Imprinted in the Internal Structure of Calcium Sulfate Single Crystals. *Cryst. Growth Des*. **2019**, *19*, 3714−3721.
[37] C. Jia, L. Wu, J. L. Fultron, X. Liang, J. J. De Yoreo, B. Guan, Structural evolution of amorphous calcium sulfate nanoparticles into crystalline gypsum phase. ***CrystEngComm,*** **2020**, ***22***, 6805-6810.
[38] C. Anduix-Canto, M. A. Levenstein, Y.-Y. Kim, J. R. A. Godinho, A. N. Kulak, C. González Niño, P. J. Withers, J. P. Wright, N. Kapur, H. K. Christenson, F. C. Meldrum, Exploiting Confinement to Study the Crystallization Pathway of Calcium Sulfate. *Adv. Funct. Mater.* **2021**
[39] J. I. Escavy, M. J. Herrero, The Use of Location-Allocation Techniques for Exploration Targeting of Place-Value Industrial Minerals: A Market-Based Prospectivity Study of the Spanish Gypsum Resources. Ore Geol. Rev. **2013**, *53*, 504-516.
[40] A. López-Delgado, S. López-Andrés, I. Padilla, M. Alvarez, R. Galindo, A. J. Vázquez, Dehydration of Gypsum Rock by SolarEnergy: Preliminary Study, *Geomaterials* **2014**, *4*, 82-91.
[41] M. Tang, X. Li, Y. Shen, X. Shen, Kinetic model for calcium sulfate α-hemihydrate produced hydrothermally from gypsum formed by flue gas desulfurization. *J. Appl. Crystallogr.* **2015**, *48*, 827–835.
[42] P. Balaz, M. Achimovicoa, M. Balaz, K. Chen, O. Dobrozhan, E. Guilmeau, J. Hejtmanek, K. Knizek, L. Kubickova, P. Levisnky, V. Puchy, M. J. Reece, P. Varga, R. Zhang, *ACS Sustainable Chem. Eng*. **2021**, *9*, 2003–2016.
[43] S. Fukugaichi, N. Matsue, One-Step Synthesis of Calcium Sulfate Hemihydrate Nanofibers from Calcite at Room Temperature. *ACS Omega*, **2018**, 3, 2820-2824
[44] S. Leukel, M. Panthöfer, W. Schärtl, M. Mondeshki, W. Tremel, Calcium sulfate nanoparticles with unusual solubility. *Langmuir* **2018**, *34*, 7096-7105.
[45] D.R.G. Mitchell, B. Schaffer, Scripting-customised microscopy tools for Digital Micrograph^{TM}. *Ultramicroscopy*, **2005**, *103*, 319-332
[46] Y. Sheng, M. Regner, Roles of Water Molecules and Counterion on HS^- Sensing Reaction Utilizing a Pyrylium Derivative: A Computational Study. *J. Phys. Chem. A* 2019, 123, 15, 3334-3343.
[47] http://www.eurogypsum.org/about-gypsum/uses-of-plaster-and-plasterboard/ , accessed 24.10.2021
[48] www.umweltbundesamt.at; Stand der Technik zur Kalk-, Gips- und Magnesiaherstellung, accessed 24.10.2021
[49] H. M. Rietveld, A profile refinement method for nuclear and magnetic structures. *J. Appl. Crystallogr.* **1969**, *2*, 65–71.
[50] A. A. Coelho, TOPAS and TOPAS-Academic: An optimization program integrating computer algebra and crystallographic objects written in C++. *J. Appl. Crystallogr.* **2018**, *51*, 210–218
[51] P. Ballirano, A. Maras, S. Meloni, R. Caminit A. Kirfel, G. Will, The monoclinic I2 structure of bassanite, calcium sulphate hemihydrate (CaSO4 0.5H2O) *Eur. J. Mineral.* **2001**, *13*, 985-993
[52] PDF-2, Release 2004, JCPDS – International Center for Diffraction Data, Newton Square (PA) US (2004).
[53] EVA 10.0 Rev. 1, Bruker AXS, Madison (WI) US (2003)

4.7 Supplementary information

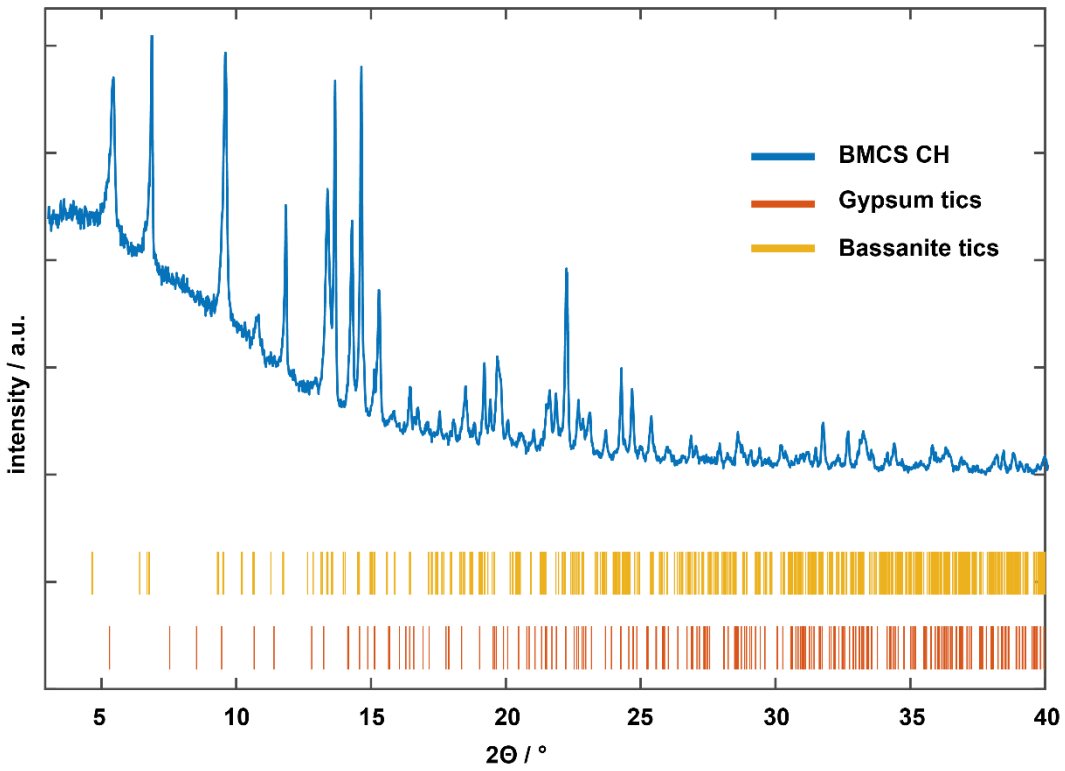

Figure S4.1: Magnified powder x-ray diffraction pattern of BMCS CH after 990 minutes of milling. Unlike in BMCS MeOH no full conversion to bassanite could be observed.

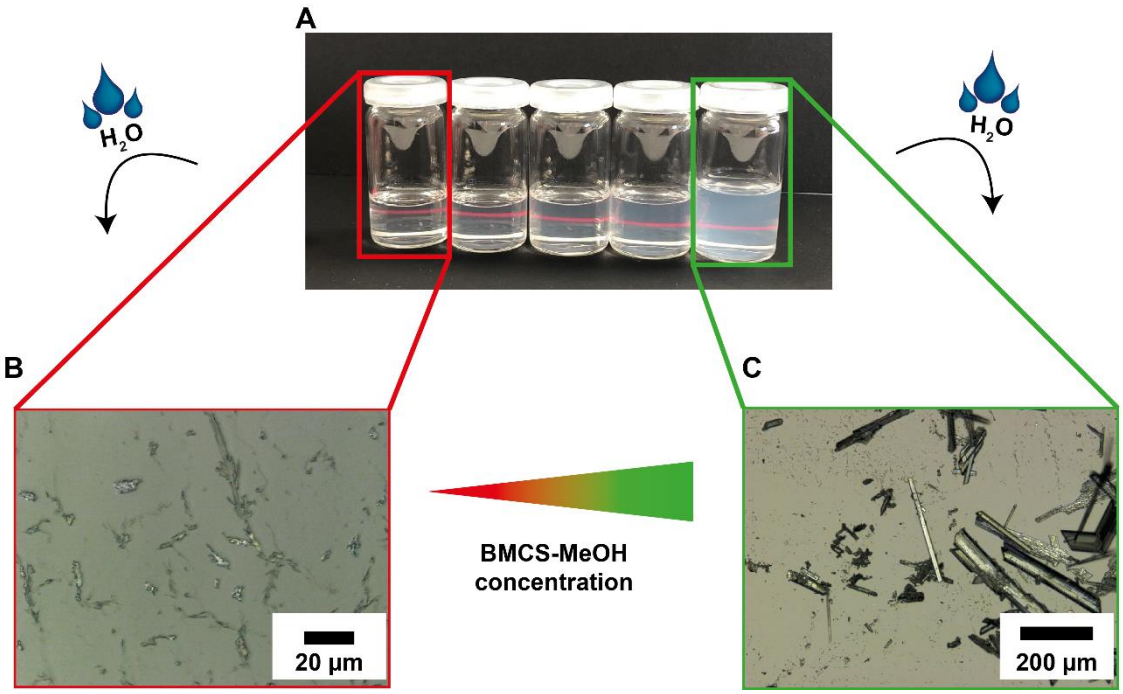

Figure S4.2: Miscibility of aCS-MeOH with ethylene glycol (A). An increase of aCS-MeOH leads to an increase in turbidity. Lower concentrated mixtures lead to slower recrystallization and crystal growth (B), whereas higher concentrated mixtures lead to faster recrystallization and crystal growth, after rehydration in water.

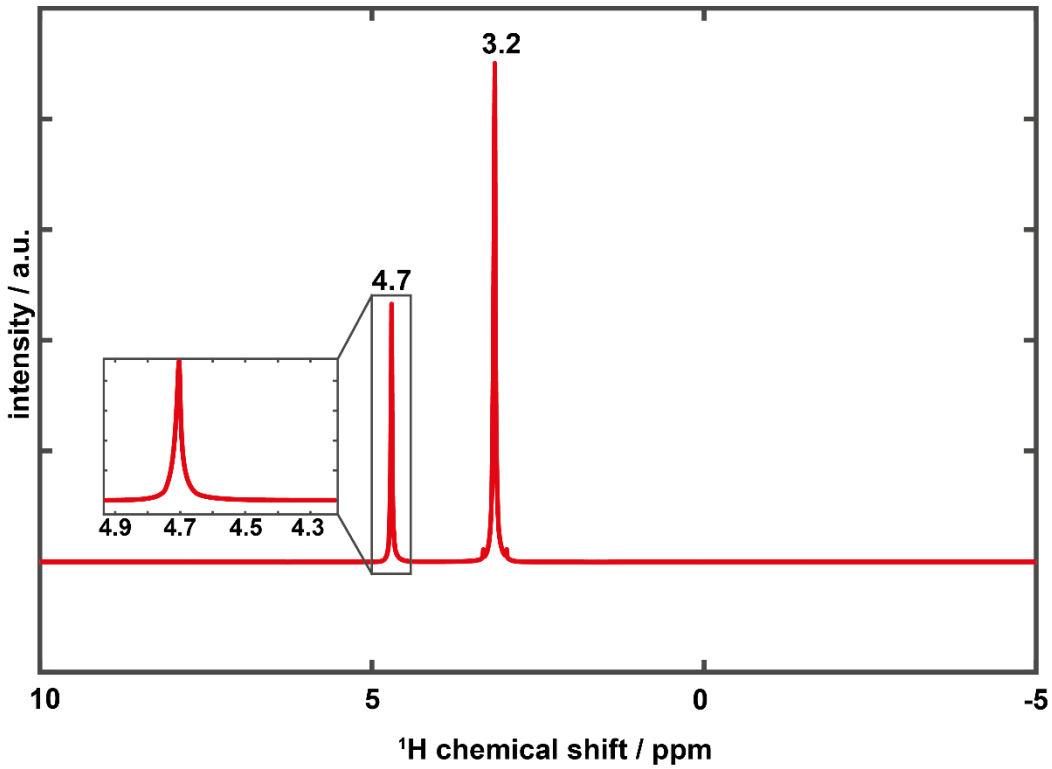

Figure S4.3: [1]H liquid NMR spectrum of pure methanol. Contrarily to aCS-MeOH no additional signal at 4.4 ppm could be observed.

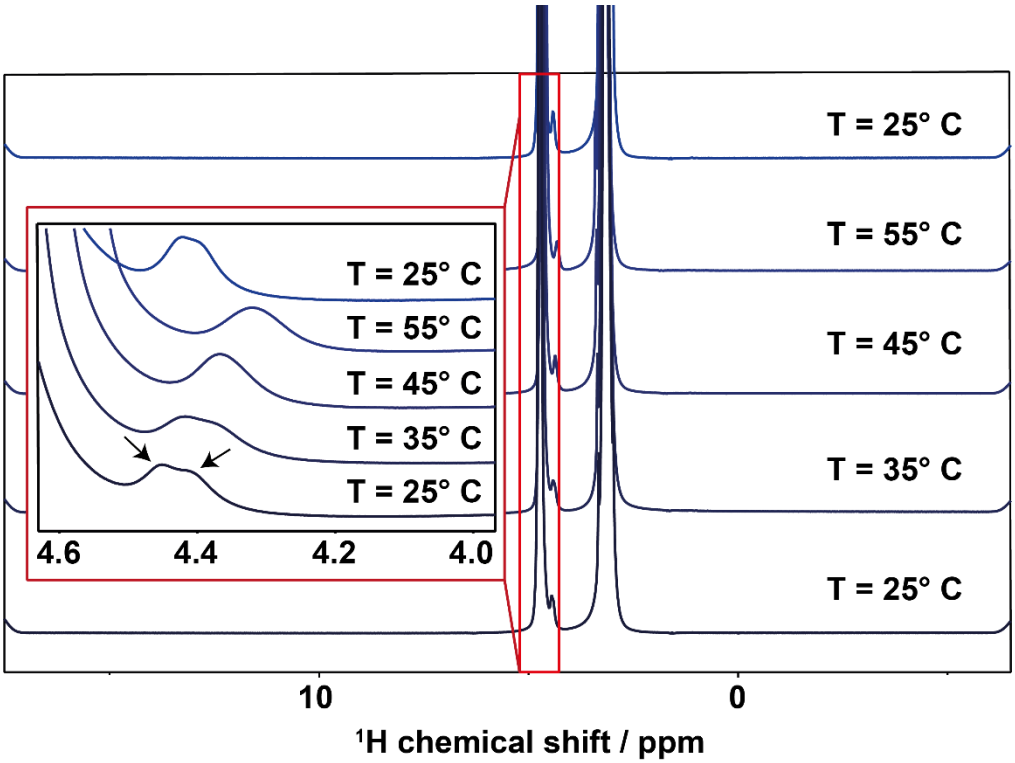

Figure S4.4: Development of ^{1}H liquid NMR spectra from BMCS MeOH at different temperatures. The inset shows two signals at 4.4 ppm which merge at higher temperatures. After cooling, a relaxation to the previous state can be observed. .

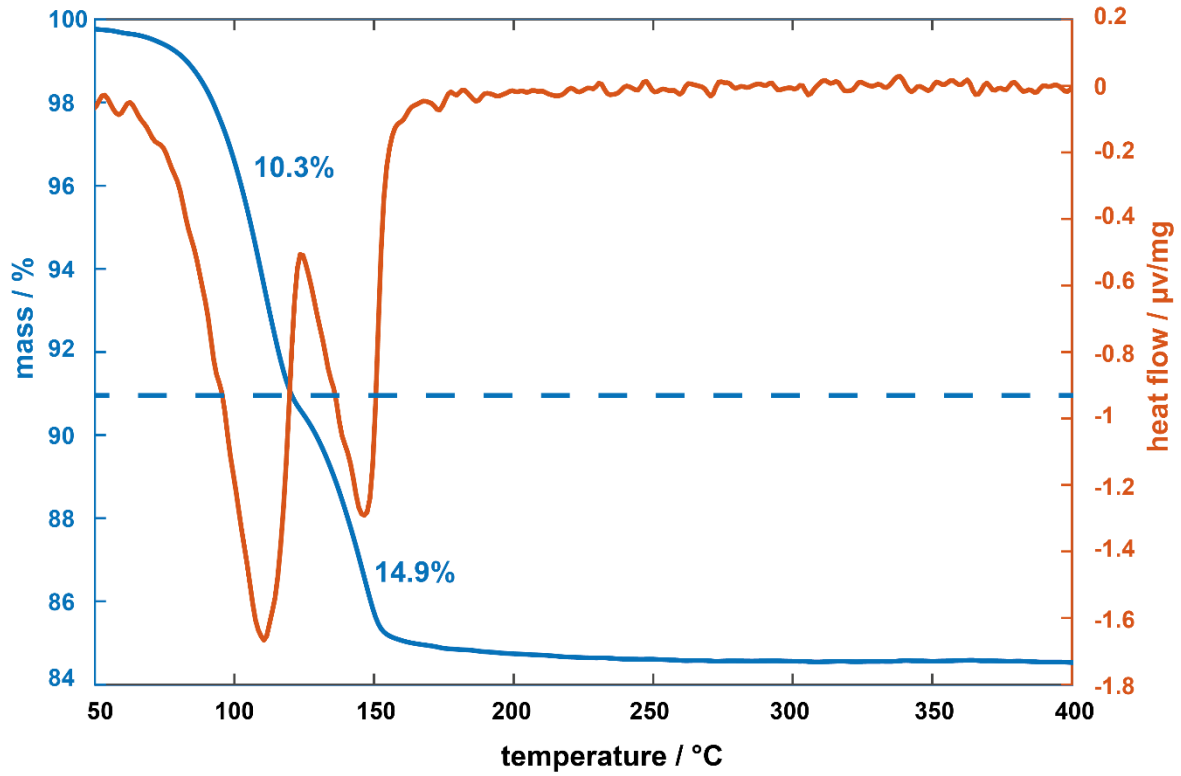

Figure S4.5: TGA (blue line) and DTA traces (red line) for powders after milling in cyclohexane. .

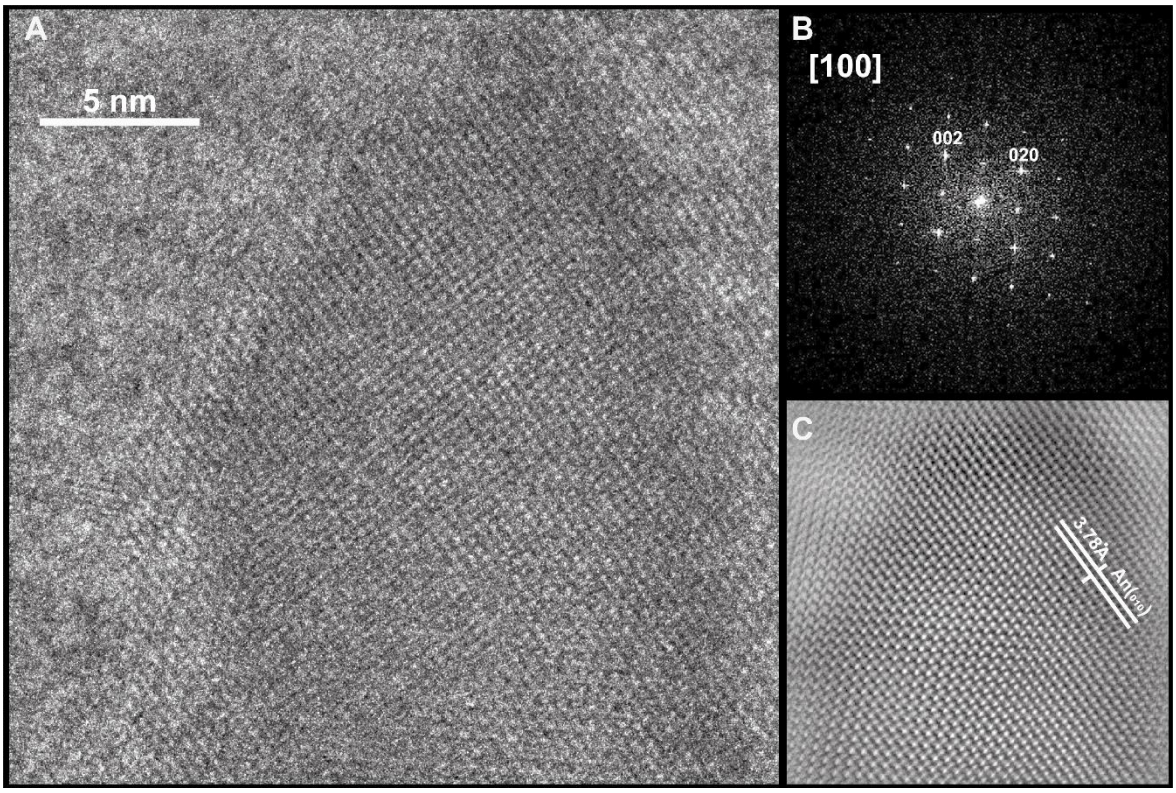

Figure S4.6: HR-TEM image (A) of an anhydrite nanoparticle from BMCS-MeOH showing that additional milling times might lead to higher degree of dehydration. The FFT (B) and reverse FFT show the high crystallinity of the nanoparticle. .

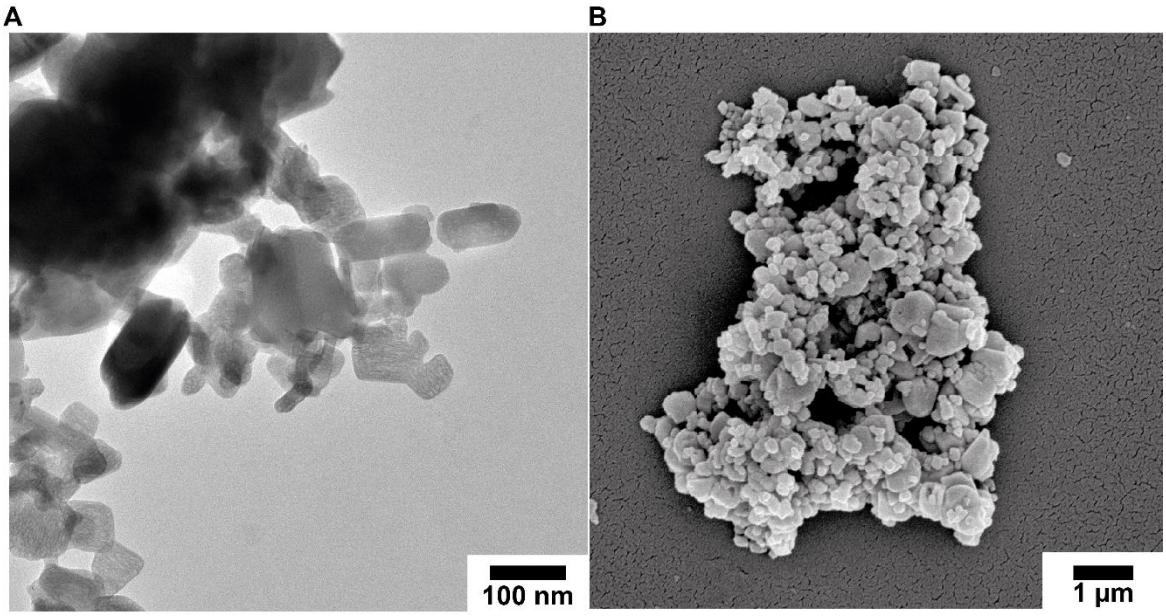

Figure S4.7: TEM image (A) and SEM image (B) of calcium sulfate milled in cyclohexane. Not exhibition of special morphologies could be observed. The material consists of agglomerated nanoparticles.

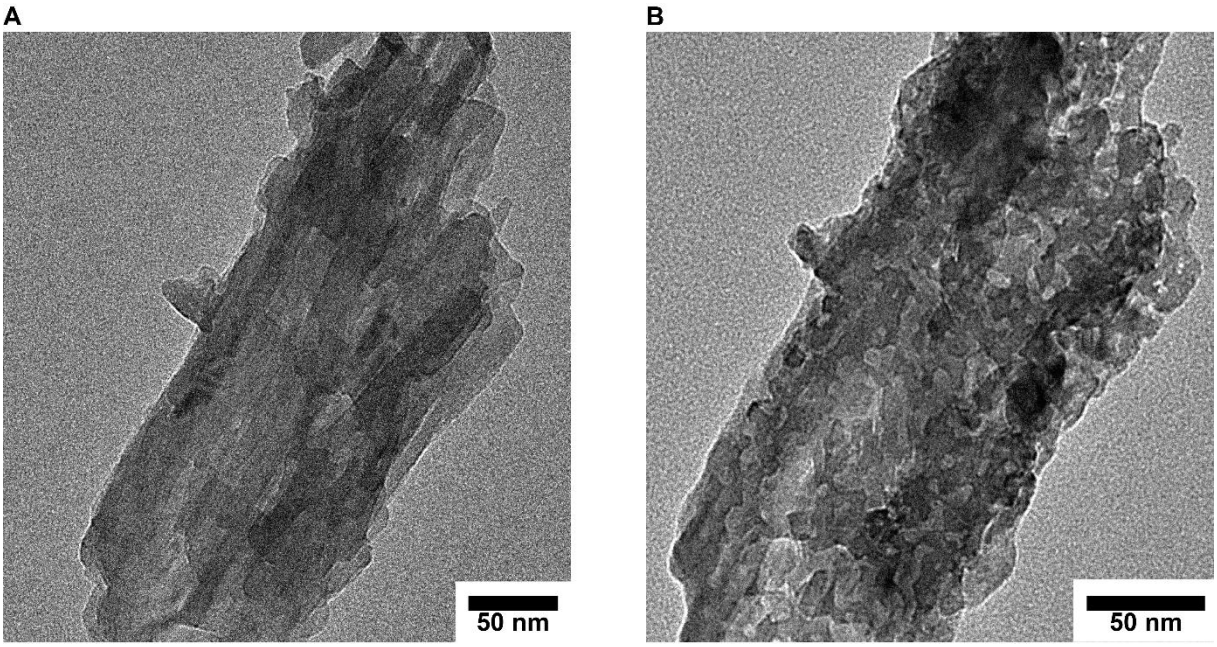

Figure S4.8: TEM images after short irradiation (A) of BMCS MeOH and after prolonged exposure (B). The material starts to decompose and the needle like morphology starts to crumble.

5

“Amorphous monohydrocalcite” with a defect hydrate network by mechanochemical process of monohydrocalcite using ethanol as auxiliary solvent

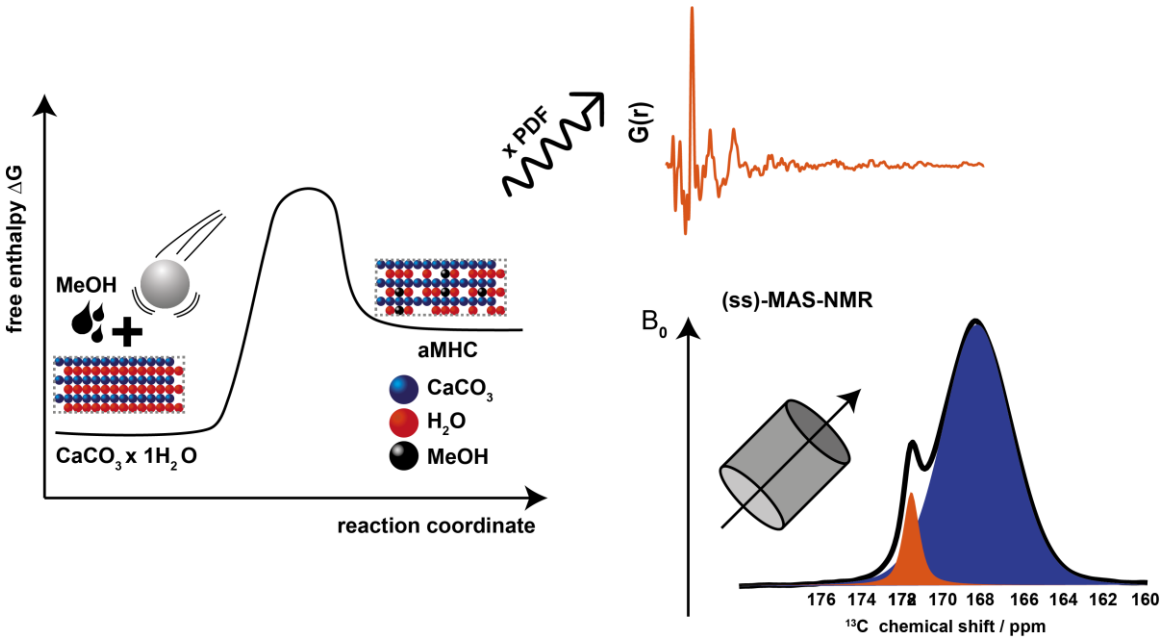

Amorphous calcium carbonate (ACC) is a precursor in the biomineralization of crystalline $CaCO_3$. The lifetime of transient ACC in nature is regulated by biomacromolecules. The relevance of ACC in material science is related to our understanding of $CaCO_3$ crystallization pathways. Hydrated ACC and monohydrocalcite (MHC) are similar in their chemical composition, precipitation condition, and thermal behavior. We describe a fast and reliable way to prepare monohydrocalcite-like ACC (aMHC) in a planetary ball mill using ethanol as auxiliary solvent. Metastable aMHC is stabilized by temporarily partially displacing structural water with ethanol, which cannot be incorporated into the hydrate network of MHC due to its molecular size.

This chapter contains a manuscript currently under review in *Chemistry of Materials.*

Authorship Contribution

Study conception and design	M. Maslyk
Acquisition of data	M. Maslyk M. Mondeshki
Analysis and interpretation of data	M. Maslyk
Drafting of manuscript	M. Maslyk
Critical Revision	W. Tremel M. Mondeshki

5.1 Relevance to doctoral thesis

As the previous projects have shown, amorphization and phase transformations are accessible by mechanochemial methods. Due to previous studies it could be shown that in the calcium carbonate system, amorphization by mechanochemistry is possible if ionic constitutents are added. Based on the calcium sulfate and zinc phosphate systems it was observed that a partial dehydration of mineral phases can induce phase transformations by use of specific solvents. To circumvent the use of sodium carbonate as an ionic constitutent in the mechanochemical amorphization process, the fifth project focused on the amorphization of a hydrated calcium carbonate phase, namely *monohydrocalcite* ($CaCO_3$ x $1H_2O$). Similar to vaterite and aragonite, monohydrocalcite is metastable and transforms to calcite or aragonite depending on the magnesium content. Not only is the crystallization pathway to monohydrocalcite of scientific interest, but it has been shown that this phase occurs in cementious systems as well, leading to industrial applications such as cements and alkali activated binders. In the first step of this study a simple synthesis route to pure monohydrocalcite has been established in reference to already published protocols. In the second step the influence of cyclohexane and ethanol in relation to phase changes have been analyzed. As in previous projects local probes as NMR, FTIR, PXRD and PDF have been applied to analyze the local structure of the underlying material. Contrarily to cyclohexane which only leads to a phase mixture of several phases, it has been shown that ethanol induces amorphization. Kinetically controlled recrystallization experiments have shown that the amorphous monohydrocalcite (aMHC) leads to aragonite after rehydration. Therefore, it could be shown that amorphization with respect to solvents is feasible in mechanochemical approches using a hydrated calcium carbonate.

5.2 Introduction

Crystallization is one of the most widely used technologies in chemical processing that is central to fields as diverse as corrosion and weathering, scale formation, food chemistry, pharmaceuticals and analysis of protein structures, or nanomaterials.[1] Calcium carbonate is a textbook model system to study crystallization processes, because it is one of the most abundant minerals found as limestone in rocks.[2] In the enlivened nature it is the main component of eggshells, snail shells, seashells and pearls.[3] It is used industrially as neutralizing agent, filler, flux and cement, and it is formed as undesired precipitate as scale on walls of heat exchangers and pipes.[4,5]Thus, the crystallization of calcium carbonate is situated at the interface of inorganic chemistry, geochemistry, biomineralization, industrial/construction chemistry and water treatment.The precipitation of $CaCO_3$ is one of the most fundamental problems in the formation of ionic crystals because it involves a complex combination of liquid/gas, protonation, solution/precipitation, and also complexation equilibria.[6] Ionic, molecular, and polymeric additives in solution have significant effects on the elemental reactions and equilibria involved, with the reactions in biological systems being particularly complex.[7] The crystallization of the anhydrous crystalline polymorphs calcite, aragonite, and vaterite has been shown to proceed *via* a complex series of nonclassical pathways[8] in which the hydrated polymorphs $CaCO_3 \cdot ½H_2O$,[9] monohydrocalcite ($CaCO_3 \cdot H_2O$),[10] ikaite($CaCO_3 \cdot 6H_2O$),[11] and amorphous calcium carbonate (ACC) play important roles and in some instances are stable or metastable end products.[12] This multistep pathway has implications for the understanding of biomineralization and crystallization in general.Due to their metastability at ambient conditions, the hydrated polymorphs are rarely found in nature, and they are difficult to obtain as pure crystals.[13,14] Under atmospheric conditions, monohydrocalcite is thermodynamically metastable with respect to calcite and aragonite.[15] Despite its description as a “pure“ calcium carbonate, Mg has been shown to play an essential role in the formation of natural and synthetic monohydrocalcite.[15,16] A detailed study by Rodriguez-Bianco et al.[17] has elucidated the crystallization pathway of monohydrocalcite as a function of the Mg content starting from Mg-rich ACC. Magnesium serves three purposes: (1) inhibiting the formation of vaterite and calcite, (2) making the Mg hydration shell more strongly bound compared to Ca, (3) and therefore a preferential incorporation of Mg in the monohydrocalcite structure. Although natural and synthetic as well as monohydrocalcite are preferentially formed in Mg-containing media, the presence of silicate promotes the formation of monohydrocalcite even in the absence of Mg.[18–20]

Pure ACC is metastable with a lifetime of minutes to hours. Magnesium[21,22] or phosphate[23] ions as well organic macromolecules,[24–27] can promote ACC stability, leading to much longer lifetimes. Factors like the pH value are important as well,[28] affecting the structure and properties of ACC through the carbonate/bicarbonate equilibrium[29] and the presence of hydroxyl groups.[30,31]Water plays a key role in ACC stabilization and transformation either as external mediator or as integral part of the ACC structure.[32,33] Compositions from 0 to 1 mol H_2O per mole $CaCO_3$ have been reported for biogenic ACC.[34,35] The reported compositions for synthetic ACC vary from 0.5 to 1.4 mol H_2O/mol $CaCO_3$.[36–38] Important questions in this context include the structure of ACC, the distinguishability of ACC from different synthesis routes,[39,40] and the mechanism for the release of water from hydrated ACC.The crystallization mechanism of ACC (nucleation and growth, multi-step nucleation pathways involving disordered, amorphous or dense liquid states preceding the appearance of crystalline phases) still remains unclear. There is evidence that crystal nucleation occurs from ACC *via* solid state transformation,[41,42], but the solid state mobility of the Ca^{2+} and CO_3^{2-} ions are incompatible with a solid state transformation at ambient conditions[43]and room temperature kinetic data of ACC crystallization could be modelled based on a dissolution-recrystallization reaction, where hydration and the binding strength of the hydration shell pose the main kinetic barrier for crystallization.[44] Thus, H_2O appears to be deeply involved in the nonclassical mineralization pathway because only the hydration energy of Ca^{2+} allows a reversible hydration/dehydration, which is essential in biological environments. Crystallization experiments in a water-dominated system revealed that water affects the transformation products and the mechanism of crystallization[32,45,46], with hydrated ACC converting to vaterite and eventually calcite *via* an anhydrous ACC intermediate.[32,45] Biogenic calcium carbonate also converts to crystalline $CaCO_3$ polymorphs via anhydrous ACC, although the structural changes are not reversible due to dehydration. [25,26]Although MHC is a suitable model for amorphous calcium carbonate (ACC) due to its chemical composition, a direct comparison of the EXAFS spectra of MHC with those of biogenic and synthetic ACC revealed significant differences in local structure, presumably due to a higher order in crystalline MHC.[47] Non-equilibrium phases can be prepared in a straightforward manner by ball milling.[48,49] Recently, it has been shown that anhydrous amorphous calcium carbonate can be prepared by ball milling calcite when the formation of long-range order is suppressed by incorporation of cationic (e.g. Mg^{2+})[46,50] or anionic (phosphate or silicate) defects.[19,51] While investigating the effect of dispersion media on the product formation of

ball milling reactions, we have discovered a new route for the production of amorphous calcium carbonate from monohydrocalcite, in which ACC is formed as “amorphous monohydrocalcite” (aMHC).

5.3 Results and discussion

Mechanochemical synthesis and characterization of aMHC

Ball milling was used to prepare an amorphous intermediate where the ionic constituents are mixed statistically on a molecular level. Amorphous $CaCO_3$ has been prepared by ball milling, when foreign cations (e.g. Na^+)[19,46] or anions (e.g. HPO_4^{2-})[51] were added in minor (5-10%) amounts to stabilize the metastable ball-milled amorphous calcium carbonate phase by defects. This randomly “frozen” mixture of ions serves as starting point for a crystallization or solid-state synthesis from the ionic building blocks, when a solvent is added in very small amounts to allow a reordering of the structural constituents. To avoid the use of ionic impurities, we started from MHC ($CaCO_3$ x H_2O), a metastable hydrated $CaCO_3$ polymorph, and used ethanol as a dispersing agent in a mechanochemical synthesis. The diffractogram (Figure 5.1A, blue line) of MHC shows the expected reflections of the crystalline phase,[10] while the diffractogram of the product, amorphous monohydrocalcite (aMHC), contains only two modulations (Figure 5.1A, black line) that are typical of X-ray amorphous compounds. In contrast, milling in cyclohexane yielded a mixture of aragonite, calcite, and MHC (Figure S5.1). Only the combination of the dispersing agent ethanol and mechanochemical activation led to an amorphous product (Figure 5.1B).

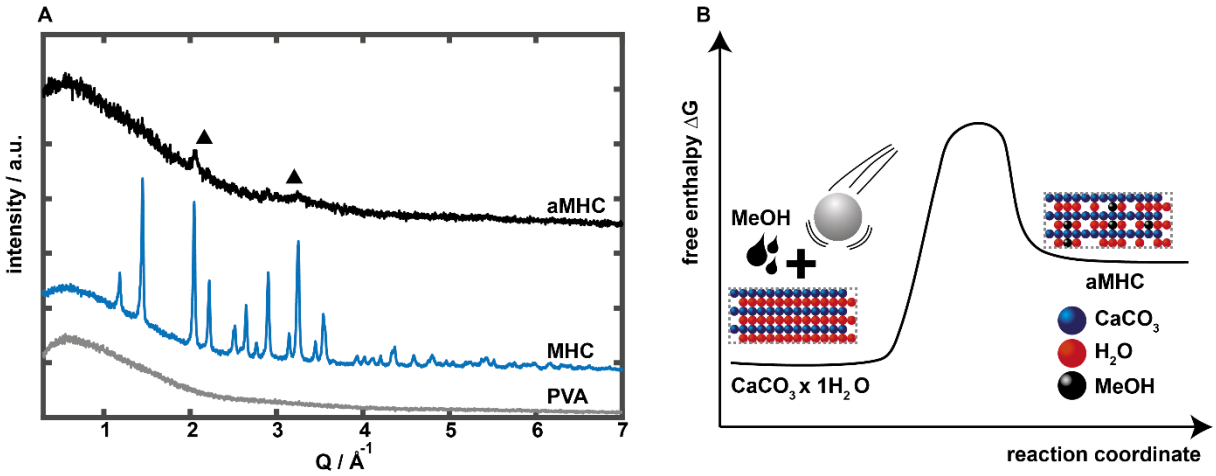

Figure 5.1. (A) X-ray diffraction patterns (B) schematic illustration of the amorphization process induced by ball milling in monohydrocalcite.

The local bonding environment in aMHC was compared to that in MHC, its crystalline counterpart, by Fourier transform infrared spectroscopy (FTIR).[52] MHC shows four characteristic carbonate and two hydroxyl modes.[10] The carbonate groups in calcite have a local D_3 local symmetry, i.e. the ν_3 mode gives a single signal and ν_1 mode is only Raman-, but not IR-active. In contrast, the ν_3 mode in MHC is split into a doublet at 1474 and 1408 cm^{-1} and the ν_1 mode appears at 1064 cm^{-1} due to the lower local symmetry (Figure 5.2A blue line).Two sharp bands at 871 cm^{-1} and 700 cm^{-1} can be attributed to the ν_2 and ν_4 modes.[53] The ν_s stretch, which is due to the incorporated water molecule of the crystal structure, is located at 3223 cm^{-1}, the corresponding ν_δ band of the bending vibration appears at 1703 cm^{-1}. After ball milling in ethanol, a significant change occurs in the carbonate bands of the IR spectra. The change is most pronounced in the ν_3 band region, where the former doublet merges into a single, broad band at 1395 cm^{-1}. In addition, the ν_1 and ν_2 bands are broadened considerably and the sharp ν_4 band of pure monohydrocalcite disappears. These findings are in good agreement with the results of previous studies of calcium carbonate.[54]

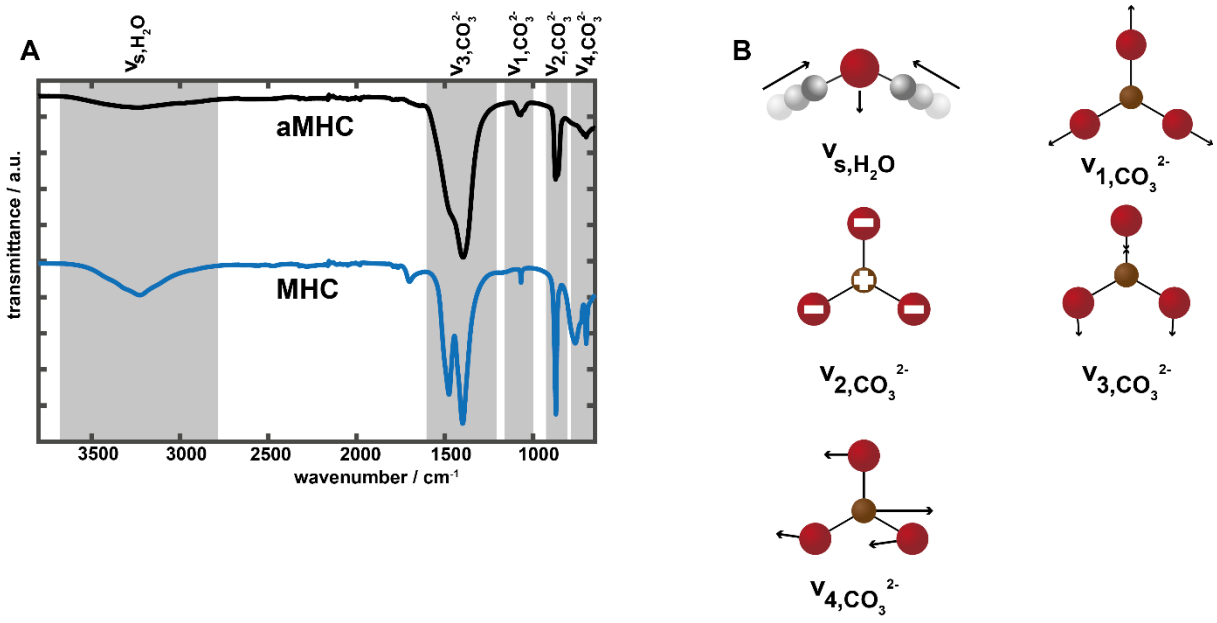

Figure 5.2. (A) FTIR spectra of monohydrocalcite (blue spectrum) and aMHC (black spectrum) and (B) schematic illustration of the different vibrational modes.

In addition to the broadening or fading of the carbonate bands, a significant change occurs in the region of stretches of the hydroxyl groups. While pure monohydrocalcite shows a prominent band at 3223 cm^{-1}, the relative intensity in aMHC decreases and the absorption shifts to wavenumbers around 2800 cm^{-1}. This can be attributed to a partial loss of water or the inclusion of ethanol which subsequently leads to a change in the strength of the

hydrogen bonding network as well as changes in the chemical shift of the water.[55] Solid state (ss) ^{1}H and ^{13}C solid-state (ss) MAS-NMR spectroscopy were applied to study the local environments in detail.[36] The ^{1}H MAS ssNMR spectrum (Figure 5.3A) is dominated by a broad water signal centered at ~4.3 ppm. Other hydrogen environments, i.e. HCO_3^- units, might also contribute to this resonance. The incorporation of ethanol instead of water into the structure is evident from the sharp signals at 4.8 ppm (OH), 3.18 (CH_2), and 1.10 ppm (CH_3), indicated by triangles. The significant difference in half-width between the signals of water (3200 Hz) and ethanol (120 Hz) highlights the sustained mobility of the ethanol solvate molecules.

Solid-state NMR spectroscopy is a valuable element-selective tool for probing the structure of aMHC, as it is not dependent like diffraction techniques on long-range order and provides information on the local and medium-range environment of the carbon nuclei through the interaction with their neighbors. Structural disorder leads to small changes in the local environment, resulting in signal broadening due to changes in chemical shielding. Therefore, the single pulse (SP) ssNMR spectrum of aMHC (Figure 5.3B) shows a broad resonance at 168 ppm (FWHM 400 Hz), wheras synthetic monohydrocalcite displays a sharp signal at 171.6 ppm (Figure S5.2). Although aMHC is amorphous according to X-ray diffraction and IR analysis, a low intensity signal appeared in the NMR spectrum at 171.6 ppm, which is attributed to residues of crystalline domains of MHC. Therefore, X-ray total scattering experiments were performed to obtain more information about the structural properties of aMHC.

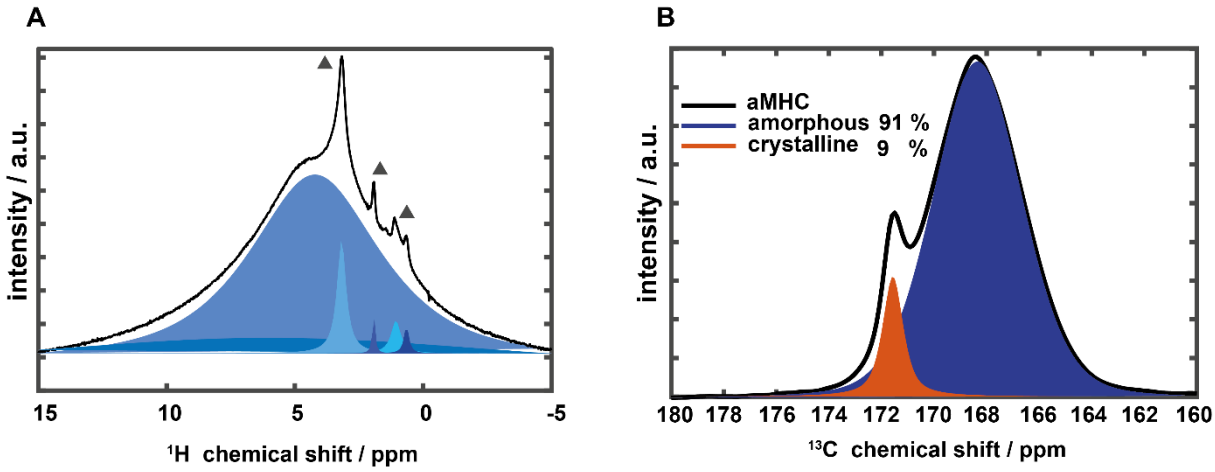

Figure 5.3. (A) ^{13}C-SP-NMR spectrum of aMHC mainly composed of an amorphous environment (blue area) with minor contributions from a crystalline environment (orange area). (B) ^{1}H NMR of aMHC with contributions from ethanol (triangles).

The PDF is the atomic density-density correlation function describing the atomic arrangement in real space without crystallographic assumptions. In short, The PDF, or reduced $G(r)$ function, gives the probability of finding pairs of atoms separated by a distance r. It is obtained from the total structure factor $S(Q)$ via a Fourier transform[56] and simultaneously reflects the long-range atomic structure manifested in the sharp Bragg intensities and the local structural imperfections manifested in the diffuse components of the total scattering pattern

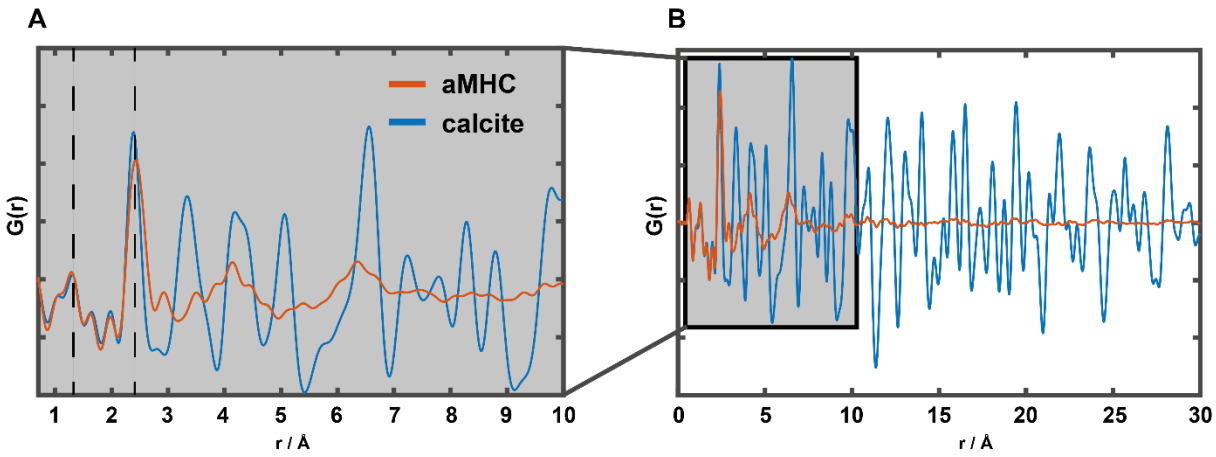

Figure 5.4. (A) Inset of the pair distribution function of aMHC and calcite in the range up to 10 Å from the full data in (B) up to 30 Å.

Solid-state NMR spectroscopy and PDF analysis are highly complementary techniques.[57] The PDF method provides structural information with atomic resolution extending to distances of several nanometers, bridging the gap between short-range NMR and long-range X-ray diffraction. A comparison of the measured data (Figure 5.4A) shows that aMHC no longer has recognizable correlations for atomic distances higher 7 Å, while correlations up to 30 Å (Figure 5.4A) can be measured in crystalline calcite. This prominent difference is due to the lack of long-range order in aMHC compared to crystalline calcite. In the magnified view up to 10 Å (Figure 5.4A) two distinct peaks appear at 1.29 Å and 2.43 Å, which can be attributed to the C-O distances of the carbonate groups and the Ca-O distances of the first coordination sphere and O-O distances within the carbonate groups. The other two peaks at 4.14 Å and 6.36 Å arise from metal-metal distances of first and second homonuclear coordination spheres (due to the high scattering cross-sections).[58] The PDF-results show that the amorphization is complete. The residual "crystalline" ^{13}C environment (*vide supra*) is either due to remnants with monohydrocalcite-like structure or to an incipient rehydration reaction.

Hydration state of aMHC

The grinding reaction in cyclohexane gave fundamentally different results than grinding with ethanol, which is known to affect crystallization pathways in the calcium carbonate system.[59] This indicates that ethanol disrupts the hydrogen network in the crystal structure of MHC. Similar findings have been reported for hydrated cobalt phosphates[60] and alkaline earth carbonates.[55]

The kinetics of thermal dehydration of MHC (Figure 5.5A) and aMCH (Figure 5.5B) was studied using thermogravimetry and differential thermal analysis. Two distinct endothermic signals appear in the temperature ranges between 180° C and 210° C as well as 670° C and 760° C for MHC ($CaCO_3 \times H_2O$, M = 188 g/mol). The first signal is associated with a mass loss of ~15.5%, in good agreement with an expected mass loss of 15.2%, due to release of structural water from MHC.[61] The second signal is associated with a mass loss of ~54%, which can be explained by a loss of water and subsequent thermal decomposition of calcium carbonate. In contrast to crystalline MHC, the differential thermal analysis of aMHC shows a broadened endothermic signal beginning at a temperature of 80°C and extending up to 260°C (Figure 5.5B). This earlier mass loss (20° C difference in comparison to monohydrocalcite) is due to the incorporation of ethanol and the lack of long-range ordering through a hydrate network.[62] In contrast to crystalline monohydrocalcite, the first mass loss accounts for only ~8 %. Taking into account that according to the NMR data (*vida supra*) only a very small fraction of the ethanol is structurally bound, the largest fraction would correspond to the hydrate water. This would result in a stoichiometric composition of aMHC as $CaCO_3 \times 0.48\ H_2O$.

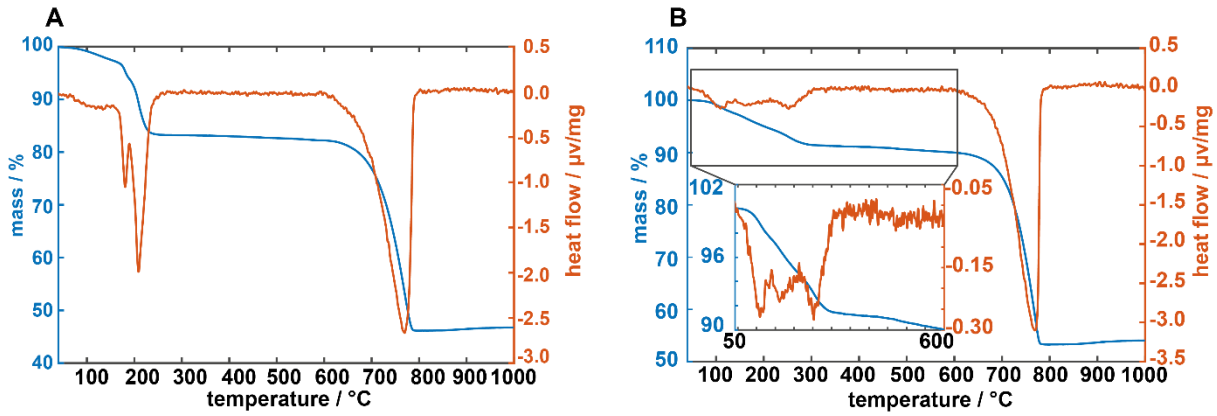

Figure 5.5. Thermogravimetric analysis (TGA, blue line) and diffential thermal analysis (DTA, red line) behavior of pure monohydrocalcite (A) and aMHC (B).

The structure of aMHC was further studied by cross-polarization (CP) NMR spectroscopy. To gain qualitative information about the distances between ^{1}H and ^{13}C species in aMHC so-called CP build-up curves have been recorded as a function of the contact time. Figure

6 A shows the ^{13}C CP ssNMR spectra and Figure 6 B the signal areas after deconvolution plotted against the contact time. The curves were fitted using equation (1) and the CP time constants T_{IS} as well as the proton $T_{1\rho}$ values were respectively obtained.

$$I(t) = I_0 \left(1 - \frac{T_{IS}}{T_{1p}^H}\right)^{-1} \left[\exp\left(\frac{-t}{T_{1p}^H}\right) - \exp\left(\frac{t}{T_{IS}}\right)\right] \quad (1)$$

The time constant T_{IS} is related to the heteronuclear dipole-dipole coupling and depends on (1) internuclear distances, (2) the number of protons in close vicinity to the ^{13}C center and (3) the local and the molecular mobility.. For a detailed interpretation the reader is addressed to the review of *Kolodziejski* and *Klinowski.*[63] $^{13}C\{^1H\}$ CP MAS experiments with variable contact times were performed on ^{13}C enriched samples of MHC (Figure S5.3) and aMHC (Figure 5.6A). As in the single-pulse NMR experiments, two environments occur in aMHC.

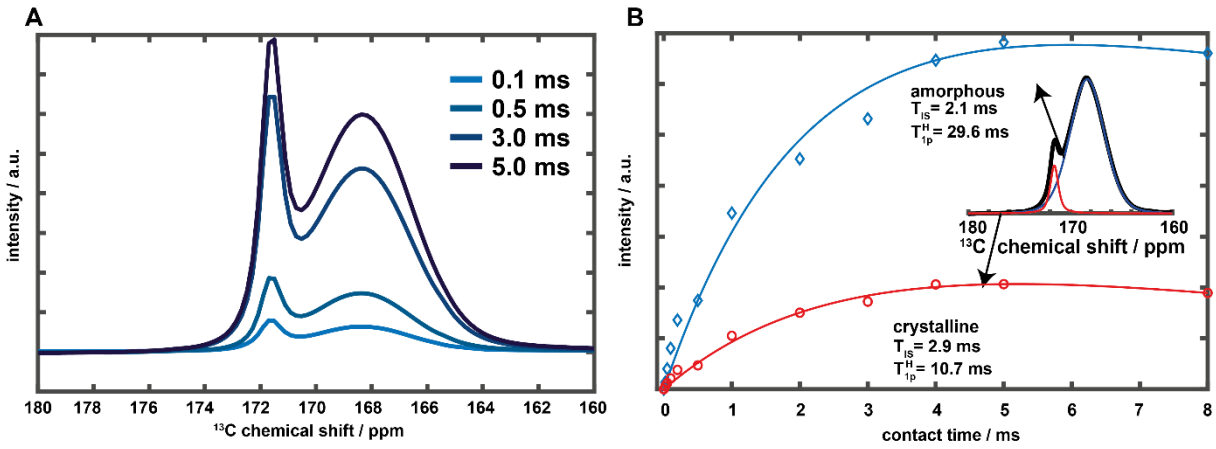

Figure 6. ^{13}C –NMR (CP) ssNMR spectra (A) and the corresponding build up curves (B) for the crystalline and amorphous environments in aMHC after deconvolution..

For an isolated pair, oscillatory behavior would be expected, but this was not observed in the experiments. Both monohydrocalcite and aMHC show an exponential increase in signal intensity with a subsequent decrease.Both monohydrocalcite and aMHC show an exponential increase of the signal intensity with a subsequent decrease. Since T_{IS} is related to a sum over carbon-proton distances,[64] the reduction of the T_{IS} values for the two environments in aMHC (Figure 5.6B, 2.9 ms and 2.1 ms) compared to MHC (Figure S5.2, 3.4 ms) can be explained by shorter average distances between the carbonate anions and water molecules due to a collapse of the underlying crystal structure. between carbonate anions and water molecules due to a collapse of the underlying crystalline system.Surprisingly, the slope of the CP build-up curve for the amorphous component is steeper than for the crystalline component. This indicates that the ^1H-^{13}C heteronuclear

dipolar couplings are stronger, i.e., the heteronuclear distances are shorter in the amorphous aMHC structure, but it should be noted that the stronger couplings may originate as well from reduced molecular dynamics. However, all spectroscopic analyses consistently show that amorphous monohydrocalcite can be produced by ball milling already through partial displacement of the hydrate water by ethanol. The generation of “defects” in the hydrate network of the MHC structure are sufficient to stabilize amorphous structure or from another point of view to suppress the stabilization of crystalline structure. For the anhydrous $CaCO_3$ polymorphs, adding foreign ions is required to generate ionic (e.g. Na^+ cations or HPO_4^{2-} anions)[46,51] defects that kinetically hinder recrystallization. This indicates that the "crystalline" domains in aMHC are indeed an integral part of the amorphous structure and are not "segregations" of a residual crystalline phase. This is also in line with the absence of any long-range ordering.

Recrystallization of aMHC

We monitored the kinetics of the re-crystallization of aMHC by FTIR (Figure 5.7A,B). Since crystallization is too rapid in pure water (immediate crystallization to calcite), the water was „diluted" by adding acetonitrile (acetonitrile with 15%v /water) to slow down the crystallization process. Acetonitrile is well suited as solvent because it is polar but aprotic and thus, unlike ethanol, cannot be incorporated transiently into the network of hydrogen bonds.[44] Immediately after exposing the sample to high temperature, the percentage of crystalline calcite increased to ca. 60 %. The intermediates of the recrystallization were taken after certain time intervals. The reaction was stopped by adding aceton and the progress of the reaction was monitored by FTIR spectroscopy. No significant changes occurred in FTIR spectra within the first 30 min. After 30 min, the width of the ν_3 band decreased and the shoulder disappeared. The ν_2 band became sharper and an additional band formed. Most importantly, the intensities of the O-H stretching band and the hydrogen bonding network decreased significantly and almost disappeared at the end of the reaction (Figure 5.7B). This indicates that an anhydrous polymorph forms upon recrystallization, which was identified as anhydrous aragonite by X-ray diffraction and Rietveld analysis (Figure 5.7C). As MHC was synthesized in the presence of Mg^{2+} cations the formation of aragonite could be related to magnesium traces in aMHC.

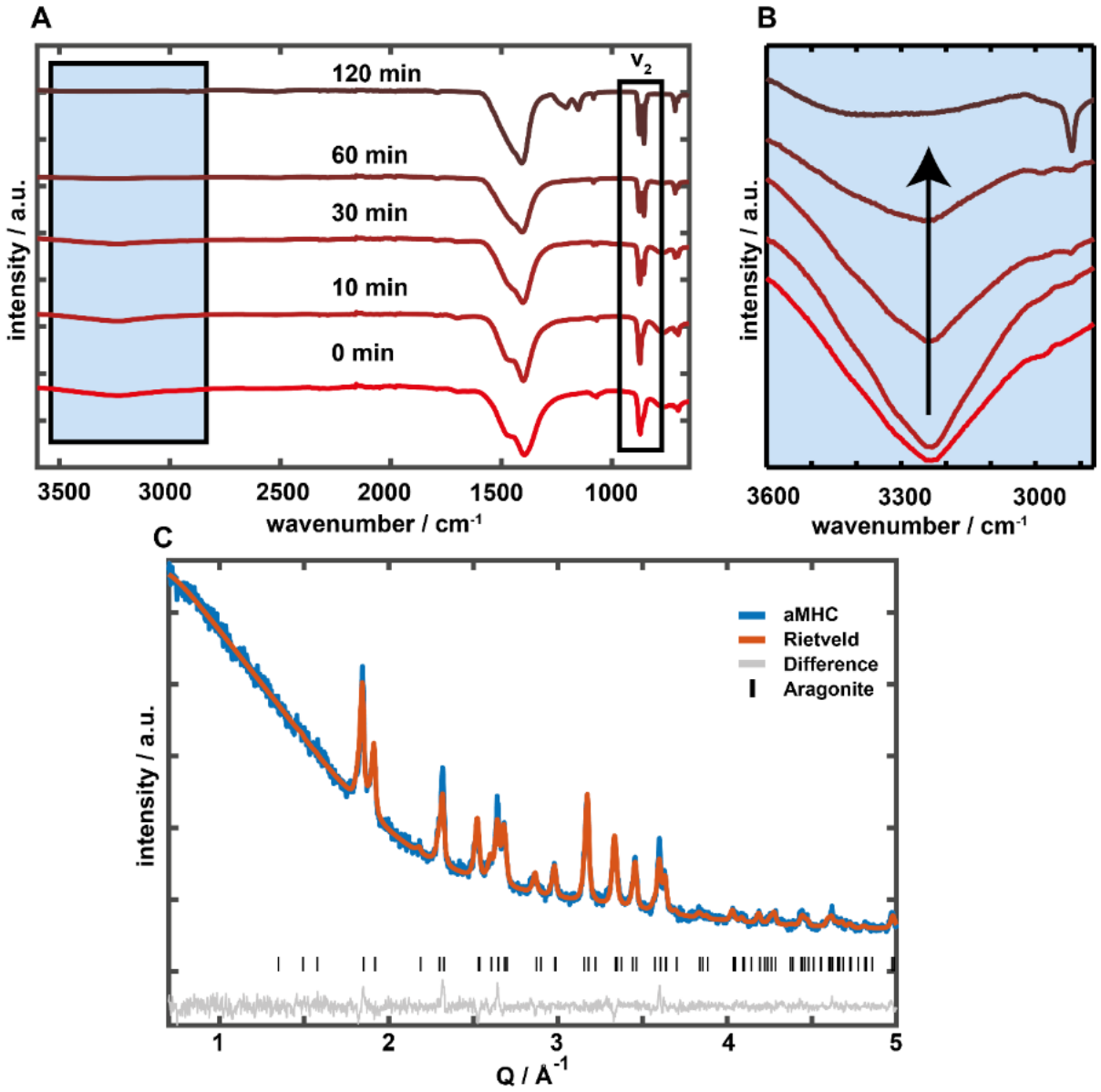

Figure 5.6. (A) FTIR spectra of aMHC recrystallized in acetonitrile mixtures at different intervals. (B) Inset of the hydroxyl stretching region during recrystallization of aMHC. (C) Rietveld refinement of the isolated product after 120 min.

CONCLUSION

Amorphous monohydrocalcite (aMHC), a new form of amorphous calcium carbonate was synthesized by mechanochemical processing of MHC in a planetary ball mill using ethanol as auxiliary solvent. Amorphization could not be achieved with apolar auxiliary solvents like cyclohexane. By combining different scattering and spectroscopy methods coupled with thermal analysis, a consistent picture of the amorphization reaction can be derived The metastable amorphous product was stabilized by partially displacing structural water with ethanol, which in return cannot be incorporated into the hydrate network of MHC due to its molecular size. The absence of structural water in aMHC played a fundamental role in the

amorphization process. Solvent “defects” in the hydrate network of the MHC structure are required to suppress the stabilization of the hydrated MHC polymorph by hydrogen bonding, whereas foreign ions (~ 10% Na^+ cations or HPO_4^{2-} anions) are required to generate ionic defects in the anhydrous $CaCO_3$ polymorphs. Based on the NMR and thermoanalytic data the approximate composition of aMHC is $CaCO_3 \times 0.48\ H_2O$. Powder diffraction and total scattering show the amorphization to be complete. The local changes to the characteristic carbonate vibrations of MHC were analyzed *via* FTIR spectroscopy.Details of the amorphous structure could be elucidated by FTIR and ^{13}C MAS NMR spectroscopy which can track changes in the local environments of the carbonate anions. Total scattering (with high-energy synchrotron radiation) and pair distribution function (PDF) analysis provide additional structural information with atomic resolution that extends to the mid-range of a few nanometers, bridging the gap between information from NMR (short-range) and X-ray diffraction (long-range).The hydrogen-bonded network of the structural water in aMHC was studied by $^{13}C\{^1H\}$ CP MAS spectroscopy on ^{13}C enriched samples of MHC and aMHC. NMR spectroscopy revealed, two environments in aMHC rather than a single one in crystalline MHC. The data are compatible with shorter average distances between the carbonate anions and structural water molecules due to a collapse of the underlying hydrogen-bonded network structure. The minimum defect concentration within the hydrate network for the successful amorphization of MHC was ~50%, i.e., every second water molecule is absent on the average. Water-induced crystallization was examined. Upon contact with water, aMHC crystallizes to aragonite without forming a another intermediate.[65] Our findings unveil the amorphization mechanism of MHC during mechanochemical treatment in the presence of ethanol as auxiliary solvent. Defects in hydration network play a key role in the formation of aMHC, because they lead, *via* alterations of the separations between the carbonate anions and water molecules, to statistical disorder of the hydrate network. The stabilization of the amorphous structure through hydrate defects, in combination with mechanochemical processing, can be considered a general strategy for the synthesis of amorphous phases in hydrated compounds and may be applicable to a variety of systems. In this way, we could synthesize a yet unknown defect-variant of MHC with distinct reactive properties, characterize its structure, and probe its crystallization behavior. This opens the field to a variety of new amorphous materials.

5.4 Experimental section

Materials. Calcium chloride dihydrate (,Sigma Aldrich), magnesium chloride anhydrous (99% Alfa Aesar) sodium carbonate (98%,Alfa Aesar), sodium cyclohexane (Analytical reagent grade, Fisher Chemicals), ethanol (absolute 99.8+%, Fisher Chemicals) and milliQ deionized water.

Synthesis of Monohydrocalcite. The samples were prepared according to a modified version of a previously described method.[31] In general stock solutions of $CaCl_2$ (0.06 mol/l) and $MgCl_2$ (0.06 mol/l) were prepared by mixing the appropriate amounts of salts into double-deionized water (resistivity > 18 mΩ cm). The solutions were mixed to give a mother solution of 200 ml with a respective Mg/Ca ratio of 20 $\%_v$. Using magnetic stirring 1.7 g anhydrous Na_2CO_3 (0.09 mol) were added and the mixture stirred for 7 days. The precipitate was filtrated and washed with 500 ml of water and subsequently with 200 ml of ethanol.

Synthesis of aMHC: Monohydrocalcite (0.500 g, 4.0 mmol) was treated in a planetary ball mill (Pulverisette 7 Classic, Fritsch). The starting material and 9 mL of methanol were transferred together with 7.5 grams of grinding balls (about 2200 balls, 1 mm diameter, ZrO_2) into ZrO_2 grinding jars. The mixture was milled for 10 h at 720 rpm. To avoid overheating, alternate 10 minutes of grinding and then a 10 minute rest phase was used. Therefore, 600 minutes of ball milling results in 1200 minutes of reaction time. Afterwards, the suspension was decanted to separate the product and grinding balls. The product was isolated by centrifugation at 10 000 rpm in which led to the separation of a solid material and dispersion.

Characterization

X-ray Powder Diffraction. X-ray diffractograms were recorded with a STOE Stadi P equipped with a Mythen 1k detector using Mo $K\alpha_1$ radiation (λ=0.7093 Å). The dry samples were prepared between polyvinyl acetate foils in perfluoroether (Fomblin Y, Aldrich). The measurements were performed in the 2θ range from 2° to 45° with a step size of 0.015° (continuous scan, 150 s/deg). Crystalline phases were identified according to the PDF-2 database using Bruker AXS.

ATR-FTIR Spectroscopy. The attenuated total reflection (ATR) FTIR spectra were recorded on a Nicolet iS10 spectrometer (Thermo scientific) using a frequency range from 550 to 4000 cm^{-1} with a resolution of 1.4 cm^{-1} per data point.

Solid-State NMR Spectroscopy. All solid state NMR spectra were recorded on a Bruker Advance 400 DSX NMR spectrometer (Bruker BioSpin GmbH, Rheinstteten, Germany operated by Topspin 1.3, 2007, patchlevel 8) at a ^{1}H frequency of 399.87 MHz. A commercial 3 channel 4 mm Bruker probe head at 10 kHz magic angle spinning (MAS) was used for all experiments. The ^{1}H NMR spectra and ^{1}H background corrected spectra were recorded averaging 32 transients with 8 s recycle delay. Spectral deconvolution were performed using self-written MatLab scripts (version 2017b).

Thermal Analysis. TGA measurements were carried out on a Netzsch STA 409 PC LUXX in the temperature range from 30 to 400 °C using heating rates of 10 K min^{-1} under air.

X-Ray Total Scattering for Pair Distribution Function Analysis. To obtain structural information about the short range order X-ray total scattering for pair distribution function (PDF) analysis was performed with data acquired from Beamline 11-ID-B of the Advanced Photon Source (APS, Argonne, Il). An incident photon energy of 58.6 keV (λ = 0.2115 Å) was used, and the samples were measured in transmission through a 3 mm polyimide (Kapton) capillary with a sample-to-detector distance of 158 mm. The scattering patterns were measured using an amorphous Si Perkin Elmer detector system (2048 x 2048 pixels, 200 × 200 μm^2 pixel size). To calibrate the sample-to-detector distance, tilt and pitch relative to the incident beam path a CeO_2 standard was used for calibration. The obtained two-dimensional scattering data was integrated from 0.5 to 24 $Å^{-1}$ in GSAS-II to produce on-dimensional scattering profiles.[35] PDFgetX3 was used to process the experimental total scattering data.[36]

Corrections such as background subtraction (by measuring the empty Kapton tube), contributions from incoherent scattering and corrections for nonlinear detector efficiency or normalization by the average atomic scattering cross section of the sample were applied using this software. The stoichiometric compositions of the amorphous material, $CaCO_3$ X 1 H_2O was used for data normalization.

5.5 References

[1] A. S. Myerson, Ed., In *Handbook of Industrial Crystallization (Second Edition)*, Butterworth-Heinemann, Woburn, **2002**, p. v.

[2] D. J. Burdige, *Geochemistry of Marine Sediments*, Princeton University Press, **2006**.

[3] H. A. Lowenstam, S. Weiner, *On Biomineralization*, Oxford University Press, New York, **1989**.

[4] T. Matschei, B. Lothenbach, F. P. Glasser, *Cem. Concr. Res.* **2007**, *37*, 551.

[5] J. Rieger, M. Kellermeier, L. Nicoleau, *Angew. Chem. Int. Ed.* **2014**, *53*, 12380.

[6] J. W. Morse, R. S. Arvidson, A. Lüttge, *Chem. Rev.* **2007**, *107*, 342.

[7] L. B. Gower, *Chem. Rev.* **2008**, *108*, 4551.

[8] H. Cölfen, M. Antonietti, In *Mesocrystals and Nonclassical Crystallization*, John Wiley & Sons, Ltd, **2008**, pp. 1–6.

[9] Z. Zou, W. J. E. M. Habraken, G. Matveeva, A. C. S. Jensen, L. Bertinetti, M. A. Hood, C. Sun, P. U. P. A. Gilbert, I. Polishchuk, B. Pokroy, J. Mahamid, Y. Politi, S. Weiner, P. Werner, S. Bette, R. Dinnebier, U. Kolb, E. Zolotoyabko, P. Fratzl, *Science* **2019**, *363*, 396.

[10] H. Effenberger, *Monatsh. Chem.* **1981**, *112*, 899.

[11] K. F. Hesse, H. Küppers, E. Suess, *Z. Kristallogr.* **1983**, *163*, 227.

[12] F. C. Meldrum, H. Cölfen, *Chem. Rev.* **2008**, *108*, 4332.

[13] I. P. Swainson, R. P. Hammond, *Mineral Mag.* **2003**, *67*, 555.

[14] I. P. Swainson, *Am. Min.* **2008**, *93*, 1014.

[15] H. Hull, A. G. Turnbull, *Geochim. Cosmochim. Acta.* **1973**, *37*, 685.

[16] R. Nishiyama, T. Munemoto, K. Fukushi, *Geochim. Cosmochim. Acta.* **2013**, *100*, 217.

[17] J. D. Rodriguez-Blanco, S. Shaw, P. Bots, T. Roncal-Herrero, L. G. Benning, *Geochimica et Cosmochimica Acta* **2014**, *127*, 204.

[18] G. Zhang, C. Verdugo-Escamilla, D. Choquesillo-Lazarte, J. M. García-Ruiz, *Nat Commun* **2018**, *9*, 5221.

[19] M. Maslyk, T. Gäb, G. Matveeva, P. Opitz, M. Mondeshki, Y. Krysiak, U. Kolb, W. Tremel, *Advanced Functional Materials n/a*, 2108126.

[20] G. Zhang, J. M. Delgado-López, D. Choquesillo-Lazarte, J. M. García-Ruiz, *CrystEngComm* **2013**, *15*, 6526.

[21] A. C. S. Jensen, S. Imberti, S. F. Parker, E. Schneck, Y. Politi, P. Fratzl, L. Bertinetti, W. J. E. M. Habraken, *J. Phys. Chem. C* **2018**, *122*, 3591.

[22] C. E. Killian, R. A. Metzler, Y. U. T. Gong, I. C. Olson, J. Aizenberg, Y. Politi, F. H. Wilt, A. Scholl, A. Young, A. Doran, M. Kunz, N. Tamura, S. N. Coppersmith, P. U. P. A. Gilbert, *J. Am. Chem. Soc.* **2009**, *131*, 18404.

[23] S. Kababya, A. Gal, K. Kahil, S. Weiner, L. Addadi, A. Schmidt, *J. Am. Chem. Soc.* **2015**, *137*, 990.

[24] L. B. Gower, D. J. Odom, *J. Cryst. Growth.* **2000**, *210*, 719.

[25] A. Shechter, L. Glazer, S. Cheled, E. Mor, S. Weil, A. Berman, S. Bentov, E. D. Aflalo, I. Khalaila, A. Sagi, *Proc. Natl. Acad. Sci. U.S.A.* **2008**, *105*, 7129.

[26] A. Akiva-Tal, S. Kababya, Y. S. Balazs, L. Glazer, A. Berman, A. Sagi, A. Schmidt, *PNAS* **2011**, *108*, 14763.

[27] S. E. Wolf, J. Leiterer, V. Pipich, R. Barrea, F. Emmerling, W. Tremel, *J. Am. Chem. Soc.* **2011**, *133*, 12642.

[28] D. J. Tobler, J. D. Rodriguez Blanco, H. O. Sørensen, S. L. S. Stipp, K. Dideriksen, *Cryst. Growth. Des.* **2016**, *16*, 4500.

[29] S. E. Wolf, L. Müller, R. Barrea, C. J. Kampf, J. Leiterer, U. Panne, T. Hoffmann, F. Emmerling, W. Tremel, *Nanoscale* **2011**, *3*, 1158.

[30] S. E. Wolf, J. Leiterer, M. Kappl, F. Emmerling, W. Tremel, *J. Am. Chem. Soc.* **2008**, *130*, 12342.
[31] V. Pipich, M. Balz, S. E. Wolf, W. Tremel, D. Schwahn, *J. Am. Chem. Soc.* **2008**, *130*, 6879.
[32] J. D. Rodriguez-Blanco, S. Shaw, L. G. Benning, *Nanoscale* **2011**, *3*, 265.
[33] P. Raiteri, J. D. Gale, *J. Am. Chem. Soc.* **2010**, *132*, 17623.
[34] S. Raz, P. c. Hamilton, F. h. Wilt, S. Weiner, L. Addadi, *Advanced Functional Materials* **2003**, *13*, 480.
[35] Y. Levi-Kalisman, S. Raz, S. Weiner, L. Addadi, I. Sagi, *J. Chem. Soc., Dalton Trans.* **2000**, 3977.
[36] H. Nebel, M. Neumann, C. Mayer, M. Epple, *Inorg. Chem.* **2008**, *47*, 7874.
[37] F. M. Michel, J. MacDonald, J. Feng, B. L. Phillips, L. Ehm, C. Tarabrella, J. B. Parise, R. J. Reeder, *Chem. Mater.* **2008**, *20*, 4720.
[38] M. Faatz, F. Gröhn, G. Wegner, *Adv. Mater.* **2004**, *16*, 996.
[39] J. H. E. Cartwright, A. G. Checa, J. D. Gale, D. Gebauer, C. I. Sainz-Díaz, *Angew. Chem. Int. Ed.* **2012**, *51*, 11960.
[40] D. Gebauer, P. N. Gunawidjaja, J. Y. P. Ko, Z. Bacsik, B. Aziz, L. Liu, Y. Hu, L. Bergström, C.-W. Tai, T.-K. Sham, M. Edén, N. Hedin, *Angewandte Chemie* **2010**, *122*, 9073.
[41] E. M. Pouget, P. H. H. Bomans, A. Dey, P. M. Frederik, G. de With, N. A. J. M. Sommerdijk, *J. Am. Chem. Soc.* **2010**, *132*, 11560.
[42] E. M. Pouget, P. H. H. Bomans, J. A. C. M. Goos, P. M. Frederik, G. de With, N. A. J. M. Sommerdijk, *Science* **2009**, *323*, 1455.
[43] H. Schäfer, *Angew. Chem. Int. Ed.* **1971**, *83*, 35.
[44] S. Leukel, W. Tremel, *Cryst. Growth. Des.* **2018**, *18*, 4662.
[45] P. Bots, L. G. Benning, J.-D. Rodriguez-Blanco, T. Roncal-Herrero, S. Shaw, *Cryst. Growth. Des.* **2012**, *12*, 3806.
[46] S. Leukel, M. Panthöfer, M. Mondeshki, G. Kieslich, Y. Wu, N. Krautwurst, W. Tremel, *Chem. Mater.* **2018**, *30*, 6040.
[47] M. Neumann, M. Epple, *Eur. J. Inorg. Chem.* **2007**, *2007*, 1953.
[48] V. Šepelák, A. Düvel, M. Wilkening, K.-D. Becker, P. Heitjans, *Chem. Soc. Rev.* **2013**, *42*, 7507.
[49] P. F. M. de Oliveira, R. M. Torresi, F. Emmerling, P. H. C. Camargo, *J. Mater. Chem. A* **2020**, *8*, 16114.
[50] P. Opitz, L. Besch, M. Panthöfer, A. Kabelitz, R. E. Unger, F. Emmerling, M. Mondeshki, W. Tremel, *Adv. Funct. Mater.* **2021**, *31*, 2007830.
[51] P. Opitz, M. P. Asta, A. Fernandez-Martinez, M. Panthöfer, A. Kabelitz, F. Emmerling, M. Mondeshki, W. Tremel, *Cryst. Growth. Des.* **2020**, *20*, 6831.
[52] L. Zedler, M. D. Hager, U. S. Schubert, M. J. Harrington, M. Schmitt, J. Popp, B. Dietzek, *Mater. Today* **2014**, *17*, 57.
[53] E. E. Coleyshaw, G. Crump, W. P. Griffith, *Spectrochim. Acta A Mol. Biomol. Spectrosc.* **2003**, *59*, 2231.
[54] F. Andersen, L. Brečević, *Acta Chem. Scand.* **1991**, 1018.
[55] S. Leukel, M. Mondeshki, W. Tremel, *Inorg. Chem.* **2018**, *57*, 11289.
[56] T. Proffen, S. J. L. Billinge, T. Egami, D. Louca, *Cryst. Mater.* **2003**, *218*, 132.
[57] J. Bréger, N. Dupré, P. J. Chupas, P. L. Lee, T. Proffen, J. B. Parise, C. P. Grey, *J. Am. Chem. Soc.* **2005**, *127*, 7529.
[58] H.-W. Wang, L. L. Daemen, M. C. Cheshire, M. K. Kidder, A. G. Stack, L. F. Allard, J. Neuefeind, D. Olds, J. Liu, K. Page, *Chem. Commun.* **2017**, *53*, 2942.
[59] S.-F. Chen, H. Cölfen, M. Antonietti, S.-H. Yu, *Chem. Commun.* **2013**, *49*, 9564.

[60] S. Bach, E. Visnow, M. Panthöfer, T. Gorelik, A. G. Buzanich, A. Gurlo, U. Kolb, F. Emmerling, C. Lind, W. Tremel, *Eur. J. Inorg. Chem.* **2016**, *2016*, 2072.
[61] T. Kimura, N. Koga, *Crystal Growth & Design* **2011**, *11*, 3877.
[62] Y. Zhao, G. Yuan, P. Roche, M. Leclerc, *Polymer* **1995**, *36*, 2211.
[63] W. Kolodziejski, J. Klinowski, *Chem. Rev.* **2002**, *102*, 613.
[64] J. Feng, Y. J. Lee, J. D. Kubicki, R. J. Reeder, B. L. Phillips, *Magn. Reson. Chem.* **2008**, *46*, 408.
[65] R. Schröder, H. Pohlit, T. Schüler, M. Panthöfer, R. E. Unger, H. Frey, W. Tremel, *J. Mater. Chem. B.* **2015**, *3*, 7079.
[66] B. H. Toby, R. B. Von Dreele, *J Appl Cryst* **2013**, *46*, 544.
[67] (IUCr) PDFgetX3: a rapid and highly automatable program for processing powder diffraction data into total scattering pair distribution functions, .

5.6 Supplementary information

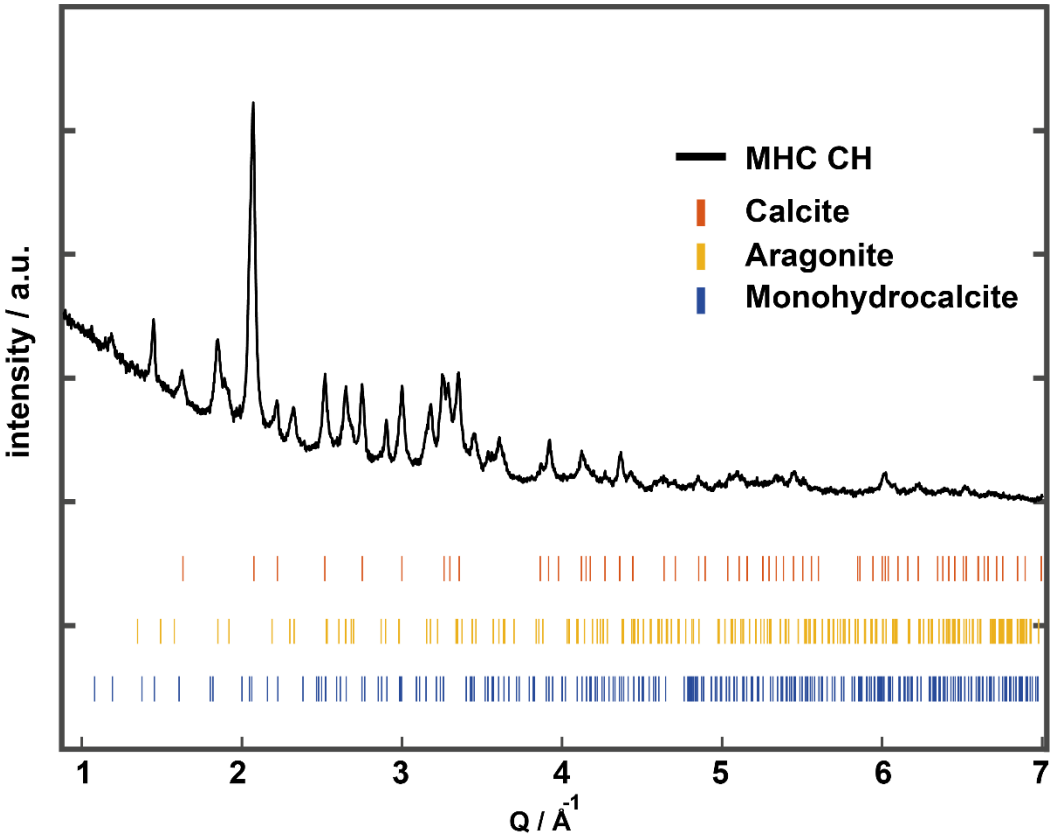

Figure S5.1: Powder x-ray diffraction pattern of monohydrocalcite milled in cyclohexane. Unlike milling in ethanol no full amorphization can be observed, but the formation of aragonite and calcite.

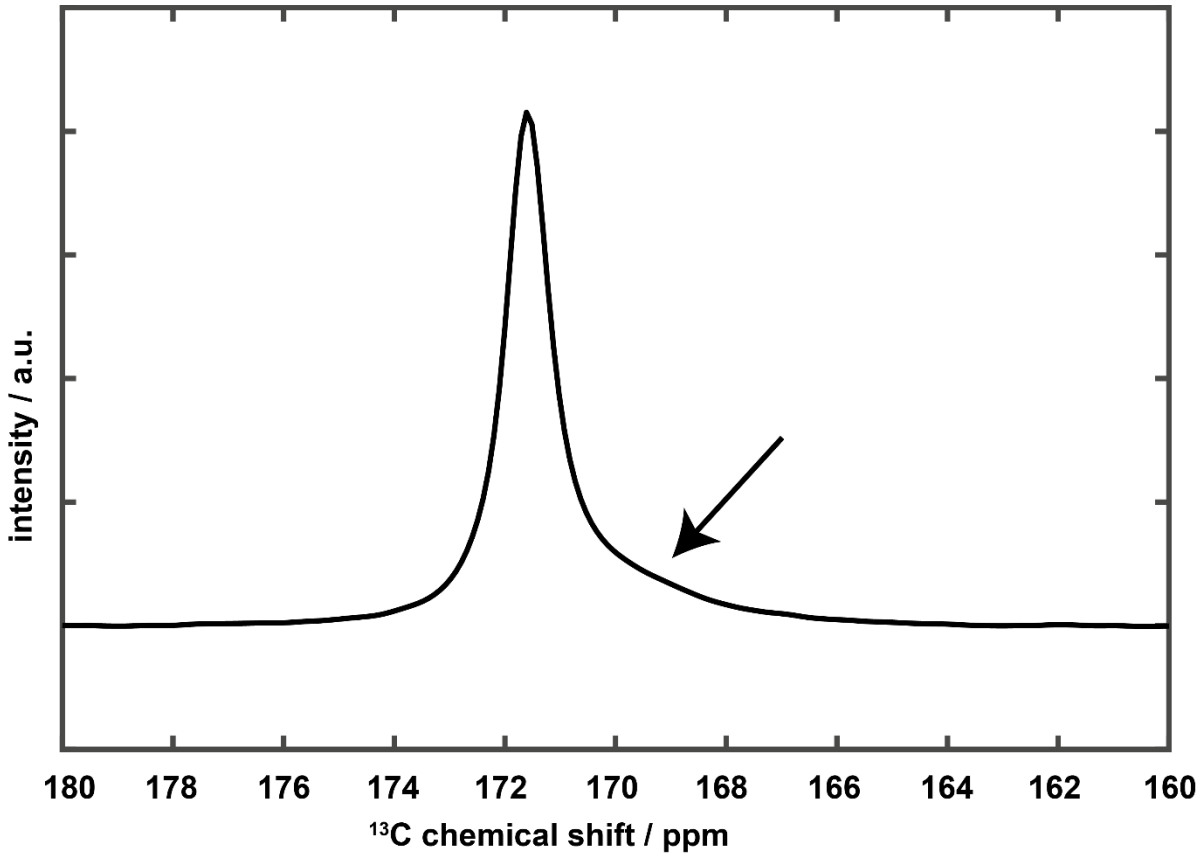

Figure S5.2: ^{13}C SP NMR spectrum of ^{13}C enriched monohydrocalcite. The spectrum shows a small asymmetry in the peak shape which probably arises minor amorphous contamination (denoted with an arrow).

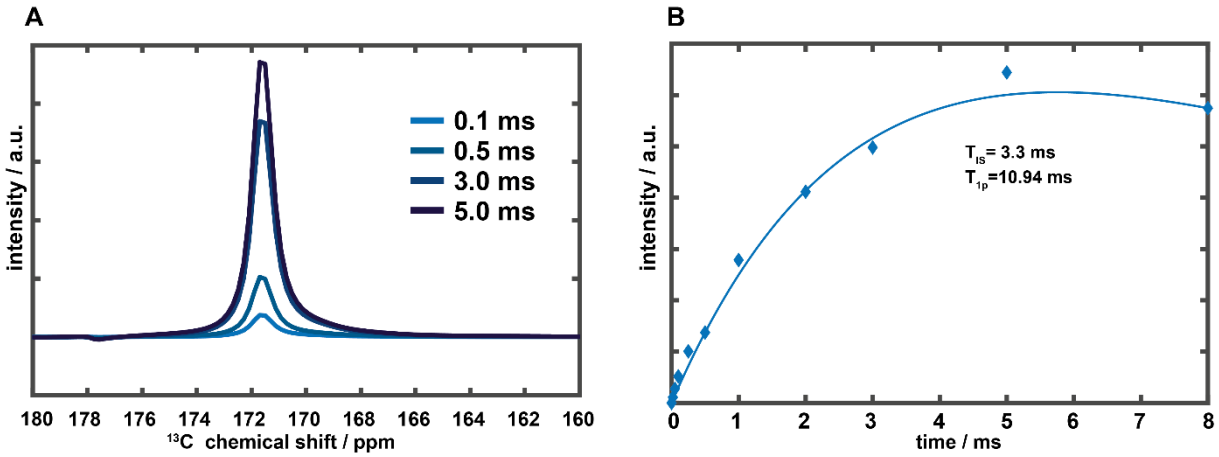

Figure S5.3: ^{13}C CP NMR spectra (A) of monohydrocalcite at different contact times and the corresponding fit (B) according to the I-S classic model (main text).

6

The long-time elusive structure of magadiite, solved by 3D electron diffraction and model building

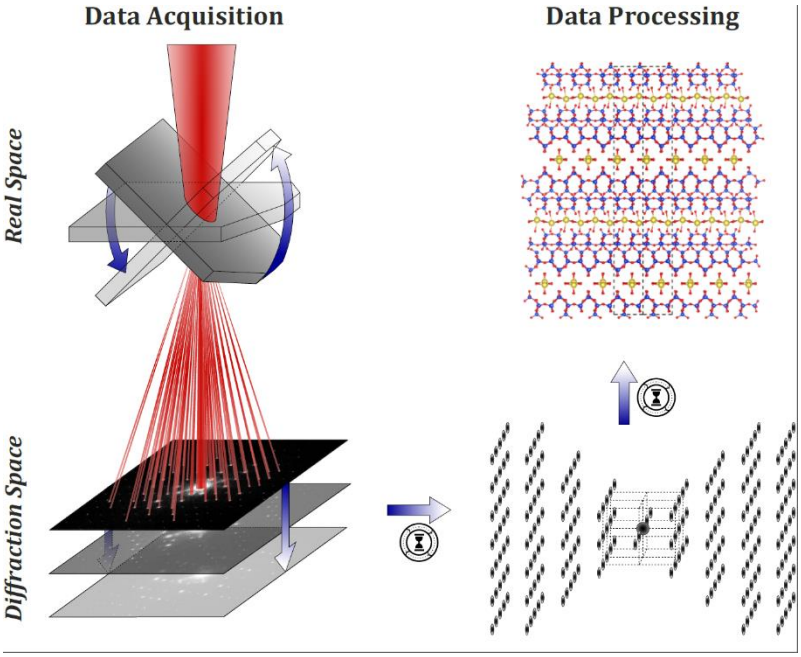

Synopsis

In addition to a great swelling ability, layered silicates also allow the functionalization of their interlayer region to form various robust green materials that are used as CO_2 adsorbents, drug carriers or catalysts. Here, the unique magadiite structure, which has resisted elucidation despite many attempts and applications the material offers, is finally described. A material-specific strategy allowed the use of 3D electron diffraction which led to the success of deciphering the atomic structure. In order to enable an ab initio structure solution of the electron beam sensitive material, a sodium-free dehydrated form of magadiite was synthetically isolated and, from that, it was subsequently possible to derive a structure model for the sodium form of magadiite, later successfully refined against powder X-ray diffraction data.

This chapter contains an adapted reproduction of *Chemistry of Materials* **2021**, DOI:10.1021/acs.chemmater.1c00107, reprinted with permission of the American Chemical Society.

Authorship Contribution

Study conception and design	Y. Krysiak M. Maslyk A. Amaral Leitao W. Tremel L. Palatinus B. Marler U. Kolb H. O. Pastore
Acquisition of data	Y. Krysiak M. Maslyk S. Plana-Ruiz H. M. Moura E. Munsignatti V. S. Vaiss
Analysis and interpretation of data	Y. Krysiak M. Maslyk H. M. Moura E. O. Munsignatti Viviane S. Vaiss

Drafting of manuscript	Y. Krysiak
	M. Maslyk
	B. Marler
	U. Kolb
	H. O. Pastore
Critical Revision	W. Tremel
	B. Marler
	L. Palatinus
	U. Kolb
	H. O. Pastore

6.1 Relevance to doctoral thesis

Material science is in permanent search of synthesis and characterization methods for new materials. So far it has been shown that several minerals and their crystallization pathways are of great interest for a broad variety of applications. Several of the underlying classes (especially silicates and phosphates) are known to form layered structures. As various sodium containing minerals have been researched throughout the dissertation, the last project focused on the synthesis of an hydrous alkali containing silicate, namely *magadiite* ($Na_2Si_{14}O_{28}(OH)_2$ x yH_2O). This mineral was first discovered in nature at Lake Magadi in Kenya in 1967. It has been used for a variety of applications, due to its inherent properties and access by hydrothermal methods. Like other hydrous layered silicates (i.e. kanemite, makatite), it can be easily intercalated, thus enabling a broad range of structural flexibility. Furthermore, the dense silicate network provides a substantial chemical stability during intercalation. Based on these characteristics many applications in regards to CO_2 capture, wastewater treatment and catalysis are imaginable and subject in different studies. Despite its frequent use as a starting material, no crystal structure for the material had been given prior to this project. As the material has been known for a long period of time, different synthesis routes have been established in this system, most of them based on hydrothermal synthesis. To find a solution to this inherent question a cooperation with Dr. Yaşar Krysiak had been established to eludicate the crystal structure by means of automated electron diffraction tomography (ADT). As natural magadiite and its synthetic analogues are prone to beam damage, in this project a partially exchanged Na-Magadiite was investigated to circumvent this problem. Firstly, a modified synthesis to synthetic magadiite was established, in which the crystallinity of the material could be enhanced. As exchange were intercalation of alkali ions are easily accessible, different series of titration experiments was conducted finally leading to partially exchanged Na-Magadiite with higher resistance to beam damage. This material could then be used in further TEM-ADT investigations for crystal structure determination. Thus, in cooperation with different research groups, a crystallographic model for natural magadiite could be established. Finally, it could be shown that the partial substitution was based on an exchange of ammonium ions and sodium ions.

6.2 Introduction

Magadiite, $Na_2Si_{14}O_{28}(OH)_2 \cdot xH_2O$, is a mineral discovered at the lake Magadi in Kenya by Hans Eugster in 1967[1]. It had been synthesized already in 1952 by Leon McCulloch[2] and titled as "A New Highly Silicious Soda-Silica Compound". Since then, it has come into focus for various applications. Magadiite is a hydrous layered alkali silicate and a member of the hydrous layer silicates (HLSs) family together with the naturally occurring kanemite[3], makatite[4], kenyaite[1,5] and many synthetic HLSs[6]. These compounds exhibit an attractive combination of properties: they are structurally very flexible thanks to the great ability for intercalation, and, at the same time, the pure, relatively thick and dense silica layers exhibit good thermal and air stability as well as chemical stability during intercalation. They have been, therefore, subject to studies for a number of applications[7]. The intercalation compounds of magadiite were investigated systematically for the first time in 1975 by Lagaly et al.[8,9] and later by Pastore et al.[10] and Wang et al.[11], who showed that magadiite intercalated with voluminous organic cations results in an organic-inorganic nanocomposite material.Magadiite is being discussed in relation to environmental issues as an alternative CO_2 capturing material[12,13] with low energy demand to desorb the gas, as well as an interesting material for wastewater treatment, thanks to its excellent adsorption properties combined with low price, environmentally friendly composition, and easy industrialization[14]. Magadiite with aluminum- and vanadium-substituted framework may be used for the dehydration of ethanol to ethylene and acetaldehyde.[15] Further applications are related to the ability of magadiite to intercalate a wide range of chemical species. For example, intercalated metal oxides have photoluminescence and magnetic properties different from the bulk materials[16]. Recently it was even shown that magadiite could be used as drug carrier[17,18] and as starting compound for the solid-state synthesis of zeolite beta[19]. Given the broad range of applications, it is surprising that the crystal structure of magadiite has so far remained unknown. The reason is that structure analysis was hindered by the strong stacking disorder and small particle size of the material. Attempts to propose a structural model were made based on ^{29}Si MAS-NMR and FTIR[20–22] and, recently, based on a PDF analysis[23]. As we will show in this work, all these attempts to solve the structure of magadiite failed. Prior to our studies, information about the structure of magadiite are mainly based on the evaluation of powder diffraction patterns. The basal spacing of the natural[1] and synthetic[24] sodium magadiite (Na-magadiite) is approximately $d \approx 15.5$ Å; its

dependency on the cation size of ion exchanged magadiite has been reported[8,9,25]. The reported basal distance of $d \approx 11.8$ Å in H-magadiite[24,25] and $d \approx 11.5$ Å in dehydrated Na-magadiite[8] is a good hint for the thickness of the silica layer. The presence of Q^3, $(Si\text{-}O)_3Si\text{-}O^-$, and Q^4, $(Si\text{-}O)_4\text{-}Si$, silicon atoms and the reported values for the Q^4:Q^3 ratio between 2 and 3[26] indicate a complex structure of the silica layers. A relatively large part of the layer should be constructed by 4-connected $[TO_4]$-tetrahedra forming a three-dimensional network[27] similar to zeolites. The interlayer region of Na-magadiite is mainly investigated based on ^{23}Na MAS-NMR[26] and FTIR[28] data showing that Na ions are hydrated and that Na ions are mutually linked through water molecules. A new possibility to crack this puzzle has appeared with the recent developments of 3D electron diffraction, 3D ED[29] (see also Supplementary Fig.S6.1). 3D ED enables structure determination from crystals smaller than 50 nm[30,31]. Developments of acquisition protocols allows the use of this technique with various transmission electron microscopes (TEMs) and allows data collection from more and more beam sensitive materials[32–35]. The ability to simulate multiple scattering also for 3D ED data by the development of dynamical refinement[36–38] and, in favorable cases, approaches the accuracy of single-crystal x-ray diffraction. Static structural disorder which leads to various kinds of diffuse scattering[39], remains a problem for structure analysis. However, even this has been successfully addressed several times with 3D ED data[40–43]. Several water-containing layered minerals have been successfully analyzed by 3D ED, despite all problems with crystal stability and specific crystal morphologies[44–47].With all the success 3D ED has had in the past years, it hits its limits when facing strongly disordered materials. In such case, computational studies based on ab initio DFT calculations can be used to strengthen the structural information. DFT has already contributed to the deeper understanding of layered materials including layered double hydroxides (LDH)[48,49], layered hydroxide salts (LHS)[50] and montmorillonite-like compounds[51]. Moreover, many applications could be investigated by computational simulations, such as ion exchange[52,53], exfoliation[54,55], catalytic processes, intercalations and reactions of molecules[56,57]. In this study, we report a comprehensive chemical and structural characterization of magadiite. The structure is solved using 3D ED and accurately refined by Rietveld refinement against Powder X-ray diffraction (PXRD) data, supported by DFT calculations. The resulting structure agrees with MAS-NMR data of magadiite. We discuss the structure of the silica layer, the chemically active surface and interlayer region of magadiite.

6.3 Experimental section

Synthesis and identification

Na-magadiite

For the preparation of both samples, sodium metasilicate pentahydrate (7.210 g, 0.034 mol, Sigma – Aldrich) was dissolved in 63.6 cm^3 of double-deionized water (resistivity >18mΩcm). After dissolution, the pH of the solution was ca. 13.6; concentrated HNO_3 (Honeywell Fluka) was added to adjust the pH of the solution to the range of pH 10.7-10.9. When the solution changed to a gel it was refluxed for 4 h at a temperature in the range of 347-349 K. After cooling to room temperature, the gel was transferred to a custom-built stainless-steel autoclave with Teflon lining for the hydrothermal treatment. For the c–NaM, the procedure from the dissolution of sodium metasilicate until the transference to the autoclave was performed under ambient conditions and the hydrothermal treatment was conducted for 66 h at 424 K[10]. For the a–NaM sample the preparation procedure took place under argon and the hydrothermal treatment was 6 h longer, at the same temperature[15]. After the hydrothermal treatment, the product was transferred to centrifuge tubes and washed ten times with 30 cm^3 of double-deionized water until the pH became neutral and finally dried in air.

NH_4-magadiite

For NH_4–magadiite synthesis, 50 mg of as-synthesized Na–magadiite were dispersed in 50 ml of double-deionized water (resistivity >18mΩcm) in a self-made Teflon beaker of 100 ml volume. At first 1 ml of a 0.28 mol L^{-1} nitric acid solution was added to the suspension at a stirring speed of 500 rpm in a regular stirring plate. Then 2 ml of a 0.26 mol L^{-1} ammonia solution was added. (NH_4^+ + NH_3) / Na^+ ratio is 11.5 and the final pH-value was determined to be 8.5 by a regular glass pHmeter. The solid product was then centrifuged and dried in air.

Differential thermal analysis and thermogravimetry

Thermal properties were investigated by simultaneous DTA/TG measurements using a TA Instruments SDT650 thermal analyser. The samples were heated in synthetic air from 30 °C to 1200 °C with a heating rate of 10 °C/min.

Scanning electron microscopy

Scanning electron micrographs were taken using a Zeiss Merlin Gemini 2 electron microscope to study the morphology of the crystals and the homogeneity of the samples. The samples were gold coated by vacuum vapor deposition prior to analysis. For a qualitative chemical analysis, an OXFORD AZtecEnergy X-ray microanalysis system (attached to the electron microscope) was used. The photographs were taken with an electron beam of 2 to 4 kV and 150 to 250 pA at a working distance of 7.3 – 9.9 mm. The chemical analysis was performed with 20 kV at a working distance of 10 mm using an OXFORD Nano detector.

Chemical analysis

Quantitative chemical analysis was performed by atomic absorption spectroscopy using a Varian SpectrAA 220 (NH_4-magadiite) and by X-ray fluorescence spectroscopy using a Rigaku ZSX Primus IV (Na-magadiite). N and H elemental analysis was performed using a Vario EL Cube under Ar atmosphere, coupled with a thermal conductivity detector. Two cycles were recorded.

3D electron diffraction

Measurements

All measurements of Na-Magadiite and NH_4-magadiite were carried out either with a transmission electron microscope (TEM) FEI Tecnai F30 S-TWIN equipped with a field emission gun (300 kV) or with a TEM FEI Tecnai 20 equipped with a LaB6 cathode (200 kV). The powdered samples were dispersed in ethanol using an ultrasonic bath and sprayed on carbon-coated copper grid using an ultra sound sonifier[58]. The grid was plunged into liquid nitrogen and then transferred to the TEM. In case of measurements performed with the FEI Tecnai F30, TEM images and electron diffraction (ED) patterns were acquired with a Gatan UltraScan4000 CCD camera (16-bit, 4096 x 4096 pixel) at hardware-binning of 2. Scanning transmission electron microscopy (STEM) images were collected by a FISCHIONE high-angular annular dark field (HAADF) detector and acquired by Emispec ES Vision software. Three-dimensional electron diffraction data were collected using the acquisition module automated electron diffraction tomography (ADT) developed for FEI microscopes[59]. A condenser aperture of 10 μm and mild illumination settings (gun lens 8, spot size 8) were used in order to produce a semi-parallel beam of 200 nm in diameter (0.26 e-/$Å^2$s). Crystal position tracking was performed in microprobe STEM mode. In case of

measurements performed with the FEI Tecnai 20, TEM images and ED patterns were taken with an Olympus Veleta CCD camera (14-bit, 2048 x 2048 pixel). Mild illumination settings were used (condenser aperture of 10 μm and spot size 8) in order to produce a semi-parallel beam of 480 nm in diameter (0.078 e-/Å^{2}s). Three-dimensional electron diffraction data were collected using own developed scripts in Olympus Soft Imaging Solutions iTEM software. For tilt experiments acquisitions were performed with a Gatan cryo-transfer tomography holder. The ED data were collected on both TEMs with electron beam precession (precession electron diffraction, PED) to improve reflection intensity integration quality[60,58]. PED was performed using a Digistar unit developed by NanoMEGAS SPRL. The precession angle was kept between 0.62° and 1.0°.

Data reconstruction

The eADT software package and PETS2.0 were used for 3D electron diffraction data processing[61,62]. It was necessary to carefully refine the orientation of each single frame due to bending and/or multiple domains of the measured particle to improve the data integration from Rint(all) = 28.2% to 25.2% (Laue class mmm)[38]. The refined frame orientations are shown in Supplementary Fig.6.7.

Structure solution of NH_4-magadiite

Ab initio structure solution was performed assuming the kinematic approximation $I \sim |F_{hkl}|^2$ by Direct Methods implemented in the program SIR2014[63]. Scattering factors for electrons were taken from Doyle and Turner[64]. The *hkl* indices of the extracted intensities were transformed with the [0 1 0; 0 0 1; 1 0 0] before structure solution with respect to the standard setting of space group *Fdd*2. The structure model was then transformed back to setting cab (*F*2*dd*). The improved intensity integration enabled a reasonable structure solution (R_F = 20.9%) with SIR2014 in space group *F*2*dd* using Direct Methods. The seven strongest maxima of the normalized scattering density map (from 1.00 down to 0.63) correspond to seven independent silicon atoms. Basically, all silicon atoms of the asymmetric unit are surrounded by four maxima which correspond to 15 of the next 16 maxima (from 0.61 down to 0.29) of the normalized scattering density. They were assigned to oxygen and thus forming a layer built by interconnected [SiO_4]-tetrahedra. One maximum (0.32) and the five weakest maxima (from 0.26 down to 0.09) were not taken into account. The scattering density map of the structure solution is overlaid with the structural model in Fig.6.3 and the maxima are listed in Supplementary Table 6.2.

Structure refinement of NH_4-magadiite

The structure was further transformed with [-1 0 0; 0 -1 0; 0 0 1] just for comparability with structure solutions based on other data resp. data treatments. Difference Fourier mapping and least-squares refinement were performed with the software JANA2006[65]. Soft distance and angle restraints were used for d(Si-O) = 1.610(5) Å resp. ∠(O-Si-O) = 109.5(5)°. Anisotropic displacement parameters were constraint to be the same for all Si sites and the same for all O sites. Additionally, the components U^{12}, U^{13} and U^{23} of the ADP parameters were fixed to be 0. The Isotropic displacement parameter of the N site was fixed at crystal chemically meaningful value to U = 0.080 Å².

The following dynamic refinement was initially carried out on the basis of the same data set. Therefore, a standard procedure was followed which is described in Palatinus et al., in more detail[66,67]. Additional parameters for the dynamical refinement are the scaling factors of each frame and typically one average thickness value per dataset. An additional dataset was used in a second step, which allowed to ignore patterns with less than 10 reflections, resolution lower than 0.8 $Å^{-1}$ and recorded from multiple domains, without decreasing reflex parameter ratio. Out of 242 images, 69 were left out for refinement. Electron diffraction is sensitive to chirality, so the twinning matrix [-1 0 0; 0 -1 0; 0 0 -1] was applied in order to refine the volume fractions of the inversion twin.

Powder X-ray diffraction

Measurements

Powder diffraction data were recorded from a Siemens D5000 powder diffractometer in modified Debye-Scherrer geometry using monochromatic CuKα_1 radiation (λ = 1.54059 Å). The diffractometer was equipped with a Braun linear position-sensitive detector covering a 2θ range of 6°. The sample was sealed in a glass capillary with a diameter of 0.3 mm to avoid preferred orientation of the plate-like crystals and the loss or uptake of water by the samples.

Rietveld refinement of Na-magadiite

The average structure of magadiite, based on the structure models as determined by the ADT method, was refined from the powder XRD data in space group symmetry *F*2dd using the FullProf 2K program[68]. No absorption correction was necessary. Soft distance restraints were used for d(Si-O) = 1.610(6) Å, d(Si...Si) = 3.10(2) Å, d(O...O) = 2.63(2) Å, No distance restraints were used for atoms occupying the interlayer region (Na, water

molecules). Isotropic displacement parameters B_{iso} were fixed at crystal chemically meaningful values: B(Si) = 1.0 Å², B(O, framework) = 2.0 Å², B(O, water) = 3.0 Å², and B(Na) = 3.0 Å². Anisotropic Lorentzian peak broadening, modelled by using spherical harmonics (9 parameters), was applied to the peak shapes of magadiite.

Density-Functional Theory calculations

Computational methodology

All the structural and electronic calculations were performed by QUANTUM ESPRESSO package[69], which are based on the Density-Functional Theory (DFT). The calculations were performed under periodic boundary conditions and plane wave functions as basis set[70,71]. The exchange-correlation potential was described by the PBE-GGA[72], with the core electrons treated by Vanderbilt Ultrasoft pseudopotentials[73]. The Kohn-Sham orbitals were expanded in a plane wave basis set up to a kinetic energy cutoff of 55 Ry and k-point grid of 2×2×1 was used to sample the first Brillouin zone for all cells according to the Monkhorst-Pack method[74]. Their geometries were optimized using a reduced unit cell, and the XRD powder patterns were simulated by Mercury program. The NMR parameters of ^{23}Na, ^{29}Si and ^{1}H nuclei were calculated according to the gauge including projector augment wave (GIPAW) method[96,97], and the spectra were plotted for the comparison with experimental data in Supplementary Fig.6.15. The reduction of unit cell and NMR methodology are described in Supplementary Information. The existing interactions between the water molecules/layer were mapped by the construction of charge density difference plots, using the following equation:

$$\Delta\rho(\vec{r}) = \rho_{[Total]}(\vec{r}) - \rho_{[Na/layer]}(\vec{r}) - \sum_{i=1}^{i=4} \rho_{[H_2O]i}(\vec{r})$$

Where ρ_{total}, $\rho_{Na/layer}$, ρ_{H2O} are the density charge of total structure, layer and Na^+ cations together and water molecules, respectively. For the calculation of the DOS and pDOS, a larger k-sampling was used. Monkhorst-Pack meshes of 6 × 6 × 3 were used for Na-magadiite and an amount of 20% of the valence states was chosen for the computation of the conduction states. All figures of the DFT-optimized structure were performed using the Xcrysden program and the display radius of Na, Si, O and H were 2.24, 1.55, 1.02, 0.53, respectively.

NMR simulation methodology

The NMR parameters were calculated with the gauge including projector augmented wave (GIPAW) approach[75,76]. The isotropic chemical shielding (σ) is compared to the experimental isotropic chemical shift by using the standard expression: $\delta_{iso} = \sigma_{ref} - \sigma_{iso}$. Experimentally the reference chemical shielding σ_{ref} is measured in an external reference. For the calibration of ^{23}Na, ^{29}Si and ^{1}H nuclei of this work, a correlation between calculated chemical shielding ($\sigma_{calculated}$) and experimental chemical shifts (experimental δ_{iso}) (Supplementary Table 9 and Supplementary Fig.6.15) was performed using a number of reference compounds reported in the literature[77–81]. The equations were found by linear regression (Supplementary Table 6.15): $\delta_{iso} = 552.95 – 1.004\ \sigma_{calc}$ for ^{23}Na nucleus; $\delta_{iso} = 293.58 – 0.8682\ \sigma_{calc}$ for ^{29}Si nucleus and $\delta_{iso} = 29.489 – 0.954\ \sigma_{calc}$ for ^{1}H nucleus.

Reduction of unit cell

The filled unit cell of Na-magadiite (without hydrogen atoms) contains 432 atoms and because of this, the reduction of the crystallographic unit cell to the primitive unit cell was necessary to decrease the computational cost. For the reduction, new vectors were identified and the new parameters were used a = 7.30 Å, b = 7.31 Å, c = 37.76 Å and angles α = 107.99°, β = 60.41°, γ = 92.14°. A model with 108 atoms and ¼ of volume was obtained. Using the reduced Na-magadiite cell, hydrogen atoms were placed on the water molecules and hydroxyl groups on the layer, keeping the balance of charge in the structure, and optimized geometry (all unit cell parameters, angles and atomic positions); the results are shown in Supplementary Table 10. After that, all the electronic calculations shown in this work were performed with the optimized model. The lattice parameters of the F-centered setting of the optimized structure are given in Supplementary Table 6.4.

6.4 Results and discussion

Synthesis of magadiite

Na-magadiite

Magadiite can be synthesized by hydrothermal treatment, in pH values between 10.4 to 10.9. More acidic reaction mixtures yield magadiite in mixture with a large amount of amorphous material. In pH values higher than 11, the magadiite yield is extremely low. It is known[82] that the nature of soluble silicon species is strongly dependent on pH and concentration; monomers and cyclic or linear oligomers, for instance, will be found in variable molar ratios in dynamic equilibrium. The polymerization degree of silicate anions

increases with the mixture concentration and with the Si/M molar ratios (M= alkaline ion). Above pH 11-12, monomeric and polymeric ions exist in solution and solid materials are usually not observed. Acidification leads to the precipitation of amorphous silica.In the present study a pH between 10.7 and 10.9 turned out to yield the most crystalline sample, albeit in a smaller yield. Two magadiite samples were prepared. In the first one (c-NaM), the reaction mixture was prepared in a standard procedure under ambient atmosphere and no special care was taken to avoid contact of the gel with the atmosphere[10,83]. A typical, disordered magadiite was obtained. The second sample (a-NaM) was synthesized using the same reaction mixture as for the first sample, but the preparation of the gel and its aging were performed under argon flow so that contact with the room atmosphere was avoided, until the reaction mixture was transferred to the autoclave and closed. Additionally, the reaction time for the hydrothermal synthesis was changed from 66 h to 72 h. This procedure led to fairly well ordered magadiite. Chemical analysis of the a-NaM by X-rays fluorescence revealed the presence of 3.30% Na_2O which corresponds to Na-magadiite with the chemical formula $Na_{1.9}[Si_{14}O_{27.9}(OH)_{2.1}]$ * 7.4 H_2O (the water content was calculated from the TG analysis of the air-dry sample revealing a weight loss of 12.6% between 30°C and 200°C).

NH_4-magadiite

a-NaM was first titrated with HNO_3 and then with NH_3. The titration resulted in a moderately crystalline material. Chemical analysis of the sample by atomic absorption spectroscopy (AAS) proved that it contains almost no sodium (0.015 wt%) and a negligible amount of aluminum (0.06 wt%). DTA-TG showed that the air-dry sample presented a very small amount of water (about 1 water molecule per 14 Si); the amount of ammonium could not be calculated from the TG curve (see section *Thermal analysis*). The chemical analysis of the titrated sample resulted in 0.94% nitrogen and 0.96% hydrogen. Thus, the composition is calculated to be $(NH_4)_{0.6}\ H_{1.4}\ [Si_{14}O_{28}(OH)_2]$ * 1 H_2O and we denote the material NH_4-magadiite.

Characterization of magadiite

Scanning electron microscopy

Scanning electron microscopy micrographs are shown in Supplementary Fig.6.2. The crystals present the typical plate-like morphology and agglomerate to globular particles. The typical lateral size of the platelets is a few micrometers, and the thickness is usually

much less than 100 nm. The platelets tend to be strongly bent. The platelets of NH_4-magadiite (Supplementary Fig 6.2) appear to be smaller and less agglomerated than the crystals of the Na-magadiite.

Powder X-ray diffraction, PXRD

PXRD patterns of the samples are shown in Fig.6.1. The comparison of the patterns shows a similarity of a-NaM and c-NaM. However, a-NaM has a visibly better crystallinity. This is documented by the appearance of a larger number of reflections in the powder pattern (marked by * in Fig. 1) as well as smaller widths of the peaks in the powder pattern of a-NaM. For example, the full width at half maximum (FWHM) of the most prominent reflection at 5.73° is 0.19° in a-NaM, while it is 0.25°for c-NaM. Based on the results of 3D ED, the powder pattern of both a- and c-NaM could be completely indexed by a single F-centered orthorhombic phase (see section *Structure determination* for more details).

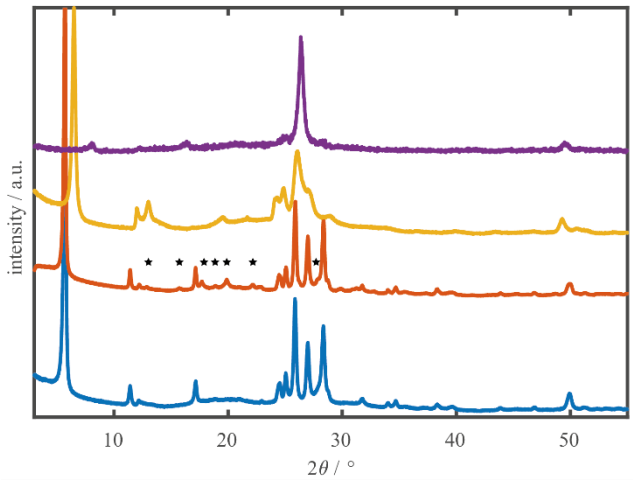

Figure 6.1. PXRD patterns (λ = 1.54059 Å) of magadiite materials obtained in different ways: c-NaM (blue) by conventional synthesis, a-NaM (red) by adapted synthesis, NH_4–magadiite (yellow) by ion exchange and H-magadiite (purple) by acid treatment. Reflections appearing in the pattern of a-NaM but missing in c-NaM are marked by *.

The powder pattern of NH_4-magadiite is markedly different from the other two samples. A generally less sharp powder pattern with a lower number of peaks and much larger FWHM of the peaks indicate much lower crystallinity of the material and probably more disorder. The most intense peak corresponding to the reflection 004 shifts markedly from 5.6° to 6.5°. This corresponds to the decrease of the basal distance from 15.52 Å to 13.78 Å as a result of the exchange of hydrated Na^+ by NH_4^+. Although it may seem that Na-magadiite is a much better candidate for structure analysis than NH_4-magadiite due to its better crystallinity, it will be shown below that the determination of the structure of NH_4-magadiite was a necessary prerequisite for the successful structure determination of Na-magadiite.

Thermal analysis

The DTA and TG curves of NH_4-magadiite and Na-magadiite are quite different (Supplementary Fig. 6.3). The most important information that can be extracted from the TG curve of NH_4-magadiite is the fact that in the temperature range from RT to 180 °C only approx. 1.4 % mass loss is recorded, indicating a very small amount of molecular water in the structure of NH_4-magadiite. Na-magadiite shows a significantly larger mass loss (12.6 %) in the same temperature interval corresponding to a composition of $Na_{1.9}[Si_{14}O_{28}(OH)_{2.1}]$*7.4 H_2O. The additional weight loss of approximately 10 % (NH_4-magadiite) recorded between 180 °C and 1000 °C is partly assigned to the concurrent removal of ammonia (decomposition of NH_4^+) and water (condensation of OH groups) and partly to the decomposition of amorphous "hydrated silica" which appears in the PXRD diagram of NH_4-magadiite as a significantly increased broad background around 24° 2θ (see Suppl. Figure 6.5 (right)). In this temperature range Na-magadiite loses only 1.9 %, exclusively due to the condensation of OH groups.

Structure determination

3D ED of Na-magadiite

Despite the fairly good quality of the powder pattern of a-NaM, it was not possible to solve the structure or even find the unit cell parameters from the powder patterns. Therefore, structure analysis of Na-magadiite was attempted using 3D ED[29]. The first experiments were performed at room temperature. Unfortunately, the reconstructed distribution of intensity in reciprocal space showed very strong one-dimensional diffuse scattering with nearly no variation of intensity along the diffuse lines (Fig. 2 and Supplementary Fig.6.4). The other two directions were well resolved and the 2D lattice derived from them agreed with the previous observations by electron diffraction with the longest d-spacing of approximately 7.38(3) Å[24]. The strong diffuse scattering was observed consistently on all investigated crystals, and contrasted with the presence of relatively strong and sharp reflections in the PXRD pattern (Fig. 6.1). It was concluded that the reason is a collapse of the structure under *in vacuo* conditions. To avoid the collapse, further experiments were performed with the sample cooled to liquid nitrogen temperature before introducing it into the TEM chamber, to keep the vapor pressure of the loosely bonded water low. The resulting 3D ED datasets exhibited less diffuse scattering. Nevertheless, even under cryo temperatures and mild illumination conditions, only one dataset allowed an estimation of

the lattice periodicity along the diffuse direction (Supplementary Fig.6.4d-f). Using the shape and symmetry of the diffuse scattering as support, the lattice was indexed as face-centered orthorhombic with approximate lattice parameters a = 10.59 Å, b = 10.04 Å, c = 62.36 Å. The indexed lattice was used to index the PXRD pattern using the program DASH[84]. Program ExtSym[85] implemented in DASH[84] suggested *F-dd*, *Fd-d*, *F-dd* and *Fddd* as the most probable extinction symbols. A more detailed analysis of the powder diffractogram revealed violations of the reflection conditions required for the presence of a *d* glide plane in direction ***a*** (for example reflections 024 and 028). Consequently, a Pawley fit was carried out with TOPAS in space group *F*2*dd* and resulted in the lattice parameters a = 10.537(2) Å, b = 10.136(2) Å and c = 62.080(4) Å (Supplementary Fig.6.5).

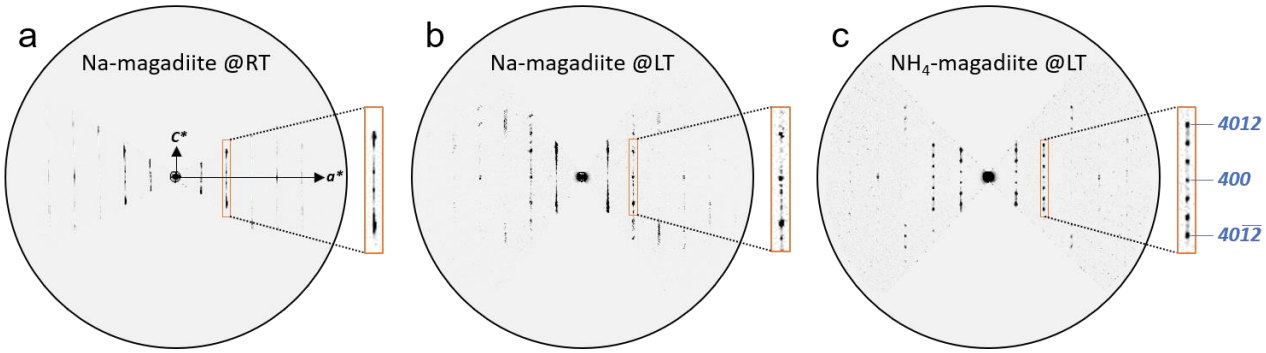

Figure 6.2. Reciprocal space sections *h0l* of (a) Na-magadiite measured at room temperature, (b) Na-magadiite measured at low temperature by cryo transfer and (c) NH_4-magadiite measured at low temperature by cryo transfer. *40l*-reflections (orange) are enlarged in (a), (b) and (c).

The intensities of the 3D ED data were extracted by the program PETS2.0[62] (R_{int}(all) = 34.5%, Laue class *mmm*), and a structure solution was attempted. Unfortunately, all attempts to solve the structure by Direct Methods or charge flipping implemented in SIR2014[63] and Superflip[86], respectively, failed.

Structure analysis of NH_4-magadiite

Tentative unit cell parameters were derived from those of Na-magadiite by contracting the length of the c parameter from ~62 Å to ~55 Å to account for the shift of the basal peak (Fig.6.1). This unit cell and the space group *F*2*dd* could be used to index the powder pattern of NH_4-magadiite very convincingly (Supplementary Fig. 5). The lattice parameters were refined by a Pawley fit to a = 10.751(9) Å, b = 10.286(8) Å and c = 55.086(3) Å.

NH_4-magadiite was cryo-transferred into the TEM to collect 3D ED data. The diffuse scattering along c^* in these data sets was much less pronounced than in the 3D ED data of Na-magadiite, (Fig.6.2, Supplementary Fig.6.6). The best data set showing the least diffuse

scattering was used for structure solution. The data were processed with PETS 2.0[62]. It turned out that the key to extracting data of quality suitable for structure solution was a careful refinement of the orientation of each single diffraction pattern (see SI for more details). The integration resulted in R_{int}(all) = 25.2% in Laue class *mmm*. The integrated data allowed a structure solution (R_F = 20.9%) with SIR2014 in space group *F*2*dd* using Direct Methods. Supplementary Table 6.1 lists the atom types, integrated maxima of the electron density map, atom coordinates, occupancies and estimated isotropic atomic displacement parameters. The initial solution was of sufficient quality to reveal the complete structure of the silicate layer. One prominent maximum in the interlayer region could be interpreted as a nitrogen atom of the ammonium cation. The scattering density map of the structure solution is overlaid with the structural model in Fig.6.3. A kinematical refinement ($I \sim |F_{hkl}|^2$) was performed in JANA2006[65] and yielded the crystallographic R-value *R*1 = 17.0% - a fairly low value for kinematical refinement against 3D ED data. As a next step, a dynamical refinement[66,67] of the structure model derived from the kinematical refinement was performed to obtain a more accurate and reliable structure model. It converged to *R*1 = 11.7% and yielded an occupancy for the nitrogen atom of 0.73(2) corresponding to approximately 1.5 NH_4^+ cations among 14 Si atoms. Further information about the kinematical and dynamical refinement is summarized in Supplementary Table 6.2. The dynamical refinement provides also an estimation of the crystal thickness. In the present case the thickness converged to rather low values (13.5 nm and 8.3 nm). Such a low refined thickness indicates that the multiple scattering effects are suppressed in the real material compared to ideal crystal. An obvious reason is the very high mosaicity of the particles and the structural disorder. Therefore, even the dynamical refinement does not provide an unbiased structure model in this case, and, to avoid overinterpretation of the results, we refrain from a more detailed analysis of the interlayer structure.

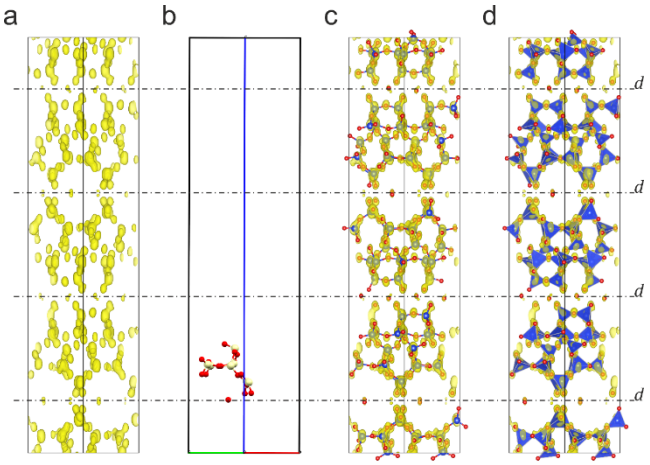

Figure 6.3. Result of ab initio structure solution plotted using VESTA and Mercury. Potential maps (ΔV) of NH_4-magadiite based on structure solution performed in SIR2014 in space group Fdd2. The results after the transformation to space group setting F2dd and calculation of Fobs which was performed in JANA2006 are shown. Transparent yellow potentials are plotted using 2σ(ΔV) threshold (σ is the standard deviation of map values). All unit cells are plotted with view along [110] and the d-glide plane in c-direction. Silicon atoms are shown in blue and oxygen in red. a Distribution of the scattering density map inside the unit cell. b Asymmetric unit of the crystal structure. c Overlay of scattering density with the crystal structure presented as ball-and-stick model. d Overlay of scattering density with the crystal structure presented as polyhedral model (polygon faces in blue).

Due to the broad reflection profiles in the PXRD pattern of NH_4-magadiite, a Rietveld refinement against this powder pattern would require careful modelling of the disorder. Such an extended disorder description would be quite challenging. It may be subject of a separate study, but it has not been performed so far. Nevertheless, a plot comparing the simulated PXRD derived from dynamical refinement with experimental PXRD (Supplementary Fig.6.8) shows a good semiquantitative match validating the structure model of NH_4-magadiite and, in particular, of its silicate layer. Because this layer is assumed to be common to NH_4-magadiite and Na-magadiite, solution of the structure of NH_4-magadiite opened a new route to the determination of the structure of Na-magadiite.

Model building and refinement of Na-magadiite

The initial structure model of Na-magadiite was constructed from the known structure of NH_4-magadiite. The structure of the silicate layer was copied and placed in the unit cell so that the interlayer gap increased to obtain the correct interlayer spacing of 15.5Å. Initial Rietveld refinement revealed immediately the positions of the sodium atoms in the interlayer. The positions of the water molecules coordinating the sodium atoms were not visible in the difference Fourier synthesis. However, their positions were derived from the analogy of the interlayer structure with that of Na-RUB-18, which possesses similar bands of interconnected $[Na(H_2O)_6]$ octahedra. Once placed, the positions of the water molecules

could be refined and remained stable. The structure, in particular the placement of the water molecules, was further validated also by DFT (Section *Structure of the interlayer region by DFT*). The Rietveld refinement converged to residual values R_{Bragg} = 0.029 and R_F = 0.022 (Supplementary Fig.6.9). The quality of the fit is satisfactory, although it was not possible to completely account for the anisotropic broadening of the reflections ($\chi 2$ = 5.8).

The Rietveld refinement was particularly valuable to reveal the arrangement of the atoms in the interlayer region. Bands of interconnected [$Na(H_2O)_6$] octahedra, similar to those of Na-RUB-18, run parallel to [110] (at z ≈ 0.125 and z ≈ 0.625) and parallel to [1-10] (at z ≈ 0.375 and z ≈ 0.875). The octahedra are markedly distorted with Na-O distances of 2.3 to 2.9 Å. The bands interact with the silicate layers through hydrogen bonds between terminal silanol/siloxy groups and the water molecules with O…O distances in the range 2.34 to 2.97 Å. Additional hydrogen bonds exist between apical water molecules (OW1 and OW2) and bridging oxygen atoms of the framework with O…O distances of 3.01 Å and larger (*vide infra* Fig.6.4).

Structure of the interlayer region by DFT

The simulation of Na-magadiite structure was performed using the model derived from the Rietveld refinement. Initially, hydrogen atoms were placed on the water molecules and on the layered silanol groups so that the charge balance in the structure is maintained. After that, all unit cell parameters and atomic positions were optimized in the structure expanded to *F*1, i.e. without imposing any symmetry other than translational. The results of the geometry optimization (Supplementary Table 6.4) show good agreement of cell parameters and volume with their respective crystallographic data, with relative errors of less than 0.5%.

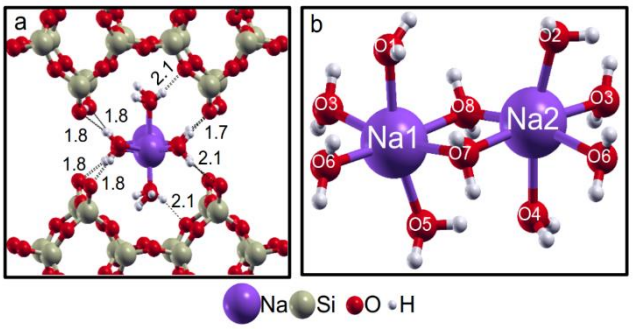

Figure 6.4. The PBE-GGA optimized structure model of Na-magadiite. (a) Overview of hydrogen bonds and (b) octahedral sodium coordination. The display radius of Na and O of frame b were fit to 1.15 and 1.25, respectively.

The octahedral coordination of each sodium atom with water molecules found by the Rietveld refinement was maintained (Fig. 4 and Supplementary Fig.6.10). The root-mean-square deviation (RMSD) between the experimental and optimized structure model in space group *F*1 was calculated (ignoring hydrogens) to be 0.141. The compared fractional coordinates are given in Supplementary Table 6.5 and an overlay of the structures is presented in Supplementary Fig. 11. A tolerance of 0.23 Å for the atomic positions of the DFT structure was needed to identify the space group *F*2*dd* with the FINDSYM[87].

In particular, the interactions between the silicate layers and the two independent $[Na(H_2O)_6]$ octahedra were analyzed in detail. The four water molecules of the equatorial plane form strong hydrogen bonds (H….O = 1.7 – 2.1 Å) with terminal silanol/siloxy groups of the layer (see Fig. 6.4a). The axial water molecules interact less strongly with atoms of the silicate layer having H….O- distances ≥ 2.1 Å. The octahedra themselves are somewhat compressed with short distances between sodium and axial water molecules and larger ones between sodium and equatorial water molecules. Moreover the octahedra are distorted to allow for additional hydrogen bonds between axial water molecules of neighboring octahedra (OW4….OW5 as shown in Fig. 6.4b).

The Rietveld refinement did not provide direct information about the positions of the hydrogen atoms, and the positions of the water oxygens were determined with a relatively large uncertainty. Therefore, a final structure model was obtained by Rietveld refinement that included water molecules restrained to positions derived from the DFT optimization (Supplementary Table 6.6).

Validation of the structure model by NMR

The NMR parameters of ^{23}Na, ^{29}Si and ^{1}H nuclei were calculated using the equations of δ_{iso} for each nucleus and compared with published experimental NMR spectra in Supplementary Figure 12. For both crystallographically independent environments Na1 and Na2 (Fig. 4b), the calculation of ^{23}Na parameters yielded constants of quadrupole C_q near 1.4 for Na1 and Na2. The asymmetry parameters η and δ_{iso} were different for the two Na ions: 0.68 and 0.29 respectively for Na1 and 0.93 (η) and 0.81 (δ_{iso}) for Na2 (Supplementary Table 7). As shown in Fig. 4b, both sodium atoms have similar environments consisting of octahedral coordination providing a very symmetrical sphere of shielding. This explains the proximity of values for chemical shifts and quadrupole constants for both cations. The convolution of both signals formed a ^{23}Na NMR spectrum in a good agreement with the experimental spectra[15,88] (Supplementary Fig 6.12 a).

In the case of the Si nuclei (Supplementary Fig. 6.12b), three distinguishable sets of Si-Q^4 and Si-Q^3 types were identified based on the agreement between experimental[15,88] and simulated NMR spectra. The calculated ^{1}H NMR spectrum (Supplementary Fig. 6.12c) contains two peaks. One corresponds to the hydrogen atoms of Si-OH groups (15 ppm) and the other to water molecules (3 ppm). These chemical shifts are close to the experimental values reported in the literature[89]. The differences in Na-OW(water) bond lengths (Supplementary Table 6.6) and water-layer hydrogen bonds (Fig. 6.4a) lead to an extended shielding region for hydrogen in the water molecules from -5 ppm to 10 ppm. The chemical shifts of the hydrogen atoms in the silanol groups are larger due to the formation of a SiO-H ····O-Si bond (Supplementary Fig. 6.12d), which is stronger than the hydrogen bonds formed by the water molecules (1.7 Å – 2.1 Å, Fig. 4a).

Discussion

The crystal structure of magadiite was studied with the help of a combination of 3D ED and PXRD experimental methods and DFT calculations. The key to the successful structural investigations was the synthesis of a dehydrated sodium free magadiite (NH_4-magadiite) which contains less water than the sodium form (Na-magadiite) but is still more ordered than a fully protonated magadiite (H-magadiite).

Na-magadiite

The samples obtained by the adapted synthesis under argon atmosphere and longer reaction time (a-NaM) are more ordered than those obtained under ambient atmosphere and shorter reaction time (c-NaM) as can be seen by sharper reflections in the corresponding PXRD (Fig.6.1). The absorption of CO_2 and formation of bicarbonate in itself are due to the alkalinity of the gel before pH decrease. Although longer times are required to observe turbidity by the naked eye, even a small decrease in pH lead to nucleation before pH lowering by addition of nitric acid. In this case (and different from the case when the acid is added) the nucleation is uncontrolled and increases as the pH drops. Beside the reaction control under argon atmosphere, it turned out that an increased reaction time of 72 h of the mixture under autogenous pressure was optimal to increase the crystallinity without obtaining cristobalite[90] or other side products[91].

At first glance, it seems contradictory that the structure could not be determined by 3D ED from the fairly ordered Na-magadiite. The answer to the apparent contradiction can be found in the ubiquitous presence of water molecules in the interlayer spaces of Na-

magadiite. The combination of vacuum in the TEM and the knock-on damage caused by the electrons to the interlayer makes the structure partly collapse even in cryogenic conditions and under mild illumination. This assumption is supported by the PXRD studies of magadiite in an evacuated chamber[24], where it could be observed that the basal spacing decreased to 13.50 Å and many reflections became broad and poorly resolved. The problem with the analysis of hydrated minerals by 3D ED is well known and has been documented for the layered minerals cyanotrichite[44] and lesukite[46]. A transition to an ordered dehydrated phase under vacuum was reported for kankite[45] and cowlesite[47].

NH_4-magadiite

The fully protonated magadiite (H-magadiite) was observed after treatment with HNO_3 (Fig. 6.1). The acid magadite is known for its low content of structural water and as such it would be a good candidate for structure analysis by 3D ED. Unfortunately, H-magadiite also consistently exhibits poor crystallinity and severe disorder, as documented by a broad basal reflection and low number of resolved peaks in almost every reported PXRD pattern[25,92]. A material mixing the characteristic low water contents of H-magadiite with better crystallinity was needed for successful structure solution. The newly developed procedure of ammonia assisted titration (Section *Synthesis of magadiite* – description in results) fulfills this requirement. It transformed the protonated form to ammonium-containing magadiite, which is much better ordered than H-magadiite (Fig. 6.1), but contains very little water, as documented by the DTA-TG measurements (Supplementary Figure 6.3).

The 3D ED data sets exhibited much less diffuse scattering than those of Na-magadiite (Fig.6.2), even though the accumulated dose per data set was comparable (approximately 19 $e^-/Å^2$). This dose applied on a crystal with dimensions of approx. 650 x 450 nm allowed the collection of sufficient diffraction signal to yield data up to a resolution of 0.9 $Å^{-1}$. Nevertheless, NH_4-magadiite exhibits intrinsic disorder. This is obvious from the larger FWHM of the reflections in the PXRD pattern, including the basal peak. A further indication of the disorder are the highly anisotropic displacement parameters (ADPs) resulting from the refinement of NH_4-magadiite against 3D ED data (Supplementary Table 6.2). The displacement parameters U33 of the silicon and oxygen atoms are, on average, about 10 times larger than the corresponding parameters U11 and U22. This indicates a variation in the basal spacing, which is most likely connected to an inhomogeneously distributed ammonium and possible residual water content. This disorder prevented both

the detailed structure analysis of NH_4-magadiite from 3D ED as well as a Rietveld-refinement from PXRD data, but the structure model was of sufficient quality to serve as a starting structure model for Na-magadiite.

Structure of Na-magadiite

Analogy with RUB-18

Even if RUB-18 has a significantly different layer thickness of about 7.3 Å, the interlayer space is very comparable to that of magadiite. The adjacent layers have a distance of approx. 4 Å (ignoring the Van der Waals radius of oxygen) to each other thus forming 8-ring channels very similar to those of Na-magadiite. This close structural relationship to RUB-18, in which bands of edge-sharing $[Na(H_2O)_6]$ octahedra are running along the 8-ring channels, helped to model the interlayer region of Na-magadiite accordingly (illustrated in Supplementary Fig.6.13).

The role of DFT

The strong overlap of Bragg reflections in the PXRD data and the additional reflection broadening caused by stacking disorder did not allow the location of hydrogen positions of the water molecules, and even the positions of the oxygen atoms of the water molecules was determined with large uncertainty. It was thus essential to validate and improve the model by DFT-based geometry optimization.

Hydrogen atoms were placed on the water molecules and on the hydroxyl groups of the layer to the positions that were suggested by the possible hydrogen-bond patterns in the interlayer. The structure was optimized by DFT-GGA calculations with a PBE functional. The structure was stable throughout the optimization, and the largest change could be observed in the tilting of the edge-sharing octahedra. The distortion of the NaO_6 octahedra, which was observed in the refined structure model, was confirmed by the DFT optimization. It is explained by the fact that the axial water molecule of one sodium octahedron forms a hydrogen bond to the axial water molecule of the neighboring sodium octahedron (see Fig.6.4b).

The geometrical interpretation of the interlayer structure was complemented by the DFT-based calculation of charge transfer between the water molecules and the silicate layer (Fig.6.5 a, b).

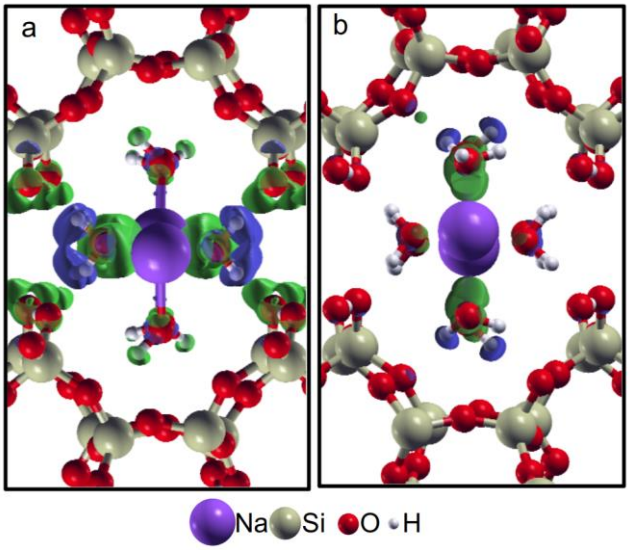

Figure 6.5. Charge density difference plot of Na-magadiite. The interactions are shown between layer and equatorial water H_2O_{eq} (a) and between layer and axial water H_2O_{ax} (b). The increase of charge density is green and the decrease is blue.

The charge transfer calculation shows that the hydrogen atoms of the equatorial water molecules interact strongly with oxygen atoms of the silanolate groups (documented by the strong charge transfer visible as large lobe sizes in Fig. 6.5a). In the case of axially coordinated water molecules (Fig. 6.5b), the charge transfer is much smaller, indicating much weaker hydrogen bonds between the hydrogens of the axial water molecules and the silicate layer than the hydrogen bonds involving equatorial water molecules. These findings together with the geometrical analysis indicate that the weak interaction of axial water molecules with the silicate layer is the main reason for the fast collapse of the periodic structure by physical processes which reduce its water content, like heating, vacuum or acid treatment.

Description of the silicate layer

The structure of the silicate layer is quite complex, as it contains 4-, 5-, 6-, 7-, and 8-rings of three- and four-interconnected [$SiO_{4/2}$] tetrahedra. Seven symmetrically independent Si atoms and 15 independent oxygen sites are present forming a dense layer of considerable thickness (11.5 Å). The symmetry can be described by the layer group *c*211. There is no two-fold axis perpendicular to the layer. Consequently, each layer is chiral, but the chirality of the stacked silicate layers in the average structure (*F*2*dd*) is alternated, due to the glide plane perpendicular to the stacking axis. In principle, it is possible to stack layers with identical handedness while preserving the channel-like voids in which bands of edge-sharing [$Na(H_2O)_6$] octahedra would find place. This entails a different stacking of the layers and could be one reason for the observed diffuse scattering. A comprehensive

discussion of the possible stacking faults is beyond the scope of this work and will be part of a second study on this topic. The chiral magadiite layer raises the question if the formation of zeolite-like frameworks would be in principal possible to form promising materials for catalysis[27] or even enantioselective separations[93,94].

The orientation of the silanol groups of adjacent layers, based on the average structure of Na-magadiite, would in principle allow a topotactic condensation to form a zeolite-like framework, whereas a hypothetical reaction to an interlayer expanded zeolite (IEZ) is not as straightforward. In order to realize the formation of an IEZ of magadiite, adjacent layers would have to be shifted and rotated by 90 degrees to one another.

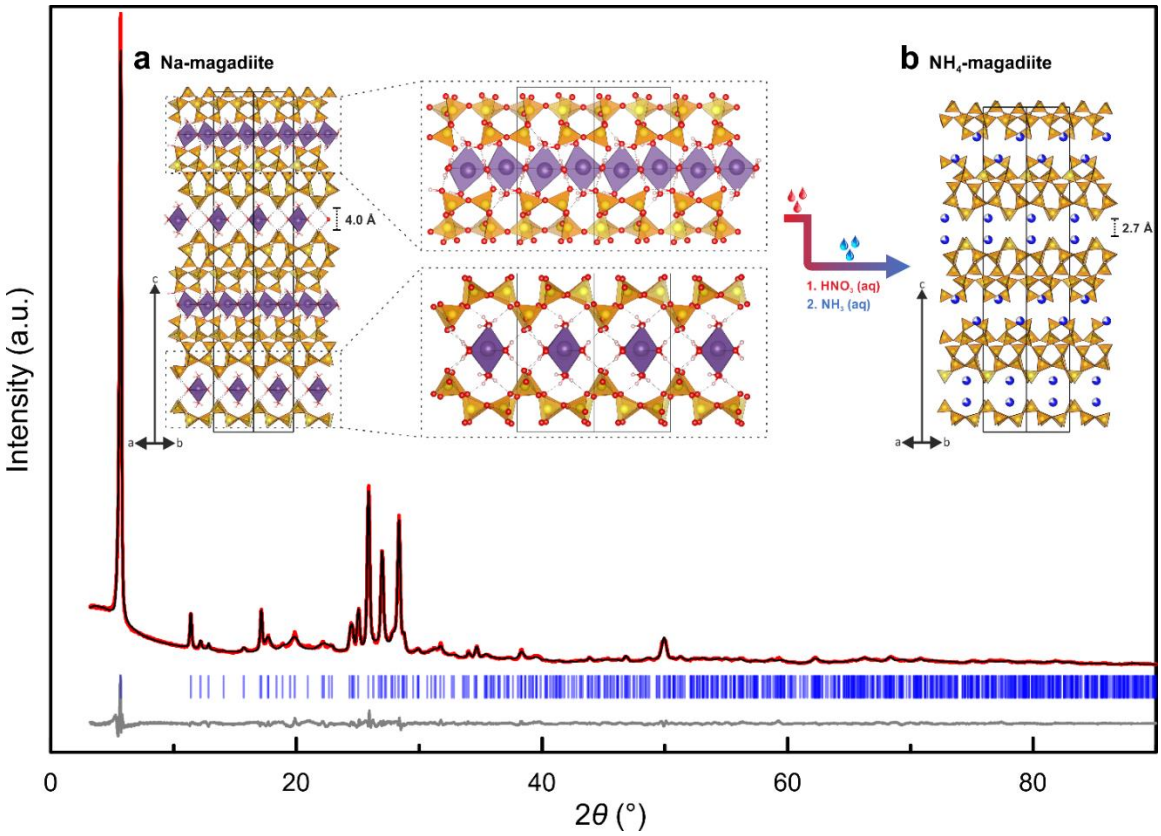

Figure 6.6. View of crystal structure of a Na-magadiite and b NH_4-magadiite along [110]. The interlayer region is magnified and shows in the upper part the edge-sharing octahedra of the interconnected band of $[Na(H_2O)_6]$. The lower magnified part illustrates the weak hydrogen bonds formed between the water molecules and silica layer. Surrounded by a plot of the final Rietveld refinement (λ = 1.54059 Å) of Na-magadiite. Red line for measured intensities (I_O), black line for fitted profile (I_C), and blue line for the difference (I_O-I_C).

Reactivity of the silicate layer by PDOS analysis

To analyze the expected behavior of the layer in chemical reactions, a PDOS analysis was performed. The density of states was calculated (Supplementary Fig.6.14) that included the contribution of silicon atoms of siloxanes and silanol groups (Si1 and Si2, respectively), oxygen atoms of water (equatorial = O1 and axial = O2) and silicate layer (Si-O-Si = O3

and Si-OH/Si-O^- = O4), and sodium cations. The closer the valence states are to the Fermi level, the stronger the basicity of the associated atoms. As expected, the density of states close to Fermi energy was found in all oxygen types, but the highest intensity occurred at O4. This indicates that the silanol groups constitute the most reactive sites in the structure for electrophilic attack in chemical reactions. This behavior has been extensively observed in functionalization reactions by alkoxysilanes[12,13]. This result explains the observations and at the same time further validates the structure model and demonstrates its predictive power for the explanation of the properties on magadiite.

Wrong structure

Recently, a structure of magadiite was proposed by Y. Ide et al.[23] who tried to confirm a predetermined structure model by a curve fitting of PDF data (PDF = pair distribution function) and the examination of additional data from a general characterization (chem. compositions, NMR spectra and infrared spectra). The structure model suggested by Ide et al. consists of two condensed octosilicate layers forming an unusual silicate layer with microchannels and a $Q^4 : Q^3$ ratio of silicon atoms amounting to 6 : 4, which does not agree with the generally accepted ratio for magadiite of 2 to 3[26]. Moreover, the model contains $[SiO_{4/2}]$ tetrahedra in an extremely distorted geometry. As shown in the present study, the structure of magadiite is in fact very different and consists of dense silicate layers without any microchannels and having a $Q^4 : Q^3$ ratio of 10 : 4. The inter-layer region of the structure of magadiite resembles channel-like voids occupied by bands of interconnected $[Na(H_2O)_6]$ octahedra and is nearly identical to the inter-layer region of octosilicate (RUB-18, ilerite). This also is at variance with the model of Ide et al. which shows a nearly random arrangement of sodium ions between layers. It can be concluded that in this case of a rather complex structure it was not possible to arrive to the correct structure model by the PDF analysis, and a fundamentally wrong model was capable of yielding good agreement with the experimental PDF profile.

6.5 Conclusions

Knowledge of the crystal structure is important to gain fundamental understanding of the synthesis mechanism and prospects to modifying the as-made material. The results of the structure analysis provided a detailed description of the silicate layers and of the chemically active interlayer nanospace. The layer contains small rings and highly twisted 7- and 8-rings forming a dense, pyknosil-like unit which precludes diffusion of molecules along the stacking direction of layers. The inner surfaces are only accessible through the narrow inter-layer region. The structural characterization of magadiite is necessary to identify the full potential of this material to act as a precursor for the transformation into commercially useful materials - e.g., efficient microporous catalysts or adsorbents. In particular, the location of the silanol/siloxy groups within the structure is important since these groups are the reactive centers used for modifying the layered precursor by condensation, pillaring, grafting and other techniques.

Moreover, the sites occupied by Al in the [Al]-magadiite catalyst and the lack of low-aluminum analogues can now be explained by the structural characteristics of lamella, while, allows the study of synthetic strategies to use specific sites within the framework. The structure determination of magadiite may prompt simulation and machine learning studies aiming at the optimization of synthesis conditions. Metastable phases like magadiite form via kinetically controlled pathways. A definite correlation of synthesis parameters like chemical composition of the reaction mixture, heating time, heating temperature or added templates and the products being formed is often impossible. Therefore, the evaluation of the energy landscape is helpful to identify attainable crystalline layered silicates for a given set of synthesis conditions.

The mystery of the structure of magadiite has finally been solved. The structure reported here, the adapted synthesis and the ammonia-based titration will have a huge impact on the research of hybrid organic−inorganic nanocomposites based on magadiite, related layered silicates and zeolite-like materials.

6.6 References

[1] Eugster, H. P. Hydrous Sodium Silicates from Lake Magadi, Kenya: Precursors of Bedded Chert. *Science* **1967**, *157* [3793], 1177–1180.

[2] McCulloch, L. A New Highly Silicious Soda—Silica Compound. *Journal of the American Chemical Society* **1952**, *74* [10], 2453–2456.

[3] Beneke, K.; Lagaly, G. Kanemite; Innercrystalline Reactivity and Relations to Other Sodium Silicates. *American Mineralogist* **1977**, *62* [7–8], 763–771.

[4] Sheppard, R. A.; Gude, A. J.; Hay, R. L. Makatite, A New Hydrous Sodium Silicate Mineral from Lake Magadi, Kenya. *American Mineralogist* **1970**, *55* [3-4_Part_1], 358–366.

[5] Beneke, K.; Lagaly, G. Kenyaite; Synthesis and Properties. *American Mineralogist* **1983**, *68* [7–8], 818–826.

[6] Marler, B.; Gies, H. Hydrous Layer Silicates as Precursors for Zeolites Obtained through Topotactic Condensation: A Review. *European Journal of Mineralogy* **2012**, *24* [3], 405–428..

[7] Sirinakorn, T.; Imwiset, K.; Bureekaew, S.; Ogawa, M. Inorganic Modification of Layered Silicates toward Functional Inorganic-Inorganic Hybrids. *Applied Clay Science* **2018**, *153*, 187–197.

[8] Lagaly, G.; Beneke, K. Magadiite and H-Magadiite: I. Sodium Magadiite and Some of Its Derivatives. *American Mineralogist* **1975**, *60*, 642–649.

[9] Lagaly, G.; Beneke, K.; Weiss, A. Magadiite and H-Magadiite. 2. H-Magadiite and Its Intercalation Compounds Compounds. *American Mineralogist* **1975**, *60* [7–8], 650–658.

[10] Pastore, H. O.; Munsignatti, M.; Mascarenhas, A. J. S. One-Step Synthesis of Alkyltrimethylammonium-Intercalated Magadiite. *Clays and Clay Minerals* **2000**, *48* [2], 224–229.

[11] Wang, S.-F.; Lin, M.-L.; Shieh, Y.-N.; Wang, Y.-R.; Wang, S.-J. Organic Modification of Synthesized Clay-Magadiite. *Ceramics International* **2007**, *33* [4], 681–685.

[12] Vieira, R. B.; Pastore, H. O. Polyethylenimine-Magadiite Layered Silicate Sorbent for CO2 Capture. *Environ. Sci. Technol.* **2014**, *48* [4], 2472–2480.

[13] Vieira, R. B.; Pastore, H. O. Soft-Pillared@Magadiite: Influence of the Interlayer Space and Amine Type on CO2 Adsorption. *Dalton Trans.* **2018**, *47* [9], 3102–3111.

[14] Mingliang, G.; Luoxiang, C.; Mingyi, D.; Guoqing, H.; Jahangir Alam, S. M. Competitive Adsorption Analyses of a Pure Magadiite and a New Silylated Magadiite on Methylene Blue and Phenol from Related Aqueous Solution. *Materials Chemistry and Physics* **2018**. https://doi.org/10.1016/j.matchemphys.2018.02.052.

[15] Paz, G. L.; Munsignatti, E. C. O.; Pastore, H. O. Novel Catalyst with Layered Structure: Metal Substituted Magadiite. *Journal of Molecular Catalysis A: Chemical* **2016**, *422*, 43–50. https://doi.org/10.1016/j.molcata.2016.02.014.

[16] Wang, Q.; Zhang, Y.; Zheng, J.; Wang, Y.; Hu, T.; Meng, C. Metal Oxide Decorated Layered Silicate Magadiite for Enhanced Properties: Insight from ZnO and CuO Decoration. *Dalton Trans.* **2017**, *46* [13], 4303–4316.

[17] Ge, M.; Tang, W.; Du, M.; Liang, G.; Hu, G.; Jahangir Alam, S. M. Research on 5-Fluorouracil as a Drug Carrier Materials with Its in Vitro Release Properties on Organic Modified Magadiite. *European Journal of Pharmaceutical Sciences* **2019**, *130*, 44–53.

[18] Mokhtar, A.; Bennabi, F.; Abdelkrim, S.; Sardi, A.; Boukoussa, B.; Souna, A.; Bengueddach, A.; Sassi, M. Evaluation of Intercalated Layered Materials as an Antimicrobial and Drug Delivery System: A Comparative Study. *J Incl Phenom Macrocycl Chem* **2020**.

[19] Zhang, S.; Lv, T.; Feng, Z.; Liu, X.; Li, X.; Wang, Y.; Meng, C. Seed-Assisted Synthesis of Zeolite Beta from Solid-State Conversion of Magadiite and an Investigation on the Crystallization Mechanism. *Ind. Eng. Chem. Res.* **2020**.

[20] Schwieger, W.; Heidemann, D.; Bergk, K.-H. High-Resolution Solid-State Silicon-29 Nuclear Magnetic Resonance Spectroscopic Studies of Synthetic Sodium Silicate Hydrates. *Rev. chim. minér* **1985**, *22* [5], 639–650.

[21] Garces, J. M.; Rocke, S. C.; Crowder, C. E.; Hasha, D. L. Hypothetical Structures of Magadiite and Sodium Octosilicate and Structural Relationships between the Layered Alkali Metal Silicates and the Mordenite- and Pentasil-Group Zeolites. *Clays and Clay Minerals* **1988**, *36* [5], 409–418.

[22] Brandt, A.; Schwieger, W.; Bergk, K.-H.; Grabner, P.; Porsch, M. Structure and Properties of Na-Magadiite Dependent on Temperature. *Crystal Research and Technology* **1989**, *24* [1], 47–54.

[23] Ide, Y.; Tominaka, S.; Kono, H.; Ram, R.; Machida, A.; Tsunoji, N. Zeolitic Intralayer Microchannels of Magadiite, a Natural Layered Silicate, to Boost Green Organic Synthesis. *Chemical Science* **2018**, *9* [46], 8637–8643. https://doi.org/10.1039/C8SC03712D.

[24] Brindley, G. W. Unit Cell of Magadiite in Air, in Vacuo, and under Other Conditions. *American Mineralogist* **1969**, *54* [11–12], 1583–1591.

[25] Eypert-Blaison, C.; Michot, L. J.; Humbert, B.; Pelletier, M.; Villiéras, F. Hydration Water and Swelling Behavior of Magadiite. The H+, Na+, K+, Mg2+, and Ca2+ Exchanged Forms. *The Journal of Physical Chemistry B* **2002**, *106* [3], 730–742. https://doi.org/10.1021/jp012981n.

[26] G. Almond, G.; K. Harris, R.; R. Franklin, K. A Structural Consideration of Kanemite, Octosilicate, Magadiite and Kenyaite. *Journal of Materials Chemistry* **1997**, *7* [4], 681–687.

[27] Li, Y.; Yu, J. New Stories of Zeolite Structures: Their Descriptions, Determinations, Predictions, and Evaluations. *Chem. Rev.* **2014**, *114* [14], 7268–7316.

[28] Huang, Y.; Jiang, Z.; Schwieger, W. Vibrational Spectroscopic Studies of Layered Silicates. *Chem. Mater.* **1999**, *11* [5], 1210–1217. https://doi.org/10.1021/cm980403m.

[29] Gemmi, M.; Mugnaioli, E.; Gorelik, T. E.; Kolb, U.; Palatinus, L.; Boullay, P.; Hovmöller, S.; Abrahams, J. P. 3D Electron Diffraction: The Nanocrystallography Revolution. *ACS Cent. Sci.* **2019**, *5* [8], 1315–1329.

[30] Kolb, U.; Krysiak, Y.; Plana-Ruiz, S. Automated Electron Diffraction Tomography – Development and Applications. *Acta Cryst B* **2019**, *75* [4], 463–474..

[31] Zou, Z.; Bertinetti, L.; Hood, M. A.; Sun, C.; Polishchuk, I.; Pokroy, B.; Mahamid, J.; Politi, Y.; Weiner, S.; Werner, P.; Bette, S.; Dinnebier, R.; Kolb, U.; Zolotoyabko, E.; Fratzl, P. A Hydrated Crystalline Calcium Carbonate Phase: Calcium Carbonate Hemihydrate. **2019**, 6.

[32] Clabbers, M. T. B.; Gruene, T.; Parkhurst, J. M.; Abrahams, J. P.; Waterman, D. G. Electron Diffraction Data Processing with DIALS. *Acta Cryst D, Acta Cryst Sect D, Acta Crystallogr D, Acta Crystallogr Sect D, Acta Crystallogr D Struct Biol, Acta Crystallogr Sect D Struct Biol* **2018**, *74* [6], 506–518.

[33] Zhou, H.; Luo, F.; Luo, Z.; Li, D.; Liu, C.; Li, X. Programming Conventional Electron Microscopes for Solving Ultrahigh-Resolution Structures of Small and Macro-Molecules. *Anal. Chem.* **2019**, *91* [17], 10996–11003.

[34] Wang, B.; Zou, X.; Smeets, S. Automated Serial Rotation Electron Diffraction Combined with Cluster Analysis: An Efficient Multi-Crystal Workflow for Structure Determination. *IUCrJ* **2019**, *6* [5], 854–867.

[35] Plana-Ruiz, S.; Krysiak, Y.; Portillo, J.; Alig, E.; Estradé, S.; Peiró, F.; Kolb, U. Fast-ADT: A Fast and Automated Electron Diffraction Tomography Setup for Structure Determination and Refinement. *Ultramicroscopy* **2020**, 112951.
[36] Palatinus, L.; Jacob, D.; Cuvillier, P.; Klementová, M.; Sinkler, W.; Marks, L. D. Structure Refinement from Precession Electron Diffraction Data. *Acta Cryst A, Acta Cryst Sect A, Acta Crystallogr A, Acta Crystallogr Sect A, Acta Crystallogr A Found Crystallogr, Acta Crystallogr Sect A Found Crystallogr* **2013**, *69* [2], 171–188.
[37] Palatinus, L.; Brázda, P.; Boullay, P.; Perez, O.; Klementová, M.; Petit, S.; Eigner, V.; Zaarour, M.; Mintova, S. Hydrogen Positions in Single Nanocrystals Revealed by Electron Diffraction. *Science* **2017**, *355* [6321], 166–169..
[38] Brázda, P.; Palatinus, L.; Babor, M. Electron Diffraction Determines Molecular Absolute Configuration in a Pharmaceutical Nanocrystal. *Science* **2019**, *364* [6441], 667–669.
[39] Welberry, T. R.; Weber, T. One Hundred Years of Diffuse Scattering. *Crystallography Reviews* **2016**, *22* [1], 2–78.
[40] Willhammar, T.; Sun, J.; Wan, W.; Oleynikov, P.; Zhang, D.; Zou, X.; Moliner, M.; Gonzalez, J.; Martínez, C.; Rey, F.; Corma, A. Structure and Catalytic Properties of the Most Complex Intergrown Zeolite ITQ-39 Determined by Electron Crystallography. *Nat Chem* **2012**, *4* [3], 188–194.
[41] Brázda, P.; Palatinus, L.; Drahokoupil, J.; Knížek, K.; Buršík, J. Calcium-Induced Cation Ordering and Large Resistivity Decrease in Pr0.3CoO2. *Journal of Physics and Chemistry of Solids* **2016**, *96*, 10–16.
[42] Krysiak, Y.; Barton, B.; Marler, B.; Neder, R. B.; Kolb, U. Ab Initio Structure Determination and Quantitative Disorder Analysis on Nanoparticles by Electron Diffraction Tomography. *Acta Crystallographica Section A Foundations and Advances* **2018**, *74* [2], 93–101.
[43] Krysiak, Y.; Marler, B.; Barton, B.; Plana-Ruiz, S.; Gies, H.; Neder, R. B.; Kolb, U. New Zeolite-like RUB-5 and Its Related Hydrous Layer Silicate RUB-6 Structurally Characterized by Electron Microscopy. *IUCrJ* **2020**, *7* [3], 522–534.
[44] Ventruti, G.; Mugnaioli, E.; Capitani, G.; Scordari, F.; Pinto, D.; Lausi, A. A Structural Study of Cyanotrichite from Dachang by Conventional and Automated Electron Diffraction. *Phys Chem Minerals* **2015**, *42* [8], 651–661.
[45] Majzlan, J.; Palatinus, L.; Plášil, J. Crystal Structure of Fe2[AsO4][HAsO4][OH][H2O]3, a Dehydration Product of Kaňkite. *European Journal of Mineralogy* **2016**, *28* [1], 63–70. https://doi.org/10.1127/ejm/2015/0027-2495.
[46] Mugnaioli, E.; Gorelik, T. E. Structure Analysis of Materials at the Order–Disorder Borderline Using Three-Dimensional Electron Diffraction. *Acta Cryst B* **2019**, *75* [4], 550–563.
[47] Mugnaioli, E.; Lanza, A. E.; Bortolozzi, G.; Righi, L.; Merlini, M.; Cappello, V.; Marini, L.; Athanassiou, A.; Gemmi, M. Electron Diffraction on Flash-Frozen Cowlesite Reveals the Structure of the First Two-Dimensional Natural Zeolite. *ACS Cent. Sci.* **2020**, *6* [9], 1578–1586.
[48] Costa, D. G.; Rocha, A. B.; Diniz, R.; Souza, W. F.; Chiaro, S. S. X.; Leitão, A. A. Structural Model Proposition and Thermodynamic and Vibrational Analysis of Hydrotalcite-Like Compounds by DFT Calculations. *J. Phys. Chem. C* **2010**, *114* [33], 14133–14140.
[49] A. Barbosa, A. C. de; G. Fonseca, C.; Wypych, F.; A. Leitão, A. Structural Analysis of Dehydrated Gibbsite-Based Layered Double Hydroxides Li–Al–X [X = F − , Cl − , Br − , I − , OH − , NO 3 − , CO 3 2− , and SO 4 2−] by DFT Calculations. *New Journal of Chemistry* **2020**.

[50] Tavares, S. R.; Vaiss, V. S.; Wypych, F.; Leitão, A. A. Theoretical Study of the Anion Exchange Properties and the Thermal Decomposition of Zn5[OH]8[NO3]22H2O and Zn5[OH]8[NO3]22NH3. *Applied Clay Science* **2015**, *114*, 103–111.
[51] Fonseca, C. G.; Vaiss, V. S.; Wypych, F.; Diniz, R.; Leitão, A. A. Structural and Thermodynamic Investigation of the Hydration-Dehydration Process of Na+-Montmorillonite Using DFT Calculations. *Applied Clay Science* **2017**, *143*, 212–219.
[52] Moraes, P. I. R.; Tavares, S. R.; Vaiss, V. S.; Leitão, A. A. Investigation on Sustainable Phosphate Release in Agriculture: Structural and Thermodynamic Study of Stability, Dehydration and Anionic Exchange of Mg-Al-HPO4 Layered Double Hydroxide by DFT Calculations. *Applied Clay Science* **2018**, *162*, 428–434.
[53] Moraes, P. I. R.; Wypych, F.; Leitão, A. A. DFT Study of Layered Double Hydroxides with Cation Exchange Capacity: [A+[H2O]6][M62+Al3[OH]18[SO4]2]·6H2O [M2+ = Mg, Zn and A+ = Na, K]. *J. Phys. Chem. C* **2019**, *123* [15], 9838–9845.
[54] Tavares, S. R.; Moraes, P. I. R.; Capaz, R. B.; Leitão, A. A. Novel 2D Materials from Exfoliation of Layered Hydroxide Salts: A Theoretical Study. *Applied Surface Science* **2019**, *483*, 762–771.
[55] N. Silva, B. N.; R. Tavares, S.; A. Leitão, A. Exfoliation of Zirconium Aminophosphonates: Investigation into Their Electronic Structures by Ab Initio Calculations. *New Journal of Chemistry* **2020**.
[56] Tavares, S. R.; Nakagaki, S.; Wypych, F.; Leitão, A. A. Ab Initio Simulations of the Intercalation of Iron[III] Porphyrinates in Zn2Al-LDH: Structural Analysis and Evaluation of Their Basic and Acid Sites. *Applied Clay Science* **2017**, *143*, 220–226.
[57] Nangoi, I. M.; Faro, A. C.; Souza, W. F.; Chiaro, S. S. X.; Leitão, A. A. Direct Comparison among the Formation of Terephthalate- and Carbonate-Intercalated Mg-Al-LDH: The Influence of the High Aluminum Content. *Applied Clay Science* **2018**, *151*, 194–200.
[58] Mugnaioli, E.; Gorelik, T.; Kolb, U. Ab-Initio Structure Solution from Electron Diffraction Data Obtained by a Combination of Automated Diffraction Tomography and Precession Technique. *Ultramicroscopy* **2009**, *109* [6], 758–765.
[59] Kolb, U.; Gorelik, T.; Kübel, C.; Otten, M. T.; Hubert, D. Towards Automated Diffraction Tomography: Part I - Data Acquisition. *Ultramicroscopy* **2007**, *107* [6–7], 507–513.
[60] Vincent, R.; Midgley, P. A. Double Conical Beam-Rocking System for Measurement of Integrated Electron Diffraction Intensities. *Ultramicroscopy* **1994**, *53* [3], 271–282.
[61] Kolb, U.; Mugnaioli, E.; Gorelik, T. E. Automated Electron Diffraction Tomography - a New Tool for Nano Crystal Structure Analysis. *Cryst Res Technol* **2011**, *46* [6], 542–554.
[62] Palatinus, L.; Brázda, P.; Jelínek, M.; Hrdá, J.; Steciuk, G.; Klementová, M. Specifics of the Data Processing of Precession Electron Diffraction Tomography Data and Their Implementation in the Program PETS2.0. *Acta Cryst B* **2019**, *75* [4], 512–522.
[63] Burla, M. C.; Caliandro, R.; Carrozzini, B.; Cascarano, G. L.; Cuocci, C.; Giacovazzo, C.; Mallamo, M.; Mazzone, A.; Polidori, G. Crystal Structure Determination and Refinement via SIR2014. *Journal of Applied Crystallography* **2015**, *48* [1], 306–309.
[64] Doyle, P. A.; Turner, P. S. Relativistic Hartree–Fock X-Ray and Electron Scattering Factors. *Acta Crystallographica Section A* **1968**, *24* [3], 390–397.
[65] Petříček, V.; Dušek, M.; Palatinus, L. Crystallographic Computing System JANA2006: General Features. *Zeitschrift für Kristallographie - Crystalline Materials* **2014**, *229* [5], 345–352.
[66] Palatinus, L.; Petříček, V.; Corrêa, C. A. Structure Refinement Using Precession Electron Diffraction Tomography and Dynamical Diffraction: Theory and Implementation. *Acta Cryst A, Acta Cryst Sect A, Acta Crystallogr A, Acta Crystallogr Sect A, Acta Crystallogr*

A Cryst Phys Diffr Theor Gen Crystallogr, Acta Crystallogr Sect A Cryst Phys Diffr Theor Gen Crystallogr **2015**, *71* [2], 235–244.
[67] Palatinus, L.; Corrêa, C. A.; Steciuk, G.; Jacob, D.; Roussel, P.; Boullay, P.; Klementová, M.; Gemmi, M.; Kopeček, J.; Domeneghetti, M. C.; Cámara, F.; Petříček, V. Structure Refinement Using Precession Electron Diffraction Tomography and Dynamical Diffraction: Tests on Experimental Data. *Acta Cryst B* **2015**, *71* [6], 740–751.
[68] Rodriguez-Carvajal, J. FULLPROF: A Program for Rietveld Refinement and Pattern Matching Analysis. In *satellite meeting on powder diffraction of the XV congress of the IUCr*; Toulouse, France, 1990; Vol. 127.
[69] Giannozzi, P.; Baroni, S.; Bonini, N.; Calandra, M.; Car, R.; Cavazzoni, C.; Ceresoli, D.; Chiarotti, G. L.; Cococcioni, M.; Dabo, I.; Corso, A. D.; Gironcoli, S. de; Fabris, S.; Fratesi, G.; Gebauer, R.; Gerstmann, U.; Gougoussis, C.; Kokalj, A.; Lazzeri, M.; Martin-Samos, L.; Marzari, N.; Mauri, F.; Mazzarello, R.; Paolini, S.; Pasquarello, A.; Paulatto, L.; Sbraccia, C.; Scandolo, S.; Sclauzero, G.; Seitsonen, A. P.; Smogunov, A.; Umari, P.; Wentzcovitch, R. M. QUANTUM ESPRESSO: A Modular and Open-Source Software Project for Quantum Simulations of Materials. *J. Phys.: Condens. Matter* **2009**, *21* [39], 395502.
[70] Hohenberg, P.; Kohn, W. Inhomogeneous Electron Gas. *Phys. Rev.* **1964**, *136* [3B], B864–B871.
[71] Kohn, W.; Sham, L. J. Self-Consistent Equations Including Exchange and Correlation Effects. *Phys. Rev.* **1965**, *140* [4A], A1133–A1138.
[72] Perdew, J. P.; Burke, K.; Ernzerhof, M. Generalized Gradient Approximation Made Simple. *Phys. Rev. Lett.* **1996**, *77* [18], 3865–3868..
[73] Vanderbilt, D. Soft Self-Consistent Pseudopotentials in a Generalized Eigenvalue Formalism. *Phys. Rev. B* **1990**, *41* [11], 7892–7895.
[74] Monkhorst, H. J.; Pack, J. D. Special Points for Brillouin-Zone Integrations. *Phys. Rev. B* **1976**, *13* [12], 5188–5192.
[75] Pickard, C. J.; Mauri, F. All-Electron Magnetic Response with Pseudopotentials: NMR Chemical Shifts. *Phys. Rev. B* **2001**, *63* [24], 245101.
[76] Yates, J. R.; Pickard, C. J.; Mauri, F. Calculation of NMR Chemical Shifts for Extended Systems Using Ultrasoft Pseudopotentials. *Phys. Rev. B* **2007**, *76* [2], 024401.
[77] Charpentier, T.; Ispas, S.; Profeta, M.; Mauri, F.; Pickard, C. J. First-Principles Calculation of 17O, 29Si, and 23Na NMR Spectra of Sodium Silicate Crystals and Glasses. *J. Phys. Chem. B* **2004**, *108* [13], 4147–4161.
[78] Koller, H.; Engelhardt, G.; Kentgens, A. P. M.; Sauer, J. 23Na NMR Spectroscopy of Solids: Interpretation of Quadrupole Interaction Parameters and Chemical Shifts. *J. Phys. Chem.* **1994**, *98* [6], 1544–1551.
[79] Hayashi, S.; Ueda, T.; Hayamizu, K.; Akiba, E. NMR Study of Kaolinite. 1. 29 Si, 27 Al, and 1 H Spectra. *J Phys Chem* **1992**, *96* [26], 10922–10928.
[80] Cadars, S.; Guégan, R.; Garaga, M. N.; Bourrat, X.; Le Forestier, L.; Fayon, F.; Huynh, T. V.; Allier, T.; Nour, Z.; Massiot, D. New Insights into the Molecular Structures, Compositions, and Cation Distributions in Synthetic and Natural Montmorillonite Clays. *Chem. Mater.* **2012**, *24* [22], 4376–4389.
[81] Marchetti, A.; Jehle, S.; Felletti, M.; Knight, M. J.; Wang, Y.; Xu, Z.-Q.; Park, A. Y.; Otting, G.; Lesage, A.; Emsley, L.; Dixon, N. E.; Pintacuda, G. Backbone Assignment of Fully Protonated Solid Proteins by 1H Detection and Ultrafast Magic-Angle-Spinning NMR Spectroscopy. *Angewandte Chemie International Edition* **2012**, *51* [43], 10756–10759.
[82] Blumberg, J. G.; Schleyer, W. L. *Soluble Silicates*; ACS Symposium Series; American Chemical Society, 1982; Vol. 194.

[83] Superti, G. B.; Oliveira, E. C.; Pastore, H. O.; Bordo, A.; Bisio, C.; Marchese, L. Aluminum Magadiite: An Acid Solid Layered Material. *Chem. Mater.* **2007**, *19* [17], 4300–4315.
[84] David, W. I. F.; Shankland, K.; van de Streek, J.; Pidcock, E.; Motherwell, W. D. S.; Cole, J. C. DASH: A Program for Crystal Structure Determination from Powder Diffraction Data. *J Appl Cryst, J Appl Crystallogr* **2006**, *39* [6], 910–915.
[85] Markvardsen, A. J.; Shankland, K.; David, W. I. F.; Johnston, J. C.; Ibberson, R. M.; Tucker, M.; Nowell, H.; Griffin, T. ExtSym: A Program to Aid Space-Group Determination from Powder Diffraction Data. *J Appl Cryst* **2008**, *41* [6], 1177–1181..
[86] Palatinus, L.; Chapuis, G. SUPERFLIP – a Computer Program for the Solution of Crystal Structures by Charge Flipping in Arbitrary Dimensions. *J Appl Cryst* **2007**, *40* [4], 786–790.
[87] Stokes, H. T.; Hatch, D. M. FINDSYM: Program for Identifying the Space-Group Symmetry of a Crystal. *J Appl Cryst* **2005**, *38* [1], 237–238..
[88] Almeida, R. K. S.; Paz, G. L.; Báfero, G. B.; Pastore, H. O. Properties of Layered [Al]- and [V,Al]-Magadiite Catalysts as Revealed by Ethanol Dehydration. *Microporous and Mesoporous Materials* **2019**, *284*, 1–9.
[89] Almond, G. G. A Nuclear Magnetic Resonance Study of Hydrous Layer Silicates. Doctoral, Durham University, 1995.
[90] Muraishi, H. Crystallization of Silica Gel in Alkaline Solutions at 100 to 180 °C; Characterization of SiO 2 -Y by Comparison with Magadiite. *American Mineralogist* **1989**, *74* [9–10], 1147–1151.
[91] Sassi, M.; Miehé-Brendlé, J.; Patarin, J.; Bengueddach, A. Na-Magadiite Prepared in a Water/Alcohol Medium: Synthesis, Characterization and Use as a Host Material to Prepare Alkyltrimethylammonium- and Si-Pillared Derivates. *Clay Minerals* **2005**, *40* [3], 369–378.
[92] Kosuge, K.; Tsunashima, A. Dispersion of H−Magadiite and H−Kenyaite Particles by Ion Exchange of H+ with Alkali Ions. *Langmuir* **1996**, *12* [5], 1124–1126..
[93] Castillo, J. M.; Vlugt, T. J. H.; Dubbeldam, D.; Hamad, S.; Calero, S. Performance of Chiral Zeolites for Enantiomeric Separation Revealed by Molecular Simulation. *J. Phys. Chem. C* **2010**, *114* [50], 22207–22213.
[94] Xu, Z.-X.; Liu, L.; Zhang, J. Synthesis of Metal–Organic Zeolites with Homochirality and High Porosity for Enantioselective Separation. *Inorg. Chem.* **2016**, *55* [13], 6355–6357.

6.7 Supplementary information

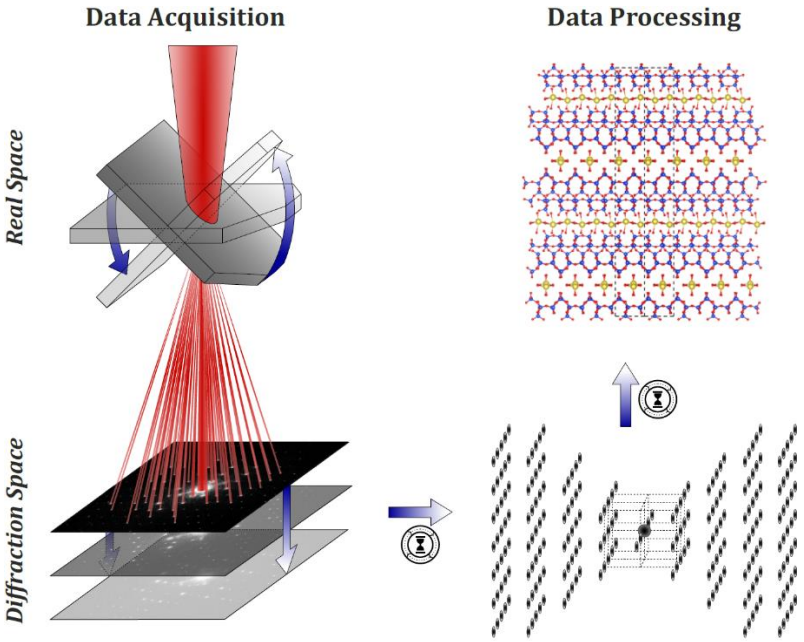

FigureS6.1 Three-dimensional electron diffraction as a tool to determine the average structure of disordered and beam sensitive polycrystalline layered silicates and their related zeolites. 1st process: The reconstruction of 2D to 3D electron diffraction data enables the determination of the unit-cell, space group. 2nd process: Specialized reflection integration and data analysis to enable structure solution and structure refinement.

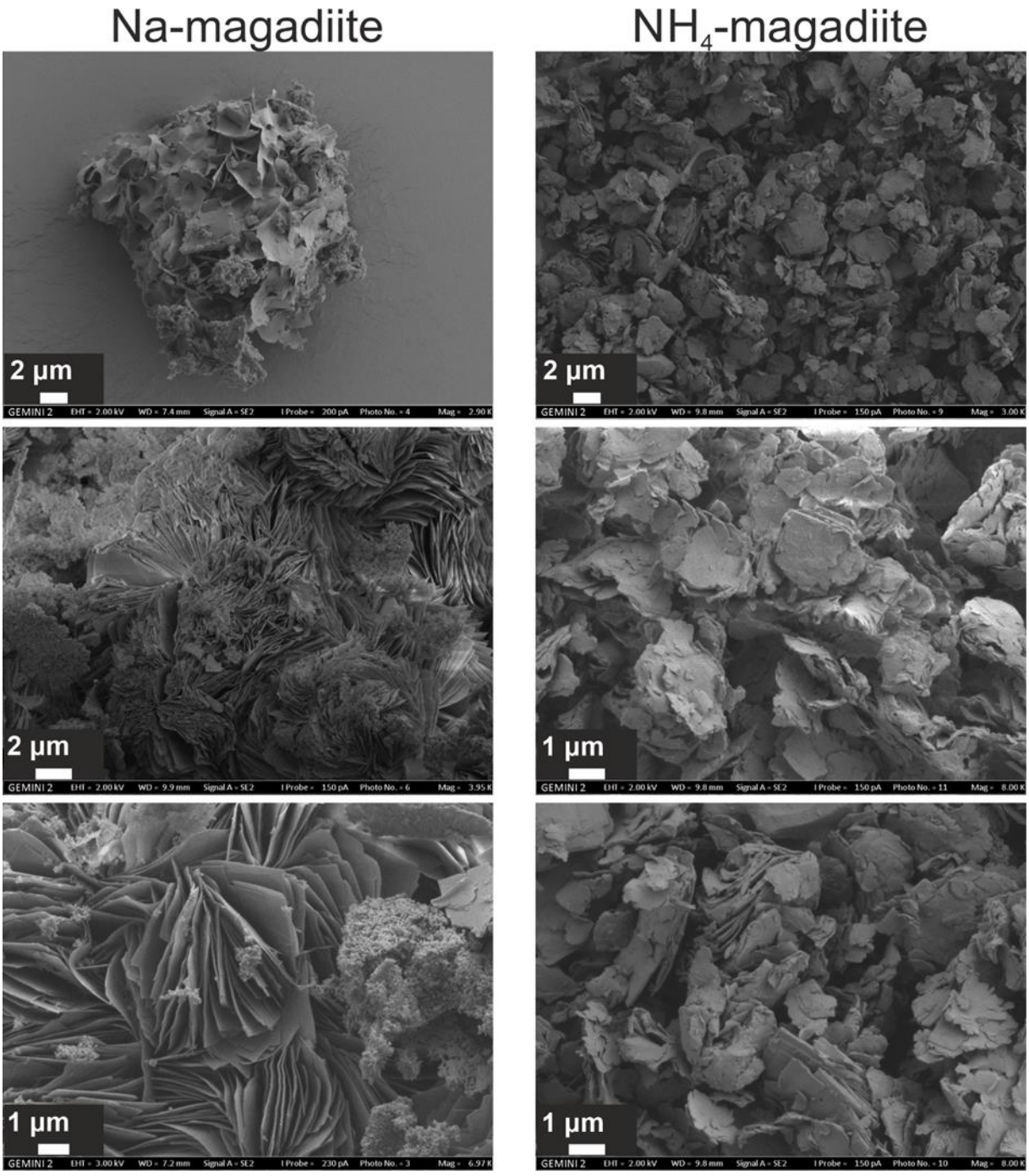

Figure S6.2 SEM micrographs of Na-magadiite (left column) and NH_4-magadiite (right column).

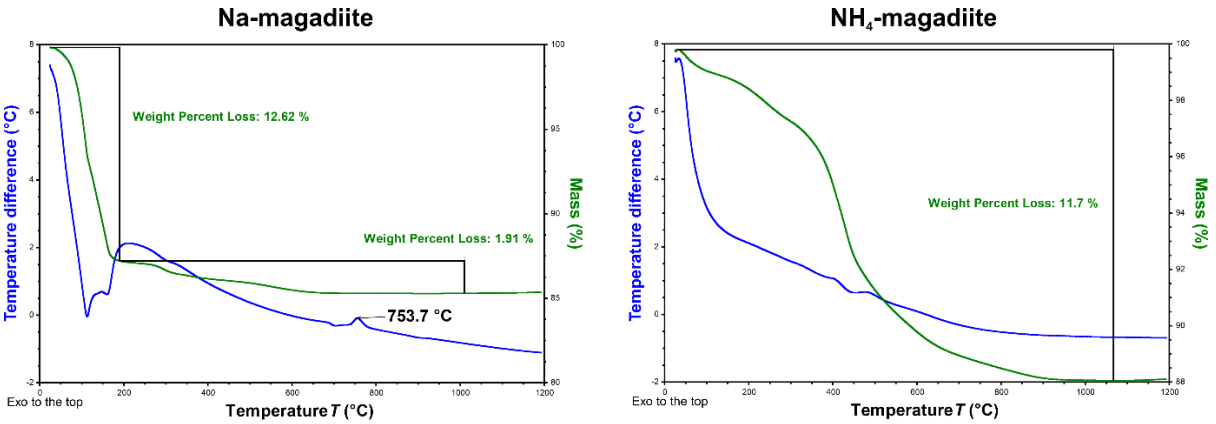

Figure S6.3 DTA (blue) and TG (green) curves of Na-magadiite (left) and NH_4-magadiite. (right) Two main steps can be distinguished: a) release of structural water between 30 °C to 180 °C and b) elimination of water molecules through the condensation of the silanol groups (and of ammonia in the case of NH_4-magadiite) between ca. 180 °C to 1100 °C.

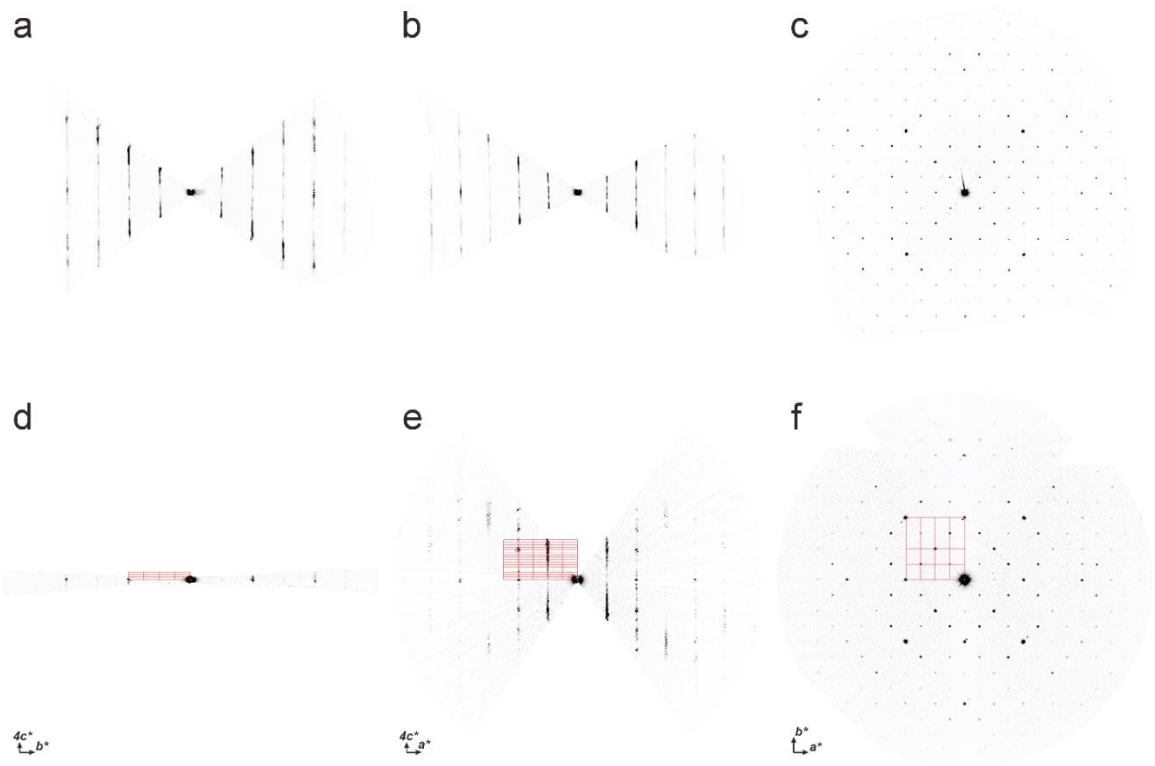

Figure S6.4 Reconstructed sections *h*0*l*, 0*kl* and *hk*0 of Na-magadiite recorded with 3D ED at room temperature (a-c) and at -176 °C (d-f).

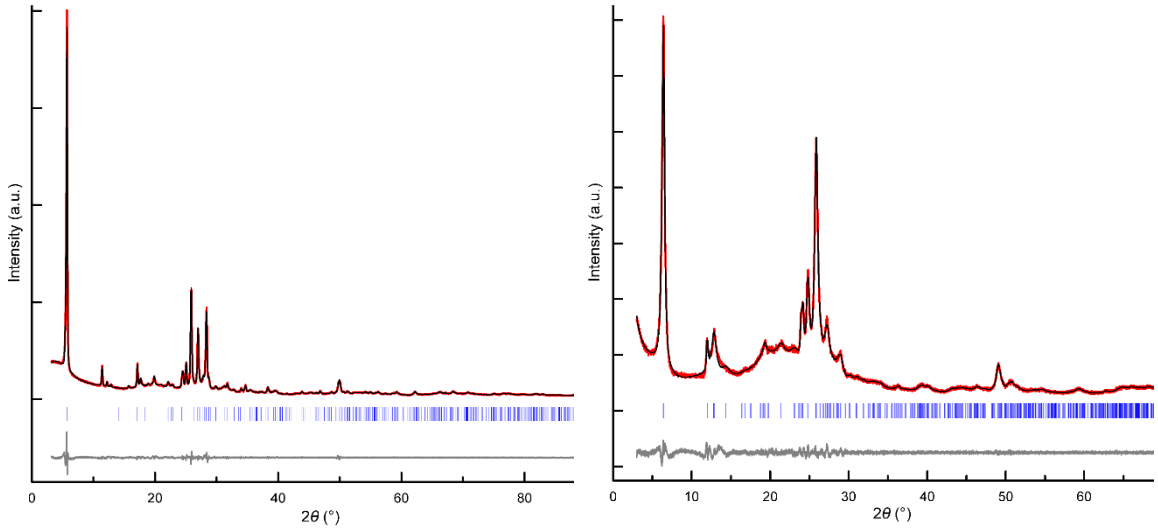

Figure S6.5 Plot of the Pawley fit of Na-magadiite (left) and NH_4-magadiite (right). Red line for measured intensities (I_O), black line for fitted profile (I_C), and gray line for the difference (I_O-I_C).

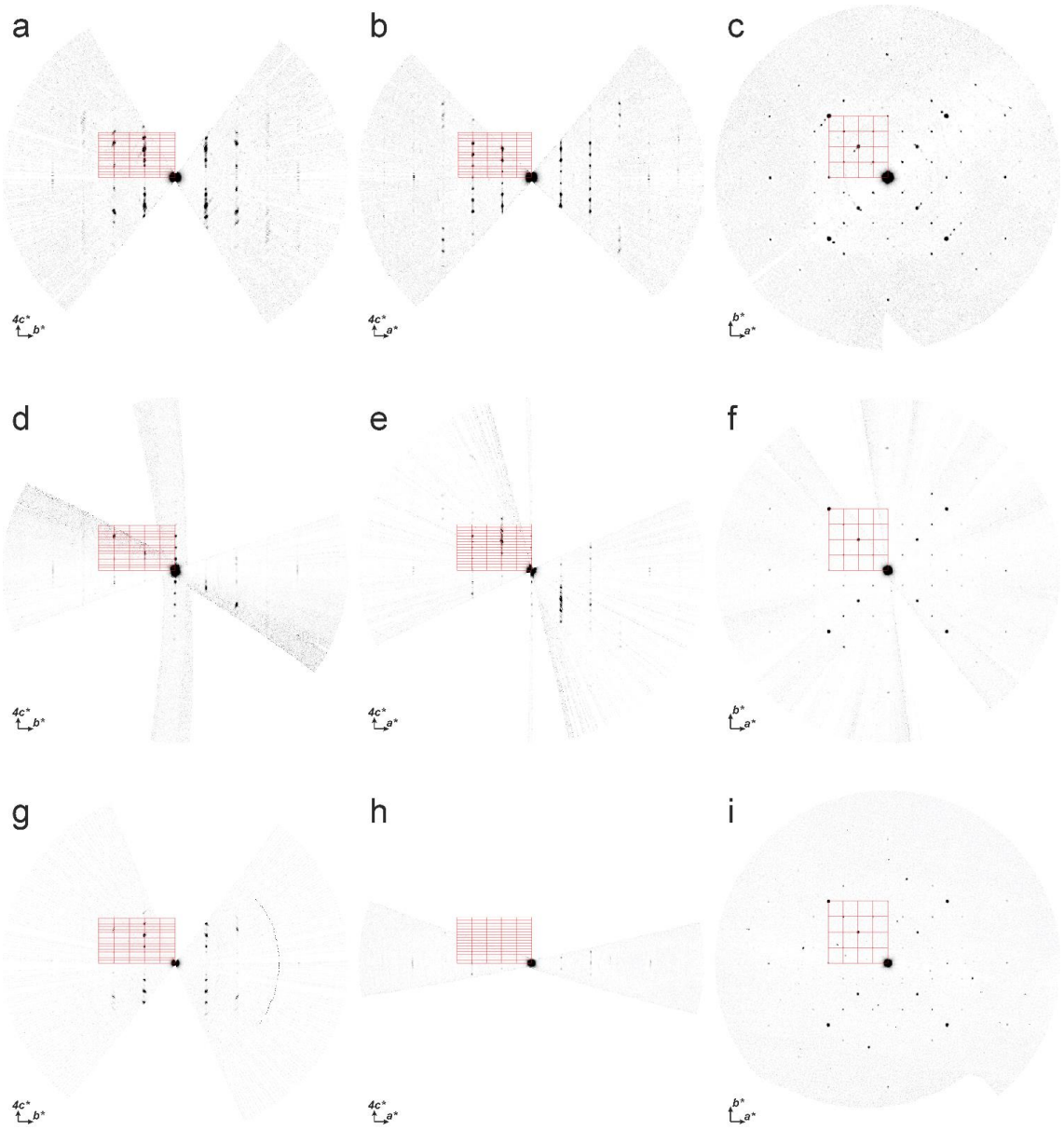

Figure S6.6 Reconstructed sections *h*0*l*, 0*kl* and *hk*0 of NH_4-magadiite recorded with 3D ED at -176 °C for three different crystals I (a-c) II (d-f) and III (g-i).

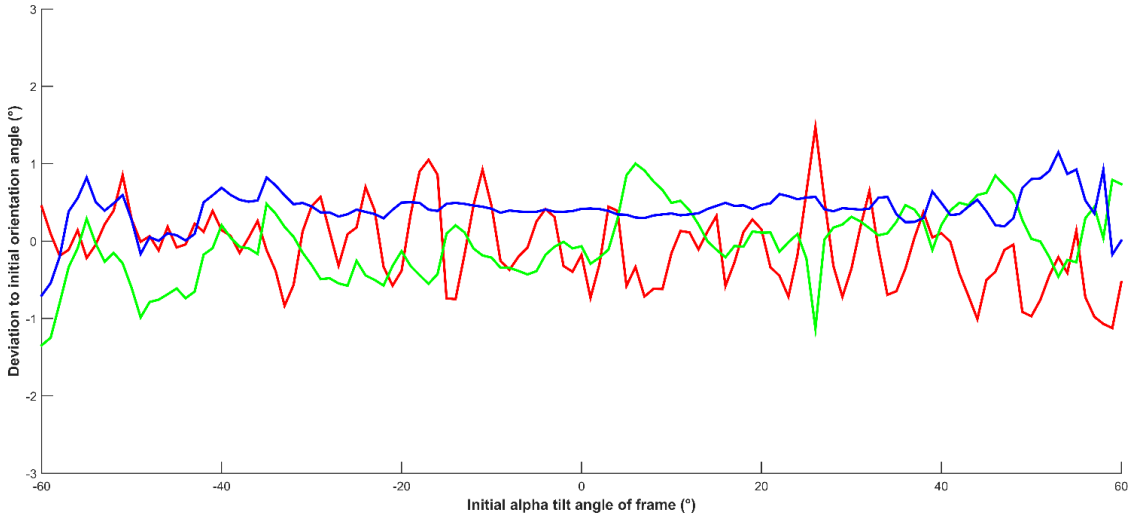

Figure S6.7 Plot of the corrected orientation angles α (red), β (green) and ω (blue) obtained by the "refinement using frame simulation" implemented in PETS 2.0 for dataset I. The initial orientation of β and ω is 0° for all frames.

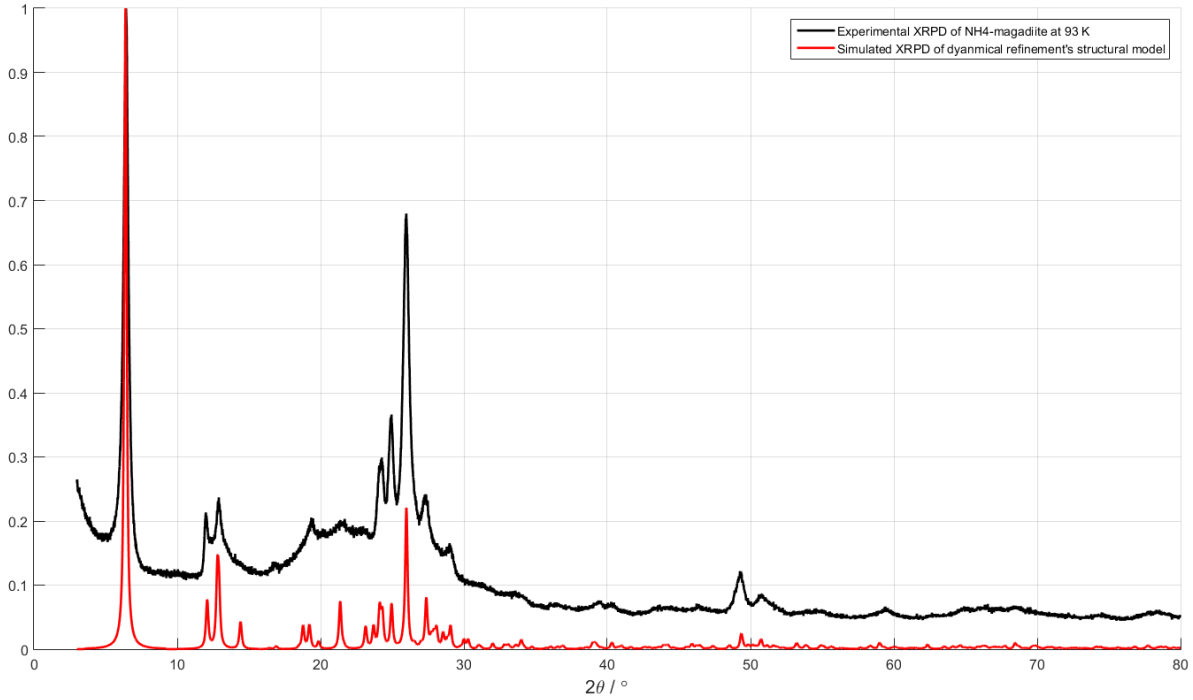

Figure S6.8 Comparison of experimental (black line) and simulated (red line) PXRD patterns (λ = 1.54059 Å). The PXRD pattern of the structure model derived from dynamical refinement was simulate with Mercury using a FWHM (2 theta) of 0.2° for the reflection profile.

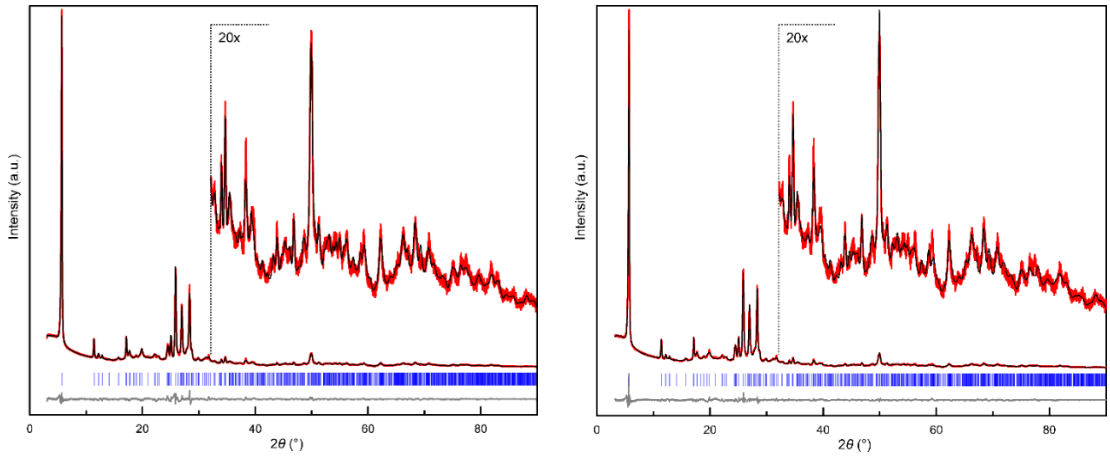

Figure S6.9 Plot of the initial (left) and final (right) Rietveld Refinement of Na-magadiite. Red line for measured intensities (I_O), black line for fitted profile (I_C), and blue line for the difference (I_O-I_C). Data were recorded using monochromatic CuKα_1 radiation (λ = 1.54059 Å)

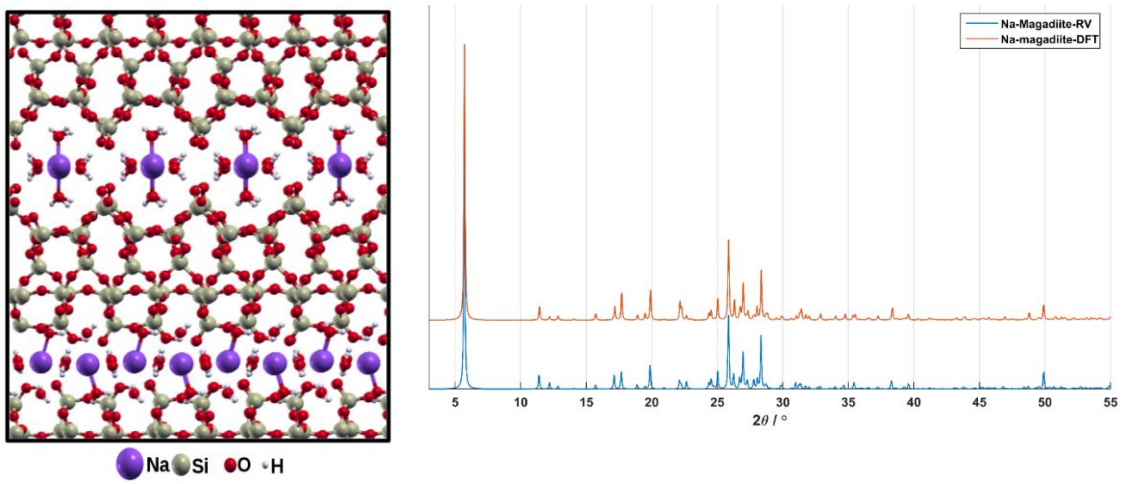

Figure S6.10 Overview of (left) PBE-GGA optimized Na-magadiite structure and (right) comparison between the simulated PXRD pattern (λ = 1.54059 Å) based on the results of the Rietveld refinement (in blue) and the DFT optimized structure (in red).

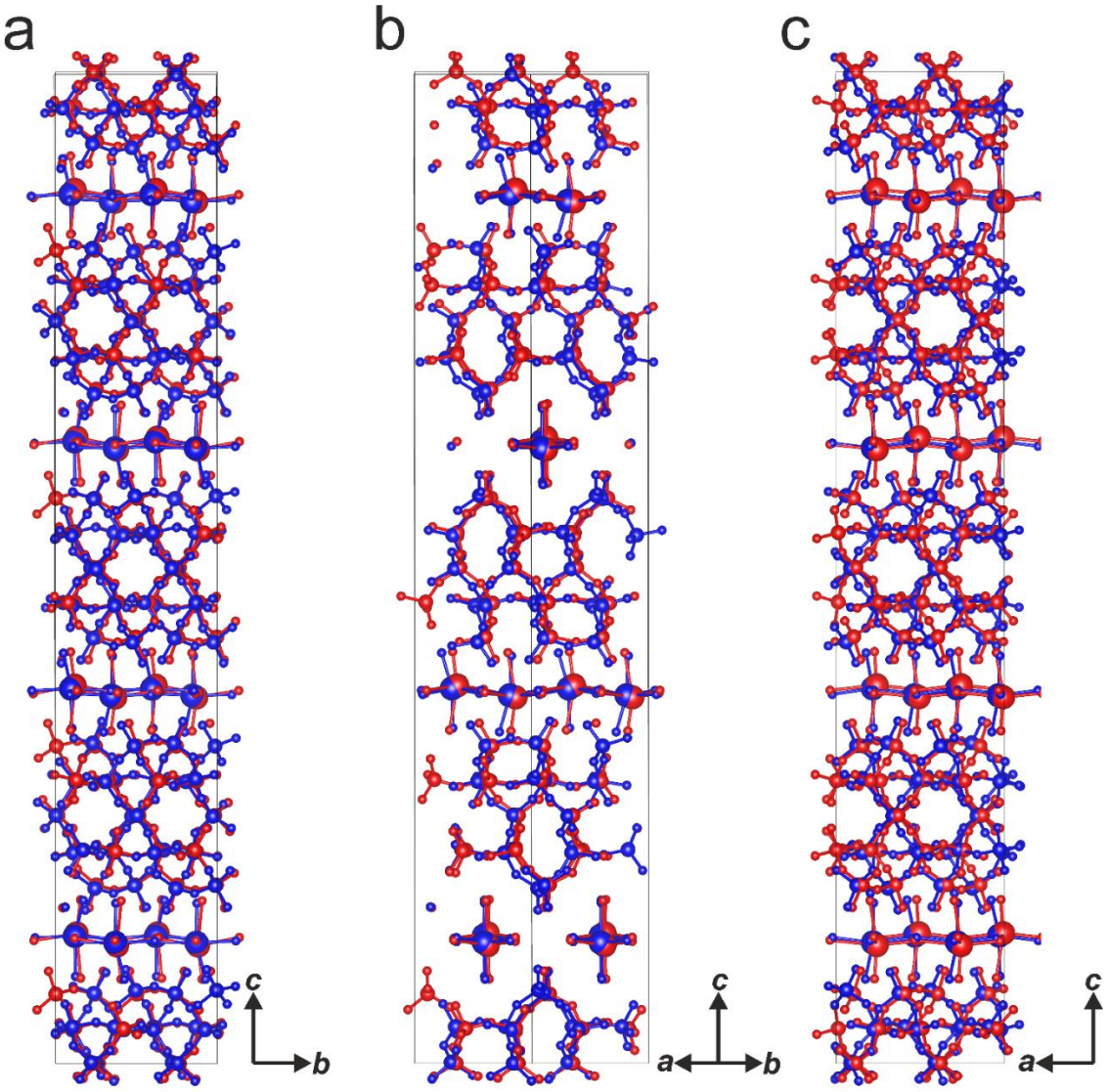

Figure S6.11 Overlay of the two structures of Na-magadiite (ignoring hydrogen atoms) as Rietveld Refinement (red) and after DFT optimization (blue).

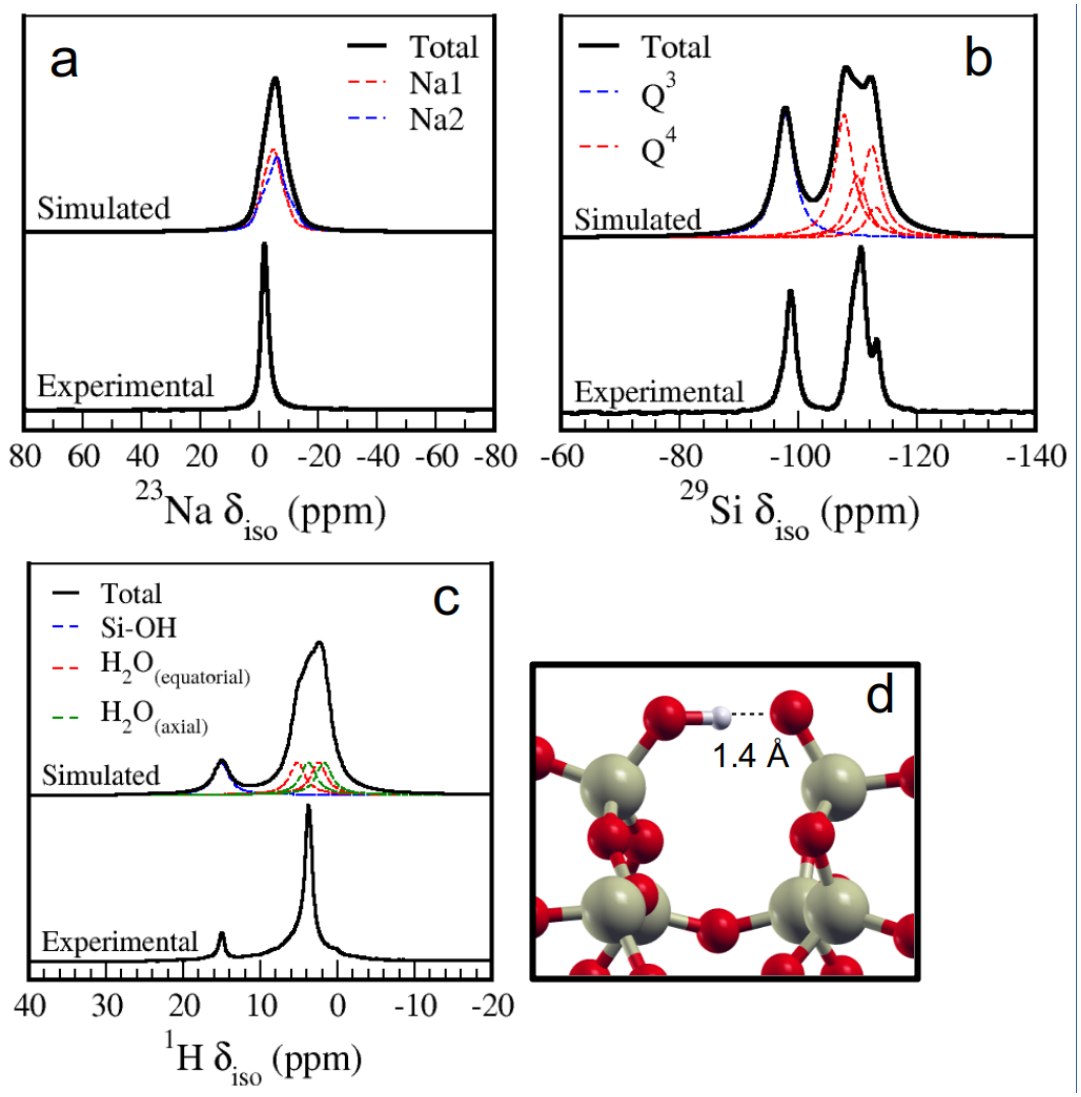

Figure S6.12 Experimental and simulated solid-state NMR spectra of (a) ^{23}Na, (b) ^{29}Si, and simulated NMR spectra of ^{1}H nuclei (c) and hydrogen bonds of silanol groups (d) of Na-magadiite.

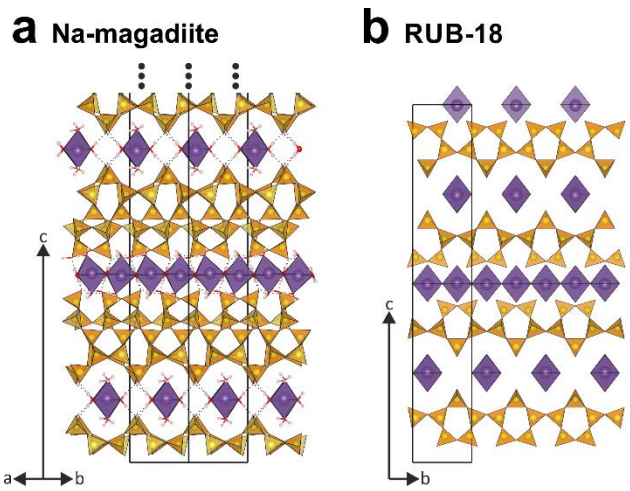

Figure S6.13 Visualization of the structure of (a) magadiite and (b) RUB-18. The interconnected bands of $[Na(H_20)_6]$ are related between the structures.

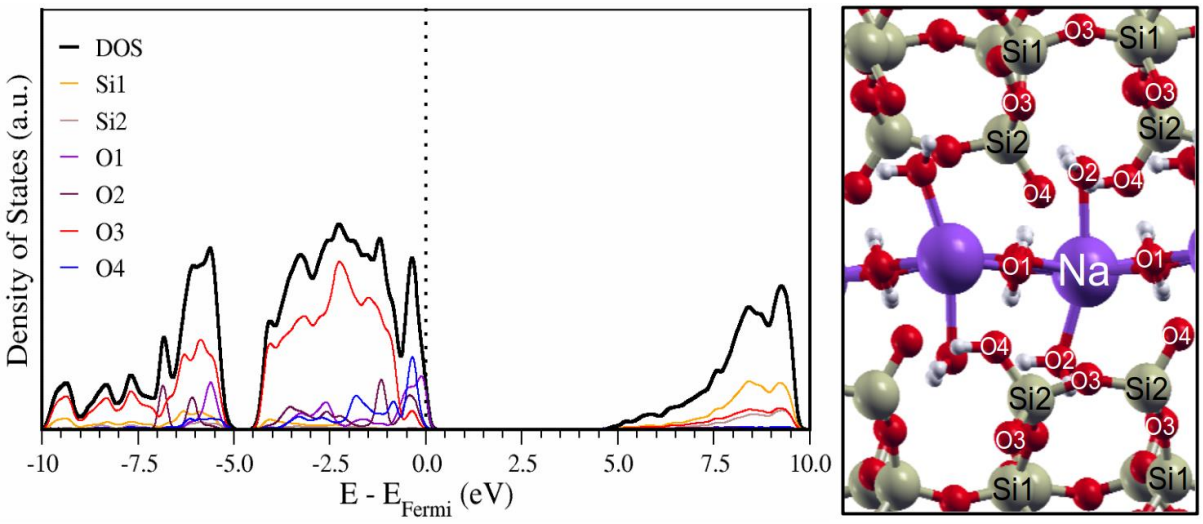

Figure S6.14 Projected Density of States of Na-magadiite. (The Fermi level was set to zero).

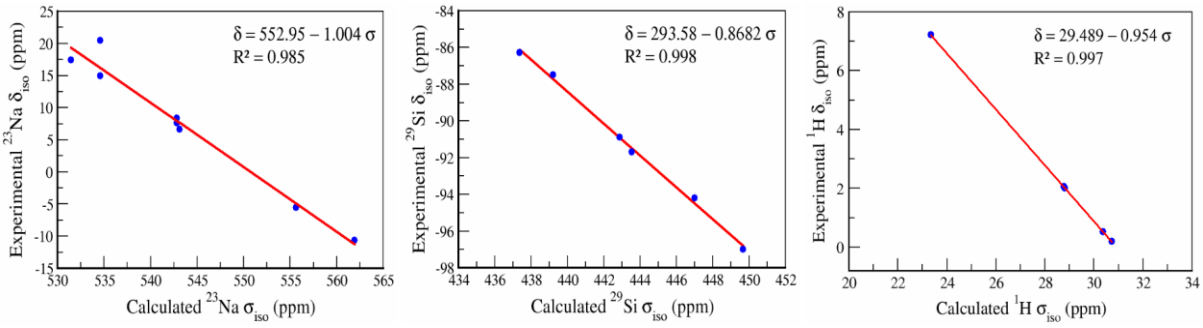

Figure S6.15 Correlation between experimental isotropic chemical shift δ_{iso} and calculated isotropic chemical shielding for ^{23} Na, ^{29} Si, ^{1} H nuclei.

Table S6.1 The atom types, integrated maxima of electron density map, atom coordinates, occupancies and estimated isotropic atomic displacement parameters (ADPs) of NH_4-magadiite's structure solution sorted by the height of the scattering potential's integrated maxima. The structure solution was performed in the standard setting of space group no. 43 in *Fdd*2 with the lattice parameters a = 10.2163 Å, b = 55.2914 Å and c = 10.6739 Å. The lattice parameters were later refined by a Pawley fit.

Atom	Label	Height ($e^{-}m^{-3}$)	Norm. Heights	x	y	z	Occ.	B_{iso} (Å²)
Si	Si1	1.98	1.00	0.732	0.498	0.067	1	1.22
Si	Si2	1.75	0.88	0.626	0.540	-0.115	1	1.13
Si	Si3	1.72	0.87	0.936	0.460	-0.042	1	0.59
Si	Si4	1.47	0.74	1.006	0.422	-0.456	1	3.24
Si	Si5	1.44	0.73	1.115	0.463	-0.271	1	4.29
Si	Si6	1.44	0.73	0.382	0.535	-0.305	1	5.72
Si	Si7	1.25	0.63	1.239	0.420	-0.652	1	5.45
O	O1	1.20	0.61	1.024	0.469	-0.164	1	1.60
O	O2	1.18	0.60	0.645	0.507	-0.026	1	2.98
O	O3	1.12	0.57	0.482	0.530	-0.197	1	2.85
O	O4	1.12	0.57	1.115	0.414	-0.554	1	2.21
O	O5	1.00	0.51	0.846	0.488	-0.007	1	4.28
O	O6	0.93	0.47	0.623	0.475	0.113	1	3.89
O	O7	0.90	0.45	0.804	0.513	0.177	1	5.99
O	O8	0.89	0.45	1.075	0.439	-0.336	1	4.96
O	O9	0.88	0.44	0.583	0.563	-0.028	1	4.93
O	O10	0.88	0.44	0.872	0.439	-0.061	1	4.09
O	O11	0.82	0.41	0.292	0.561	-0.260	1	8.63
O	O12	0.81	0.41	0.466	0.541	-0.453	1	6.50
O	O13	0.76	0.38	0.740	0.541	-0.218	1	5.14
O	O14	0.75	0.38	0.939	0.393	-0.422	1	4.65

O	O15	0.64	0.32	0.500	0.500	-0.094	1	6.53
O	O16	0.58	0.29	1.304	0.394	-0.673	1	2.51
O	O17	0.52	0.26	0.719	0.378	-0.502	1	6.36
O	O18	0.51	0.26	1.094	0.383	-0.137	1	17.69
O	O19	0.44	0.22	0.983	0.374	-0.258	1	9.27
O	O20	0.36	0.18	0.807	0.550	-0.278	1	4.51
O	O21	0.24	0.12	0.857	0.410	-0.255	1	16.87
O	O22	0.17	0.09	0.721	0.381	-0.106	1	56.03

Table S6.2 3D ED parameters, residuals and crystallographic data for kinematical and dynamical refinement of NH_4-magadiite.

	NH_4-magadiite
Crystal data	
Crystal system, space group	orthorhombic, *F*2*dd*
a (Å), *b* (Å), *c* (Å), *V* (Å³)	10.592(1), 10.337(1), 54.860(6), 6007(1)
Z	8
Unit cell content	$(NH_4)_{12}H_4[Si_{112}O_{224}(OH)_{16}]$
Data collection	
Radiation type	electrons, 200 kV
Wavelength (Å)	0.0251
Temperature (K)	97
Precession angle (deg.)	0.65 resp. 0.92
Projected crystal dimension (nm²)	650x450
Resolution ($Å^{-1}$)	0.9
Tilt step (deg.)	1
No of frames	121
Completeness	87%
Kinematical structure refinement	
Nitrogen amount per unit cell	9.92 (occ = 0.62(3))
Calculated density ($g.cm^{-3}$)	1.97 (without hydrogens)
U11, U22 and U33 for Si / O (Å²)	0.029(3),0.034(3),0.173(9) / 0.031(3),0.050(4),0.27(1)
No. of used reflections (obs/all)	935/1994
R1(obs)/R1(all), wR1(obs)/wR1(all) (%)	17.01/26.90, 15.81/16.19

goodness of fit (obs/all)	6.06/4.16
No. of refined parameters	78

Dynamical structure refinement

Nitrogen amount per formula unit	11.68 (occ = 0.73(2))
Calculated density ($g.cm^{-3}$)	1.98 (without hydrogens)
U11, U22 and U33 for Si / O ($Å^2$)	0.009(2),0.020(2),0.093(6) / 0.011(2),0.022(2),0.245(9)
No. of used reflections (obs/all)	2708/8298
Average crystal thickness (nm)	13.5 and 8.3
gmax, Sgmax(matrix), RSg, Nor	0.9, 0.01, 0.8, 64
R1(obs)/R1(all), wR1(obs)/wR1(all) (%)	11.66/26.59, 11.00/12.13
goodness of fit (obs/all)	3.65/2.24
No. of refined parameters[1]	79+173

[1] Split into the terms of the sum structural parameters and scale factors.

Table S6.3 Experimental and crystallographic parameters for the structure analyses of Na-magadiite by Rietveld refinement. Left: Refinement prior to DFT calculations ignoring the protons, right: Refinement including the protons as determined by DFT.

Parameter	a-Na-magadiite	
	Without protons	Including protons
Diffractometer	Siemens D5000 with 6° PSD	
Wavelength (Å)	1.54059	
2θ range of data (°)	4.0 - 94.0	
Step size (°2θ)	0.007754	
No. steps	11790	
No. contributing reflections	954	
No. geometric restraints	90	111
No. structural parameters	83	110
No. profile parameters	18	14+3+1
FWHM at ca. 24° (°2θ)	0.28 – 0.73	
R_F	0.022	0.038
R_{wp}	0.107	0.048
R_{exp}	0.045	0.022
Fit parameter	5.8 (chi^2)	2.2 (GOF)
Space group	*F*2*dd*	
a (Å)	10.540(2)	10.534(1)
b (Å)	10.134(2)	10.1346(9)
c (Å)	62.068(4)	62.050(4)
V (Å³)	6629(1)	6624(1)
Unit cell content	$Na_{16}[Si_{112}O_{224}(OH)_{16}] * 64\ H_2O$	
ρ (g/cm³) (calculated)	2.13	2.14

Table S6.4 Structural parameters of models of Na-magadiite.

Parameters	***Rietveld refinement***	***DFT Optimization***
space group	*F*2*dd*	*F*1
a (Å)	10.54	10.53
b (Å)	10.13	10.14
c (Å)	62.07	61.89
Volume	6628.6	6609.7
α	90.00°	90.07°
β	90.00°	89.97°
γ	90.00°	89.99°
Basal spacing (Å)	15.52	15.47

Table S6.5 Comparison of fractional coordinates and atom displacement in Ångström between the Na-magadiite structure model (in space group *F*1) based on the Rietveld Refinement, the DFT geometry optimization and the DFT geometry optimization with an applied origin shift of Δ*xyz* = [0.02270, -0.00502, 0.00227].

	Rietveld Refinement			Optimization by DFT				DFT model with origin shift			
label	x	y	z	x	y	z	Δd (Å)	x	y	z	Δd (Å)
Si1	0.380	0.234	0.500	0.388	0.226	0.499	0.15	0.411	0.221	0.501	**0.02**
Si2	0.380	0.766	0.500	0.388	0.758	0.498	0.19	0.411	0.753	0.500	**-0.06**
Si3	0.130	0.484	0.250	0.138	0.478	0.248	0.15	0.161	0.473	0.250	**-0.03**
Si4	0.130	1.016	0.250	0.136	1.010	0.249	0.13	0.159	1.005	0.251	**-0.01**
Si5	0.246	0.389	0.465	0.253	0.374	0.464	0.18	0.276	0.369	0.466	**0.00**
Si6	0.246	0.611	0.535	0.253	0.610	0.532	0.18	0.276	0.605	0.534	**-0.13**
Si7	-0.004	0.639	0.285	0.003	0.629	0.283	0.18	0.026	0.624	0.285	**-0.09**
Si8	-0.004	0.861	0.215	0.003	0.858	0.214	0.10	0.026	0.853	0.216	**-0.01**
Si9	0.545	0.123	0.465	0.569	0.115	0.461	0.35	0.592	0.110	0.463	**-0.09**
Si10	0.045	0.377	0.535	0.068	0.369	0.535	0.26	0.091	0.364	0.537	**0.04**
Si11	0.295	0.373	0.285	0.320	0.371	0.286	0.27	0.343	0.366	0.288	**0.22**
Si12	0.295	1.127	0.215	0.320	1.117	0.211	0.37	0.343	1.112	0.213	**-0.11**
Si13	0.485	0.579	0.465	0.497	0.556	0.464	0.28	0.520	0.551	0.466	**0.00**
Si14	0.485	0.421	0.535	0.497	0.428	0.532	0.21	0.520	0.423	0.534	**-0.08**
Si15	0.235	0.829	0.285	0.246	0.812	0.283	0.24	0.269	0.807	0.285	**-0.08**
Si16	0.235	0.671	0.215	0.248	0.677	0.214	0.16	0.271	0.672	0.216	**0.10**
Si17	0.712	0.379	0.464	0.736	0.373	0.461	0.32	0.759	0.368	0.463	**-0.01**
Si18	0.712	0.621	0.536	0.735	0.610	0.535	0.27	0.758	0.605	0.537	**0.06**
Si19	0.462	0.629	0.286	0.486	0.631	0.285	0.26	0.509	0.626	0.287	**0.14**
Si20	0.462	0.871	0.214	0.487	0.860	0.211	0.32	0.510	0.855	0.213	**0.00**
Si21	0.342	0.006	0.320	0.354	-0.008	0.319	0.19	0.377	-0.013	0.321	**0.09**
Si22	0.342	0.494	0.180	0.353	0.492	0.178	0.18	0.376	0.487	0.180	**0.06**
Si23	1.092	0.256	0.430	1.103	0.241	0.428	0.24	1.126	0.236	0.430	**0.07**
Si24	0.092	0.744	0.570	0.102	0.743	0.569	0.14	0.125	0.738	0.571	**-0.03**
Si25	0.144	0.247	0.320	0.170	0.236	0.322	0.31	0.193	0.231	0.324	**0.23**
Si26	0.644	0.753	0.180	0.667	0.749	0.175	0.42	0.690	0.744	0.177	**0.03**
Si27	0.894	0.497	0.430	0.916	0.483	0.424	0.44	0.939	0.478	0.426	**-0.16**
Si28	-0.106	0.503	0.570	-0.085	0.500	0.572	0.25	-0.062	0.495	0.574	**0.13**
Na1	0.507	0.369	0.369	0.509	0.353	0.370	0.17	0.532	0.348	0.372	**0.16**
Na2	0.507	0.631	0.631	0.507	0.627	0.627	0.27	0.530	0.622	0.629	**-0.20**
Na3	0.757	0.119	0.381	0.757	0.105	0.377	0.30	0.780	0.100	0.379	**-0.10**
Na4	0.257	0.381	0.619	0.256	0.376	0.620	0.06	0.279	0.371	0.622	**0.10**
O1	0.627	-0.011	0.469	0.639	-0.022	0.468	0.19	0.662	-0.027	0.470	**0.08**
O2	0.127	0.511	0.531	0.137	0.506	0.529	0.18	0.160	0.501	0.531	**-0.08**
O3	0.377	0.239	0.281	0.389	0.234	0.279	0.18	0.412	0.229	0.281	**0.04**
O4	0.377	1.261	0.219	0.387	1.256	0.217	0.15	0.410	1.251	0.219	**-0.01**
O5	0.277	0.317	0.487	0.266	0.287	0.486	0.33	0.289	0.282	0.488	**-0.03**
O6	0.277	0.683	0.513	0.266	0.696	0.510	0.25	0.289	0.691	0.512	**-0.11**
O7	0.027	0.567	0.263	0.015	0.544	0.260	0.31	0.038	0.539	0.262	**-0.18**
O8	0.027	0.933	0.237	0.015	0.945	0.236	0.19	0.038	0.940	0.238	**0.07**
O9	0.446	0.113	0.446	0.484	0.100	0.439	0.59	0.507	0.095	0.441	**-0.26**
O10	-0.054	0.387	0.554	-0.016	0.384	0.557	0.44	0.007	0.379	0.559	**0.21**
O11	0.196	0.363	0.304	0.240	0.356	0.308	0.53	0.263	0.351	0.310	**0.39**
O12	0.696	0.637	0.196	0.737	0.631	0.189	0.63	0.760	0.626	0.191	**0.03**
O13	0.804	0.632	0.516	0.841	0.617	0.516	0.42	0.864	0.612	0.518	**0.17**
O14	0.804	0.368	0.484	0.841	0.366	0.480	0.47	0.864	0.361	0.482	**-0.02**
O15	0.054	0.382	0.234	0.090	0.368	0.231	0.45	0.113	0.363	0.233	**-0.10**
O16	0.054	1.118	0.266	0.087	1.123	0.265	0.36	0.110	1.118	0.267	**0.05**
O17	0.505	0.354	0.558	0.505	0.336	0.554	0.31	0.528	0.331	0.556	**-0.19**

O18	0.505	0.646	0.442	0.505	0.650	0.442	0.04	0.528	0.645	0.444	**0.10**
O19	0.255	0.604	0.192	0.257	0.585	0.193	0.20	0.280	0.580	0.195	**0.09**
O20	0.255	−0.104	0.308	0.253	−0.097	0.305	0.22	0.276	−0.102	0.307	**−0.07**
O21	0.612	0.494	0.471	0.630	0.480	0.468	0.29	0.653	0.475	0.470	**−0.06**
O22	0.612	0.506	0.529	0.629	0.504	0.528	0.20	0.652	0.499	0.530	**0.05**
O23	0.362	0.744	0.279	0.380	0.739	0.278	0.20	0.403	0.734	0.280	**0.07**
O24	0.362	0.756	0.221	0.379	0.754	0.219	0.23	0.402	0.749	0.221	**0.05**
O25	0.462	0.672	0.485	0.465	0.641	0.485	0.32	0.488	0.636	0.487	**0.02**
O26	0.462	0.328	0.515	0.465	0.343	0.511	0.29	0.488	0.338	0.513	**−0.14**
O27	0.212	0.922	0.266	0.212	0.897	0.262	0.37	0.235	0.892	0.264	**−0.25**
O28	0.212	0.578	0.234	0.217	0.592	0.236	0.18	0.240	0.587	0.238	**0.28**
O29	0.784	0.418	0.443	0.798	0.418	0.438	0.33	0.821	0.413	0.440	**−0.13**
O30	−0.216	0.582	0.557	−0.203	0.565	0.558	0.23	−0.180	0.560	0.560	**0.04**
O31	0.034	0.168	0.307	0.054	0.175	0.307	0.23	0.077	0.170	0.309	**0.10**
O32	0.534	0.832	0.193	0.551	0.812	0.189	0.36	0.574	0.807	0.191	**−0.09**
O33	−0.024	0.359	0.513	−0.020	0.329	0.515	0.33	0.003	0.324	0.517	**0.13**
O34	0.476	0.141	0.487	0.482	0.156	0.482	0.38	0.505	0.151	0.484	**−0.20**
O35	0.226	1.109	0.237	0.230	1.076	0.231	0.50	0.253	1.071	0.233	**−0.41**
O36	0.226	0.391	0.263	0.227	0.409	0.266	0.25	0.250	0.404	0.268	**0.33**
O37	0.211	0.697	0.555	0.222	0.705	0.553	0.19	0.245	0.700	0.555	**−0.05**
O38	1.211	0.303	0.445	1.223	0.280	0.443	0.28	1.246	0.275	0.445	**0.07**
O39	0.461	0.447	0.195	0.474	0.453	0.193	0.18	0.497	0.448	0.195	**0.12**
O40	0.461	0.053	0.305	0.471	0.033	0.303	0.25	0.494	0.028	0.305	**0.05**
O41	0.372	0.476	0.459	0.388	0.447	0.459	0.34	0.411	0.442	0.461	**0.06**
O42	0.372	0.524	0.541	0.387	0.536	0.537	0.31	0.410	0.531	0.539	**−0.14**
O43	0.122	0.726	0.291	0.138	0.700	0.288	0.37	0.161	0.695	0.290	**−0.18**
O44	0.122	0.774	0.209	0.137	0.784	0.209	0.19	0.160	0.779	0.211	**0.15**
O45	0.635	0.247	0.459	0.675	0.228	0.457	0.48	0.698	0.223	0.459	**0.07**
O46	0.135	0.253	0.541	0.174	0.256	0.540	0.43	0.197	0.251	0.542	**0.01**
O47	0.385	0.497	0.291	0.425	0.486	0.290	0.44	0.448	0.481	0.292	**0.13**
O48	0.385	1.003	0.209	0.427	1.005	0.207	0.47	0.450	1.000	0.209	**0.14**
O49	0.254	0.136	0.325	0.273	0.122	0.327	0.28	0.296	0.117	0.329	**0.25**
O50	0.254	0.364	0.175	0.272	0.365	0.170	0.35	0.295	0.360	0.172	**−0.09**
O51	1.004	0.386	0.425	1.021	0.369	0.420	0.41	1.044	0.364	0.422	**−0.10**
O52	0.004	0.614	0.575	0.020	0.616	0.576	0.18	0.043	0.611	0.578	**0.09**
O53	0.402	−0.046	0.343	0.408	−0.085	0.340	0.44	0.431	−0.090	0.342	**−0.03**
O54	0.402	0.546	0.157	0.405	0.567	0.156	0.21	0.428	0.562	0.158	**0.21**
O55	1.152	0.204	0.407	1.155	0.165	0.406	0.40	1.178	0.160	0.408	**0.09**
O56	0.152	0.796	0.593	0.154	0.817	0.590	0.28	0.177	0.812	0.592	**−0.10**
O57	0.103	0.292	0.343	0.107	0.294	0.344	0.06	0.130	0.289	0.346	**0.15**
O58	0.603	0.708	0.157	0.607	0.690	0.153	0.31	0.630	0.685	0.155	**−0.08**
O59	0.853	0.542	0.407	0.857	0.545	0.403	0.26	0.880	0.540	0.405	**−0.08**
O60	−0.147	0.458	0.593	−0.143	0.439	0.593	0.20	−0.120	0.434	0.595	**−0.01**
O61	0.546	0.344	0.414	0.502	0.360	0.410	0.54	0.525	0.355	0.412	**−0.21**
O62	0.546	0.656	0.586	0.503	0.630	0.586	0.52	0.526	0.625	0.588	**−0.05**
O63	0.796	0.094	0.336	0.754	0.109	0.337	0.47	0.777	0.104	0.339	**0.06**
O64	0.296	0.406	0.664	0.253	0.379	0.660	0.58	0.276	0.374	0.662	**−0.27**
O65	0.525	0.114	0.377	0.525	0.109	0.372	0.33	0.548	0.104	0.374	**−0.18**
O66	0.025	0.386	0.623	0.023	0.368	0.624	0.20	0.046	0.363	0.626	**0.07**
O67	0.275	0.364	0.373	0.276	0.363	0.375	0.11	0.299	0.358	0.377	**0.21**
O68	0.275	0.636	0.627	0.274	0.619	0.622	0.35	0.297	0.614	0.624	**−0.30**
O69	1.034	0.132	0.376	0.998	0.096	0.371	0.59	1.021	0.091	0.373	**−0.29**
O70	0.534	0.368	0.624	0.497	0.381	0.625	0.42	0.520	0.376	0.627	**0.08**
O71	0.783	0.382	0.374	0.751	0.349	0.375	0.48	0.774	0.344	0.377	**0.04**
O72	0.783	0.618	0.626	0.747	0.631	0.621	0.51	0.770	0.626	0.623	**−0.29**
O73	0.520	0.344	0.335	0.550	0.305	0.333	0.51	0.573	0.300	0.335	**0.04**
O74	0.520	0.656	0.665	0.554	0.679	0.663	0.45	0.577	0.674	0.665	**0.01**
O75	0.770	0.094	0.415	0.797	0.058	0.413	0.48	0.820	0.053	0.415	**0.10**
O76	0.270	0.406	0.585	0.302	0.431	0.583	0.43	0.325	0.426	0.585	**−0.02**

Table S6.6 Chemical bond lengths and angles of octahedral hydrated sodium of optimized Na-magadiite.

Chemical bonds	**Length (Å)**	**Chemical bonds**	**Angle**
Na1 - OW5	2.35	*OW5 - Na1 - OW7*	80.48°
Na2 - OW2	2.35	*OW6 - Na1 - OW1*	81.18°
Na2 - OW7	2.46	*OW7 - Na2 - OW4*	82.25°
Na1 - OW6	2.47	*OW4 - Na2 - OW3*	83.41°
Na1 - OW7	2.48	*OW8 - Na1 - OW1*	84.51°
Na2 - OW8	2.48	*OW7 - Na1 - OW8*	85.16°
Na2 - OW4	2.49	*OW3 - Na2 - OW2*	86.20°
Na1 - OW1	2.51	*OW8 - Na2 - OW7*	87.34°
Na2 - OW3	2.56	*OW8 - Na2 - OW2*	104.69°
Na1 - OW8	2.56	*OW6 - Na1 - OW5*	107.98°

Table S6.7 ^{23}Na NMR parameters of Na-magadiite.

Atom	σ_{iso}	δ_{iso}	C_q	η
Na1	550.46	0.29	1.38	0.68
Na2	549.94	0.81	1.50	0.93

Table S6.8 Experimental δ_{iso} and theoretical σ_{iso} ^{23}Na, ^{29}Si, and ^{1}H NMR parameters of reference systems of known structure.

^{23}Na			^{29}Si			^{1}H		
Compound	**σ_{iso}***	**δ_{iso}**	**Compound**	**σ_{iso}***	**δ_{iso}**	**Compound**	**σ_{iso}***	**δ_{iso}**
α-$Na_2Si_2O_5$	531.4	17.3[a]; 17.4[b]	α-$Na_2Si_2O_5$	447.0	-94.2[a]	Adamantane	28.8[f]	1.9[e]
β-$Na_2Si_2O_5$	534.6	14.9[a]; 20.4[b]	β-$Na_2Si_2O_5$	437.4	-86.3[a]	Bohemite	23.4[f]	7.2[d]
	542.9	7.6[a]; 8.3[b]		439.2	-88.2[a]			
NaCl	543.2	6.6[f]	Talc	449.7	-97.0[d]	Brucite	30.7[f]	0.0[d]
$Na_3P_3O_9$	555.7	-5.6[b]	Kaolinite	442.9	-90.9[c]	Pyrophyllite	28.8[f]	2.2[d]
NaH_2PO_4 . H_2O	561.9	-10.7[b]		443.5	-91.5[c]	Talc	30.4[f]	0.7[d]

[a] Ref. 1, [b] Ref. 2, [c] Ref. 3,[d] Ref. 4, [e]Ref. 5, [f] Ref. 6.

* σ_{iso} values are theoretical. The structures of all references were optimized and σ_{iso} values were calculated by DFT (GIPAW method). In the case of ^{1}H NMR, σ_{iso} were calculated again in this work, but the same values are presented in the Ref. 6.

Table S6.9 PBE-optimized cell parameters and atomic positions of Na-magadiite.

Cell Parameters

-5.264090440 5.070454705 -0.004012812

5.265145806 5.072009282 -0.002119436

-21.052040841 5.050343631 30.939622742

Atomic Positions (cartesian x y z in Å)

Si	-1.175204906	2.288453729	-0.086013627	-9.072511714	7.091721776	17.796623369
Si	-4.544608821	3.739074093	2.166278722	-11.694254913	7.431838327	17.274745590
Si	-0.034670606	4.341441331	2.007826114	-10.834056733	5.395416149	18.753612997
Si	2.473496235	6.188006209	2.178103431	-13.126479795	4.079574313	18.857742832
Si	-2.603532429	6.181877932	1.999874617	-15.216543520	6.831090842	19.002974087
Si	-6.159673154	5.070838634	4.438610830	-12.915999042	6.291164931	20.240288543
Si	-4.191687034	7.533170928	4.237146069	-13.396513364	9.204661634	16.450218907
Si	-6.805565622	4.983155733	11.000485577	-9.607809846	11.378862375	16.405047595
Si	-3.504428443	7.589916388	10.799892780	-11.316995521	9.990648245	17.914315872
Si	-9.077206031	4.837308927	15.357830750	-11.792467665	12.552994380	17.224941069
Si	-7.916571256	6.856968975	13.244603083	-13.263215376	8.673489318	19.065904407
Si	-5.402650147	8.709628956	13.082427424	-14.664180666	8.040772948	21.259533862
Si	-12.426357944	6.249001484	13.052670886	-9.998860087	8.155113262	20.617181559
Si	-10.496399241	8.694634817	13.231656036	-13.112316524	11.236632201	20.817970314
Si	-10.495072491	6.364920605	17.501189463	-12.878970917	8.734895732	23.184722795
Si	-12.061693950	4.979809560	19.767512138	-16.756097228	9.265818330	21.041542124
Si	-7.939609735	8.220277833	17.519175405	-15.528966752	11.231579964	23.001589776
Si	-14.003068702	7.453619349	19.909473077	-15.807418073	6.030203441	22.985431779
Si	-9.089505380	10.238021935	15.372968190	-14.160313778	6.728457068	25.145609923
Si	-12.419289393	8.823837710	17.672933270	-18.415206400	8.599125584	23.194667962
Si	-10.673501719	11.458026134	17.628576813	-17.922452782	5.641145843	25.575324001
Si	-14.707434593	7.497901987	26.459099728	-15.561646258	8.793140718	25.981305786
Si	-20.327989743	6.219016518	28.536592853	-17.290712337	10.577990086	24.922960957
Si	-18.572397708	8.838543653	28.518458596	-15.958782916	11.136633661	27.182627341
Si	-16.673994693	9.956897065	26.260557520	-17.911720760	9.293346148	27.119759120
Si	-23.647749934	8.849412747	28.694791878	-21.028472539	8.707166765	25.384542663
Si	-21.080069269	10.692226966	28.692581338	-18.707282998	12.965746969	27.421731253
Si	-22.226661667	12.738035922	30.785428391	-20.995423496	11.642263386	27.369156085
Na	-10.457663770	6.351375473	7.832684767	-19.685956097	9.921370521	28.971918346
Na	-2.571808648	3.813429362	7.403511325	-17.458518665	8.763940320	29.699113152
Na	-10.428187826	8.633319696	22.878171562	-22.232949712	9.588182606	28.399785742
Na	-18.350619561	6.123763751	23.309079678	-21.417001620	11.549554414	30.026045820
O	3.589437337	6.261881382	0.998198030	-19.214517705	7.367907856	28.248818646
O	1.358509142	5.109635127	1.716481733	-23.515738531	7.965460910	30.064722514
O	-0.372701066	3.477809349	0.679038901	-21.243968521	6.632742062	29.795947702
O	0.053757491	3.406669349	3.341333154	-19.593988374	4.829306679	28.932260851
O	-1.192721709	5.439227852	2.297517958	-18.463627572	11.258469405	25.081633654
O	-2.466161560	7.054999067	0.623874721	-17.231640306	4.936349589	25.577150586
O	-0.204933100	8.405000350	0.908494584	-17.590260046	6.279514576	26.233667892
O	-0.168085104	8.963003183	3.521492774	-21.156466274	7.888688818	25.910724915
O	0.036489047	6.390865133	5.319882207	-20.171615631	9.069645021	25.681708044
O	-2.930521712	7.147226877	3.262637820	-9.556402554	8.773095235	20.002935007
O	-2.138700166	0.654614454	3.581420803	-9.365819752	7.398967828	20.649056278
O	-3.428056218	2.590928817	2.443929117	-12.294417749	11.693485290	20.543127526
O	-3.816328743	5.132950445	1.776029234	-13.154380464	10.422009569	20.270619354
O	-2.086916025	4.363096115	5.157687447	-15.670511917	8.652950198	21.123224955
O	-5.051601838	6.240792591	4.704205470	-6.977118804	8.604652844	10.185966710
O	-3.644441478	8.278793930	5.564842612	-8.013497822	9.741837547	10.416237883
O	-2.381999707	6.269975565	7.555865858	-9.287995231	7.603120423	10.073018476
O	-6.766370560	4.450923214	5.779357950	-9.612488092	6.266029343	10.750260837
O	-5.019923660	3.729782040	7.682537791	-5.326361067	6.281552288	9.622345701
O	-5.295395799	8.931354851	7.752755591	-7.970418196	3.745357807	5.619609526
O	-4.136410068	6.994438540	9.459359406	-1.744428650	3.749163132	4.481567630

O	-7.923148961	6.393713638	7.480074919	-1.409259799	5.080575631	5.162541309
O	-6.267441014	5.739305670	9.674865953	0.924815809	6.102467797	5.034394347
O	-7.667316367	3.692279559	10.527359784	-0.129955588	7.226863159	4.832319457
O	-5.537370779	4.584531015	11.961887239	-16.170961441	11.010228816	23.740888101
O	-9.958317291	6.878352631	10.074229781	-15.861413134	10.672078185	22.264039634
O	-7.820667301	5.920452888	11.912223253	-13.207244880	8.199669537	23.938249726
O	-7.864207515	8.909476309	9.915332628	-13.522201169	8.497997873	22.458632084
O	-4.724162987	8.224270717	11.703616361	-15.426534754	6.652936681	22.318632314
O	-6.532083950	7.641795048	13.532281028	-15.288750204	6.259459528	23.799504586
O	-9.086725524	7.941849890	12.953370188	-18.041919794	9.237435996	23.856181669
O	-8.236288480	5.990074060	14.576849497	-17.886312337	8.818142926	22.380331020
O	-8.028812796	11.459649444	11.675808507	-7.423902194	6.188160130	8.310328932
O	-11.294378674	5.112230302	12.790957138	-7.522352548	5.751498536	6.835043877
O	-9.577121101	3.725298654	14.285828764	-5.348452875	4.267934665	8.433112575
O	-13.368527219	5.832511952	14.292645577	-2.711914441	6.798144233	6.798735480
O	-10.364163289	5.504135429	16.114643710	-5.656882846	3.977560515	6.945134567
O	-11.720224000	7.654258419	13.448616745	-3.017149121	6.526563303	8.291337910
O	-10.372650472	9.577798222	14.602380942	-4.890907106	8.299406590	8.405557568
O	-8.291327570	9.085604367	16.194803827	-4.789625489	8.724445412	6.926334982

further atoms in 2nd column

References

[1] Charpentier, T., Ispas, S., Profeta, M., Mauri, F. & Pickard, C. J. First-Principles Calculation of 17O, 29Si, and 23Na NMR Spectra of Sodium Silicate Crystals and Glasses. *J. Phys. Chem. B* **108**, 4147–4161 (2004).

[2] Koller, H., Engelhardt, G., Kentgens, A. P. M. & Sauer, J. 23Na NMR Spectroscopy of Solids: Interpretation of Quadrupole Interaction Parameters and Chemical Shifts. *J. Phys. Chem.* **98**, 1544–1551 (1994).

[3] Hayashi, S., Ueda, T., Hayamizu, K. & Akiba, E. NMR study of kaolinite. 1. 29 Si, 27 Al, and 1 H spectra. *J Phys Chem* **96**, 10922–10928 (1992).

[4] Cadars, S., Guégan, R., Garaga M. N., Bourrat, X. Le Forestier, L., Fayon, F., Huynh, T.V., Allier, T., Nour, Z. Massiot, D. New Insights into the Molecular Structures, Compositions, and Cation Distributions in Synthetic and Natural Montmorillonite Clays. *Chem. Mater.* **24**, 4376–4389 (2012).

[5] Marchetti, A., Jehle, S., Felletti, M., Knight, M. J., Wang, Y., Xu, Z.-Q., Park A. Y., Otting, G., Lesage, A., Emsley, L., Dixon, N. E., Pintacuda, G. Backbone Assignment of Fully Protonated Solid Proteins by 1H Detection and Ultrafast Magic-Angle-Spinning NMR Spectroscopy. *Angewandte Chemie International Edition* **51**, 10756–10759 (2012).

[6] Fonseca, C. G., de Carvalho, G. S. G., Wypych, F., Diniz, R. & Leitão, A. A. Na+ as a probe to structural investigation of dehydrated smectites using NMR spectra calculated by DFT. *Applied Clay Science* **126**, 132–140 (2016).

7

Conclusion

In this dissertation, new pathways to thermodynamically metastable phases, starting from commonly known mineral phases have been explored by means of mechanochemistry. Phosphates, carbonates, sulfates and silicates are commonly found in mineral deposits and are thus, not only interesting model systems in the investigation of crystallization pathways, but usually of fundamental relevance to industrial processes. By application of different analytical methods, the transformation pathways were monitored *ex situ* to gain insight into structural changes, thus eludicating the mechanistic processes during ball milling.

The inherent nature of these compounds led to different synthetic approaches for the induction of phase transitions by mechanochemistry. Although the different starting compounds cannot be linked chemically to a common class of materials, they share distinct attributes, especially their polymorphism. The introduction of chemical "impurities" by ball milling led to metastable phases and eventually even amorphous states. To underline that this approach is feasible in different classes this work can be structured into three principal investigations: (i) the zinc-phosphate-hydrate system which corresponds to the natural analogue *hopeite* (ii) the calcium-carbonate-(hydrate) system, in respect to sodium – silicate – hydrates, thus including the minerals *calcite, monohydrocalcite* and *magadiite* (iii) and lastly the calcium-sulfate-(hydrate) system, corresponding to the natural analogues of *gypsum, bassanite* and *anhydrite*.

Each of the underlying studies required individual synthetic approaches for preparation of the individual phases. In mechanochemical synthesis it could be shown that inorganic "impurities", not only play a crucial role in the amorphization process, but impact the recrystallization of the obtained material drastically. Furthermore, it could be shown that a clever application of specific solvents in mechanochemical processes must be considered, as the reaction pathways during milling are affected fundamentally by these auxiliary solvents. In addition, it could be shown that the atmospheric environment of a precursor can affect the crystallinity of the product severly even under hydrothermal conditions.

In the first part of this thesis the mechanochemically induced amorphization of *hopeite* was investigated. During milling experiments in a stainless steel container, the abrasion of iron

was observed which led to an amorphization of hopeite to BM-Fe-AZP. To investigate the mechanism of the reaction in detail, elemental iron was added in zirconia equipment to simulate the underlying reaction. The kinetics of amorphization were shown to have an exponential behavior by FTIR and PXRD. The systematic use of TGA and REDOR experiments could be applied to show a partial dehydration during the amorphization process. In addition, examination of the aqueous recrystallization by FTIR spectroscopy showed that the transformation occurred *via* dissolution and rerystallization. Furthermore, a partial oxidation of Fe^{2+} to Fe^{3+} was observed during the milling reaction by ^{57}Fe Mößbauer spectroscopy. These iron impurities were found throughout the amorphous material by TEM EDX. In conclusion, this project not only presents a detailed investigation of a simple top-down synthesis of amorphous zinc phosphate, it sheds also light on the chemical consequences of contamination effects during ball milling. As elemental iron can be used to affect thermal and aqueous crystallization pathways, future studies could provide insight if other elements like Co and Mn which are known as substitutes for Zn would show a similar behavior. Furthermore, the question of a partial substation by different anionic constituents (i.e. hydrogenphosphates, silicates, carbonates) remains to be solved.

Despite the easy access to amorphous zinc phosphate by addition of elemental iron, the amorphization of *limestone* (calcite) can only be achieved with ionic constituents. Therefore, the second project focused on the addition and influence of a silicate component into calcium carbonate, to possibly attain a cementious compound by mechanochemistry. By FTIR and NMR spectroscopy, as well as TEM and SEM imaging and total scattering methods (PDF analysis) it could be shown that an amorphization due to a reaction between sodium metasilicate and calcium carbonate to amorphous sodium silicate calcium carbonate (aNaSiCC) is possible. Application of a kinetically governed recrystallization method enabled the analysis of the reaction pathway through several metastable states (i.e. *pirssonite*, *gaylussite*, *monohydrocalcite*) by FTIR, PXRD and ADT. Based on CP NMR experiments and TEM and SEM imaging a possible rehydration model was established. Most interestingly, it could be shown that a metathesis reaction between silicate and carbonate is the driving force for the mechanochemical reaction. From these findings, a calcium silicate environment was deduced and found to form a calcium-silicate-hydrate like phase. In summary, this study not only led to a new amorphous calcium carbonate phase, but also opened an easy access to different metastable polymorphs, and a new ecologically friendly way to cementious phases by circumventing decarbonation of limestone in conventional high temperature reactions. This reduces CO_2 emissions of cement production

immensely. Still, a number of questions remain to be answered. Future studies could focus on the addition of different controlling agents as magnesium containing carbonates and silicates, as well as aluminates and ferrites to mimic real cement. In addition, bulk studies in an upscaled method could provide insight into the macroscopic behavior (i.e. tensile strength, viscosity) of the materials.

A new aspect of ball-milling was analyzed in the third project. While the grinding reactions in the first two projects used cyclohexane as the dispersion medium to dissipate the frictional heat during the grinding process, it was found that serious changes occurred in the mechanochemical reactions in polar and protic solvents. Therefore, in the third and fourth projects, the effect of alcohols as polar and protic solvents on amorphization and phase changes during grinding were investigated. The third project used a solvent effect to partially dehydrate gypsum. Different from the calcium carbonate hydrate system, no amorphization could be achieved in the calcium sulfate hydrate system. Analysis by FTIR and NMR spectroscopy, PXRD and TEM/SEM imaging revealed that ball milling gypsum in methanol induced a phase change to bassanite. The procedure was interrupted after different time intervals and monitored by TEM and SEM imaging. It was shown that gypsum platelets are broken up into needle-shaped nanoparticles. This is due to a reverse self-organization process. A stable bassanite dispersion was formed with longer grinding time. By using liquid NMR, the surfaces of the nanoparticles were shown to be functionalized by ethanol. The auxiliary is weakly and thus reversibly bound. The binding of the dispersant ethanol provides insight into the mechanism of dehydration and stabilization of gypsum compared to bassanite nanoparticles. HRTEM experiments also showed the formation of anhydrite, This leaves the question of whether prolonged milling in a polar solvent could even lead to complete dehydration of calcium sulfate. In summary, this study provides a novel and, most importantly, energy-saving synthetic route for the preparation of bassanite. This is important because bassanite (e.g., for gypsum boards) is one of the most important chemical products worldwide in terms of mass and volume, and its production requires an enormous amount of energy. Since the grinding process is easily scalable, energy (and thus greenhouse gas.emission) could be conserved on a large scale. Although *calcite* needs an ionic impurity for amorphization, a systematic investigation of the milling reaction of *monohydrocalcite* by PXRD and NMR revealed that the phase transformation to an amorphous intermediate (aMHC) is promoted by alcohols. This was confirmed by PDF analysis as well. From TGA/DTA and CP-NMR data, the amorphization could be related to a partial loss and substitution of structural hydrate water by ethanol. A

kinetically controlled recrystallization led to the formation of aragonite, assumed to be induced by Mg^{2+} contaminations from the controlled synthesis of monohydrocalcite. Thus, a synthesis to a new form of amorphous calcium carbonate could be achieved without the needs for ionic impurities. The reaction mechanism could be associated with a partial loss of water. Future research could be conducted to kinetically stabilize other phases (i.e., $CaCO_3$ hemihydrate) by tuning the water and magnesium content.

Hydrated layered silicates are a common class of synthetic silicates. Despite their wide use in composite applications, the structure of one particular silicate, magadiite, was unknown until the completion of this investigation. A major problem in the analysis of this hydrous sodium silicate was the lack of single crystals for structure determination and the inherent disorder in this material. Since the previous projects provided insights into layered structured materials, a systematic study of the synthetic parameters in the preparation of magadiite was carried out to improve its crystallinity. However, even with an optimized synthesis, structural characterization of magadiite by ADT was impossible due to the high beam sensitivity of the material.

Therefore, it was assumed that the structural disorder was due in particular to the hydrated interlayers and ion coordination with hydate water molecules. To circumvent the instability due to hydration, a partial replacement of the hydration water was performed by titration with ammonia. This resulted in a product that remained stable under the conditions of the TEM diffraction experiments. Thus, it was finally possible to determine the structure of the modified magadiite and subsequently to transfer the structural model to the structure of the pure magadiite. Based on titration experiments, a number of new questions emerged. Partially exchanged magadiite is relatively easy to access, so titration with an ion-sensitive electrode could provide information about the kinetics of the exchange. In addition, snapshots of the exchange reaction could be taken and evaluated using ADT to provide a general model for the chemical and structural arrangements that occur.

Overall, this work provides a fundamental insight into the phase transformations of mineral phases induced by milling. It is shown that phase transformations induced by inorganic additives provide access to new materials through controlled recrystallization processes. Thus, this work not only contributes to advancing the understanding of mechanochemical reactions, but also provides scalable methods for industrial manufacturing processes and applications.